Diagnosis of Mildly Relativistic Electron Velocity Distributions by Electron Cyclotron Emission in the Alcator C Tokamak

Kosuke Kato

Plasma Fusion Center
Massachusetts Institute of Technology
Cambridge, MA 02139

September 1986

DIAGNOSIS OF MILDLY RELATIVISTIC ELECTRON VELOCITY

DISTRIBUTIONS BY ELECTRON CYCLOTRON EMISSION

IN THE ALCATOR C TOKAMAK

by

KOSUKE KATO

Bachelor of Science and Master of Science
Massachusetts Institute of Technology
(1983)

Submitted to the Department of Nuclear Engineering
in Partial Fulfillment of the Requirements for the Degree of

DOCTOR OF SCIENCE IN NUCLEAR ENGINEERING

at the

MASSACHUSETTS INSTITUTE OF TECHNOLOGY

September 1986
© Massachusetts Institute of Technology 1986

Signature of Author _____
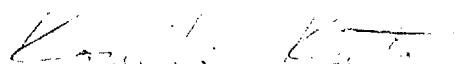
Department of Nuclear Engineering
August 12, 1986

Certified by _____

Ian H. Hutchinson, Thesis Supervisor

Accepted by _____

Allan F. Henry, Chairman,
Nuclear Engineering Departmental Committee

1

Diagnosis of Mildly Relativistic Electron Velocity
Distributions by Electron Cyclotron Emission
in the Alcator C Tokamak
by
Kosuke Kato
Submitted to the Department of Nuclear Engineering on August 12, 1986
in partial fulfillment of the requirements for the Degree of
Doctor of Science in Nuclear Engineering

Abstract

Mildly relativistic electron velocity distributions are diagnosed from measurements of the first few electron cyclotron emission harmonics in the Alcator C tokamak. The approach employs a vertical viewing chord through the center of the tokamak plasma terminating at a compact, high-performance viewing dump. The cyclotron emission spectra obtained in this way are dominated by frequency downshifts due to the relativistic mass increase, which discriminates the electrons by their total energy. In this way a one-to-one correspondence between the energy and the emission frequency is accomplished in the absence of harmonic superpositions. The distribution, described by f_p, the line-averaged phase space density, and Λ, the anisotropy factor, is determined from the ratio of the optically thin harmonics or polarizations. Diagnosis of spectra in the second and the third harmonic range of frequencies obtained during lower hybrid heating, current drive, and low density ohmic discharges are carried out, using different methods depending on the degree of harmonic superposition present in the spectrum and the availability of more than one ratio measurement. Results indicate generally parallel enhanced distributions for all three cases, with parameters in the range $1.4 \times 10^{-3} \leq \bar{n}_{tail}/\bar{n}_e \leq 3 \times 10^{-3}$, $80 \leq T_{eff}(keV) \leq 125$, $30 \leq T_{\perp}(keV) \leq 60$, and $180 \leq T_{\parallel}(keV) \leq 290$, qualitatively consistent with theoretical expectations. Discussions of transient phenomena, the radiation temperature measurement from the optically thick first harmonic, and the measurements compared to the angular hard X-ray diagnostic results illuminate the capabilities of the vertically viewing electron cyclotron emission diagnostic.

Thesis Supervisor: Dr. Ian H. Hutchinson
    Title: Associate Professor of Nuclear Engineering

Thesis Reader: Dr. Kim Molvig
    Title: Associate Professor of Nuclear Engineering

to Keiko

Acknowledgements

First and foremost, my greatest measure of gratitude goes to Professor Ian Hutchinson, my thesis supervisor. It was his continuing interest and close involvement with generous provision of assistance that made this thesis a reality. I have lost track of the countless times his limitless knowledge of the physical sciences helped me solve many difficult problems.

I am thankful to Dr. Steve Wolfe, with whom I have had the pleasure of long and friendly association, for his many precise advice and stimulating discussions.

Professors Jeff Freidberg, Lawrence Lidsky, Kim Molvig, and Dieter Sigmar are among the many faculty in the Nuclear Engineering Department whose teaching and criticisms on my project are responsible for my professional growth. I especially thank Professor Molvig for assuming the role of my thesis reader.

The pleasure of working with the Alcator group, headed by Professor Ron Parker, is priceless. Among the many scientific and technical staff, I would like to extend my sincere thanks especially to Professor Parker, Drs. Dave Gwinn, Bruce Lipschultz, Scott McDermott, Messrs. Frank Silva, Charles Park, Ed Thibeault, Frank Tambini, Bob Childs, Norton Pierce, Mark Iverson, Frank Shefton, Joe Bosco, Bill Parkin and Anatole Chernomordik for their dedicated efforts in the machine operation and assistance on my experiment. In short, they have kept me out of trouble and my experiment in working order. I also thank the Alcator RF group, Professor Miklos Porkolab, Drs. Steve Knowlton, Scott Texter, Yuichi Takase, and Paul Bonoli, without whose efforts most of the measurements would not have existed.

Laurie Pfeiffer, Carol Costa, Nancy Lee and their predecessors beginning with Layla McKnight and Saba Simsek, the Alcator secretaries, are a special breed of individuals whose ability to work with a smile on their faces under the most intense pressure clearly made a difference. I pale before the enormous burden of fully thanking each and every one of them.

Individuals who have been my fellow student colleagues enhanced the quality of my experience at the MIT Plasma Fusion Center immeasurably. These great friends include Drs. Dave Petti, Jeff Parker, Camilo Gomez, Rene LeClaire, Alan Wan, Godehard Hilfer, Joy Maneke, Messrs. John Machuzak, Arnie Pachtman, and Russ Benjamin.

I shall treasure forever the support and encouragement from my parents, Yukihiko and Yumiko, and the companionship (via the international telephone network) of my fiancée Keiko, to whom I dedicate this thesis.

4

Contents

List of Figures

9

List of Tables

Chapter 1

INTRODUCTION

1.1 Overview

1.1.1 Nuclear Fusion

Einstein's well-known equation[1],

$$E = mc^2 \tag{1.1}$$

states the equivalence of energy and mass. The conversion of mass into energy is commonly observed in nature in exothermic nuclear decay processes. Conventional nuclear reactors utilize exothermic fission reactions of heavy elements such as U^{235} or Pu^{239} at room temperatures to generate electricity.

Fusing of light nuclei, which is the reaction taking place in the sun and which is the process behind generation of nuclear fusion power, has a much higher temperature(energy) threshold, of above $1 \times 10^8 K$. The branch of fusion reaction pursued vigorously today owing to its relatively low temperature requirement and large reaction cross-section is

$$D + T \rightarrow He^4 + n + 17.6 keV, \tag{1.2}$$
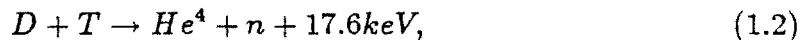
the so-called DT reaction. At present, the pursued method is to heat the deuterium-tritium mixture to the required temperature thermally, thus creating a dense hot ionized fluid called 'plasma'. For the energy from this reaction to break even

with the energy required to sustain this plasma, a temperature of approximately $10keV(116,000,000K)$ and a Lawson parameter(density(n) $\times$ energy confinement time(τ_E)) of approximately $10^{20}m^{-3}s$ are required.

1.1.2 Tokamak Approach to Fusion

Magnetic field lines, along which plasma particles are trapped, are used in order to confine high temperature high density plasmas. One of the magnetic 'bottle' configuration is called the *tokamak*[2], a Russian acronym for 'magnetic torus.' Schematic diagram of the tokamak concept is shown in Fig. 1.1. The main(toroidal) field, B_T, is produced by the windings around the torus(toroidal coils), while a secondary electric current, I_p, is produced in the plasma from the primary winding(ohmic heating coil) located in the hole of the torus. The poloidal magnetic field, B_p, induced by the plasma current is in turn used along with the toroidal field to create the field confining the plasma.

This tokamak approach is by far the most advanced amongst the many magnetic configurations today; its research being conducted at many institutions around the world. Problems with this configuration from the commercial reactor view point are its pulsed nature of operation, arising from the need to use the transformer action to create the confining field, and the tight space on the inboard side, which provides a formidable engineering problem of placing both the magnet and the energy recovering blanket structure there. Methods other than transformer induction are considered for the plasma current generation, and realistic designs of inboard assembly have been produced.

1.1.3 Motivation for Distribution Function Diagnosis

One way of sustaining the steady-state plasma discharge in a tokamak is to create the plasma current non-inductively. This can be done by using the lower hybrid current drive[3], or electron cyclotron resonance heating(ECRH)[4], both requiring injection of high power radio frequency waves. In either of these cases,

the resulting high energy electron distribution in velocity space deviates from the Maxwellian(thermal), and becomes appreciably anisotropic. Similar distributions can be created during 'runaway' or 'slideaway' discharges in tokamaks, usually occurring during the start-up or in a low density operation[5].

In these plasmas with anisotropic velocity distribution of electrons, the knowledge of the exact shape of the distribution is of vital importance. For example, in lower hybrid heated plasmas, the electron 'tail' which receives almost all the radio frequency(RF) energy may contain a considerable fraction of the total plasma kinetic energy, as well as carrying essentially all the current. Hence, the development of plasma diagnostics to measure the electron velocity distribution in these situations is motivated.

1.2 Background

1.2.1 Electron Distribution Diagnostics

For a Maxwellian(thermal) distribution, the determination of the density and the temperature completely specifies the distribution, and various diagnostics exist to measure these two quantities of the electron population. When the distribution is nonthermal however, more information is needed for detailed characterization of the population. Restricting the scope of our discussion to those diagnostics that measure quantities in addition to the 'density' and the 'temperature' of electrons, we find, as electron distribution diagnostics, the directional edge probe[6], angular bremsstrahlung measurement[7], and the use of electron cyclotron emission(ECE) with different degrees of sophistication[8].

The various ECE techniques are discussed below in a separate sub-section. The first two methods will be discussed briefly here. The directional edge probe is capable of measuring the velocity distribution of electrons along the magnetic field. However, since this is a material probe that perturbs the plasma, its use is limited

14

to fairly low(a few eV) temperature plasmas, such as those in a compact tabletop device or plasmas that exist at the extreme edge of larger devices.

The angular bremsstrahlung measurement is, at present, proven to measure parallel and perpendicular(to the magnetic field) temperatures. In particular, it is sensitive to the forward–backward asymmetry because of its angular view. It can also infer some information about the spatial profile of the non-Maxwellian distribution[9]. The difficulties involved with this diagnostic are the fairly complicated deconvolution process, and the presently low count rate of X-rays, which requires the signal to be integrated over many plasma discharges resulting in the loss of temporal information in the process.

1.2.2   Electron Distribution Diagnostics using ECE

ECE is a widely researched and documented subject with well established theories [10,11], and it offers the capability for diagnosing thermal plasma parameters, T_e and n_e[12]. In practice, although T_e-profile measurements using the second harmonic extraordinary mode emission that take advantage of the $1/R$ magnetic field variation have been successful on a number of tokamaks[13,14,15,16], two effects sometimes prevent straightforward interpretation of the data by simple theory of emission from a plasma in thermal equilibrium. These effects are multiple wall reflections and superthermal electron emissions[17]. Multiple wall reflections have the effect of enhancing and depolarizing the emission, and superthermal electrons radiate copiously even though their population may be a minute fraction of the bulk electron population.

Since ECE spectrum is very sensitive to the high energy electron population, it is ideally suited for their detection, and detailed analysis of this population can in principle be achieved. The effort towards this end can be divided into three categories. First, theories of emission from general arbitrary distribution of electrons are needed. Then, based on these theories, an algorithm by which the observed ECE spectra can result in the determination of the radiating electron distribution should

be established. Finally, the experimental measurements, subject to the constraints imposed by the algorithm(such as a specific viewing angle), must be carried out.

At the most general level, theoretical works investigate the electron cyclotron emission from arbitrary energetic distributions, taking into account the effect of the cold background plasma[18]. Numerical calculations provide insight into the variation in the emissivity with the propagation angle, plasma density, and other parameters of the model distribution, such as the Maxwellian temperature and its shift[19]. Theoretical works narrower in focus target anisotropic distributions of the specific origin(e.g., runaway and RF current drive) to produce analytical relationships between the emission and the distribution[20,21], allowing simplified interpretations which are, in some cases, made possible by the a priori assumption of the distribution shape stemming from the physical process of its creation(e.g., the lower hybrid current drive wave couples to electrons within a specific energy range).

It is difficult to apply these numerical and analytical models to the actual measurements, because modifications to the ideal plasma emission that are unique to each experiment inevitably take place. Although numerical investigations taking into account the tokamak configuration exist[22,23], such considerations are probably best treated on a case-by-case basis.

Perhaps for this reason, the distribution function determination algorithm development often evolves concurrently with the experimental measurement itself. Here, two different categories exist. Nonthermal ECE creates two signatures on the spectrum different from a low temperature thermal spectrum. First is the high intensity emission at low($l \leq 3$) harmonics, at frequencies not limited to the thermal resonances. This is caused by the relativistic electron mass increase and the Doppler effect. These emissions have structures arising from the energetic distribution itself, as well as from the bulk thermal plasma effects. Second is the appearance of

high intensity emission at high($l \geq 4$) harmonics, where now, due to the small optical depth and the large relativistic broadening, the spectrum is usually a smooth continuum with a logarithmic slope.

The continuum measurement is less sensitive to the exact viewing geometry in general, but with at most two slopes of the continuum(extraordinary(X) and ordinary(O) mode) to work with, the number of parameters that can be measured is limited. The discrete harmonic measurement has the advantage of a possibility for a much more resolved (in energy) analysis, but this depends critically on controlling the field of view.

The use of continuum spectra to measure the temperature and a loss-cone or an anti-loss-cone angle has been performed on EBT[24] and PLT[25]. Prescriptions for distribution function determination in this area include the identification of parameter(temperature and characteristic pitch-angle) space for which either the polarization ratio or the harmonic slope is a sensitive measurement of the parameters, supported by tabulation of numerical results[26,27,28].

The use of low harmonic, discrete spectra to obtain the distribution has been tried in both mirrors and tokamaks. In mirrors with MeV electrons[29,30], $\beta = \beta_\perp$ is assumed and $f(\gamma)$ profile is deduced from the measurement of the low harmonic spectrum. In toroidal devices, a radial view has been used to measure the down-shifted nonthermal population in ASDEX[31] and Wega stellarator[32]. The interpretation is difficult however, since nonthermal emission from the center and thermal reabsorption from the outboard side of the toroidal plasma compete at the same frequencies. Hence, in this horizontal configuration, only a few parameters are deduced. In PLT, a vertical view was used to measure transmission of down-shifted first harmonic frequency[33], the result of which is also fitted by a distribution function of a few parameters.

Multiple wall reflections contaminate most measurements. For the continuum measurement, polarization scrambling prevents the use of I_o/I_x ratio, where I_o and I_x are the ordinary and extraordinary mode intensities respectively. Unavailability

of a reliable polarization ratio of the continuum may severely limit deducible parameters. In the low harmonic discrete measurement, Doppler broadening introduced by multiple reflections may be on the order of the harmonic structure width, severely distorting the latter. In all documented cases, the polarization, $(I_x - I_o)/(I_x + I_o)$, appear too large for it to be entirely due to the plasma temperature effect. The values usually are up to 50% for thermal plasmas of at most a few keV[34]. Numerical models that account for wall reflections have been used to estimate the tail characteristic(with a few parameters) from TFR[35].

Attempts to control the wall reflection take on many forms. With two sufficiently large apertures at opposite ends of the confinement chamber, a carefully aimed and focussed viewing chord will avoid the wall reflection altogether, although some reflections from the windows will remain[36]. A similar approach is possible with a single aperture and a retro-reflector(usually a spherical mirror) at the target area of the vacuum vessel[8,24]. A more exotic approach is to use efficient microwave absorbers placed on the vacuum vessel wall.

In summary, many innovative works have succeeded in characterizing the non-thermal electron distribution in plasma confinement devices. The characterization is at present limited to a few parameters, or to a class of distributions with a priori restrictions regarding their shape. The obstacle to obtaining complete description of the distribution has been the difficulties associated with the measurement of just the desired quantity. These difficulties include those that are inherent in ECE physics, such as the harmonic overlap at high harmonics and large energies, and those that are constraints from the experiment, such as wall reflections.

1.3 Vertical Viewing ECE Diagnostic

In an attempt to obtain more detailed information about the electron velocity distribution from ECE, the Alcator C vertical viewing electron cyclotron emission(VECE)

diagnostic was conceived. The first few cyclotron harmonics are targeted for the measurement in order to obtain maximum detail.

Detailed theory is provided in Chapter 2. Here, a simplified picture is given to illuminate the concept. When a perpendicular ECE from a region of constant magnetic field is measured, the frequency broadening is dominated by downward shifts in frequency due to the relativistic mass increase. In this way, the electrons can be discriminated according to their total energy. To determine the pitch-angle distribution of the electrons at each of these energies, polarization or harmonic ratios of emissions, which are sensitive measures of the anisotropy, are measured at each energy level. With the anisotropy information in hand, a single harmonic spectrum can then be used to deduce the absolute number density of the distribution for each energy. Such a distribution determined in this way can be characterized by the phase space density and an anisotropy parameter.

The critical requirement for this diagnostic is that frequency broadening mechanisms other than the relativistic broadening be eliminated or contained to manageable levels. It is for this reason that the vertical view through the center of a tokamak plasma is employed to suppress field and Doppler broadening.

To insure isolation of this viewed region, an efficient microwave absorber(viewing dump) is used to suppress the wall reflected radiation. Such a dump poses challenging design problems since it must be placed inside the Alcator C vacuum chamber, which requires it to be compact, vacuum compatible, and to be able to withstand the high particle and heat fluxes. The restricted access of Alcator C also necessitated novel approaches to the focussing optics design.

1.4   Alcator C Tokamak

The Alcator C tokamak at the M.I.T. Plasma Fusion Center[37] is a compact, very high field tokamak of high performance which has made significant contributions to the effort of fusion power development and the understanding of plasma behavior.

Machine Design and Performance

Major machine parameters and typical plasma parameters are given in Table 1.1 while the cutaway view is shown in Fig. 1.2. The Alcator C machine design was based on a philosophy that fusion relevant plasmas can be created by first going to high density(using high magnetic field) rather than building a machine whose plasma dimensions are larger and closer to the reactor size. High field is achieved by toroidal field coils of Bitter plate construction, for which expertise exists at M.I.T.'s Francis Bitter National Magnet Laboratory. Powerful ohmic and equilibrium field coils complete the set. The entire machine is cooled by liquid nitrogen to lower the electrical resistance and hence the power dissipation. A disadvantage of using this Bitter plate construction is the extremely tight space left for the access ports[38].

Standard plasma diagnostics on Alcator C include magnetic measurements using current loops; FIR(far infrared) density interferometer; Thomson scattering electron temperature diagnostic; ECE electron temperature diagnostic; soft and hard X-ray electron temperature diagnostics; D-D product neutron counter and charge exchange ion temperature diagnostics; and different edge plasma and impurity spectroscopy diagnostics in operation at various times.

Noteworthy Achievements

Alcator C was built as the successor to Alcator A[39], which in 1978 attained the then record Lawson parameter of $n\tau_E = 3 \times 10^{19} m^{-3} s$[40]. Alcator A also established the 'Alcator Scaling', $\tau_E \propto na^2$, an observation that the energy confinement time scales linearly with the plasma density. Alcator C, with a larger minor radius to exploit the 'Alcator Scaling', in turn produced a new scaling result, the 'neo-Alcator Scaling', $\tau_E \propto nR^2a$. Other tokamaks' Lawson parameters are found to obey this scaling law closely[40].

In addition to standard ohmically confined plasma experiments, Alcator C has made significant contributions in the areas of frozen pellet fueling and lower hybrid RF current drive and heating. By injecting frozen pellets of hydrogen fuel into the plasma at high velocities, the density can be increased without degrading confinement. The result was the achievement for the first time of the breakeven Lawson condition(at higher temperatures) of $n\tau_E = 8 \times 10^{19} m^{-3} s$ in 1983[41]. The performance of Alcator C plasma is shown in a diagram plotting $n\tau$ vs. T_i(ion temperature) along with other tokamaks' achievements in Fig. 1.3. Using over $1MW$ of $4.6GHz$ lower hybrid waves injected by phased waveguide arrays, non-inductive current of up to $I_p \simeq 200kA$ was driven, and heating of $\Delta T_e \sim \Delta T_i \sim 1keV$ has also been achieved[42,43].

1.5 Thesis Organization

This thesis consists of seven chapters including the present one, and two appendices. Chapter 2 formulates the theory behind the VECE distribution diagnostic, identifying key quantities of interest. Numerical and analytical studies of these quantities reveal the relationship between the electron distribution shape and the emissivity. Here the special form for describing the electron distribution that takes full advantage of measured parameters is defined for use throughout the thesis. Issues related to the implementation of the measurement are also discussed.

Chapter 3 describes the key components constituting the diagnostic. Specific topics include the Michelson interferometer, the viewing dumps, diffraction analysis, the data acquisition environment, and the calibration.

In Chapter 4, measured VECE data are analyzed to determine the system performance, and are interpreted in comparison to conventional horizontal ECE data and theoretical expectations. The need for post processing of measured spectrum prior to the distribution function analysis is also assessed.

21

In Chapter 5, we present three different approaches to the distribution function diagnosis of the VECE data, depending on the origin of the radiating electrons and availability of additional information. The three different cases are the lower hybrid heating discharge, the lower hybrid current drive discharge, and the low density ohmic discharge.

In Chapter 6, the measured distribution functions are discussed in relation to and in terms of more conventional parameters used to describe such distributions. Comparison with theoretical models and other experimental observations, and analyses of transient phenomena are included.

In Chapter 7 the entire work is summarized. We also propose topics of interest for future studies.

Throughout this thesis, the term 'frequency' is used in a broad context. Mathematical expressions often employ ω to denote the frequency while numerical results favor f or ν $(f = \nu = \omega/2\pi)$.
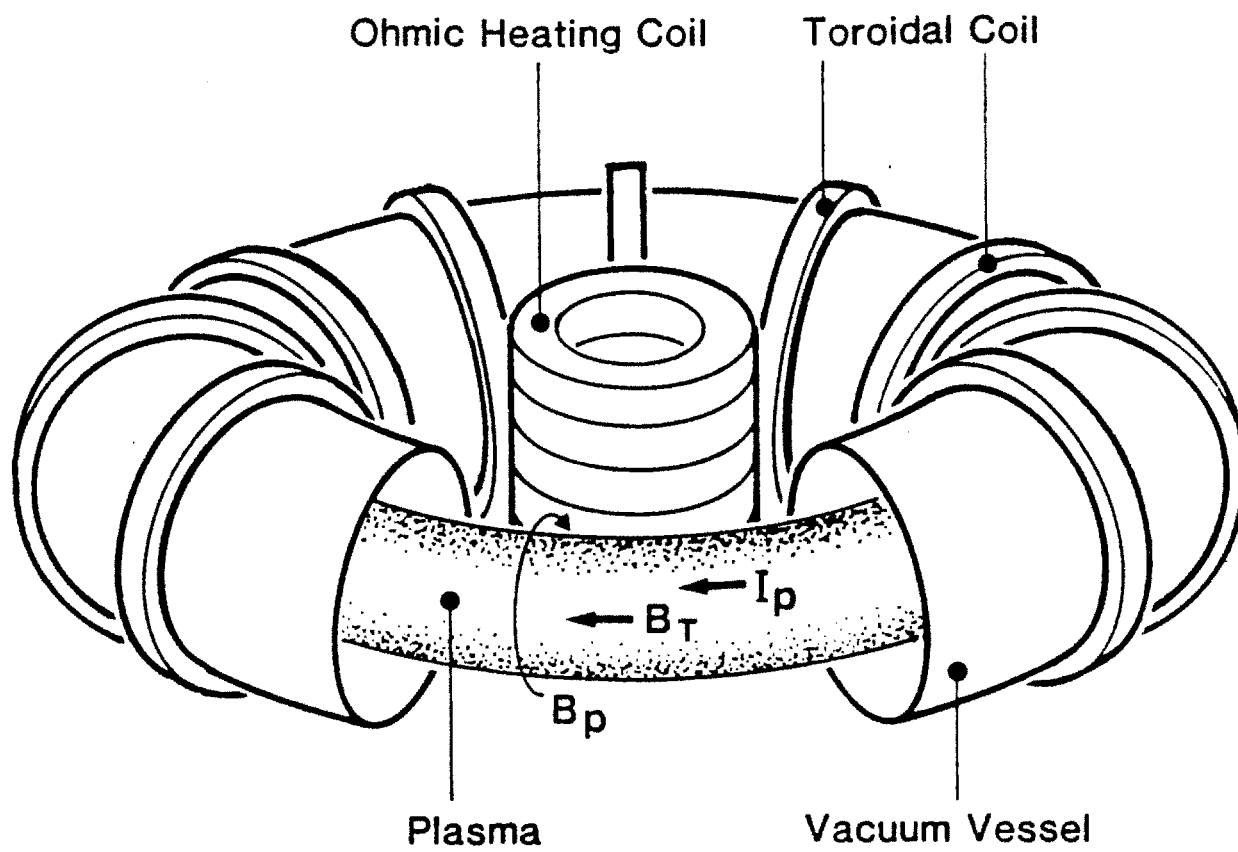
Figure 1.1:
A schematic figure of a tokamak experimental device.
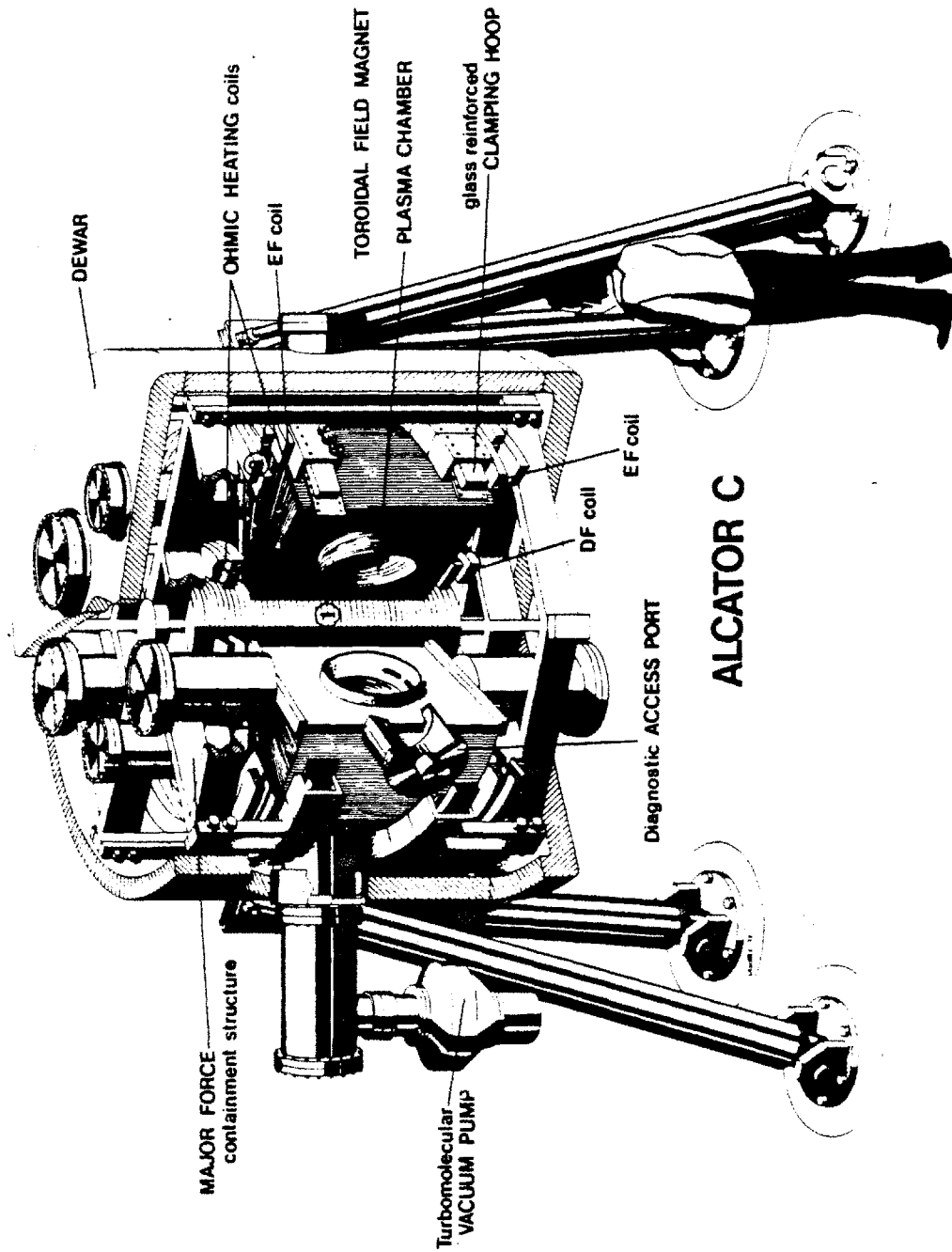
Figure 1.2:
A cutaway view of the Alcator C tokamak.
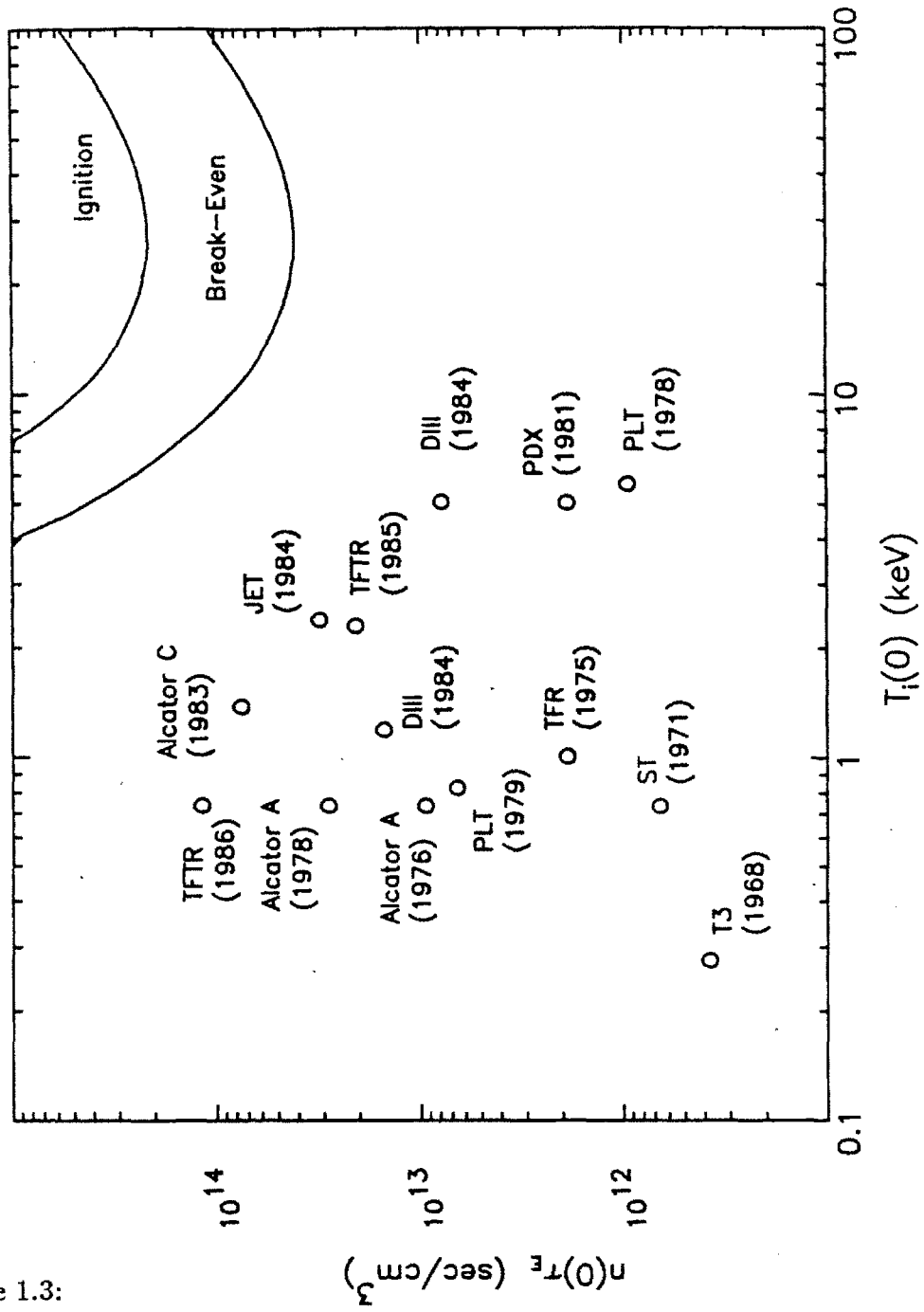
Figure 1.3:
Lawson diagram with experimental data points from major tokamak experiments.

Table 1.1:
Alcator C machine and plasma parameters[44].

Quantity	Symbol	Value
Major Radius	R	$64cm$
Minor Radius	a	$16.5cm(11.5cm)$
Toroidal Field	B_T	$\leq 12T$
Plasma Current	I_p	$\leq 1MA$
Plasma Density	n_e	$1 \times 10^{19} - 2 \times 10^{21}m^{-3}$
Electron Temperature	T_e	$1 - 3keV$
Ion Temperature	T_i	$0.6 - 1.5keV$
Energy Confinement Time	τ_E	$\leq 50ms$
Lawson Product	$n\tau$	$\leq 8 \times 10^{19}m^3s$
LHRF Power	P_{LH}	$\leq 3MW(4.6GHz)$
ICRF Power	P_{IC}	$\leq 0.5MW(200MHz)$
Peak Power Requirement	P_P	$\leq 240MW_e$
Pulse Length	τ_{pulse}	$\leq 0.5s$

Chapter 2

THEORY

2.1 Introduction

In this chapter, a new algorithm based on established physical treatment of electron cyclotron emission and absorption physics for the interpretation of nonthermal electron cyclotron emission spectra measured by the VECE diagnostic is given.

The physics of electron cyclotron emission and absorption is a widely researched and documented field[45], so that any attempt here at a concise and complete summary of the subject would be difficult at best, and probably redundant. Therefore, we shall concentrate only on the aspect of the theory directly relevant to the VECE spectrum interpretation. Section 2.2 discusses the electron cyclotron resonance condition that is of relevance to all distribution function measurements, with specific emphasis on the case of our diagnostic where the perpendicular propagation is measured. Section 2.3 and 2.4 treats emission and absorption, respectively. More emphasis is placed on the discussion of emission since this is the major quantity of interest, and since similar aspects of absorption processes can be derived from the emission counterpart. In Section 2.5, implementation issues, which include the interpretation under finite absorption conditions and practical experimental considerations, are discussed. Section 2.6 shows qualitatively the effects of harmonic superposition on the distribution parameters we seek to measure. Section 2.7 is the chapter summary.

2.2 Vertical Viewing ECE Resonance

The general resonance condition between an electron in a magnetic field and electromagnetic radiation of frequency ω can be written,

$$\omega = \frac{l q_e B}{m_e \gamma} \frac{1}{1 - \beta_{\parallel} \cos\theta},$$
(2.1)

where q_e is the electron charge, m_e is the electron rest mass, γ is the relativistic factor, $1/\sqrt{1 - v^2/c^2}$, $\beta_{\parallel} = \vec{v} \cdot \vec{B}/c$, and θ is the angle between the propagation vector, $\vec{k}$, and the magnetic field. Thus, there are three frequency(spectral line) broadening mechanisms apparent in Eqn. 2.1. First is the magnetic field broadening. This mechanism is the basis for the highly successful electron temperature profile measurement in tokamaks where $B = B(R)$[12]. Second is the frequency broadening downward due to increase in energy, through increase in γ. Thirdly, for non-perpendicular emission from electrons with finite parallel velocity, the familiar Doppler shift(up or down) is introduced.

In general, a casual view of an experimentally produced, magnetically confined plasma will result in contributions from all three broadening mechanisms, primarily due to the multiple reflection of radiation off metallic walls used to contain the plasma. When the magnetic field and the propagation angle are fixed however, the resonance frequency ω maps to an elliptical 'resonance contour' in momentum space, described by,

$$\frac{(p_{\parallel} - d)^2}{a^2} + \frac{p_{\perp}^2}{b^2} = 1,$$
(2.2)

where

$$a^2 = \left[\frac{l^2 \Omega^2}{\omega^2 (1 - N_{\parallel}^2)} - 1 \right] \frac{1}{(1 - N_{\parallel}^2)}$$

$$b^2 = \left[\frac{l^2 \Omega^2}{\omega^2 (1 - N_{\parallel}^2)} - 1 \right]$$
(2.3)

$$d = \frac{l \Omega N_{\parallel}}{\omega (1 - N_{\parallel}^2)},$$

28

Ω is the fundamental rest-mass cyclotron frequency($q_e B/m_e$), and $N_\parallel$ is the parallel refractive index, $kc\cos\theta/\omega$. $p_\parallel$ and $p_\perp$ are the normalized parallel and perpendicular(to the magnetic field) electron momentum, respectively. Thus, elimination of magnetic field and Doppler broadening effects(i.e., measurement of emissions from a specific propagation angle) yields discrimination of electrons in momentum space, described by these elliptical contours. Further simplification of the electron grouping is accomplished for $\theta = \pi/2$ ($N_\parallel = 0$), i.e., perpendicular propagation, where the resonance contour becomes a circle($d = 0, a^2 = b^2$) and the discrimination is over total electron energies. Resonance contours in momentum space, for representative values of $N_\parallel$ and ω/Ω, are given in Fig. 2.1.

In this thesis, the case of perpendicular propagation, $N_\parallel = 0$, is considered exclusively, for which the resonance condition reduces to

$$\omega = \frac{l\Omega}{\gamma}. \tag{2.4}$$

Thus, electrons can be discriminated in frequency space according to their total momentum(energy). We justify this choice by noting that it is the simplest one, requiring a minimum of deconvolution analysis. It is also the most realistic in terms of the experimental geometry. In addition, this choice also minimizes the harmonic superposition(see Section 2.6). A notable drawback of perpendicular emission measurement is the lack of information on the parallel asymmetry. This has consequences for the analysis of decidedly asymmetric distributions present during lower hybrid RF current drive or electron runaway discharges.

2.3 Cyclotron Emission

The general single particle emission coefficient for electrons in a vacuum magnetic field is given by[11]

$$\eta(\omega, v, \theta) = \frac{q^2\omega}{8\pi^2\epsilon_o c} \left\{ \sum_1^\infty \left(\frac{\cos\theta - \beta_\parallel}{\sin\theta} \right)^2 J_l^2(x) + \beta_\perp^2 J_l'^2(x) \right\} \delta(y) \tag{2.5}$$

where

$$x = \frac{\omega\gamma}{\Omega}\beta_\perp \sin\theta$$

$$y = l\frac{\Omega}{\gamma} - \omega(1 - \beta_\parallel \cos\theta)$$

and J_l is a Bessel function of order l. The quantity y is just the resonance condition of Eqn. 2.1. Neglecting collective effects, emissivity from a unit volume of plasma is a straightforward sum of the contribution from all the particles so that

$$j(\omega, \theta) = \int \eta(\omega, v, \theta) f(v) d^3 v. \tag{2.6}$$

2.3.1 Perpendicular Emission Coefficient

As stated previously, we shall restrict our discussion to perpendicular propagation ($\theta = \pi/2$). We also restrict our analysis to the range of frequency where low temperature thermal cyclotron resonance does not exist. This is justified since our interest lies in emissions from electrons whose γ is appreciably different from unity. This is not to say that the background plasma is unimportant, however. The bulk cold plasma population is assumed to determine the wave properties such as the refractive index and the polarization. In this case,

$$j_l(\omega) = \frac{e^2\omega^2}{8\pi^2\epsilon_o c}\frac{N_r^2}{N_\pm} \int \left\{ \frac{p_\parallel J_l}{N_- K J_l \gamma + p_\perp J_l'} \right\}^2 \frac{1}{\gamma^2}\delta\left(\omega - \frac{l\Omega}{\gamma}\right) f(\vec{p}) d^3 p, \tag{2.7}$$

where upper and lower signs and terms correspond to ordinary (Ewave $\parallel B_{\text{external}}$) and extraordinary ($E$wave $\perp B_{\text{external}}$) modes of propagation, respectively[18]. This is a more general form of Eqn. 2.5, where normalized momentum, $p = v\gamma/c$, is used instead of β, $f(\vec{p})$ is the unnormalized electron momentum distribution, and

30

N_r is the ray refractive index[11],

$$N_r^2 = \left| N_\pm^2 \sin\theta \frac{\left[1 + \left(\frac{1}{N_\pm}\frac{\partial N_\pm}{\partial\theta}\right)^2_\omega\right]^{1/2}}{\frac{\partial}{\partial\theta}\left\{\frac{\cos\theta + \left(\frac{1}{N_\pm}\frac{\partial N_\pm}{\partial\theta}\right)_\omega \sin\theta}{\left[1 + \left(\frac{1}{N_\pm}\frac{\partial N_\pm}{\partial\theta}\right)^2_\omega\right]^{1/2}}\right\}} \right|. \tag{2.8}$$

The argument of the Bessel functions, J_l, is $lN_\pm p_\perp/\gamma$, and K is defined as

$$K \equiv \frac{\omega_p^2 \Omega\omega}{(\omega^2 - \omega_p^2)^2 - \Omega^2\omega^2}, \qquad \omega_p^2 = \frac{n_e e^2}{m_e \epsilon_o} \tag{2.9}$$

where ω_p is the familiar electron plasma frequency. Compared with Eqn. 2.5, this expression separates out the two modes of propagation(which is well resolved at $\pi/2$ propagation) and is expressed for a single harmonic. Further, the effect of finite density has added a refractive index term and an extra K term in the X-mode expression.

The delta function in Eqn. 2.7 can be evaluated in spherical coordinates (p, θ_p, ϕ_p) to give

$$j_l(\omega) = \frac{e^2\omega}{8\pi^2\epsilon_o c} 2\pi p^3 \frac{N_r^2}{N_\pm} \int_0^\pi \left\{ \begin{array}{c} \cos\theta_p J_l \\ N_- K(\gamma/p)J_l + \sin\theta_p J_l' \end{array} \right\}^2 f \sin\theta_p d\theta_p, \tag{2.10}$$

where we have assumed gyro-symmetry in the ϕ_p(azimuthal) direction, and θ_p denotes the momentum pitch-angle. The remaining integral is over the sphere $p = \sqrt{(l\Omega/\omega)^2 - 1}$. Thus, given f, general emission spectrum can be evaluated at each value of momentum.

2.3.2 VECE Electron Distribution

It is desirable to derive the parameters which define the distribution directly and uniquely from measured quantities. This consideration results in the choice of our distribution introduced below.

31

We choose, as our distribution,

$$f(\vec{p}) = f_p(p)f_\theta(p, \theta_p), \tag{2.11}$$

where $f_p(p)$ is the line-averaged phase space density of electrons at p, and f_θ is the pitch-angle distribution of electrons at p. Hence, consistent with this definition, we further define (in an 'ad hoc' manner) the form of f_θ,

$$f_\theta(p, \theta_p) = L \exp\{-\Lambda(p) \cos^2 \theta_p\}, \tag{2.12}$$

where L is the normalization constant[1],

$$L = 2\sqrt{\frac{\Lambda}{\pi}} \frac{1}{\mathrm{erf}(\sqrt{\Lambda})}, \tag{2.13}$$

so that

$$\int_0^\pi f_\theta(p, \theta_p) \sin \theta_p d\theta_p = 2. \tag{2.14}$$

The quantity Λ is henceforth referred to as 'the anisotropy factor'. A positive Λ implies a loss-cone type of distribution(oblate in shape), and a negative Λ implies an enhancement in the parallel direction(prolate). When $\Lambda = 0$, the pitch-angle distribution is isotropic. The pitch-angle distribution, f_θ, is plotted for different Λ as a function of θ_p in Fig. 2.2. In the case of extreme anisotropies, $|\Lambda| >> 1$, this choice of f_θ approximates a gaussian spread along $p_\parallel = const.$ ($\Lambda << -1$), or $p_\perp = const.$ ($\Lambda >> 1$).

Note that f_θ defined in this way cannot distinguish parallel asymmetry. No loss of information occurs however, since parallel asymmetry cannot be determined from the vertical viewing ECE resonance in any case as discussed in Section 2.2. A Maxwellian distribution (of temperature $= T$) can be described by this form by setting $f_p(p) \rightarrow \exp\{\sqrt{1 + p^2}m_e c^2/T\}$ and $\Lambda = 0$ for all p.

---

[1]Error function of imaginary argument(for $\Lambda < 0$) is to be interpreted, via the defining integral, as a 'Dawson' function.

We shall, for future use, define the pitch-angle integral in Eqn. 2.10 as

$$\Theta_l^{\pm}(p) \equiv N_{\pm} \int_0^{\pi} \left\{ \begin{array}{c} \cos\theta_p J_l(x_+ \sin\theta_p) \\ N_- K_p^{\gamma} J_l(x_- \sin\theta_p) + \sin\theta_p J_l'(x_- \sin\theta_p) \end{array} \right\}^2 f_\theta \sin\theta_p d\theta_p. \quad (2.15)$$

where $x_{\pm} = lN_{\pm}p/\gamma$. Thus, all the pitch-angle information is contained in $\Theta_l^{\pm}(p)$, and

$$j_l^{\pm}(\omega) = \frac{e^2 \omega}{8\pi^2 \epsilon_o c} 2\pi p^3 \frac{N_r^2}{N_{\pm}^2} f_p \Theta_l^{\pm}(p). \quad (2.16)$$

It is convenient to work with $\Theta_l^{\pm}$ instead of $j_l^{\pm}$ since the former is independent of the actual frequency, magnetic field strength, and the plasma density(in the tenuous limit). Also for the purpose of comparing different harmonic or polarization emissions from the *same* electrons, most of the proportionality constants are removed in $\Theta_l^{\pm}$. For example, the harmonic and the polarization ratios are given in terms of Θ by

$$\frac{j_l}{j_m} = \frac{l\Theta_l}{m\Theta_m}, \quad \text{and} \quad \frac{j^+}{j^-} = \frac{\Theta^+}{\Theta^-}. \quad (2.17)$$

Note that only f_θ can be determined from these ratios. Relative f_p can be determined from a single spectrum of Θ and uncalibrated intensity, but the full emissivity equation must be used to determine f_p absolutely.

2.3.3 Tenuous Plasma

In the limit $\omega >> \omega_p$, the description of $\Theta_l^{\pm}(p)$ can be simplified considerably. This limit is applicable to high($l \geq 3$) harmonics in most present day experiments, or to harmonics as low as the second in low density discharges. Setting $N_{\pm} = N_r = 1$ and $K = 0$ for this limit in Eqn. 2.15, we obtain

$$\Theta_l^{\pm}(p, \Lambda) = 2 \int_0^{\pi/2} \left\{ \begin{array}{c} \cos\theta_p J_l(x \sin\theta_p) \\ \sin\theta_p J_l'(x \sin\theta_p) \end{array} \right\}^2 L \exp(-\Lambda \cos^2\theta_p) \sin\theta_p d\theta_p, \quad (2.18)$$

where we have taken advantage of the assumed parallel symmetry and reduced the range of the integral. Figs. 2.3 through 2.6 plot $\Theta_l^{\pm}$ for $l = 1$ through 4 as a function

33

of Λ for different electron energies. Note the difference in variation with Λ between the two modes.

Fig. 2.7 plots the third-to-second harmonic ratio, $j_3^\pm/j_2^\pm$, for the two modes. A larger ratio implies positive Λ or perpendicular enhancement of the distribution. In Fig. 2.8, the polarization ratios at the second and the third harmonic are plotted. The polarization ratios for the two harmonics are quite similar. For the polarization, large ratio implies negative Λ or parallel enhancement.

2.3.4 Extreme Anisotropies

As noted above, for $|\Lambda| \gg 1$, the shape of f_θ approximates gaussian distributions parallel to $p_\perp$ or $p_\parallel$ axis. Simplifications to ratio calculations can be made in this situation, and some revealing analytical results are obtained.

Strong Parallel Enhancement, $-\Lambda \gg 1$

In this case, the electrons are confined to a narrow 'cigar shaped' region along the $p_\parallel$ axis. Approximating $\sin\theta_p \simeq \theta_p$, $\cos^2\theta_p \simeq (1 - \theta_p^2)$, and $J_l \simeq (x\theta_p/2)^l/l!$ (since $J_l(\Delta) \simeq (\Delta/2)^l/l!$ for $\Delta \ll 1$), we obtain

$$f_\theta \simeq 2(-\Lambda)\exp(\Lambda\theta_p^2), \tag{2.19}$$

where the normalization is derived from applying Eqn. 2.14. Then,

$$
\begin{aligned}
\Theta_l^\pm &\simeq 2\int_0^\infty \left\{ \begin{array}{c} (x\theta_p/2)^l/l! \\ l(x\theta_p/2)^l/xl! \end{array} \right\}^2 (-\Lambda)\exp(\Lambda\theta_p^2)2\theta_p d\theta_p \\
&= \frac{2}{(-\Lambda)^l l!}\left(\frac{pl}{2\gamma}\right)^{2l}\left\{ \begin{array}{c} 1 \\ \gamma^2/p^2 \end{array} \right\},
\end{aligned} \tag{2.20}
$$

where we have used $x = lp/\gamma$ in the second identity. Note that the integral is now effectively over a vertical straight-line segment(dashed line in Fig. 2.9(a)) on

which $f \propto \exp(\Lambda p_\perp^2/p^2)$. Therefore, this limit models a distribution with gaussian perpendicular variation corresponding to a 'perpendicular temperature',

$$T_\perp = \frac{m_e c^2}{-\Lambda} \frac{p^2}{2\gamma},$$
(2.21)

by analogy to a conventional gaussian, $\exp\{-m_e\gamma v_\perp^2/2T_\perp\}$. In this limit of narrow perpendicular spread, the emissivity of the l-th harmonic is proportional to the $2l$-th moment of the perpendicular momentum. We evaluate Eqn. 2.10 in this limit with

$$\begin{aligned}
\cos\theta_p J_l &= (lp_\perp/2\gamma)^l/l! \\
\sin\theta_p J_l' &= (lp_\perp/2\gamma)^l \gamma/(lpl!),
\end{aligned}$$
(2.22)

and change the integration variable from θ_p to $p_\perp$ to obtain

$$j_l^\pm \simeq \frac{e^2\omega}{8\pi^2\epsilon_o c} \frac{2}{p} \left(\frac{l}{2\gamma}\right)^{2l} \frac{1}{l!^2} \left\{\frac{p^2}{\gamma^2}\right\} \int_0^\infty f(\vec{p}) p_\perp^{2l} 2\pi p_\perp dp_\perp.$$
(2.23)

This is true regardless of the shape of f[21]. In the event that f is gaussian, the ratio of the harmonics directly provides the perpendicular temperature.

The error in Θ produced by the use of the straight-line approximation rather than the full pitch-angle integral can be estimated by recognizing that the integral is dominated by contributions from a rather narrow region in θ_p near the peak of the integrand of Eqn. 2.20, $\propto \theta_p^{2l+1} \exp(\Lambda\theta_p^2)$. This angle, $\theta_p|_{max}$ is given by

$$\theta_p|_{max}^2 = \frac{2l+1}{-2\Lambda},$$
(2.24)

from straightforward maximization by differentiation.

The crucial difference between the straight-line approximation and the proper angle integral is then that the straight-line integral is over $p_\parallel = const.$ rather than

35

$p = const.$ At the maximum angle $\theta_p|_{max}$ then, the value of the total momentum, p_{max}, is larger for the straight-line approximation by the factor

$$\left(1 + \frac{p_{\perp max}^2}{p_{\parallel}^2}\right)^{1/2} \simeq \left(1 + \frac{2l+1}{-2\Lambda}\right)^{1/2}. \tag{2.25}$$

Therefore, substituting p_{max} for p in the last expression of Eqn. 2.20, we obtain an estimate of Θ_l for the straight-line approximation which is larger than that for the proper($p = const.$) angle integral by the factor

$$\left(1 + \frac{2l+1}{-2\Lambda}\right)^{\left\{\begin{array}{c} l \\ l-1 \end{array}\right\}}. \tag{2.26}$$

Thus, for example, the value of $T_{\perp}$ deduced from the ratio, j_3/j_2 using the 'straight-line' approximation is an overestimate by already 25% when $\Lambda \simeq -20$. Hence this approximation is accurate only for extremely parallel-enhanced distributions.

Strong Perpendicular Enhancement, $\Lambda >> 1$

When $\Lambda >> 1$, the electron distribution is restricted to a 'disc' near the $p_{\perp}$ axis. Therefore, setting $\sin\theta_p = 1$, and $\cos\theta_p = \pi/2 - \theta_p = \phi$, we find

$$f_\theta \simeq 2\sqrt{\frac{\Lambda}{\pi}} \exp\{-\Lambda\phi^2\}. \tag{2.27}$$

Again from Eqn. 2.18 we obtain,

$$\Theta_l^{\pm} \simeq \left\{\begin{array}{c} J_l^2(x) \\ J_l'^2(x) \end{array}\right\} 2 \int_0^{\infty} \left\{\begin{array}{c} \phi^2 \\ 1 \end{array}\right\} 2\sqrt{\frac{\Lambda}{\pi}} \exp(-\Lambda\phi^2)d\phi \tag{2.28}$$

where now, Bessel functions are independent of the pitch-angle dependence. Thus,

$$\Theta_l^{\pm} \simeq \left\{\begin{array}{c} J_l^2(x)/\Lambda \\ 2J_l'^2(x) \end{array}\right\}. \tag{2.29}$$

36

In this case, the approximately straight line segment shown in Fig. 2.9(b), to which the integral is restricted, is horizontal and $f \propto \exp(-\Lambda p_{\parallel}^2/p^2)$, modelling a distribution with gaussian parallel variation with a parallel temperature,

$$T_{\parallel} = \frac{m_e c^2}{\Lambda} \frac{p^2}{2\gamma}, \tag{2.30}$$

in the same manner as Eqn. 2.21. The emissivity is in fact a simple moment of the parallel momentum, again regardless of the precise form of the distribution. Using $p_{\parallel} = p\phi$,

$$j_l^{\pm}(\omega) \simeq \frac{e^2 \omega}{8\pi^2 \epsilon_o c} \left\{ \begin{array}{c} J_l^2(x) \\ J_l'^2(x) \end{array} \right\} 2\pi \int_{-\infty}^{\infty} f(\vec{p}) \left\{ \begin{array}{c} p_{\parallel}^2 \\ p^2 \end{array} \right\} dp_{\parallel}. \tag{2.31}$$

The polarization ratio thus provides a direct measurement of the second moment of $p_{\parallel}$,

$$\frac{j_l^+}{j_l^-}(\omega) \simeq \frac{J_l^2(x)}{J_l'^2(x)} \frac{\int_{-\infty}^{\infty} f(\vec{p}) p_{\parallel}^2 dp_{\parallel}}{p^2 \int_{-\infty}^{\infty} f(\vec{p}) dp_{\parallel}}, \tag{2.32}$$

and hence the 'mean parallel energy',

$$T_{\parallel} \equiv \frac{m_e c^2}{\gamma} \frac{\int p_{\parallel} f(\vec{p}) dp_{\parallel}}{\int f(\vec{p}) dp_{\parallel}} = \frac{m_e c^2 p^2 J_l'^2(x) j_l^+}{\gamma J_l^2(x) j_l^-}. \tag{2.33}$$

Summary

These analytical approximations, valid for highly anisotropic distributions, are useful for understanding the results already observed in the numerical curves for $|\Lambda| \gg 1$. However, it is likely that most experimental plasmas will be insufficiently anisotropic for these to be accurate approximations. As an example, the exact and approximate results are plotted in Fig. 2.10 for the second harmonic.

2.3.5 Finite Density Effects

In a plasma in which the electron density is appreciable, i.e., when the inequality $\omega_{pe} \ll \omega$ no longer holds, collective plasma effects become important. In particular, the refractive index may become appreciably different from unity which introduces changes in the wave phase and group velocities. The gradient in N also introduces curvature to the ray path which has consequences for the propagation of emission(Section 2.5).

When the plasma density is such that significant deviations to the refractive index occur, the full emissivity formula of Eqn. 2.16 must be used. Values of the refractive indices for perpendicular propagation are:

$$N_+^2 = 1 - \frac{\omega_p^2}{\omega^2} \tag{2.34}$$

$$N_-^2 = 1 - \frac{\omega_p^2(\omega^2 - \omega_p^2)}{\omega^2(\omega^2 - \omega_p^2 - \Omega^2)}, \tag{2.35}$$

a result obtained straightforwardly from the Appleton-Hartree cold plasma dispersion relation[46].

The corrections are of three basic types. First, the argument of the Bessel function, $lk_\perp v_\perp/\omega$, is altered by the additional factor $N_\pm$ because $k_\perp$ is different. Second, the emissivity is enhanced by the factor $N_r^2/N_\pm$. Third, since K is no longer zero an extra term must be included in the pitch-angle integral for the X-mode. This third correction arises because of modification of the wave polarization[18].

The ordinary wave, whose polarization is unchanged at perpendicular propagation, has no correction of the third type above. Therefore, our previous results for the angle integrals can be used directly, provided $N_+ p$ instead of p is used inside the integral, and the emissivity enhancement factor N_r^2/N_+ is included. Fig. 2.7, the harmonic ratio plot, cannot be used directly since the correction factors will be different for different harmonics. Generally, the effect will be to reduce the low harmonic intensities relatively more than the higher harmonics compared to the

tenuous plasma calculations; thus, for example, j_3^+/j_2^+ is increased by finite density effects.

Due to the addition of an extra term inside the integral, the X-mode cannot be dealt with exactly by simple prescriptions. Obtaining the correction would require a calculation of the angle integral for every desired value of ω_p/Ω. However, provided we exclude frequencies close to a wave resonance($N \rightarrow \infty$), which in any case will tend not to be easy to deal with experimentally, an approximate correction scheme which enables us to use the angle integrals already evaluated can be employed.

The approach is to use approximations to the Bessel function integrals for the coefficient of K. This will give an adequate result provided $K \leq 1$, which holds for most frequencies of interest. The recurrence formula for Bessel functions($J_l(x) = (J_l' + J_{l+1})x/l$) gives, for our case,

$$J_l(lN_-p\sin\theta_p/\gamma) = \frac{N_-p\sin\theta_p}{\gamma}(J_l' + J_{l+1}), \qquad (2.36)$$

with all the arguments being the same. The J_{l+1} term may also be treated as small, provided $N_-p\sin\theta_p/\gamma < 1$(since $J_{l+1}/J_l' \simeq x^2/(2(l+1)l)$). Therefore, the finite-density correction term inside the integral can be written as $N^2K(1 + J_{l+1}/J_l')$ times a term of the same form as the tenuous plasma term, $\sin\theta_p J_l'$, i.e.,

$$\Theta_l^-(p) = N_- \int_0^\pi \left[\left\{N_-^2 K\left(1 + \frac{J_{l+1}}{J_l'}\right) + 1\right\}\sin\theta_p J_l'\right]^2 f_\theta \sin\theta_p d\theta_p. \qquad (2.37)$$

Although J_{l+1}/J_l' is a function of θ_p, it represents only a second-order correction, so that sufficient accuracy shall be obtained if it is treated as a constant, equal to its value at the angle at which the tenuous plasma integrand is maximum. Using the small-argument expansion of the Bessel function,

$$\{\sin\theta_p J_l'\}^2 f_\theta \sin\theta_p = \sin^3\theta_p \frac{l^2(x/2)^{2l}}{x^2 l!^2}\exp\{-\Lambda\cos^2\theta_p\}, \qquad (2.38)$$

39

this angle is given by

$$\sin^2 \theta_p|_{max} = \frac{l + 1/2}{-\Lambda} \quad \text{for} - \Lambda > l + 1/2$$

$$= 1 \quad \text{otherwise.} \tag{2.39}$$

Therefore, the approximate form we obtain for the finite-density angle integral for the X-mode then reduces to(using the expansion for the Bessel functions)

$$\Theta^-(p) = \left[1 + N_-^2 K \left\{ 1 + \frac{N_-^2 p^2}{2\gamma^2} \frac{l}{l+1} \sin^2 \theta_p|_{max} \right\} \right]^2 N_- \Theta^-_{tenuous}(N_- p). \tag{2.40}$$

This approximate form introduces an error of less than about 10% in the coefficient of K for $N_- p/\gamma < 1$, and it becomes exact in the limit $p_\perp \to 0$(i.e., $\Lambda \to -\infty$ or $p \to 0$).

Fig. 2.11 is a plot of $\Theta_l^\pm p^3 \omega / N_\pm^2 \Omega$, the normalized emissivity, as a function of ω, showing how the finite-plasma corrections alter the emissivity(calculated exactly). The approximate treatment of the X-mode is indistinguishable in the figure from the full-angle integration of the exact equations. The purpose of plotting this particular quantity(= $\Theta_l^\pm p^3 \omega / N_\pm^2 \Omega$) is that it is a normalized form of the radiation source function, j/N_r^2, i.e.,

$$\frac{\Theta_l^\pm p^3 \omega}{N_\pm^2 \Omega} = \left(\frac{4\pi\epsilon_o c}{e^2} \right) \frac{1}{f_p \Omega} \frac{j_l^\pm}{N_r^2}, \tag{2.41}$$

equivalent to Eqn. 2.16. Thus, it takes the shape of the emission spectrum from a plasma in which $f_p = const.$ In Fig. 2.11 we have cut off each harmonic at the point where it would overlap with the next lower harmonic, so as to avoid confusion. Naturally, if f_p extends to high enough energy in a practical situation, superposition will occur. Emission between Ω and $(\omega_p^2 + \Omega^2)^{1/2}$, the upper hybrid frequency, has been suppressed for clarity and also because it will tend to be inaccessible.

2.4 Cyclotron Absorption

Absorption of radiation by gyrating electrons is just the reverse process of emission, so that mathematical formulations are very similar. Taking the special limit of $\theta = \pi/2$ again, the absorption coefficient, $\alpha_l^{\pm}(\omega)$, can be recovered by replacing $f(\vec{p})$ in Eqn. 2.10 by

$$- \frac{8\pi^3\gamma}{N_r^2\omega^2 m_e} \frac{1}{p_\perp} \frac{\partial f}{\partial p_\perp}. \tag{2.42}$$

Thus, our results from the calculation of Θ coefficients will be directly applicable to the determination of $\partial f/\partial p_\perp$ if we regard it to be expressed in the form

$$\frac{\partial f}{\partial p_\perp^2} = \left(\frac{\partial f}{\partial p_\perp^2} \right)_p L \exp\{-\Lambda \cos^2 \theta_p\}. \tag{2.43}$$

This, of course, is not consistent with the distribution used for emission. The perpendicular derivative of the VECE distribution (Eqn 2.11) is more complicated and is given by

$$
\begin{aligned}
2\frac{\partial f}{\partial p_\perp^2} &= \frac{1}{p} \left(\frac{\partial f}{\partial p} + \frac{\cot\theta_p}{p} \frac{\partial f}{\partial \theta_p} \right) \\
&= \frac{1}{p} \left(\frac{\partial}{\partial p}(f_p f_\theta) + \frac{2\Lambda \cos^2 \theta_p}{p} f_p f_\theta \right).
\end{aligned} \tag{2.44}
$$

The existence of $\partial/\partial p$ term prevents us from obtaining isolated informations on any specific resonance sphere.

The forward problem of obtaining the absorption coefficient from distribution of Eqn. 2.11 is straightforward however, and it will serve as a check for the calculation of the optical depth and the validity of tenuous plasma approximation.

The absorption coefficient integral, containing the derivative $\partial f/\partial p_\perp$, can be evaluated by integration by parts in the limit of strong parallel enhancement($-\Lambda \gg$

41

1) discussed in 2.3.4. For this case, again regardless of the shape of f (as long as it vanishes at $p_\perp \to \infty$ which is true by assumption),

$$\alpha_l^\pm = \frac{2e^2\pi}{m_e\epsilon_o c\omega}\frac{\gamma}{p}\left(\frac{l}{2\gamma}\right)^{2l}\frac{2l}{l!^2}\left\{\begin{array}{c}p^2\\\gamma^2\end{array}\right\}\int_0^\infty f(\vec{p})p_\perp^{2(l-1)}2\pi p_\perp dp_\perp. \qquad (2.45)$$

This form shows α to be the $2(l - 1)$-th moment of the distribution, two orders smaller than the emission of the same harmonic (Eqn. 2.23).

By taking the quotient j_l/α_l, the Rayleigh-Jeans type of blackbody expression for the perpendicular temperature,

$$\frac{j_l}{\alpha_l} = \frac{\omega^2 T_\perp}{8\pi^3 c^2} \qquad (2.46)$$

with

$$T_\perp = \frac{1}{l}\frac{\int_0^\infty f p_\perp^{2l} 2\pi p_\perp dp_\perp}{\int_0^\infty f p_\perp^{2(l-1)} 2\pi p_\perp dp_\perp} \qquad (2.47)$$

is recovered.

2.5 Implementation Issues

Preceding theoretical formulations were based on the idealized observation of phase space point quantities. In this section, we shall discuss how to relate measurements obtained in practice to these theoretical formulations.

The use of emission as a source for $f(\vec{p})$ measurement can become complicated if in propagating out of the plasma the emission encounters regions of non-negligible absorption. Since both the emission and the absorption coefficient depend on $f(\vec{p})$, full spatial knowledge of $f(\vec{p})$ will be required for correct accounting of the observed intensity in this case. Below, a brief treatment of radiation transport will highlight the problem. This is followed by other experimental considerations.

2.5.1 Radiation Transport

Change in the radiation intensity as it passes through a dielectric medium(such as the plasma) is given by

$$\frac{d}{ds}\left(\frac{I(\omega,s)}{N_r^2(s)}\right) = \frac{j(\omega,s)}{N_r^2(s)} - \frac{\alpha(\omega,s)I(\omega,s)}{N_r^2}, \qquad (2.48)$$

where $I(\omega,s)$ is the specific intensity at frequency ω, and s is the distance along the ray path. Other quantities are as defined previously, but spatial dependence is included to reflect the subject matter. This expression is a simple statement to the effect that change in the intensity is given by the difference between emission and absorption.

In order to solve Eqn. 2.48, we define

$$S(\omega,s) = \frac{1}{N_r^2}\frac{j(\omega,s)}{\alpha(\omega,s)} \qquad : \text{source function,}$$

$$d\tau = -\alpha(\omega,s)ds \qquad : \text{differential optical depth.} \qquad (2.49)$$

Then Eqn. 2.48 becomes

$$\frac{d}{d\tau}\left(\frac{I(\omega,s)}{N_r^2(s)}\right) = \frac{I(\omega,s)}{N_r^2(s)} - S(\omega,s). \qquad (2.50)$$

This equation is readily solved, and for definite limits, $s = A$ and $s = B$,

$$\frac{I(\omega,A)}{N_r^2(A)}e^{-\tau(A)} = \frac{I(\omega,B)}{N_r^2(B)}e^{-\tau(B)} + \int_{\tau(A)}^{\tau(B)} S(\omega,\tau)e^{-\tau}d\tau. \qquad (2.51)$$

The geometry for this situation is shown in Fig. 2.12. Hence, observed intensity at A is the sum of the transmitted radiation originating at B and the sum total of emission at all interior points but reduced by the factor $e^{-\tau}$ that accounts for absorption[11].

The source function, $S(\omega)$ can be written in the form

$$S(\omega) = \frac{\omega^2}{8\pi^3c^2}\kappa T_r \qquad (2.52)$$

43

where κ is the Boltzmann's constant and T_r is referred to as the 'radiation temperature'. It should be emphasized here that $S(\omega)$ is independent of the density of the medium. In the limit that the electrons have a Maxwellian distribution with temperature T, $T = T_r$ identically.

It is revealing to substitute Eqn. 2.52 into Eqn. 2.51 and evaluate the integral assuming $S(\omega)$ is independent of τ. Setting $I(\omega, B) = 0$ and $\tau(A) = 0$, we get

$$I(\omega) = \frac{\omega^2 \kappa T_r}{8\pi^3 c^2}(1 - e^{-\tau_o}). \tag{2.53}$$

In the limiting case that $\tau_o \gg 1$, i.e., when the medium is highly absorbing, the intensity asymptotically approaches the source function value. This is the case of optically thick emission, and the intensity is characterized by the medium's radiation temperature.

In the limit $\tau_o \ll 1$, the optically thin case, the absorption is negligible so that the intensity is the sum of all emissivities along the ray path, $I(\omega) = \int j(\omega, s)ds$. When τ_o is between these two limits, the medium is said to be optically grey, and in this case complete knowledge of $j(\omega, s)$ and $\alpha(\omega, s)$ is required to account for the observed intensity.

Thus, the tenuous plasma emissivity can be precisely observed only when the medium is optically thin. For experimental plasmas of interest, τ is usually sufficiently large for thermal plasmas at the first and the second harmonic X-mode and at the first harmonic O-mode. Experimental observations indicate that τ may also be appreciable for the nonthermal plasma at the first harmonic[33]. It was based on these past observations that first harmonic was excluded from the ratio analysis examples of Figs. 2.7 and 2.8. The disadvantage of using higher harmonics is the low energy ceiling(limiting $\gamma = 1.5$ for $l = 3$ compared to 2 for $l = 2$) before the harmonic superposition sets in. This point is illustrated in Fig. 2.13, where the frequency-energy correspondence for different harmonics are plotted on a normalized frequency scale.

The appreciable optical depth of the first harmonic may however provide an independent temperature measurement. A key parameter of the distribution function, the 'perpendicular temperature', $T_\perp$, can be obtained from an optically thick(or grey) harmonic,

$$T_\perp \simeq \frac{T_r}{(1 - \exp(-\tau_1))},\qquad(2.54)$$

a result derived from Eqn. 2.53 on the basis that T_r is characterized by the second-order momentum in $p_\perp$ of the distribution. Thus, an agreement between $T_\perp$ obtained from the first harmonic and the shape of $f(\vec{p})$ obtained from the the harmonic or the polarization ratio analysis will strengthen the experimental results.

2.5.2 Experimental Considerations

In executing the actual measurements of data which contain the kind of information discussed in Section 2.3, several issues must be examined in addition to the optically thin plasma requirement discussed above.

As in any other plasma diagnostic, a view of the plasma will provide only the line-integrated intensity. Thus, in the absence of spatial information from other sources, the observed radiation intensity should be interpreted as a line-averaged quantity. It is, in principle, possible to execute multi-chord measurements to provide the spatial information if so required.

When the plasma refractive effect is non-negligible, the emissivity must be corrected for this fact by

$$I = \int \frac{j}{N_r^2} dl.\qquad(2.55)$$

The $1/N_r^2$ term accounts for the variation in the propagation solid-angle introduced by refraction. It was in anticipation of this point that Fig. 2.11 plotted the quantity given by Eqn. 2.41, which is the appropriately normalized source function observed by emission measurements in finite-density plasmas. Although refractive effects will change the propagation direction of the radiation, they will not usually alter the

45

propagation angle with respect to the magnetic field of the perpendicularly emitted radiation. This is a consequence of the plasma homogeneity along the field line in most magnetically confined plasmas, which conserves the initial value of the parallel wave vector(here equal to zero).

As stated previously, perpendicular emission viewed through a region of approximately constant magnetic field is realized in a tokamak by viewing vertically through the plasma center. However, the field along the view is not absolutely constant. The poloidal field typically contributes a negligible $\leq 1\%$ to the variation of the field magnitude, but possibly a more limiting factor is the finite spot size across the toroidal field gradient, which introduces a variation of order

$$\frac{\Delta B}{B} = \frac{d}{R}, \tag{2.56}$$

where d is the spot size and R is the major radius. Refractive effects mentioned above may effectively increase the acceptance angle and hence contribute to increase in the magnetic field variation.

This variation in the magnitude of the magnetic field within the measured region places a lower limit on the electron energy resolution. The spread in resonant energy($\Delta\gamma$) due to the variation of the field(ΔB) is given by

$$\frac{\Delta\gamma}{\gamma} = \frac{\Delta B}{B}. \tag{2.57}$$

Thus, the fractional spread in kinetic energy($\gamma - 1$) increases with decreasing γ. For example, a 5% variation in the magnetic field will introduce a 10% spread in the value of the kinetic energy of the radiating electrons at $511 keV$, while the spread is increased to 15% at $256 keV$.

A final critical point, which will be addressed in Chapter 3, is the necessity of isolating the viewing chord using an effective viewing dump so that wall-reflected radiation does not enter the detection system.

2.6 Harmonic Superposition

Theoretical treatments of Section 2.3 apply to the actual measured spectrum provided the harmonic superposition is negligible. It will be seen later that this is seldom the case for most nonthermal emissions, and superpositions dominate at higher harmonics where the cyclotron continuum is formed.

It is impossible to remove precisely the superposition without knowing the electron distribution beforehand. In this section, the effects of superpositions on Λ determined from the harmonic ratio and the polarization ratio are discussed. It will be shown that the same superposition works to modify Λ in the opposite direction for the two ratios, giving us at least a range of Λ, and perhaps a better estimate of the exact magnitude of the superposition and Λ.

Effect of Harmonic Superposition on the Polarization Ratio

For simplicity, we limit the discussion here to the polarization ratio at the second harmonic, $j_2^+(\omega)/j_2^-(\omega)$, for $\Omega \leq \omega \leq 2\Omega$. We also assume that the harmonic superposition is dominated by the down-shifted third harmonic, $j_3^+(\omega)$ and $j_3^-(\omega)$. Let $p_2(\omega)$ be the momentum of electrons whose $l = 2$ radiation is emitted at ω. Similarly, let $p_3(\omega)$ be the momentum of electrons whose $l = 3$ radiation is emitted at ω. Then,

$$\frac{< j_2^+(p_2) >}{< j_2^-(p_2) >} = \frac{j_2^+(p_2) + j_3^+(p_3)}{j_2^-(p_2) + j_3^-(p_3)}, \tag{2.58}$$

where angular brackets indicate uncorrected, observed emissivities. This equation can be rewritten as,

$$\frac{< j_2^+(p_2) >}{< j_2^-(p_2) >} = \frac{j_2^+(p_2)(1 + j_3^+/j_2^+)}{j_2^-(p_2)(1 + j_3^-/j_2^-)}. \tag{2.59}$$

If the harmonic superposition is to result in an overestimate of the polarization ratio, i.e., $< j_2^+ > / < j_2^- > > j_2^+/j_2^-$,

$$\frac{j_3^+(p_3)}{j_2^+(p_2)} > \frac{j_3^-(p_3)}{j_2^-(p_2)} \tag{2.60}$$

must be satisfied. This expression can be rewritten as

$$\frac{j_3^+(p_3)}{j_3^-(p_3)} > \frac{j_2^+(p_2)}{j_2^-(p_2)}. \tag{2.61}$$

It is easy to see that this is satisfied at all times, provided Λ does not vary dramatically, if one notes that j^+/j^- ratio for a given p is approximately the same for $l = 2$ and $l = 3$ (see Fig. 2.8), and that it increases with p. Since p_3 is always considerably greater than p_2(the difference in the kinetic energy is $\geq 250keV$), it follows that Eqn. 2.61 is always satisfied. Thus, harmonic superposition increases the observed polarization ratio, which results in an underestimate of Λ.

Effect of Harmonic Superposition on the Harmonic Ratio

Although rigorous mathematical proof cannot be easily provided, extensive computer modelling unambiguously shows that, given mildly-relativistic, smoothly-varying distributions,

$$\frac{< j_3(3\omega) >}{< j_2(2\omega) >} > \frac{j_3(3\omega)}{j_2(2\omega)}. \tag{2.62}$$

Qualitatively, this is a consequence of the fact that harmonic superposition increases with frequency since the values of γ at a frequency among the neighboring harmonics become closer.

Consider, for example, a flat electron distribution with a cut-off at 254keV. The emissivity will then have the spectral feature given in Fig. 2.11. In this case, the emission in the range $\Omega < \omega \leq 2\Omega$ is solely from the second harmonic, while the emission in the range $2\Omega < \omega \leq 3\Omega$ has contributions from the third and the fourth harmonic. Hence, at least for $0.89\Omega \leq \omega \leq \Omega$,

$$\frac{< j_3(3\omega) >}{< j_2(2\omega) >} = \frac{j_3(3\omega) + j_4(3\omega)}{j_2(2\omega)} > \frac{j_3(3\omega)}{j_2(2\omega)}. \tag{2.63}$$

This result, according to the computer modelling, is general and applies to any j_3/j_2 given a smooth, mildly-relativistic distribution. Fig. 2.13 helps to clarify this idea by illustrating the frequency-energy correspondence for different harmonics.

Thus, given this fact and the results of Fig. 2.7, it is clear that overestimate in the harmonic ratio tend to overestimate Λ for both polarizations.

Advantage of Having Both Ratios

It has been shown that given realistic assumptions, the harmonic superposition works to increase the observed harmonic or polarization ratio. This trend helps us to recognize the superposition problem quantitatively, since a harmonic ratio with superposition tends to overestimate(i.e., more positive) Λ, while the polarization ratio with superposition tends to underestimate(i.e., more negative) Λ. Thus, having both the harmonic and the polarization ratio will, at the very least, provide a reasonable range of Λ, and perhaps will provide both Λ very close to the actual value and a realistic value of the magnitude of the superposition.

2.7 Summary

In this chapter, the general theory of electron cyclotron emission and absorption was adapted to the specific case of the VECE diagnostic. Removal of the field and Doppler broadening effects from the cyclotron resonance condition identifies elliptical contours in momentum space, corresponding to resonance frequencies. In particular, for a perpendicular view($\vec{k} \perp \vec{B}$), the contour is a circle and there is a one-to-one correspondence between the electron energy and the observed frequency of emission.

In Section 2.3, cyclotron emissivity was derived for an arbitrary non-Maxwellian distribution in a form suitable for direct interpretation of VECE measurement. The effect of finite density on emission is also discussed in terms of modifications to the tenuous emission formula. Using these calculations it is possible to determine directly the anisotropy and the phase space density as a function of the total electron energy from measurements of two distinct optically thin harmonics or polarizations.

49

Several important quantities are defined and identified in Section 2.3. The VECE distribution function is specified by f_p and Λ, where f_p is the phase space electron density and Λ is the anisotropy factor, negative for parallel enhancement and positive for perpendicular enhancement. In the emission formula, all the anisotropy information is grouped into the quantity Θ. Thus, harmonic and polarization ratios can be expressed as simple relations of this quantity. The way in which the distribution function is computed from the frequency spectrum, through the measurement of harmonic or polarization ratios, is shown graphically in Fig. 2.14.

Next, in Section 2.4, electron cyclotron absorption coefficient was derived from a similar basis. Straightforward complementary use of j and α is not possible with the VECE distribution function, since the separability of f_p and f_θ vanishes when the perpendicular derivative is evaluated.

In section 2.5, issues which introduce complications to the observation of emission are discussed. Review of radiation transport shows that unless the medium is optically thin, $f(\vec{p})$ parameters cannot be deduced directly using formulations outlined in this chapter. A measurement of an optically thick or known τ harmonic may however provide additional information about the electron temperature. The finite length and cross-section of the viewing chord can introduce several effects. A measurement of single chord of finite length will necessarily limit the observation to line-average quantities. The chord cross-section, possibly increased by plasma refraction effects, can introduce finite magnetic field broadening which will place a lower limit on the achievable energy resolution. Finally, an effective viewing dump is required in order to achieve isolation of the viewing chord from emissions external to the chord.

The unique correspondence between the frequency and the electron energy is severed when more than one harmonic are radiated at a single frequency, i.e., when harmonic superpositions occur. The effect of the harmonic superposition on the $f(\vec{p})$ determination was discussed in Section 2.6. It is found that superpositions

tend to bias Λ in opposite directions for harmonic and polarization ratios. The superposition also limits the energy range of $f(\vec{p})$ measurement.
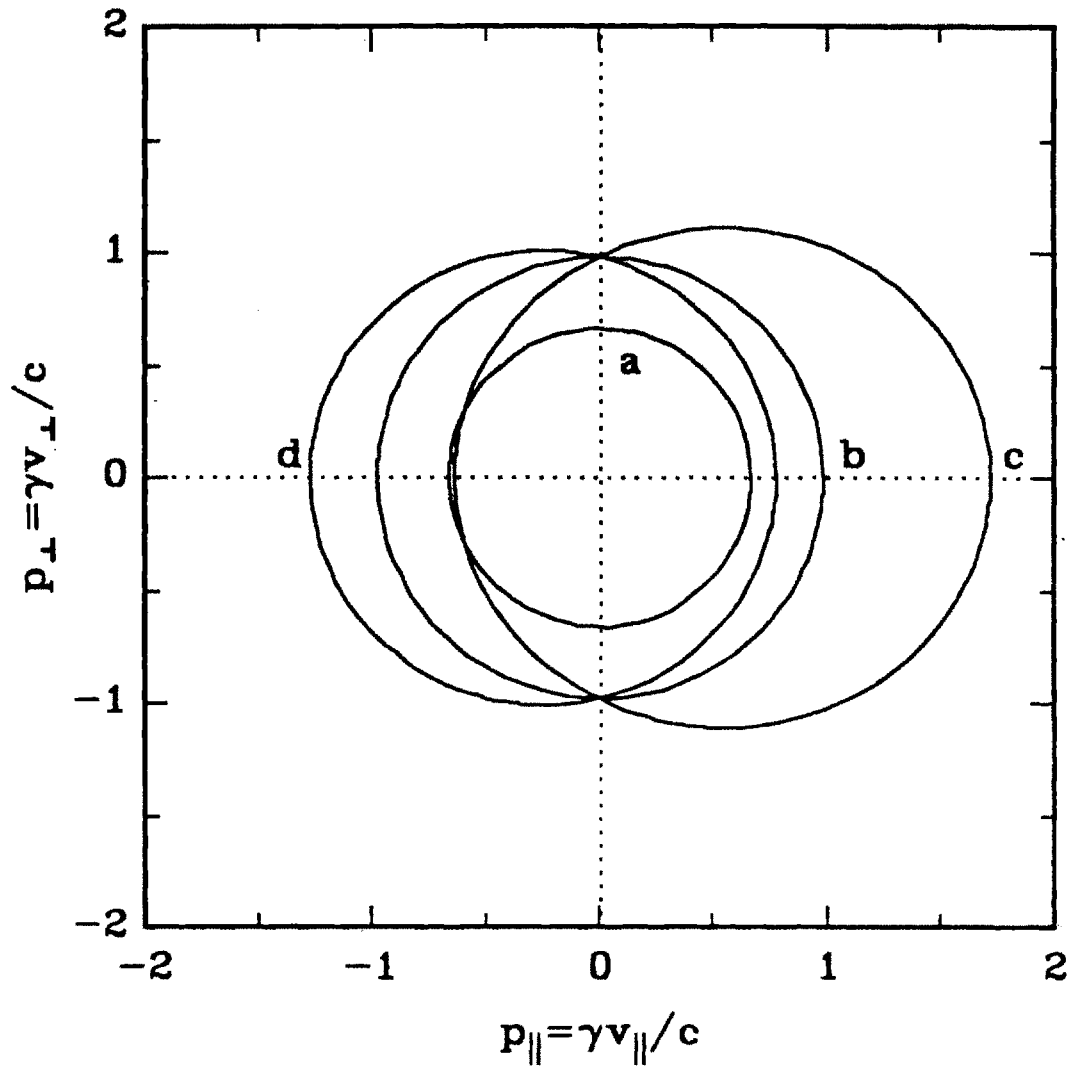
Figure 2.1:
ECE resonance contours in momentum space. (a)$N_\parallel = 0, \omega/\Omega = 0.84$. (b)$N_\parallel = 0, \omega/\Omega = 0.72$. (c)$N_\parallel = 0.34, \omega/\Omega = 0.72$. (d)$N_\parallel = -0.17, \omega/\Omega = 0.72$.
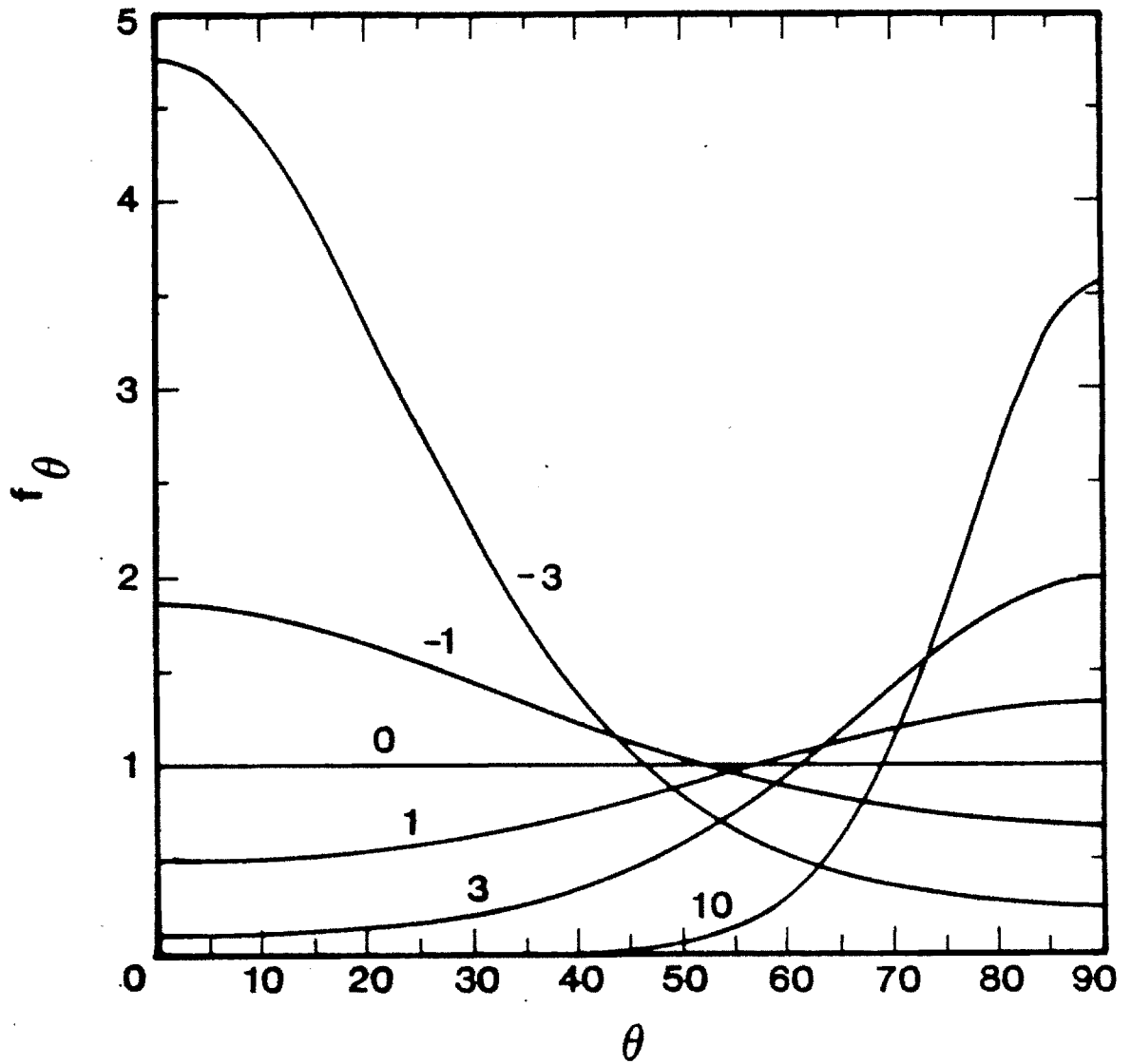
Figure 2.2:
The pitch-angle distribution, f_θ, versus the momentum pitch-angle, θ_p, for representative values of the anisotropy factor, Λ.
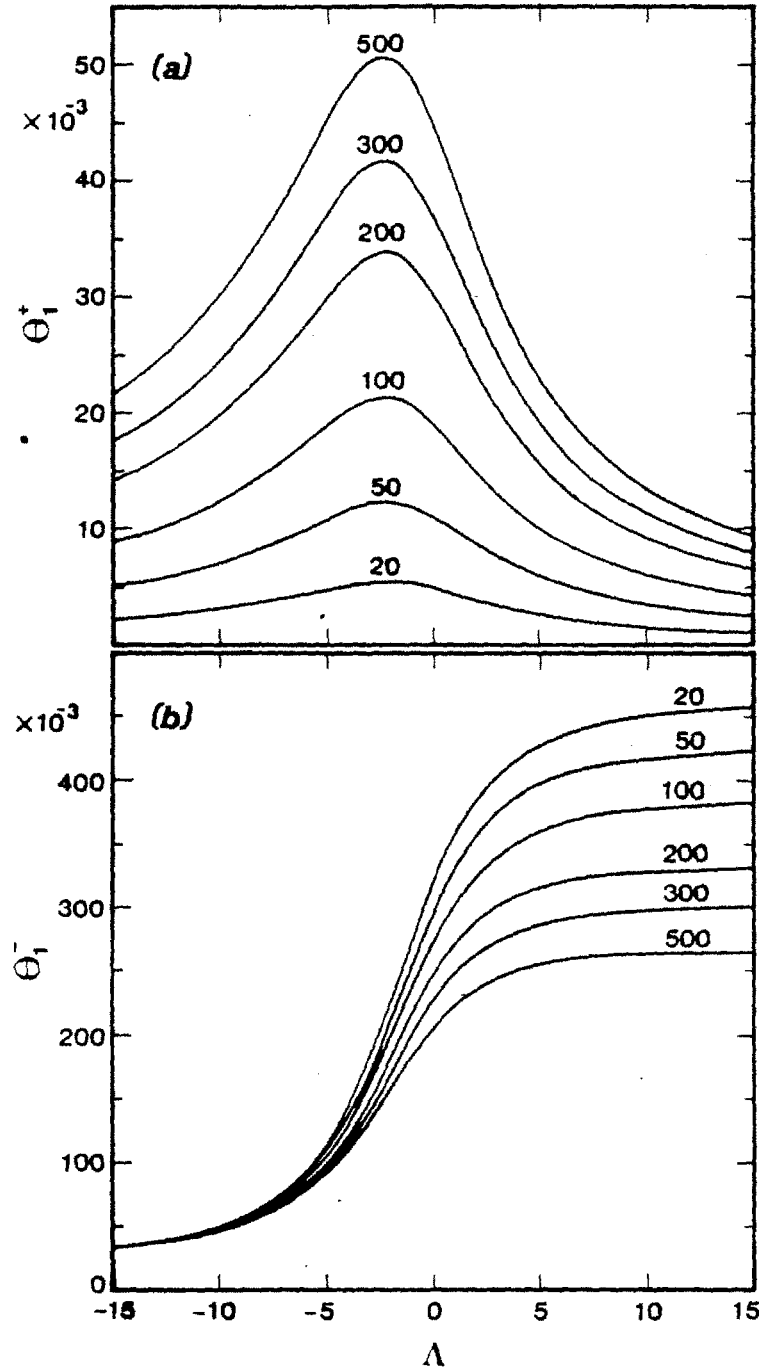
Figure 2.3:
The first harmonic cyclotron emission pitch-angle integral, Θ_1, versus the anisotropy factor, Λ, for (a) O-mode, (b) X-mode. The different curves correspond to different total energy (in keV) as indicated on the figure.
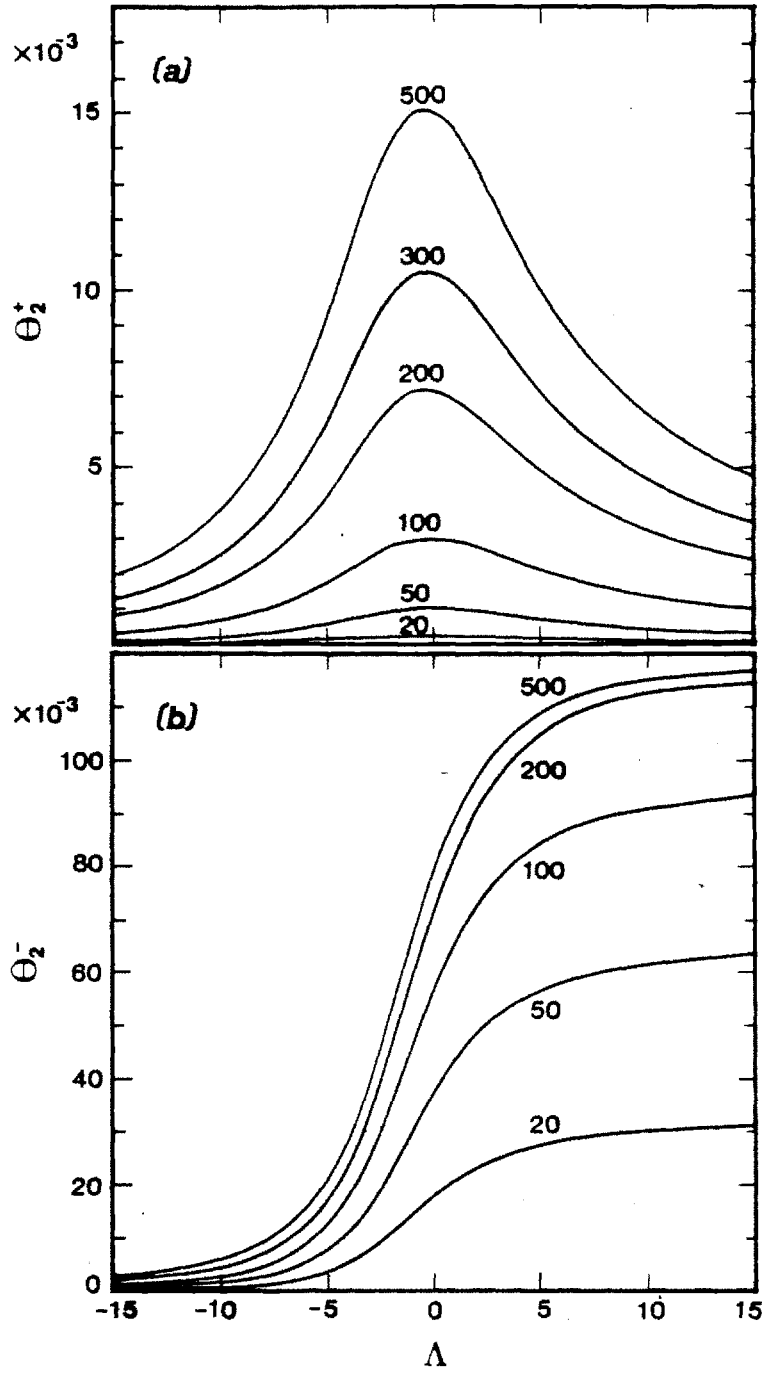
Figure 2.4:
As for Figure 2.3, but for the second harmonic.
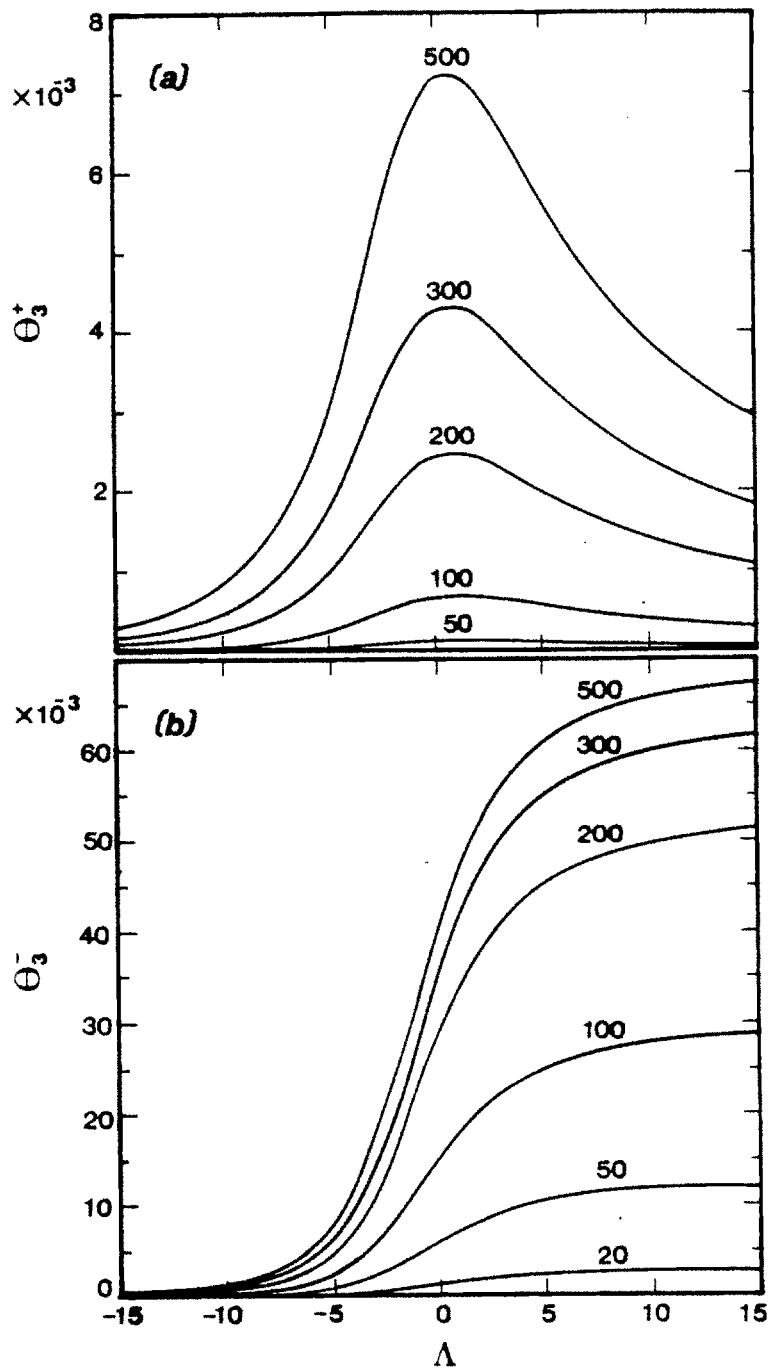
Figure 2.5:
As for Figure 2.3, but for the third harmonic.
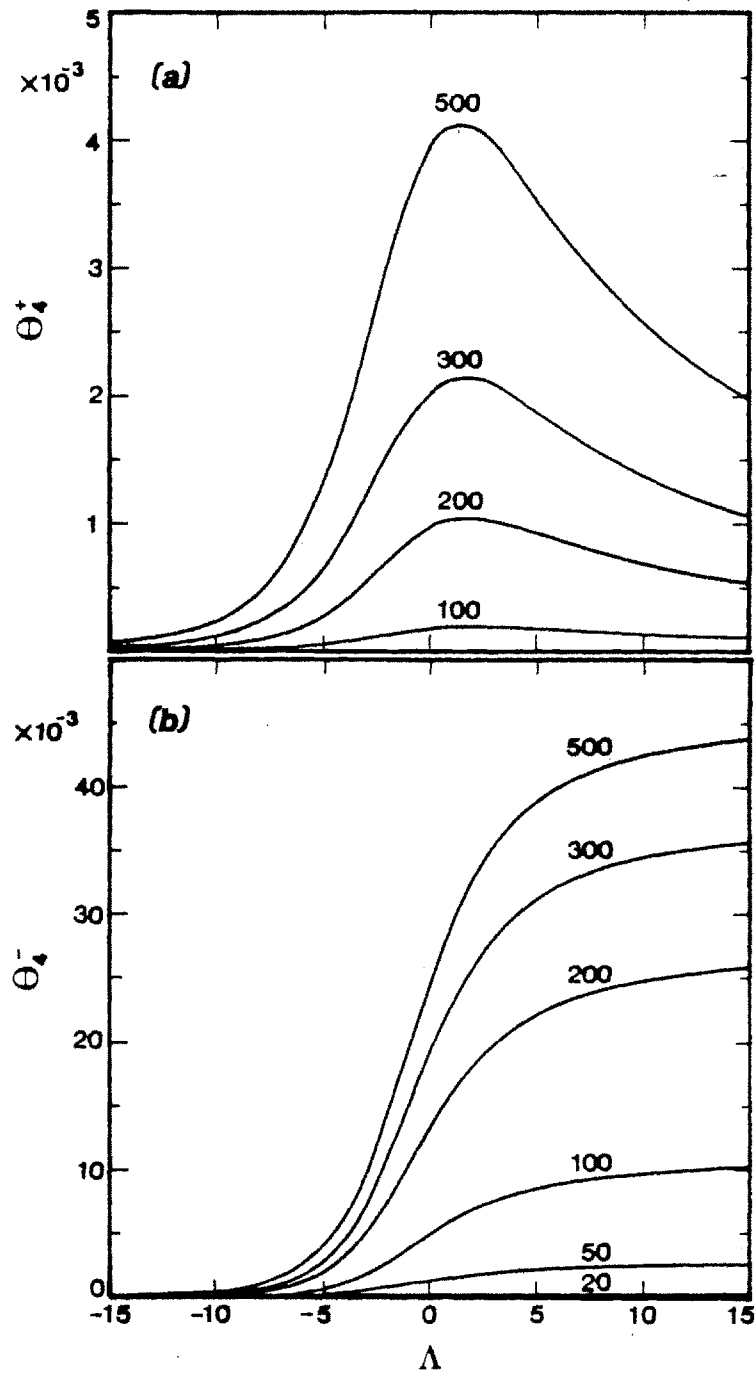
Figure 2.6:
As for Figure 2.3, but for the fourth harmonic.
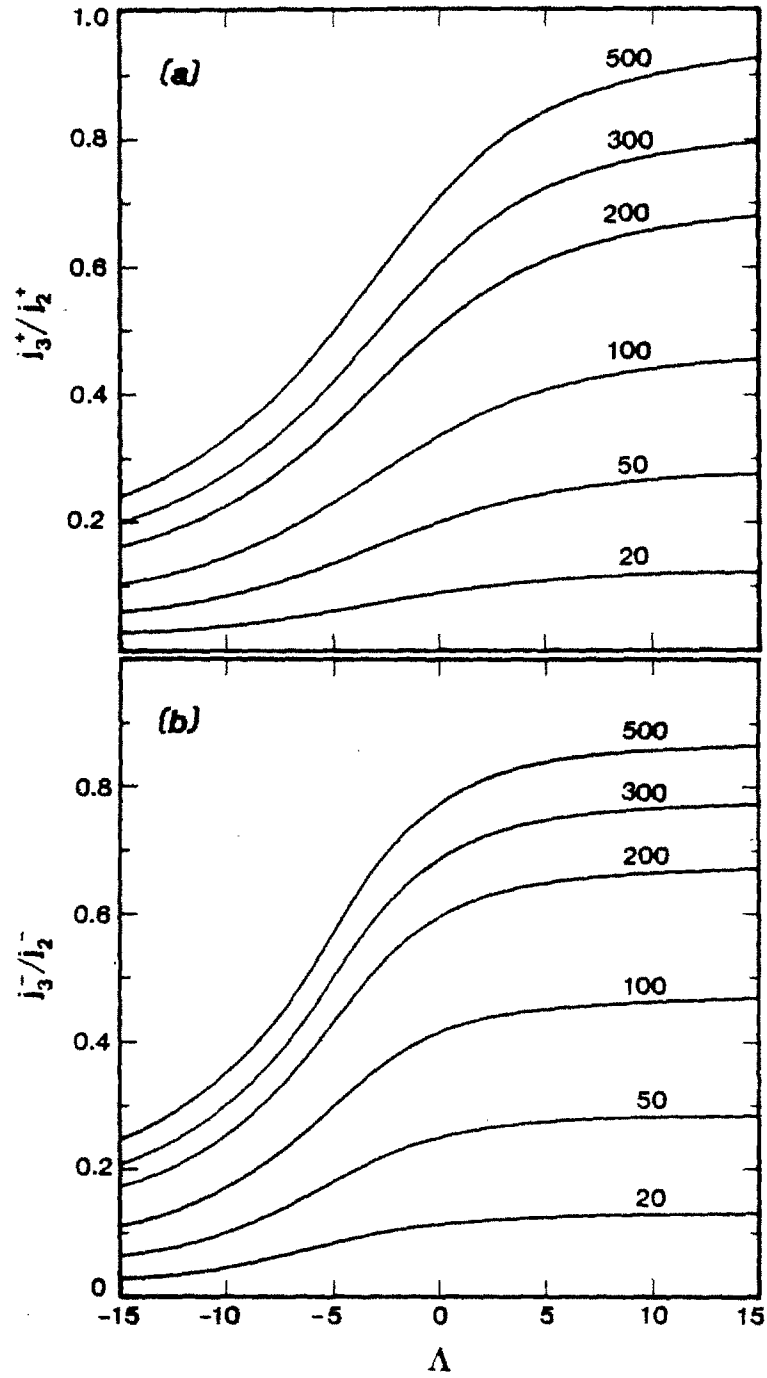
Figure 2.7:
The harmonic ratio, j_3/j_2, versus the anisotropy factor, Λ, for different values of the total electron energy; (a) O-mode, (b) X-mode.
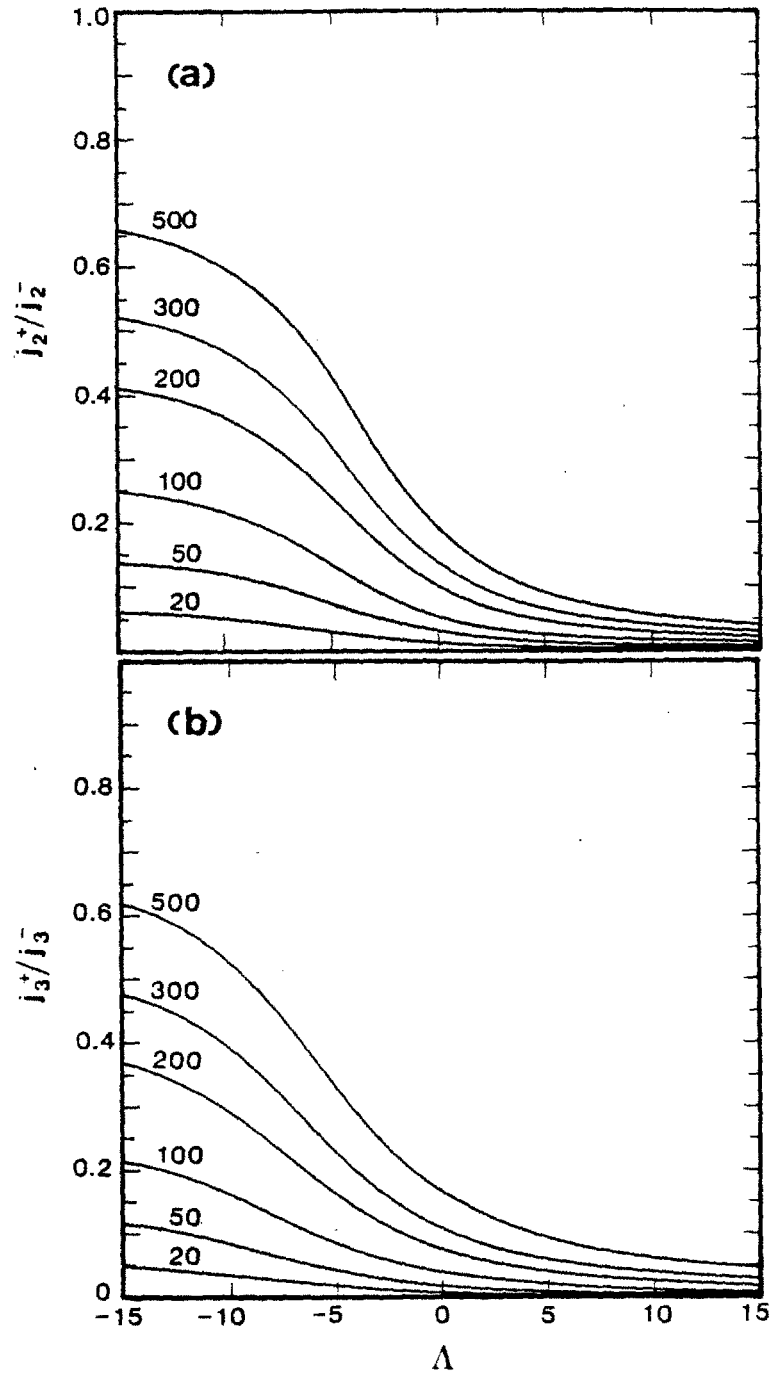
Figure 2.8:

Polarization ratio of the second(a) and the third(b) harmonic emission, j^+/j^-, versus the anisotropy factor, Λ, for different values of the total electron energy.
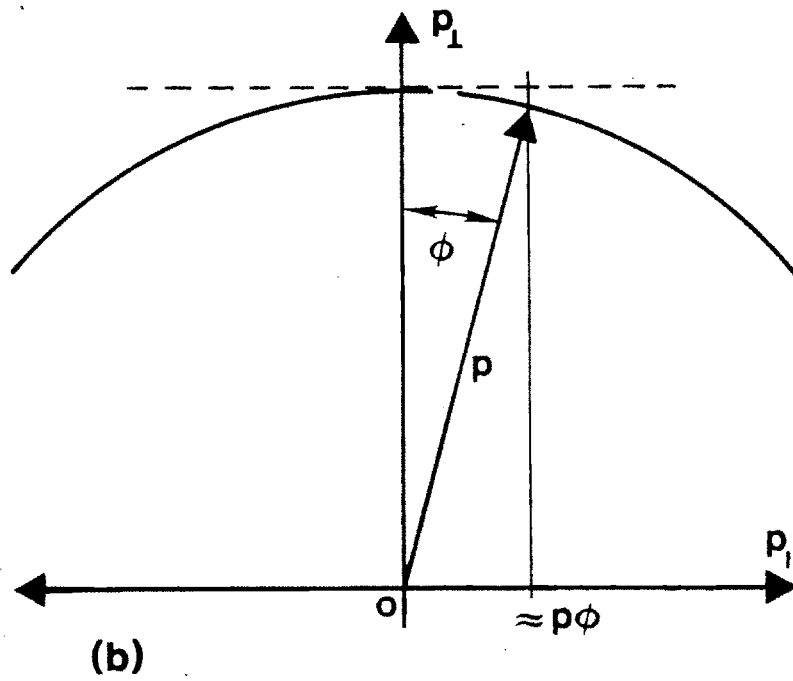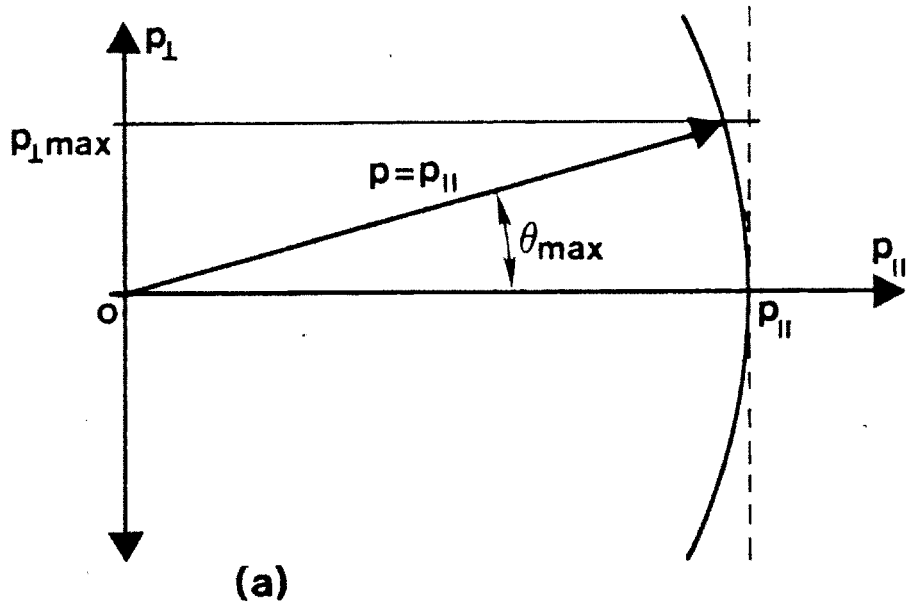
Figure 2.9:
Straight-line approximations for extreme anisotropies, $|\Lambda| \gg 1$ in momentum space. (a)$-\Lambda \gg 1$. (b) $\Lambda \gg 1$.
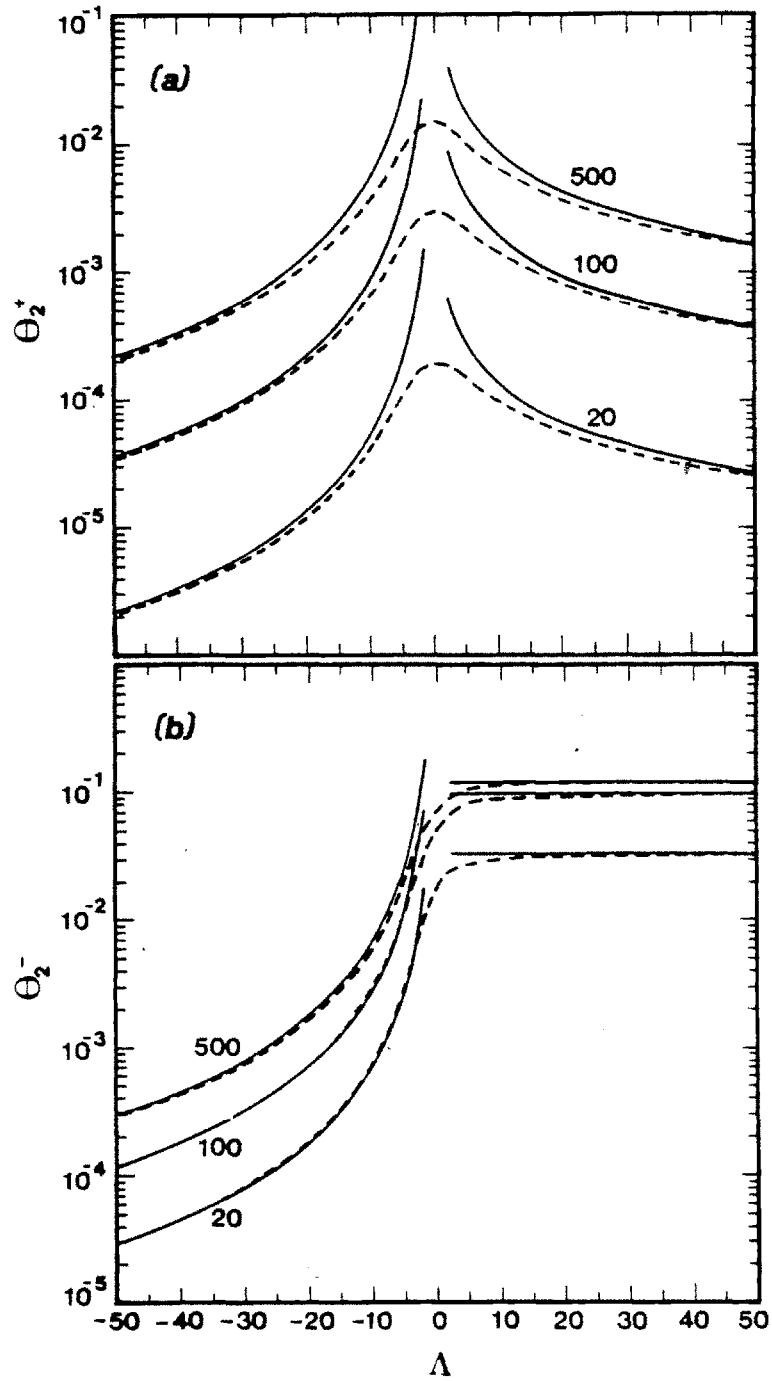
Figure 2.10:
Approximations to the second harmonic cyclotron emission pitch-angle integral, Θ_2, versus the anisotropy factor, Λ, for (a) O-mode and (b) X-mode. For $|\Lambda| \gg 1$, these approximations agree well with the exact solutions, shown by the broken lines.
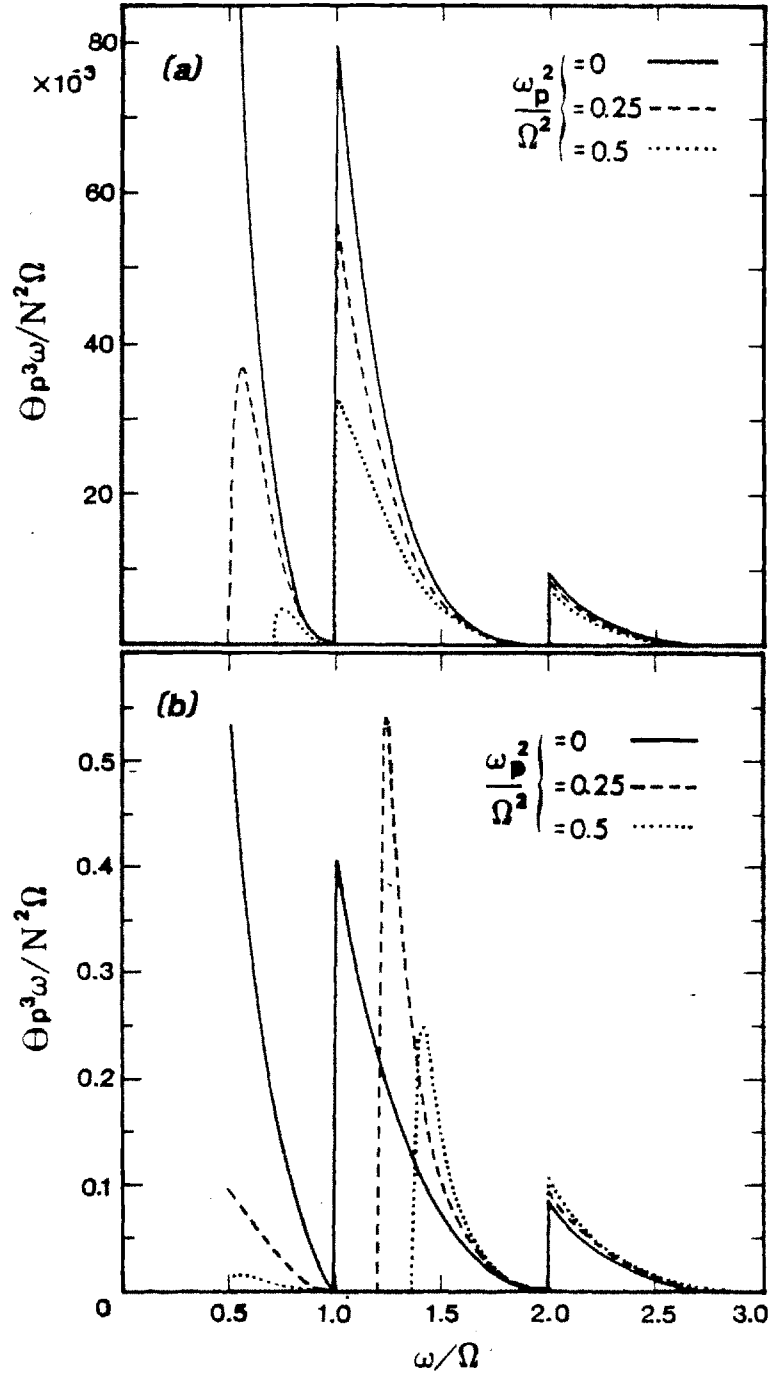
Figure 2.11:

Normalized emissivity, $\Theta_l p^3 \omega / N^2 \Omega$, versus the normalized frequency, ω/Ω, for the first three harmonics with $\Lambda = 0$; at three densities, $\omega_p^2/\Omega^2 = 0, 0.25, 0.5$. Harmonic overlap is suppressed. (a) O-mode, (b) X-mode.
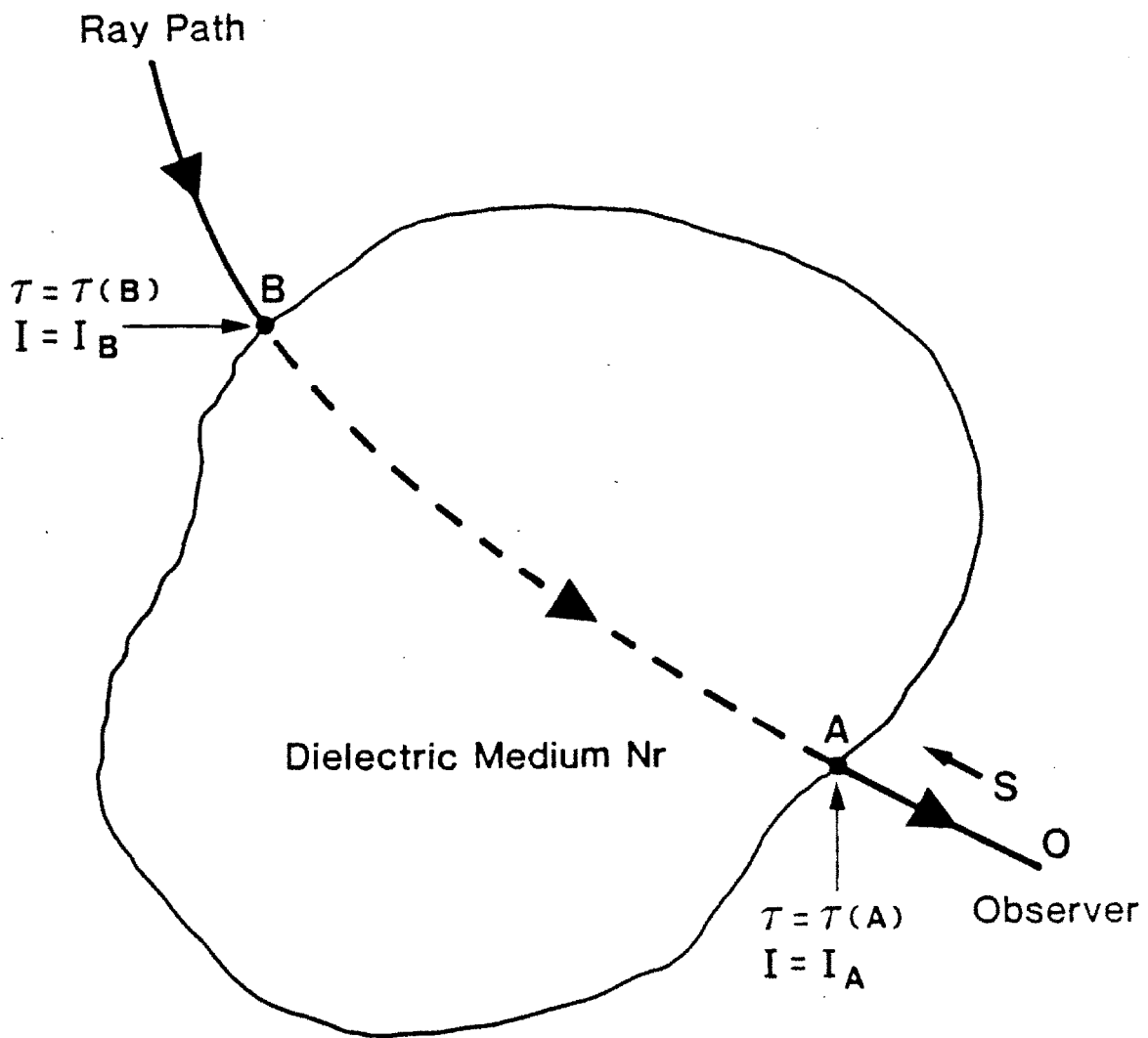
Figure 2.12:
Radiation transport through a dielectric medium, the quantities are defined in Eqn. 2.48.

FREQUENCY VS. ENERGY
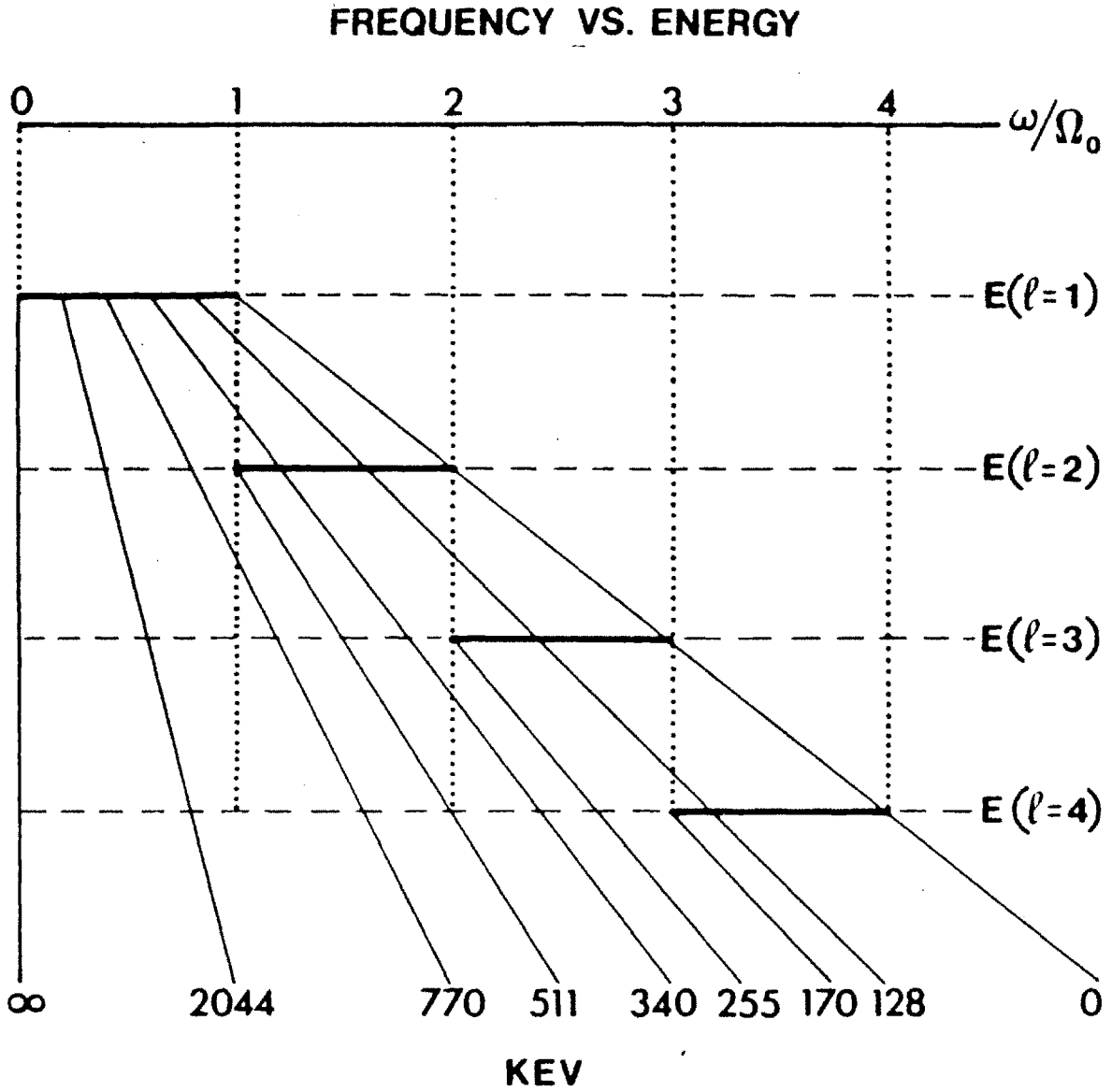
Figure 2.13:
Frequency vs. energy diagram for the first four harmonics.
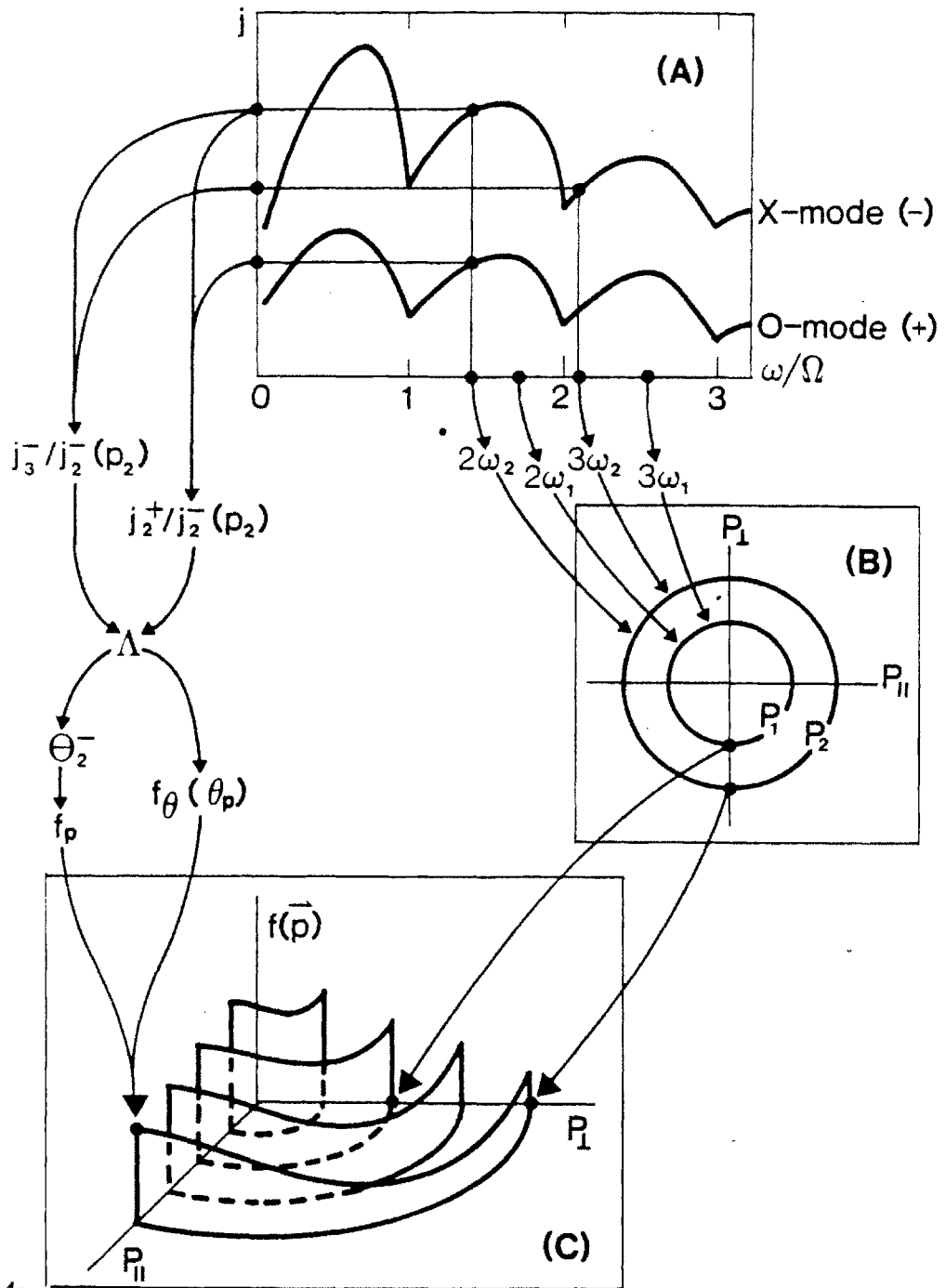
Figure 2.14:
A schematic diagram showing the flow of information leading to $f(\vec{p})$ determination.

Chapter 3

DEVICE AND CALIBRATION

3.1 Introduction

The key components of the vertical viewing ECE diagnostic are discussed in this chapter. These components include the viewing dump to suppress reflection, well collimated optics arrangement to view only a narrow region of the plasma, and the Michelson interferometer with which the frequency spectrum is measured. These were assembled with the following goals in mind.

1. Observation only of the perpendicularly emitted radiation from within the viewing chord.

2. Acquisition of calibrated frequency spectra with acceptable time and frequency resolution.

While the Michelson interferometer is used for ECE measurement at many sites and therefore fairly standard[16], the design of the dump and the focussing optics require innovative approaches tailored to constraints imposed by the limited access and the compact size of the Alcator C tokamak.

The VECE diagnostic was used to collect data at various times between August, 1984 and May, 1986. The system configuration unavoidably underwent many

modifications, mostly with little effect on the measurement. However, the data collected in 1986 comes from a decidedly different plasma compared to the past, with a different viewing dump in place as well.

The data previous to 1986 is referred to as the 'Phase I' data. During this phase, the Alcator plasma was discharged at its nominal minor radius of 16.5cm, and correspondingly, a small viewing dump with a surface area of $7 \times 7cm$ was used. During the 1986 period, Alcator was operated with 11.5cm minor radius to accommodate extra hardware inside the vacuum chamber. We also took advantage of this by inserting a larger($14 \times 14cm$) dump. This period is referred to as 'Phase II.' Thus, the major difference is the dump size. This has implications on the interpretation of polarization measurements. The system description in this chapter normally refers to its final form, except where explicitly noted.

3.2 System Overview

The optical system is designed for measurement of ECE spectra in the frequency range 200GHz to 700GHz, approximately corresponding to $\Omega \leq \omega \leq 3\Omega$ for typical $B_T = 8T$ operation of Alcator C. The elevation and plan views of the optical system are shown in Fig. 3.1. Distances between key optical components are tabulated in Table 3.1. Emission from the plasma in the line of sight first encounters the vertical access port, called the 'keyhole' on Alcator, whose width of 2.5cm in the toroidal direction is comparable to the viewing chord spot size. The vacuum interface is formed by a fused quartz window during Phase I, and by a Z-cut crystal quartz window during Phase II. The emission then propagates up to where a set of three front-surface aluminized mirrors, including one $f = 152cm$ spherical mirror, redirect and focus the emission onto a 2.5cm diameter circular aperture before the emission enters the detection system. The detection system consists of a rapid-scan polarizing Michelson interferometer and a liquid helium cooled indium-antimonide(InSb) crystal detector, described in Section 3.3. A distance of approximately 130cm is

placed between the aperture and the interferometer inlet due to spatial constraints in the experimental cell, and to reduce the effect of stray magnetic field from the tokamak on the detector. The 2.5cm aperture was attached to the Michelson inlet by a 5cm diameter copper light pipe in Phase I, but since the light pipe was found to produce significant depolarization, it was removed and the aperture is free-standing in Phase II.

The viewing dump, to which Section 3.4 is devoted, is placed at the bottom of the torus where the rays in Fig. 3.1 originate. This placement is essential since the size of the view is larger than the bottom keyhole(due to solid angle and diffraction effects). The dump size is constrained by the requirement that the dump and its protective frame made of graphite and stainless steel stay within the plasma limiter shadow. Although the keyhole geometry is up-down symmetric, the viewing dump is located at the bottom of the chamber in order to avoid loss of the dump material in the event of breakage due to thermal or mechanical shock. In Phase I, the dump area was $7 \times 7cm$ and the frame, whose outside dimension is $1.5cm \times 9.4cm \times 9.4cm$, was made of Poco graphite when the tokamak had graphite limiters, and was made of stainless steel with molybdenum side plates facing the field lines when the tokamak had molybdenum limiters. These considerations were made so as not to increase the number of impurity species in the plasma. Accounting for the 19cm radius of curvature of the vacuum vessel, the closest distance between the frame and the limiter edge was designed to be no less than 1cm. The distance between the surface of the frame facing the plasma and the tip of the dump grooves is 0.5cm so that a minimum of 1.5cm is placed between the plasma and the dump tip. As was stated earlier, dump size was increased in Phase II, an action made possible by more generous spacing due to the smaller plasma.

During operation, the entire system is enclosed in a plexiglas housing, consisting primarily of 15cm diameter pipes, and purged with dry nitrogen or air to eliminate absorption of the radiation by atmospheric water vapor molecules, which,

if untreated, adversely affect the spectrum[47]. We have succeeded in partial reduction of the absorption line width, but complete dryout of the system has not been achieved.

The spherical focussing mirror is used at a 20° angle of incidence to deliberately introduce spherical aberration in the toroidal direction[48]. The shorter focal length, f_a, is given by

$$f_a = f_o \cos \theta = (152)(0.94) = 143cm, \tag{3.1}$$

where f_o is the mirror focal length and θ is the angle of incidence. This dual focus enables the image of the 2.5cm circular aperture to be formed above the keyhole in the toroidal direction, while the image in the major radius direction is formed further down in the keyhole. This concept is illustrated schematically in Fig. 3.2, which shows the ray configuration in and near the keyhole. The solid and dotted geometrical rays, which are in the radial and the toroidal direction respectively, show the dual focus configuration attained by the introduction of the spherical aberration. In this way, propagation through the keyhole in the toroidal direction is treated as a parallel-plate waveguide problem, and in the major radius direction, as a free space problem owing to the generous dimension of the keyhole in this direction. Diffraction analysis of these optical elements are given in Section 3.5. Section 3.6 provides description of the data acquisition hardware configuration. Calibration methods and results of the system are provided in Section 3.7.

3.3 Michelson Interferometer and InSb Detector

The components of the Michelson interferometer[49] and the InSb detector are shown schematically in Fig. 3.3. The radiation enters through the 5cm diameter opening at the top(in the figure), and is polarized upon entry by the 1000 lines-per-inch(lpi) polarizing grid. The radiation is then divided inside the second box by a beam-splitter, which is just a wire-grid polarizer oriented at 45° to the wave polarization. After being reflected from a fixed mirror and a vibrating mirror, the

divided radiation recombine at the beam splitter. The combined power, appropriately embedded with the interference information, then proceeds to the polarizer which acts as a reflector this time and sends the radiation to the detector.

The vibrating mirror is translated sinusoidally at approximately $30Hz$ period and $1 \sim 1.5cm$ amplitude, using an electromagnetic transducer driven by an audio amplifier[50]. The moving mirror is connected to the vibrator via an air bearing and a flexible joint[51]. This configuration isolates the mirror from any wobbling motion in the vibrator. Step size information of the moving mirror is provided by a Moire fringe counter and processor[52], which produces a digital pulse every $40\mu m$. The air supplied to the bearing is routed through a series of interlocks that prevent the vibrator from engaging when there is no air flow. With a mirror amplitude of $1.0 \sim 1.5cm$, the theoretical frequency resolution is approximately $15GHz$, the actual, accounting for apodization[53], is about $20GHz$. The time resolution is $\sim 15ms$(for $30Hz$ vibration).

The output of the Michelson interferometer is detected by an InSb crystal[54,55] mounted inside a cryogenic dewar[56] kept at a liquid helium temperature of $4.2K$. The data thus obtained for each excursion of the mirror is called the 'interferogram'. This is then bracketed and Fourier transformed according to

$$I(k) = \int_0^\infty S(\delta) \cos(2\pi k\delta) d\delta \qquad (3.2)$$

where $I(k)$ is the frequency spectrum, here written as a function of the wavenumber, k, and $S(\delta)$ is the interferogram as a function of the mirror path-difference, δ. The transform is computed by a Fortran software, where the integral in practice is performed over the finite path-difference interval[53,57].

3.4 Viewing Dumps

If we assume the vacuum chamber to be a crude laboratory-blackbody cavity, the relationship between single-chord-integrated intensity, I_o, and the observed intensity

out the cavity hole, I_B, is given by[58]

$$I_B = \frac{I_o}{1 - R_{eff}},\tag{3.3}$$

where R_{eff} is the reflectivity of the cavity wall. If we take R_{eff} to be 0.9 for example[34], $I_B = 10I_o$ and the single-chord emission is totally dwarfed by multiple reflections. In order to reduce the multiply reflected component, I_B, to $0.1I_o$ for instance, reflectivity opposite the cavity hole(keyhole) must be reduced to 0.01.

In this section, the viewing dump, which is the key component of the experiment, is discussed. A total of four dumps were fabricated, three for Phase I and one for Phase II. The discussion in this section centers primarily on the Phase I dumps. In addition to our application, vacuum compatible viewing dumps that absorb electromagnetic radiation in the far infrared and millimeter wavelengths are required in plasma experiments such as electron density profile measurements using conventional ECE[12], and ion temperature measurements using FIR Thomson scattering[59]. Without viewing dumps, these measurements are severely contaminated by reflections off the metallic walls. A simple approach of using an eccosorb screen, which is an urethane foam impregnated with carbon[60], is not satisfactory for this purpose since the dump must be compatible with the high vacuum and the high temperature environment of the plasma confinement vessel.

In the past, dumps made of graphite have been used at $385\mu m(780GHz)$ for Thomson scattering in Alcator C[61], but with little success owing to the graphite's relatively high reflectivity. Eccosorb filled glass capsules have been used at frequencies below $30GHz$ providing increase in measured polarization of ECE from the Tokapole device[62].

3.4.1   Design and Fabrication

The requirements for dumps discussed here include high absorptivity in the wide frequency range and plasma compatibility. An absorptivity of greater than 99%

is used as the design goal. A spatial constraint, arising from the small access and limited space in Alcator C limits the size of the dump(especially the thickness) to $7cm \times 7cm \times 1cm$ in Phase I. For design purposes, two assumptions are made.

1. The dump material is chosen to have a large absorption coefficient although still with the real part of the refractive index much greater than the imaginary part.

2. Geometrical optics is valid.

The first assumption allows us to consider the fraction of the ray which is transmitted into the material to be completely absorbed. The second assumption allows us to execute simple ray-tracing to plot the ray trajectory. The ray's angle of incidence obtained in this way enables the calculation of the transmitted and the reflected electric field components for a given wave polarization and the refractive index of the material.

These assumptions are at best crude. The assumption of large absorptivity breaks down when the thickness of the dump is small compared to the reciprocal of the absorption coefficient. In this case, a fraction of the transmitted ray can reemerge, contributing to the reflected power. The second assumption of geometrical optics breaks down when the dimensions of the viewing dump structure becomes comparable to the wavelength. Hence, both of these assumptions tend to underestimate the reflectivity for dumps of size comparable to the inverse absorption coefficient or the wavelength, respectively.

Shapes often used for viewing dumps include conic structure, pyramid arrays, an array of horns, or straight grooves. These all have the effect of increasing absorption by inducing multiple reflections. The first three shapes are difficult to fabricate, but the reflectivity is independent of the relative orientation of the dump and the polarization vector. On the other hand, a groove structure is somewhat easier to make, but is sensitive to the polarization. The shape of the dumps discussed here is the straight groove structure, selected primarily for its ease in fabrication.

Three candidate materials are selected, which have both good vacuum properties and absorption properties. They are Pyrex, Macor[63], and alumina(Al_2O_3)[64]. All three materials are compatible with the Alcator vacuum($10^{-9}Torr$), with low reflectivity and high absorption coefficient. Table 3.2 shows the frequency averaged refractive indices for these materials. The absorption coefficient, $\alpha(cm^{-1})$, at $400GHz$ for Pyrex, Macor, and alumina are 6.2[65], 5.1, and 0.41[66], respectively. From this data, Pyrex is expected to provide the best performance, followed by Macor, then alumina. Both Macor and alumina can withstand temperatures in excess of $1000°C$. Pyrex has a softening point temperature of approximately $800°C$.

The relationships amongst incident, reflected, and transmitted electric fields of the wave are given by[67],

$$\left(\frac{E_r}{E_i}\right)_{\parallel} = \frac{(N_2/N_1)^2\cos\theta - \sqrt{(N_2/N_1)^2 - \sin^2\theta}}{(N_2/N_1)^2\cos\theta + \sqrt{(N_2/N_1)^2 - \sin^2\theta}},$$

$$\left(\frac{E_r}{E_i}\right)_{\perp} = -\frac{\cos\theta - \sqrt{(N_2/N_1)^2 - \sin^2\theta}}{\cos\theta + \sqrt{(N_2/N_1)^2 - \sin^2\theta}}, \qquad (3.4)$$

$$\left(\frac{E_t}{E_i}\right)_{\parallel} = \frac{N_1}{N_2}\left(1 + \left(\frac{E_r}{E_i}\right)_{\parallel}\right),$$

$$\left(\frac{E_t}{E_i}\right)_{\perp} = 1 - \left(\frac{E_r}{E_i}\right)_{\perp},$$

where E is the electric field, N is the refractive index(here assumed to be purely real), $r, t,$ and i refer to reflected, transmitted, and incident rays, respectively, and 1 and 2 refer to the different dielectric media. The symbols and geometries used in the above equations are shown in Fig. 3.4. In general, parallel polarization is reflected less throughout most of the range of angles of incidence.

The angle of the straight grooves is determined by applying the above equations to a ray-tracing result for various groove angles. In general, the relationship between k, the number of front surface reflections before the ray reemerges from the groove,

and θ_g, the groove angle can be written,

$$k = \frac{\pi}{\theta_g}, \tag{3.5}$$

for a ray normally incident on the dump. A fractional k indicates that the ray eventually emerges non-normal to the dump. This relationship arises as a simple consequence of geometrical ray-tracing, and is illustrated in Fig. 3.5 using real space(a), and semi-circle representation(b). The groove angle shown here is 45°.

Also shown in Table 3.2 are the front surface reflectivities computed using Eqn. 3.4 for Pyrex, Macor, and alumina for normally incident rays and for various groove angles. The values indicate that for Pyrex and Macor, the design goal of 99% absorption can be achieved with a groove angle of 45° or with four reflections. The requirement becomes more critical for alumina, which requires an angle of 30°. In all cases, it is seen that parallel polarized waves have much lower front surface reflectivity. In spite of the calculated results of Table 3.2, all three dumps were made with the 45° groove angle, so the alumina dump is not expected to fulfill the design goal.

The size of the dump structure was determined subject to the dimensional constraints of the vacuum chamber and are listed in Table 3.3. and the schematic of the Phase I dump with dimensions is shown in Fig. 3.6(a). While it was possible to make this out of one piece of Macor by machining, Pyrex and alumina, which had to be ground, were made of many identical groove pieces as shown in Fig. 3.6(b)[68]. The pieces were then placed together to form the entire dump. The lip along the perimeter is used to hold the dump in place.

3.4.2 Broadband Measurement

The performance of the Phase I dumps was evaluated in the frequency range $100GHz$ to $1000GHz$. The measurement configuration is shown in Fig. 3.7. A mercury arc lamp[69] with a chopper is used as the broad band source, and the reflected signal is detected by the InSb detector connected to a lock-in amplifier. The

spectral response of the mercury arc lamp—InSb detector system is ideally matched to the frequency range of interest, with the peak of the spectrum at $550GHz$ and FWHM of $700GHz$[70]. To minimize the angle subtended by the source and the detector, a 1-inch diameter copper circular lightpipe extension was attached to the detector, placing it behind the source. In this way, a minimum angle of 20° between the source and the detector is achieved while still ensuring that the detector only sees the dump surface. For polarization measurements, fine wire 1000 lpi grid polarizers were placed between the source(with an integral chopper) and the dump. The sample dump was held in place by an aluminum frame covered with eccosorb microwave absorber. The angular spread of the reflected radiation is obtained by scanning the detector in a circular path about the dump.

Both polarized and unpolarized radiation were used as the source. In addition, since the detector can only be scanned in the plane of the table, measurements were taken for the two orientations of the groove, vertical and horizontal(Fig. 3.7 shows the dump in vertical orientation). A measurement with a stainless steel slab placed in the dump frame is used for reflected power normalization.

Specular Measurement

Table 3.4 shows the results of specular reflection measurement for the three polarizations; unpolarized, electric field vector parallel to the plane of incidence, and perpendicular to the plane of incidence. (H) and (V) after the dump material name indicate horizontal and vertical orientation, respectively. All measurements are normalized to the specularly reflected power of the stainless steel slab(= 100). Measured values indicate higher absorption for the parallel polarization in general, in qualitative agreement with results of Table 3.2. The ordering of the effectiveness also agrees with the calculations. Pyrex is found to be the most effective, with Macor slightly worse, and alumina being the worst of the three. However, the quantitative agreement is only approximate for the perpendicular polarization, and is off by orders of magnitude for the parallel polarization. We believe these discrepancies

75

are due to incomplete absorption of the transmitted power in the body of the dump, and may therefore be reduced in a thicker dump such as that for Phase II. Note that the specular reflectivity value for a given dump depends on the groove orientation. The horizontal orientation always gives larger values.

Angular Reflection Measurement

Fig. 3.8 shows the reflected power as a function of the detector angle measured from the specular position for unpolarized radiation. The measurements obtained with the grooves horizontal are referred to as the H-scan while the measurements with grooves oriented vertical are referred to as the V-scan. The V-scan shows a relatively low peak and a wide tail, extending to large angles. The cause of this wide tail is believed to be low frequency ($f \leq 250GHz$) waves diffracting off the dump grooves, and internal reflections within the dump giving rise to waves reemerging in random directions. The H-scan shows a relatively high peak with narrow width, extending approximately to 15°. The shapes of the profiles for a given dump orientation are quite similar for all materials and polarizations. Measurements with the polarized source produce similar profiles, shifted up or down by the relative value of reflection at the specular angle.

The difference in the specularly reflected power for different groove orientations is accounted for mainly by the retrodirective nature of the front surface reflected rays. As an example, the ray shown by a dashed line in Fig. 3.5(a) enters the groove at 10° to the normal and exits it parallel to the original ray. Thus, in the V-scan, these retrodirective reflections do not get detected, and a lower value for reflected power results. This differential at the specular peak gives rise to inconsistency when we make the assumption (discussed below) that these angular distributions are good approximations to the normal incidence measurements. To correct this, we take a rather simple approach of adding the retrodirective power component from the H-scan to the V-scan so as to make the peak value at normal reflection equal, as shown schematically in Fig. 3.9. Insofar as the angular distribution of reflected

76

power can be approximated as a retrodirective peak plus other broader features, this will provide a reasonable estimate, regardless of the exact cause of the broader scattering.

For most applications including the VECE diagnostic, the key quantity of interest is the total reflectivity into the entire hemisphere. We obtain this by taking the ratio of the total power reflected from the dump to that from the stainless steel slab. Given the localization of our data in the H and V directions, a reasonable interpolation is required to estimate the reflected intensity everywhere on the hemisphere(equivalent to $\theta_H - \theta_V$ plane in Fig. 3.9). The approach we take is to assume that the orientation-averaged reflection is equal to the average of the H-scan and V-scan reflected power, so that

$$P_R = 2\pi \int_0^{\pi/2} \frac{f_H(\theta) + f_V(\theta)}{2} \sin\theta d\theta, \tag{3.6}$$

where P_R is the reflected power for any of the dumps or the stainless steel slab, and θ is the angle from the normal, equivalent in this case to θ_H and θ_V. This prescription is by no means unique, but it is found that the result is not strongly dependent on the particular prescription and we believe this one to provide a reasonable estimate of the total reflectivity. Numbers obtained in this way are given as the angle integrated total reflectivity in Table 3.5. It shows that the design goal of less than 1% reflection is achieved with the Pyrex dump regardless of the source polarization. The goal is also achieved for parallel polarization with the Macor dump, but alumina dump is noticeably worse.

3.4.3 Frequency Response Measurement

The spectral response of the dump was measured using the steady-state mercury arc lamp radiation as the source and the rapid-scan polarizing Michelson interferometer in place of the broad band detector. This is a particularly difficult and time consuming measurement since the level of the arc lamp radiation reflected off the dump is equivalent to that of $T \leq 30K$ blackbody. A single measurement was

made for the Macor dump, in the H-scan orientation for the parallel polarization. The normalized reflected power curve, measured by co-addition of more than 40,000 interferograms, is shown in Fig. 3.10. Further attempt to reduce the noise appears impractical. The smoothed approximation indicated by the solid line shows less absorption at the low frequency end where geometrical optics breaks down and the absorption coefficient is lower. Small amplitude features of the smoothed curve at higher frequencies are probably not statistically significant. The frequency integrated response, appropriately weighted by the source spectrum, is in fair agreement with the value shown in Table 3.4. The inferior performance at low frequency is also supported by a separate measurement conducted for all dumps using a low pass filter(LPF) with a $440GHz$ cut-off frequency placed at the detector aperture. The result of LPF measurement is also summarized in Table 3.4.

3.4.4 Dump Performance

The VECE measurement results using the dump will be discussed in detail in Chapter 4. Here, we shall discuss only the dump plasma compatibility issues. The dumps were used in stretches of up to three weeks, which translates to about 1,000 plasma discharges, each $\leq 0.5s$ long. The Pyrex dump was found to have cracked at the groove tips (apparently because of thermal shocks) after this time. while there was no structural damage to the Macor dump(also after three weeks). No obvious performance degradation from either dump was observed during the three week period, despite metal particle deposits on the surface. Furthermore, no additional plasma impurity problems caused by the dump were observed, despite its close proximity to the plasma.

3.5 Diffraction Analysis

The diffraction from the focussing mirror in the major radius(radial) direction and from the keyhole in the toroidal direction determines the fraction of the view that

78

is captured by the dump. Since this is a critical quantity in the interpretation of the measured spectra, fairly detailed diffraction calculations have been performed to quantify the dump-captured fraction of the view, especially for Phase I.

In this section, it will be convenient to consider the propagation in time-reversed manner, i.e., the spot size of the 2.5cm diameter aperture image is to be calculated at the dump plane inside the tokamak. Hence, the top of the keyhole is referred to as the keyhole entrance, and the bottom as the keyhole exit in the following text. There are four problems to be considered.

1. The determination of the spatial intensity distribution at the dump plane in the radial direction(along Axis C of Fig. 3.2). Diffraction is caused by the 15cm diameter spherical focussing mirror.

2. The determination of the spatial *amplitude* distribution at the entrance of the keyhole in the toroidal direction(along Axis A of Fig. 3.2). Diffraction is caused by the 15cm diameter spherical focussing mirror.

3. The determination of the propagation mode inside the keyhole, subject to boundary conditions. Initial amplitude at the entrance is given by the solution to Problem 2.

4. The determination of the spatial intensity distribution at the dump plane in the toroidal direction(along Axis B of Fig. 3.2). Diffraction is caused by the keyhole exit. The spatial distribution of wave intensity at the keyhole exit is given by the solution to Problem 3.

These four problems can be approximated and solved by one of three physical formulations.

1. Circular aperture Fresnel diffraction(Problems 1 and 2).

2. Parallel-plate waveguide propagation(Problem 3).

3. Long slit Fresnel diffraction(Problem 4).

Basic principles of these formulations are given in Appendix A.

For determination of the radial-direction intensity distribution at the dump plane(Problem 1), Section A.1 provides the method for calculating amplitude and intensity distributions near a focus from a spherical wave diffracting off a circular aperture. In order to take into account the finite size of the $2.5cm$ aperture, we divide the aperture up into 52 pixels. The diffraction by the mirror of radiation emanating from each pixel is calculated. The location at which the intensity distribution is evaluated depends on the relative placement of the dump plane coordinate system(the B–C coordinate of Fig. 3.2) and the optical axis coordinate system(Fig. A.1(a)), determined by the pixel location. The aggregate diffraction profile is obtained by summing appropriately the contributions from all 52 pixels. The crucial assumption here is that the time-reversed radiation emanates from the aperture with no spatial coherence. Such diffraction patterns for 200 and $700GHz$ are shown in Fig. 3.11(a), where the edge of the Phase I dump, extending $3.5cm$ from the axis, is shown by a dotted line. The area under these curves at selected frequencies are calculated, and the distances at which 85, 90, 95 and 99% of the power is captured are shown in Fig. 3.12(a). Comparison of these 'constant-capture-fraction contours' with the dump edge line shows that more than 95% of the power is captured by the dump over the frequency range of interest.

The problem of determining the toroidal-direction amplitude distribution at the keyhole entrance(Problem 2) is solved by obtaining the out-of-focus amplitude distribution in much the same way as before. Fig. 3.13 shows the wave amplitude distribution at the keyhole entrance from one of the pixels near the center of aperture. As expected, the shorter wavelength $700GHz$ wave has an amplitude distribution with a shorter period compared to the $200GHz$ wave. Such shorter period has the effect of coupling to higher order modes inside the keyhole.

To solve the third problem, wave amplitude profiles at the keyhole entrance are Fourier analysed according to the prescription of Section A.3. Although the

input amplitude profile from a frequency is the same for both O- and X-modes, the boundary conditions for their propagation in a parallel-plate waveguide are

$$
\left(\frac{\partial E_n}{\partial n} \right)_{wall} = 0 \qquad \text{for O-mode}
$$

$$
\text{and} \qquad\qquad\qquad\qquad\qquad\qquad (3.7)
$$

$$
E_t|_{wall} = 0 \qquad \text{for X-mode}
$$

where t and n refer to tangential and normal components to the wall, respectively, so that coupling calculations have to be performed separately for each polarization.

Finally for the evaluation of dump-plane intensity distribution in the toroidal direction(Problem 4), the diffraction spectrum from each waveguide mode is calculated according to the long-slit Fresnel diffraction formulation, outlined in Section A.2. Again we assume that different waveguide modes propagate independently. The aggregate diffraction spectra for the O- and X-modes are obtained by summing the intensity distributions of the respective components. In Fig. 3.11(b) and (c), we again show these spectra at the boundary frequencies. The 'constant-capture-fraction contours' calculated from these are shown in Fig. 3.12(b). This figure shows the capture to be greater than 99% for X-mode above $550GHz$ and well above 95% over most of the frequency range. For the O-mode, the capture fraction is noticeably worse at slightly larger than 95% over the range.

In summary, substantially detailed analysis of the viewing spot size at the dump plane was carried out. The values of the calculation put the overall system effectiveness in removing the wall reflections at equal to or better than 95% for Phase I, and more for Phase II. However, vacuum propagation was assumed and the possibly important processes of ray refraction and scattering by the plasma have not been considered.

3.6　Data Acquisition

The information required for the Fourier transform spectroscopy and subsequent analysis in conjunction with other plasma data include the interferograms and the time information. Because of the constant-distance interval requirement imposed on the interferogram measurement, which does not occur in fixed time intervals, the LeCroy 8212 ADC/Data Logger[71] is run in an external clock mode, with the clock pulse provided by the Moire fringe counter.

Both the time information and the mirror turn-around point(indicating the beginning of a new scan) are obtained from a time ramp device, which produces an output voltage with constant dV/dt upon a start trigger. The absolute voltage provides the local time with respect to the known trigger time, and the slope, dV/dp, where p is the memory address('points') reveals the mirror turn-around point, given by $dV/dp = $ local maximum.

The signal from the InSb detector is amplified by a $100kHz$ bandwidth DC voltage amplifier with a gain of 1000[72], followed by a $\pm 5V$ DC off-set circuit to utilize the full range of digitization of the ADC module$(-5 \sim +5V)$. This detector signal occupies data channel 1, while the signal from the time-ramp is fed into ADC channel 2, and the external clock and the start trigger are appropriately connected. 8kByte per channel of data are taken, which is usually sufficient for shots lasting up to $0.5s$.

After each plasma discharge, data retrieval software run from the VAX 11/750 computer compresses and dumps the ADC memory content into a VAX disk file through the CAMAC highway. Triggers for the time-ramp, ADC, and VAX software are supplied from the Alcator data system. All this flow of data through various hardware is shown in a block diagram of Fig. 3.14.

Fig. 3.15 shows a typical data stream obtained after each plasma discharge. Vertical axis is the voltage in ADC module bit units, and the horizontal is the memory address number, here referred to as 'points.' This axis is quasi-temporal,

since memory address is advanced for each fringe count. Trace 1 shows the raw detector signal, whose periodicity (~ 500 points per period) is the result of mirror's scanning motion. The signal increase that occurs midstream is an indication of the RF injection into the plasma which enhances the ECE level. Trace 3 is the time ramp, which is shown modulated as discussed above. Finally, Trace 2 shows the square wave generated from the power to the vibrator. This information is there to qualitatively confirm the mirror motion and amplitude.

3.7 Calibration

In VECE as in any experimental measurement, obtaining relative and absolute calibration of the measuring instrument is of paramount importance. In this section, the calibration procedure and the results are presented. The goal is to obtain adequate calibration at least in the range $200 - 700 GHz$ where most of the data analysis is carried out.

3.7.1 Relative Frequency Response Calibration

Uneven frequency response can be introduced all along the optical train. Likely source of this include the top of the keyhole, from which waves of different frequency radiate with different antenna patterns, the quartz window forming the vacuum interface, the detector element and its mount, and the light cone inside the cryogenic dewar. In order to take every effect into account, calibration of the entire system is performed using a simulated mock-up. On site calibration was ruled out because it was impossible to place the calibration source inside the vacuum chamber. The mock-up is different from the on-site system in following respects.

1. The quartz window is left out of the mock-up. Its transmission curve (measured independently) is folded in to the system response curve at a later stage.

2. A replica keyhole made of aluminum was used(the real keyhole on the tokamak is made from stainless-steel).

83

3. The two front surface flat mirrors are removed. This enables the entire optical axis to be in a single plane, greatly simplifying the construction.

4. Plexiglas enclosures were not used.

The extreme difficulty of calibrating an instrument which measures plasma ECE in the FIR range comes from the lack of desirable calibration source. A calibration source must (1) emit a known frequency spectrum, and (2) have sufficient intensity. A blackbody of known temperature emits a well known radiation spectrum, although the intensity is usually orders of magnitude below the plasma ECE level. FIR lasers can produce sufficient intensity but are discrete in frequency, and the effort and the time involved in collecting enough frequency points from different lasers can become prohibitive quickly. A blackbody source of realistic temperature located in place of the plasma has intensities at or below the noise level of the detector, so that steps must be taken to improve the signal-to-noise ratio by decreasing the noise-level below what is usually acceptable during data acquisition from the plasma.

Common calibration sources are a room temperature and liquid nitrogen cooled (LN_2) eccosorb, and a high-pressure-mercury-arc lamp[69]. The eccosorb provides a large area source, but at 300 and $77K$, the radiated power level is extremely low. The arc lamp, with low voltage($\sim 100V$) discharge, emits at approximately $5000K$. The drawbacks of the lamp are the filamentary size of its arc and the need to account for the transmission by its glass envelope, usually made of fused quartz. Focussing optic is needed to produce collimated large area emission, so that transmission characteristic of this optic also needs to be taken into account. In spite of these complications, the steady-state arc lamp radiation is used as the primary calibration source because of its higher intensity. The effect of the fused quartz envelope is taken into account by reducing the effective source temperature at the high frequency end[73].

Prior to the full mock-up calibration, frequency spectra were measured with both the arc lamp and the eccosorb at the entrance to the Michelson. The purpose of this exercise was to compare the two sources, in a configuration providing maximum signal. The results show that the eccosorb and the arc lamp response curves agree to better than 10% over the designated frequency range when the lamp response is corrected for its temperature variation with frequency. This indicates that the arc lamp with appropriate correction provides an adequate blackbody spectrum.

The full-system calibration spectrum was obtained by continuously operating the Michelson interferometer and averaging approximately 15,000 interferograms each for the measurement with the source switched on and off. Afterwards, the interferogram whose contribution is the source alone(i.e., exclusive of background emission) is produced by taking the difference of the two, which is then Fourier transformed according to Eqn. 3.2. The final product, which is the system response curve shown in Fig. 3.16, is the calibration spectrum divided by the source spectrum(i.e., the modified blackbody curve). In Fig. 3.16, the dotted line shows the raw response curve while the solid line shows the smoothed response curve in which features narrower than approximately $50GHz$ have been smoothed out. The latter is to be used for processing of actual data because the unsmoothed curve applied to the data produces the wrong results by introducing additional $\leq 50GHz$ noise onto the data. We believe this to be the result of uncertainties, possible causes of which include insufficient averaging, difference between averaging and single-scan data taking, and some unidentified difference between the on-site and the mock-up.

Despite time consuming efforts, the certainty of the response curve still appears to be low. We believe that the response curve, as shown in Fig. 3.16, is accurate to within $\pm 15\%$ in the frequency range $200 \sim 700GHz$. Below $200GHz$, the response is dominated by noise so that in this region the response is approximated by a flat gain. We believe this is accurate to within a factor of two. Above $700GHz$, the detector sensitivity falls off rapidly, and while the response curve accuracy may not degrade

too quickly, practical application shows that the data spectrum is dominated by noise and is unsuited for quantitative analysis.

In a well executed calibration, narrow frequency($30 \sim 50GHz$) spectral features that are the artifact of wave interference in various components can be removed. Alternatively, these features can be found by comparing spectra taken under a variety of conditions and identifying features that are constant in frequency regardless of the source condition. Since these features could not be removed by our response curve, manual removal of these features was carried out, whereby each identified feature is approximated by a gaussian and removed. Fig. 3.17(a) shows uncalibrated spectra taken under different magnetic fields, in which several narrow spectral features caused by the system hardware are clearly identified, marked by arrows. The large dip at $560GHz$ is excluded because this is due to atmospheric water vapor absorption. By visual inspection, a weighting function, f_W, of the form shown in Fig. 3.17(b) is used to multiply out the features which results in the 'smoothed' spectra of Fig. 3.17(c). That a single smoothing profile works for all the spectra is an unambiguous justification for such processing. The magnitude of change in the spectrum introduced by these visual smoothing is 20 to 40%.

3.7.2 Absolute Sensitivity Calibration

In addition to the frequency response, absolute sensitivity calculation is needed to determine the radiation temperature or the number of emitting particles. Since the spectral calibration was done using a quasi-blackbody of known temperature, the absolute sensitivity of the system can readily be calculated. Another method is to use the plasma of known temperature (and therefore intensity) as the source. The absolute calibration by these two methods agree to within 50%.

In summary, a calibration acceptable for our purposes has been obtained. We feel that the level of calibration certainty we have reached is probably the practical limit with the present system. A calibration of better quality can in principle be obtained by using a more elaborate construction with precise simulation of the on-site system,

quieter electronics and/or higher sensitivity detector, clever optical arrangements such as the roof-top mirror on the Michelson, or extended time commitment.

3.8 Summary

In this chapter, key issues and components of the VECE diagnostic were addressed. The system consists roughly of three major parts; the detection system, the viewing dump, and the relaying optics. Quantitative characterizations of the effectiveness of the dump, the viewing spot size, and the frequency response of the entire system are necessary for design and execution.

In Section 3.3, we described the Michelson interferometer — InSb detector system. This set-up produces, as a directly measured quantity, an interferogram which is then transformed into frequency spectrum by a Fourier transform computer software.

The viewing dump is a critical component of the system requiring high absorptivity of electromagnetic radiation. In addition, these dumps, placed inside the torus chamber, must be compatible with high-vacuum, high heat and particle flux environment of the experiment. Such dumps have been fabricated from Macor, Pyrex and alumina using a straight groove structure. Measurements of these dumps using a broad-band source show that more than 99% of the incident radiation is absorbed for both Macor and Pyrex, while alumina is slightly worse. The performance of the Macor and Pyrex are satisfactory for the VECE diagnostic.

Due to limited space in the torus, the dump size is marginal compared to the viewing spot size. Since the estimate of dump-captured-fraction of the view is crucial, detailed diffraction calculations were carried out to quantify this. Results show better than 95% of the view terminates at the dump, but additional effects of plasma refraction and scattering may affect this value.

In Section 3.6, key components used for signal processing have been described, and the method for data retrieval and storage has been outlined.

Proper treatment of a wide frequency spectrum measurement requires good calibration. Obtaining one is difficult in this case particularly due to the lack of a desirable source. Mercury-arc lamp was used for the calibration, the relatively low intensity of which necessitated averaging of a total of more than 30,000 interferograms. Although the frequency response curve obtained in this way appears to be accurate to within $\pm 15\%$, it appears not to reproduce the fine scale characteristics of the frequency spectrum completely so that additional processing using plasma data are also incorporated.

In summary, this chapter described in detail the complete VECE system. Concise table of major specifications is provided in Table 3.6.

(a)

325 cm

215 cm

To Michelson

f = 152 cm Spherical Mirror

Fused Quartz Vacuum Window

TF Structure

ALCATOR C Torus

a = 16.5 cm Limiter

Viewing Dump

0   .1   .2   .3   .4   .5 m

R = 64 cm

(b)

40°

To Michelson
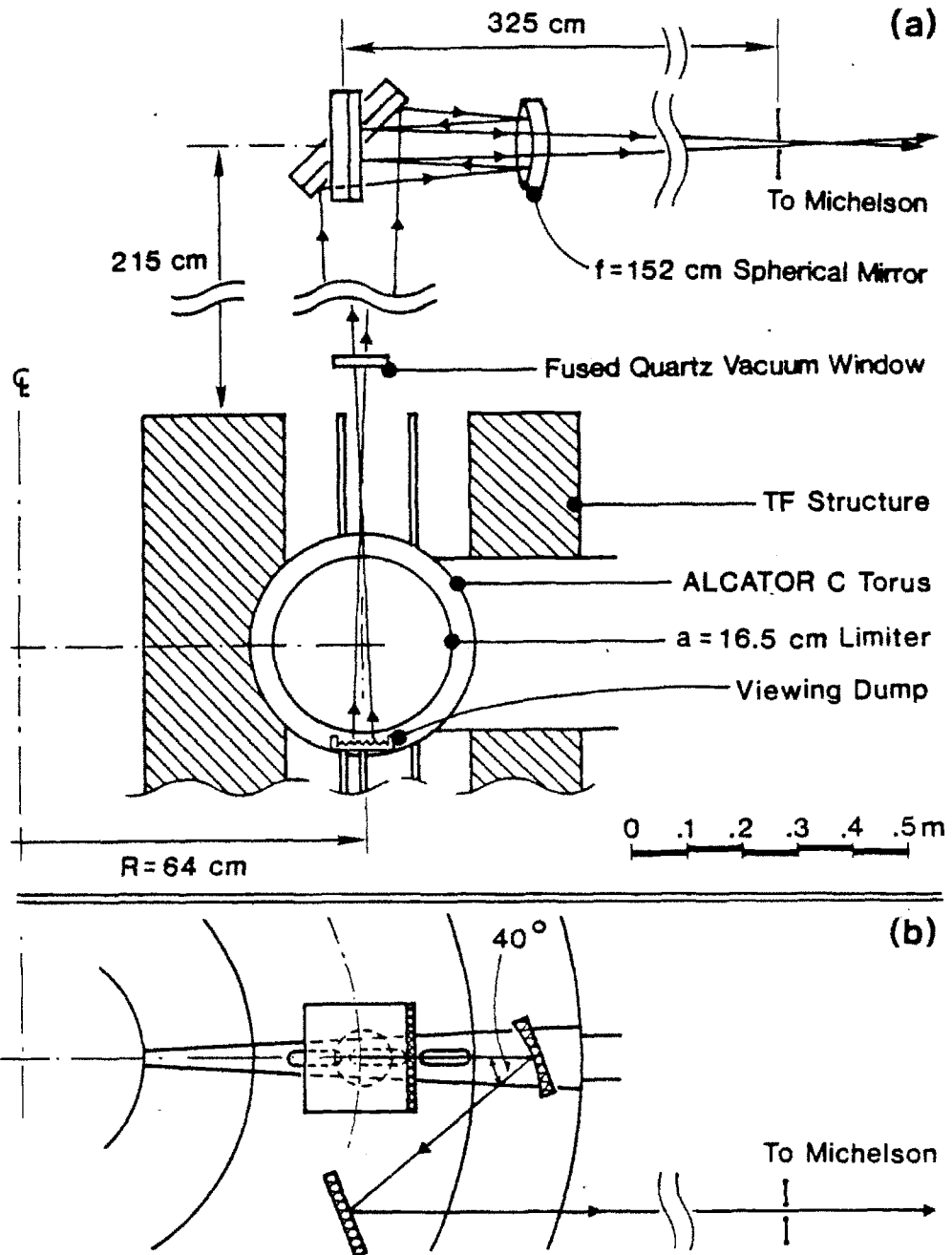
Figure 3.1:
Elevation and plan views of the system.
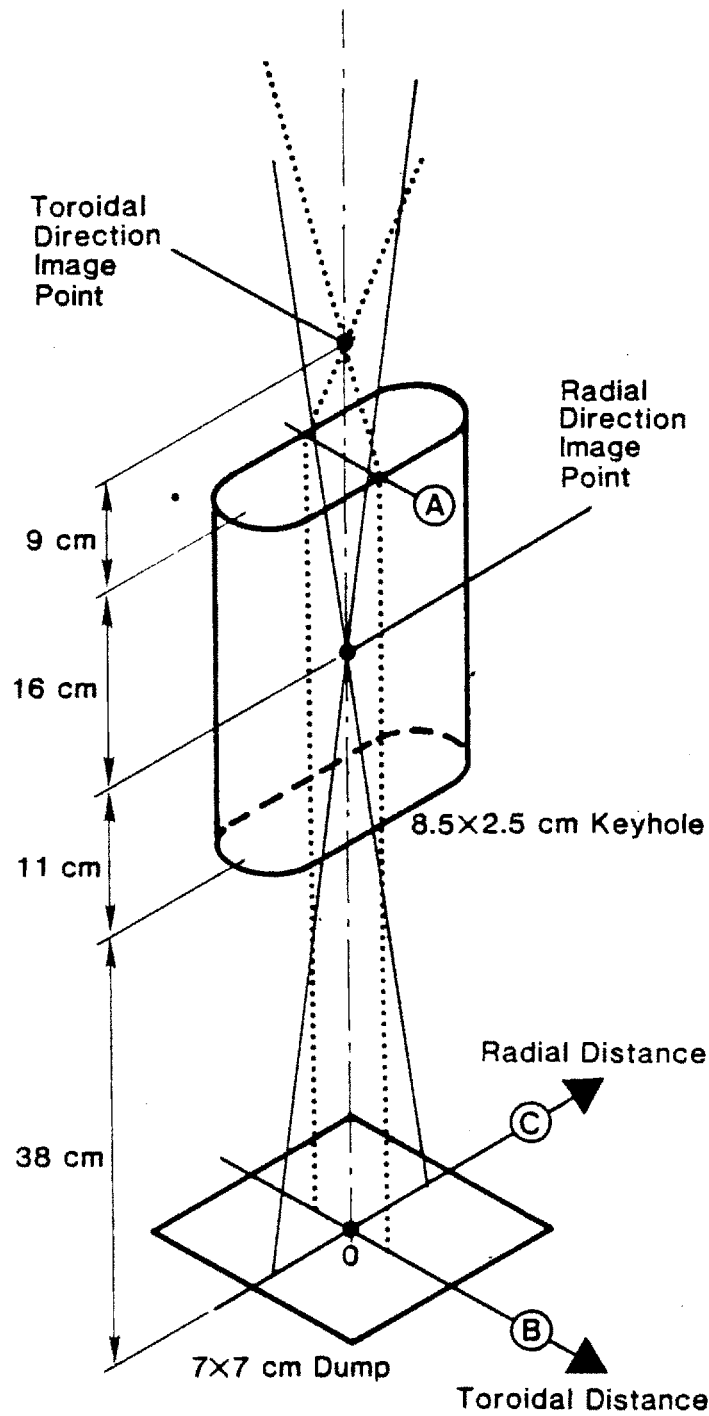
Figure 3.2:
Ray configuration in and near the keyhole. (A) Keyhole entrance level. (B) Dump plane toroidal direction axis. (C) Dump plane radial direction axis. Solid ray is in the radial direction, while the dotted ray is in the toroidal direction.
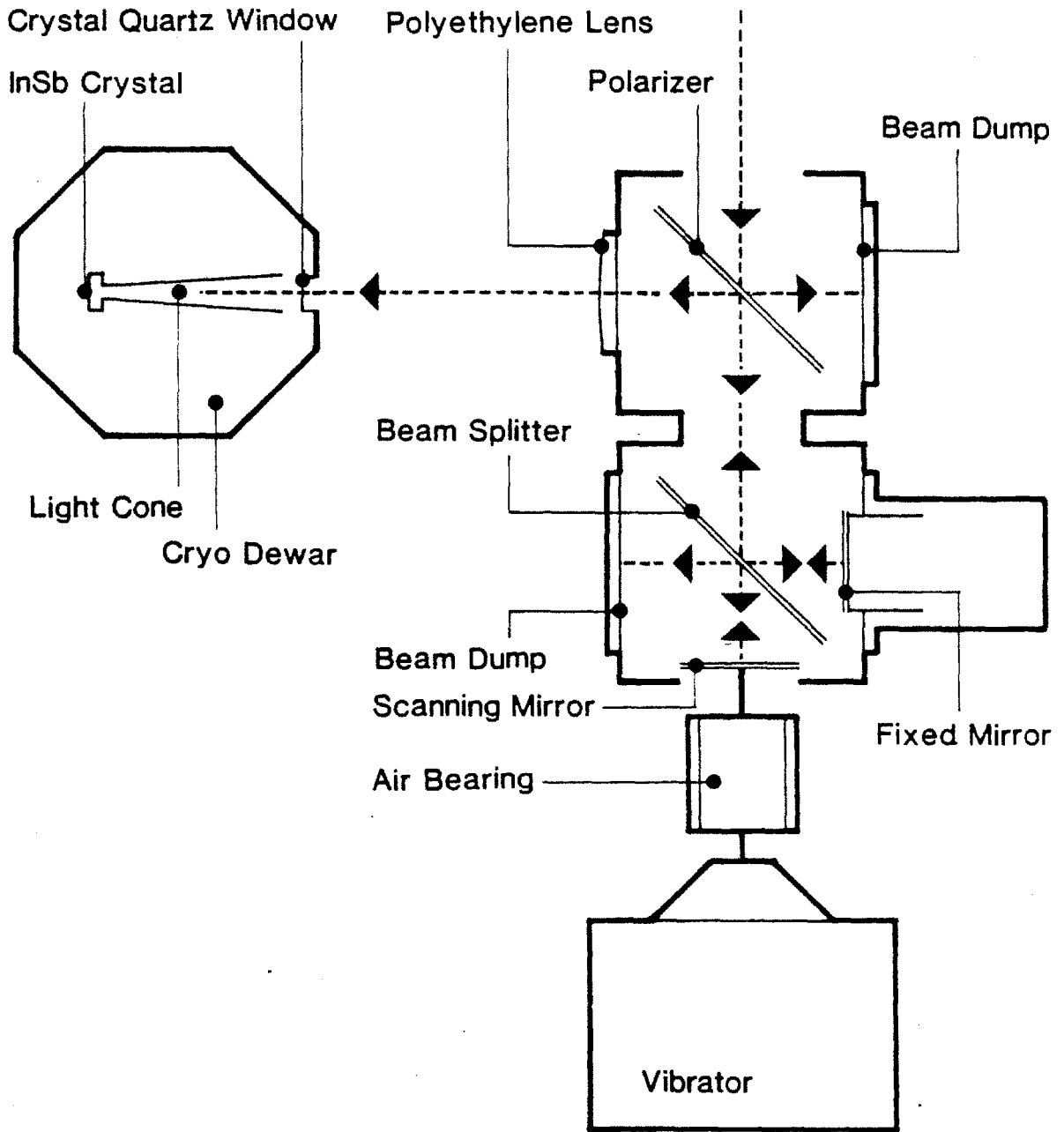
Figure 3.3:
Schematic diagram of the Michelson interferometer system as viewed from above.
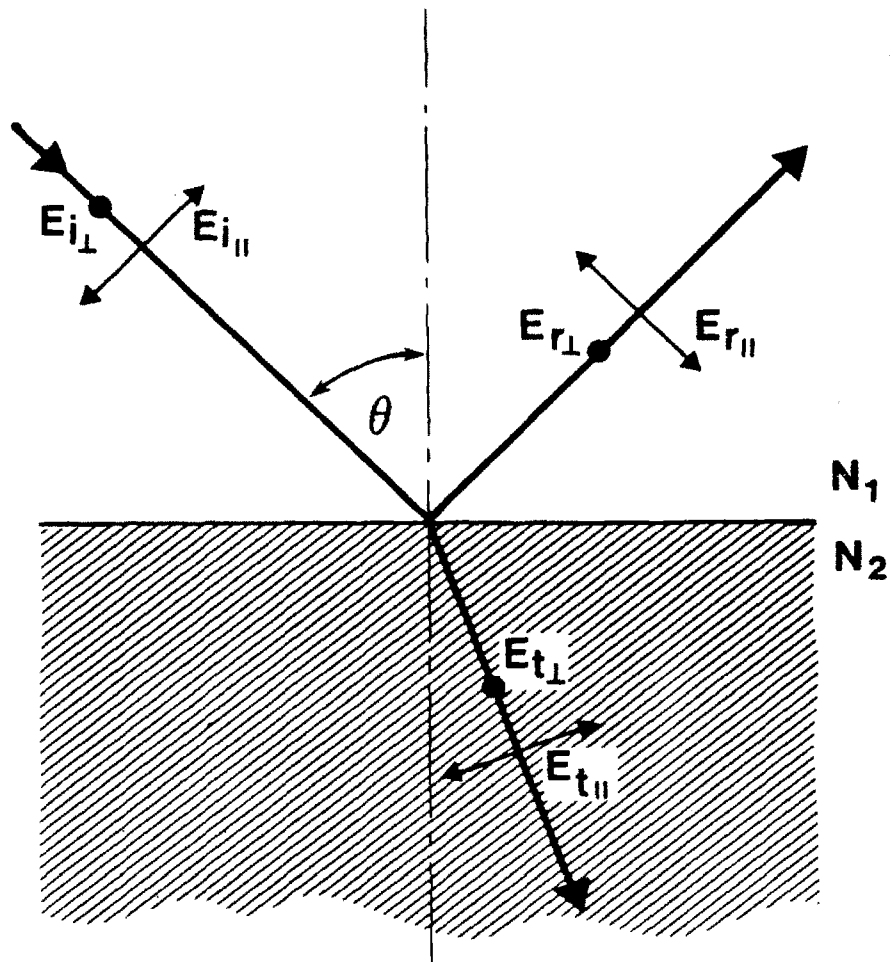
Figure 3.4:
Notation of field vectors at a dielectric interface, used in Eqn. 3.4.
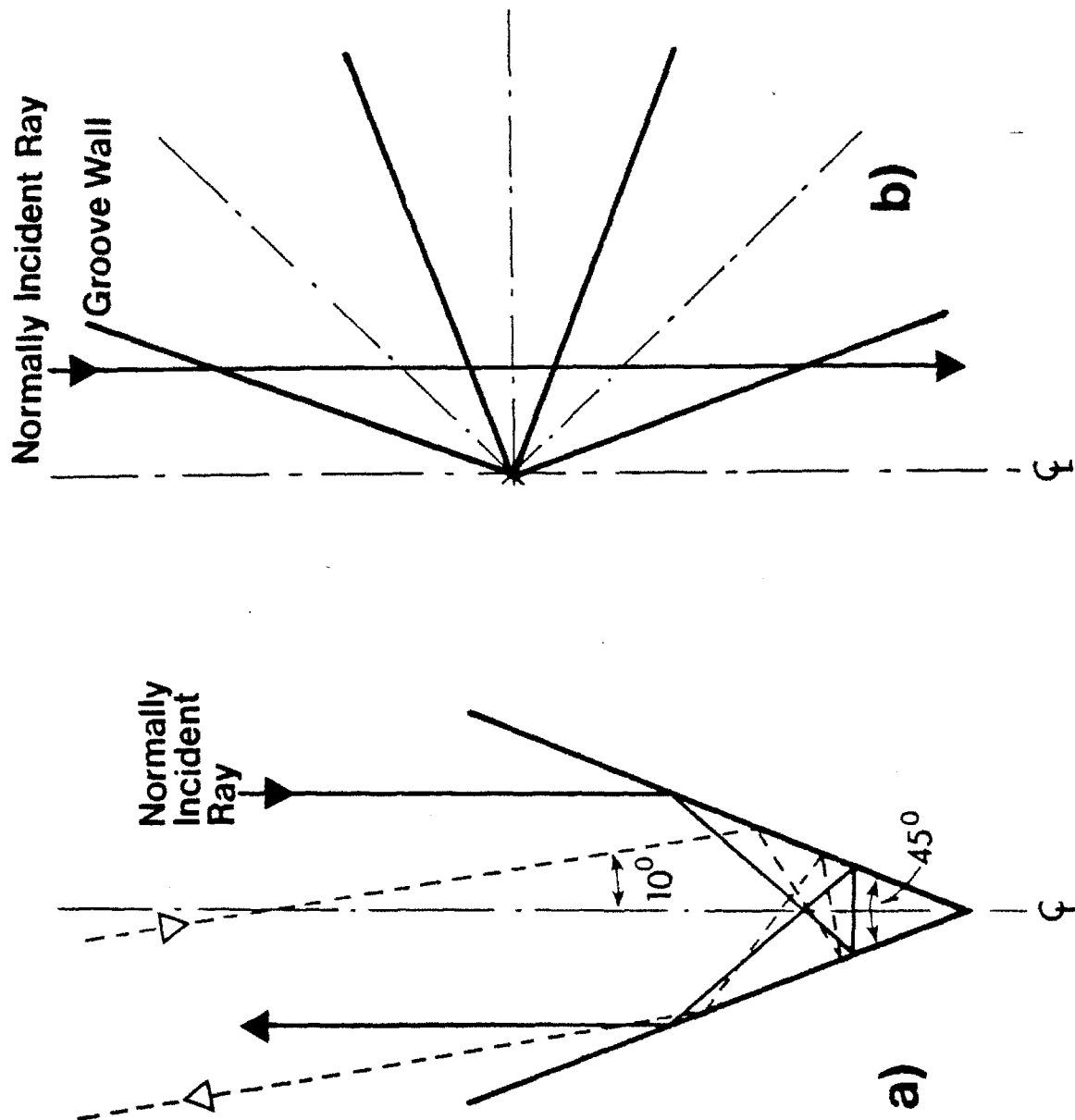
Figure 3.5:

(a) Path of a normally incident ray through a 45° groove in real space(solid line). The path of a ray incident at 10° to normal is shown by the dashed line. (b) Path of a normally incident ray through a 45° groove in semi-circle representation. The groove is duplicated and spread into a semi-circle so that the path of the ray is shown by a straight line.
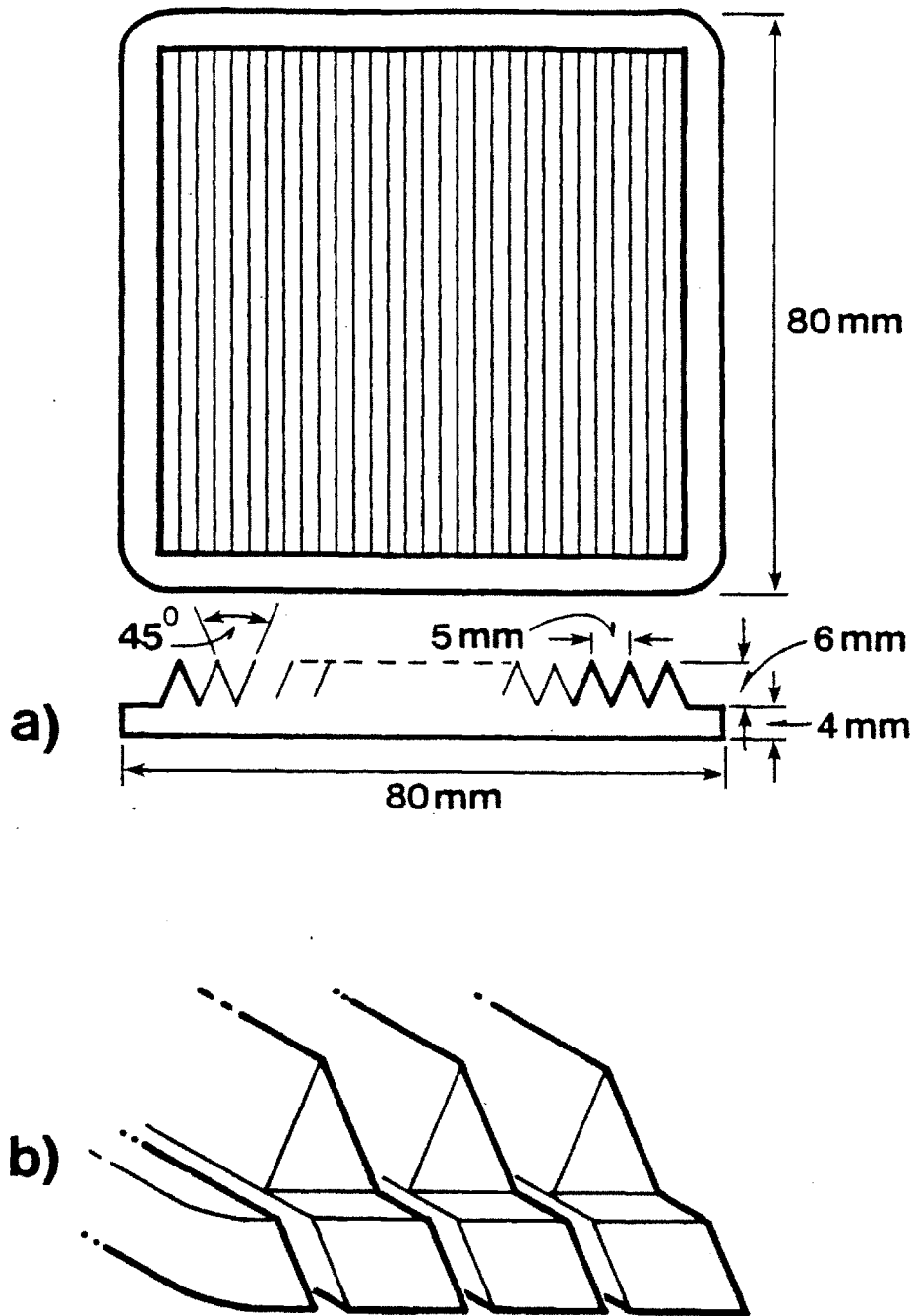
Figure 3.6:
(a) Schematic of the viewing dumps. (b) Modular construction of the Pyrex and the alumina dumps.
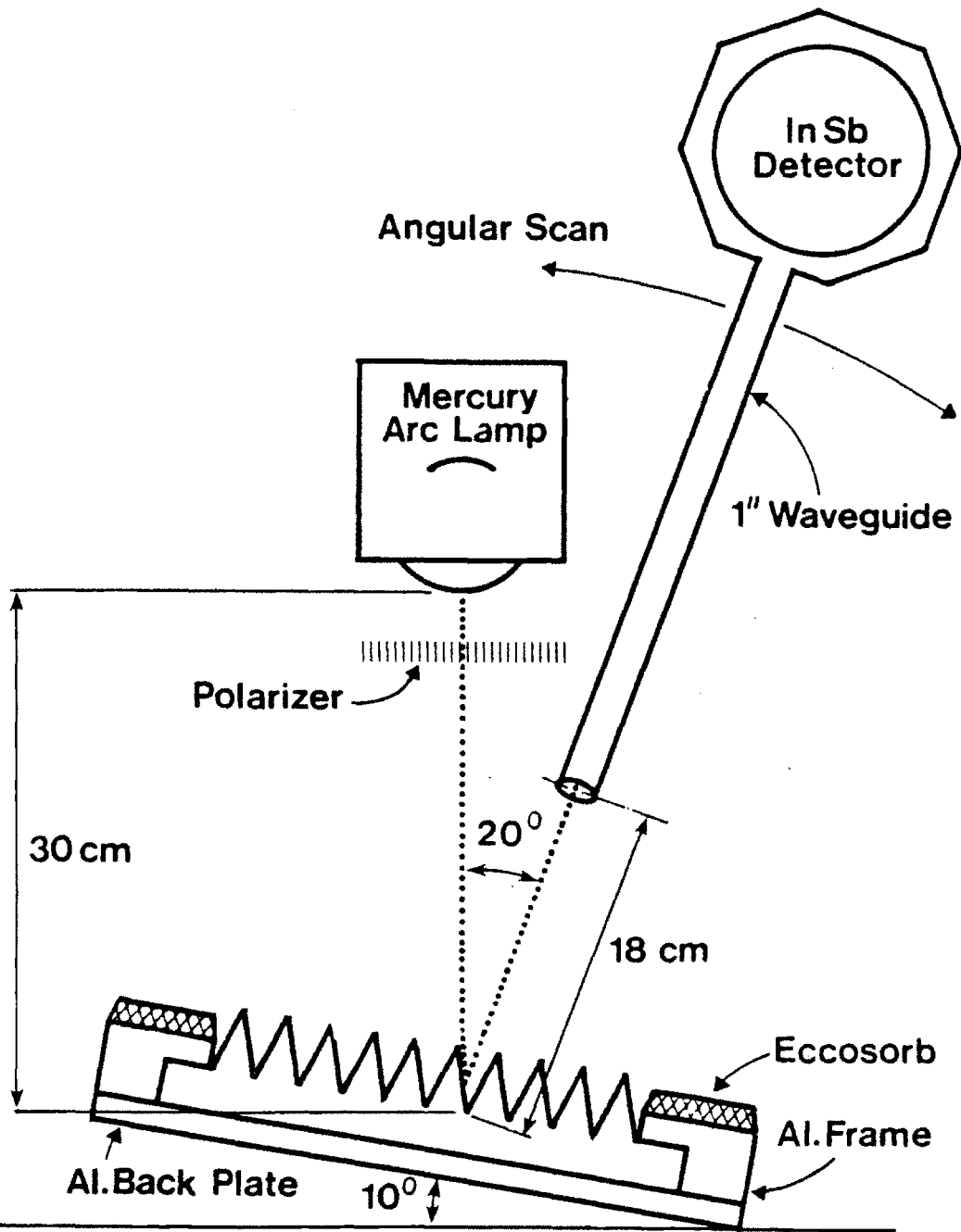
Figure 3.7:
Dump Measurement configuration viewed from above(not to scale).
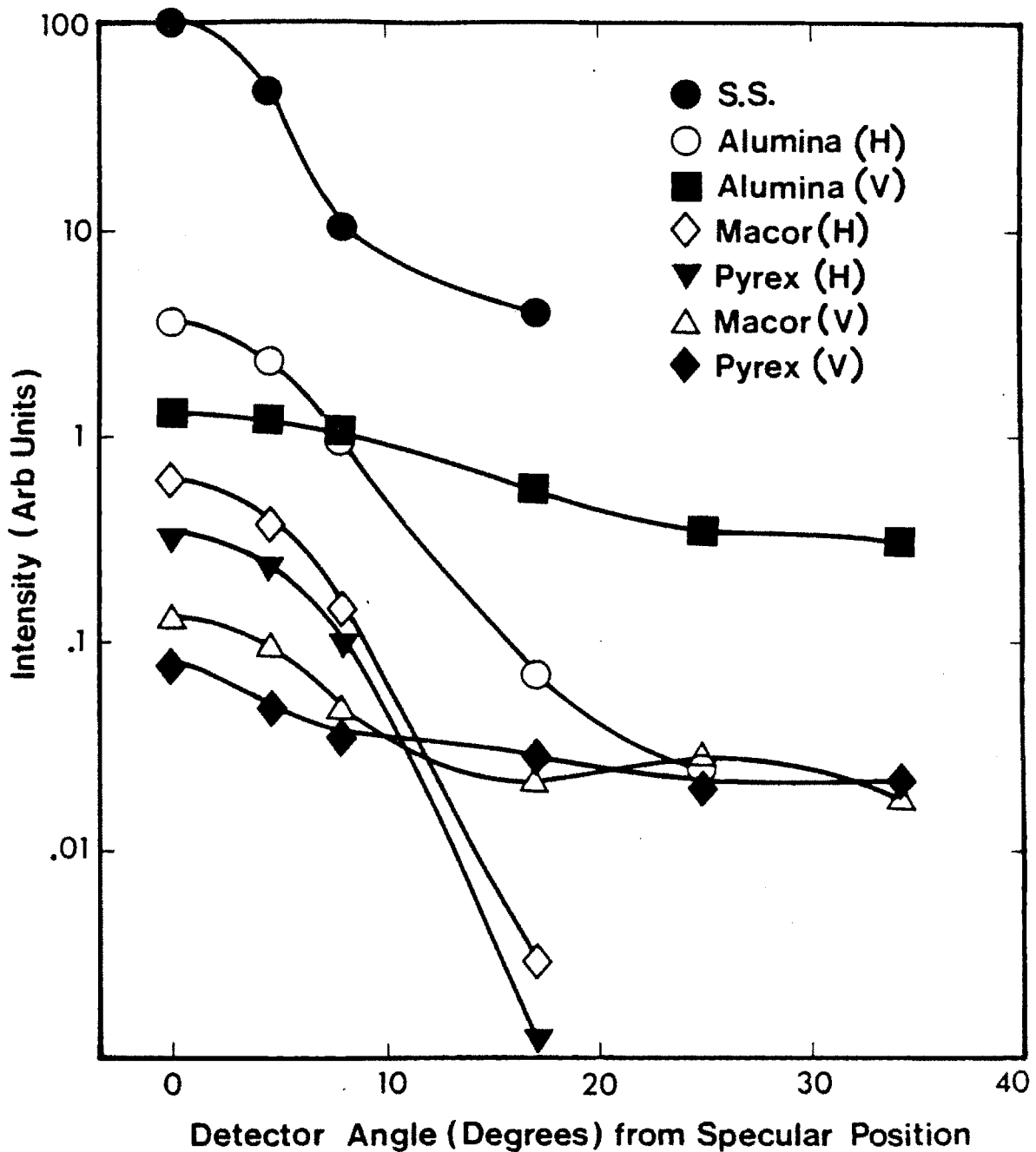
Figure 3.8:
Reflected power from different dumps as a function of the detector angle. (Noise level $\simeq 5 \times 10^{-3} A.U.$)
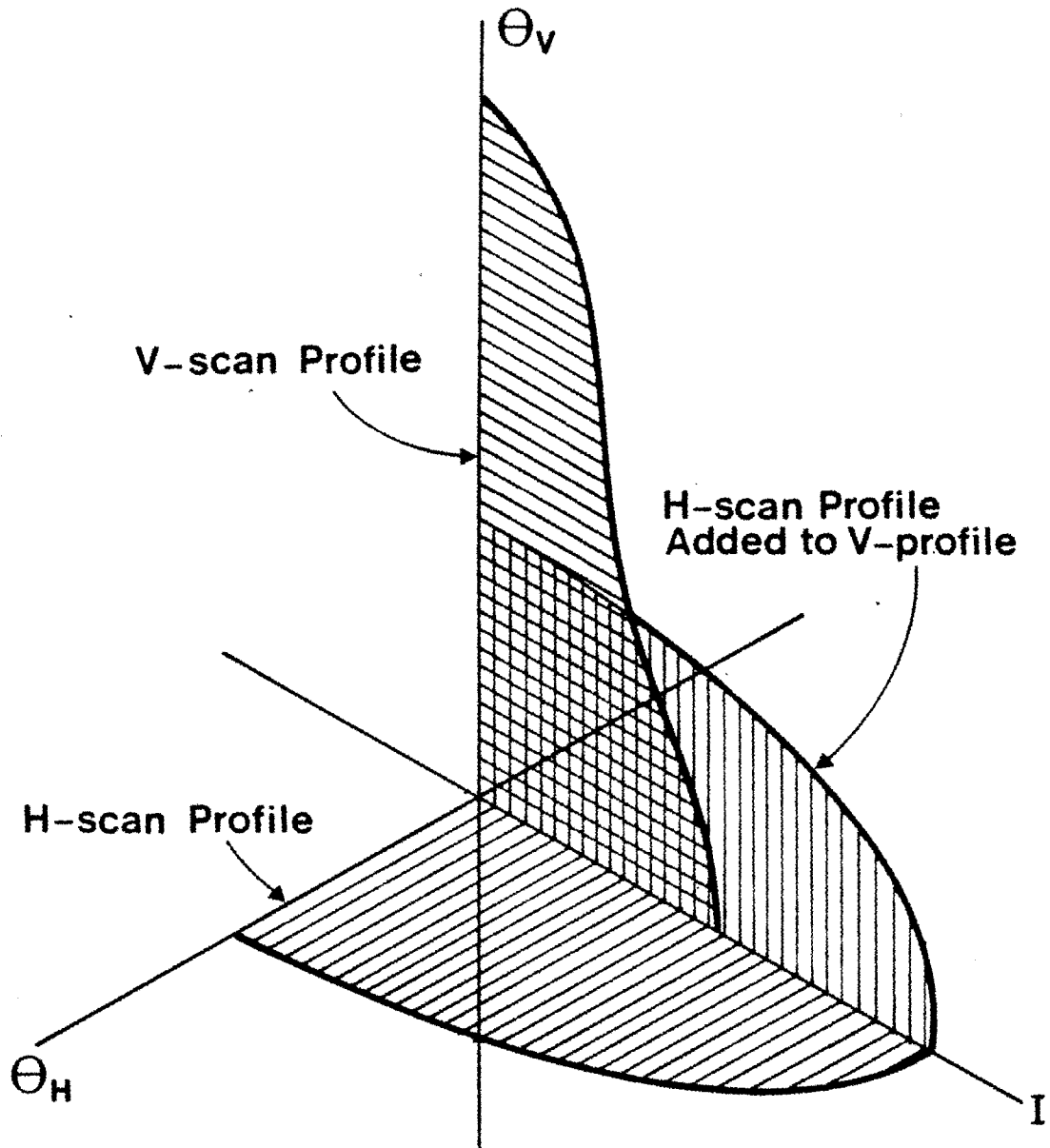
Figure 3.9:
Schematic picture of the normal incidence approximation. The angular distribution of the reflected power, I, is plotted as a function of the two orthogonal orientations, θ_H for the H-scan, and θ_V for the V-scan.
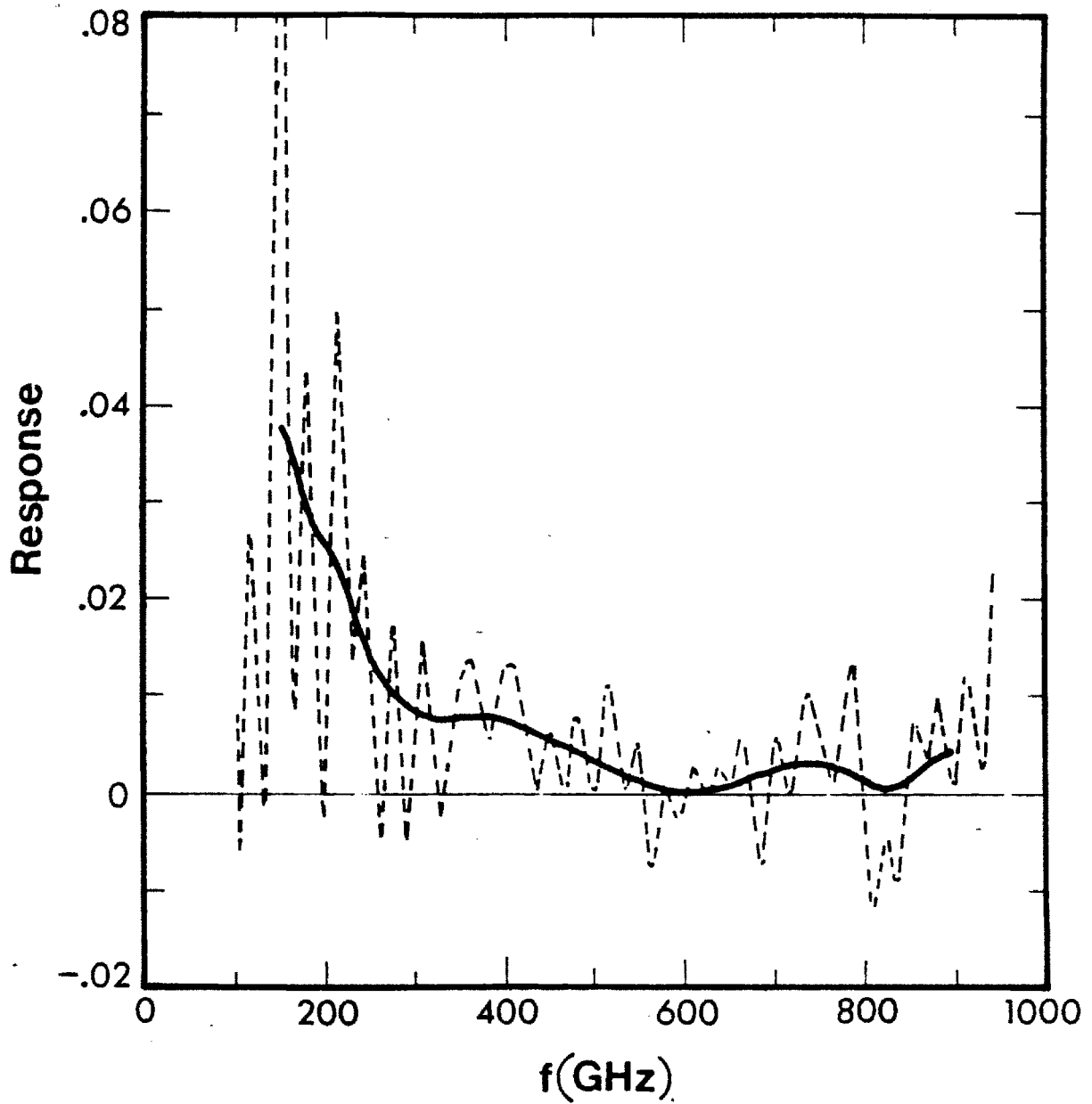
Figure 3.10:
Frequency response of the Macor dump at 10° specular orientation, with grooves oriented in the H-scan direction and for the parallel polarization. Broken line shows the measured spectrum. Solid line is the smoothed approximation.

(a)
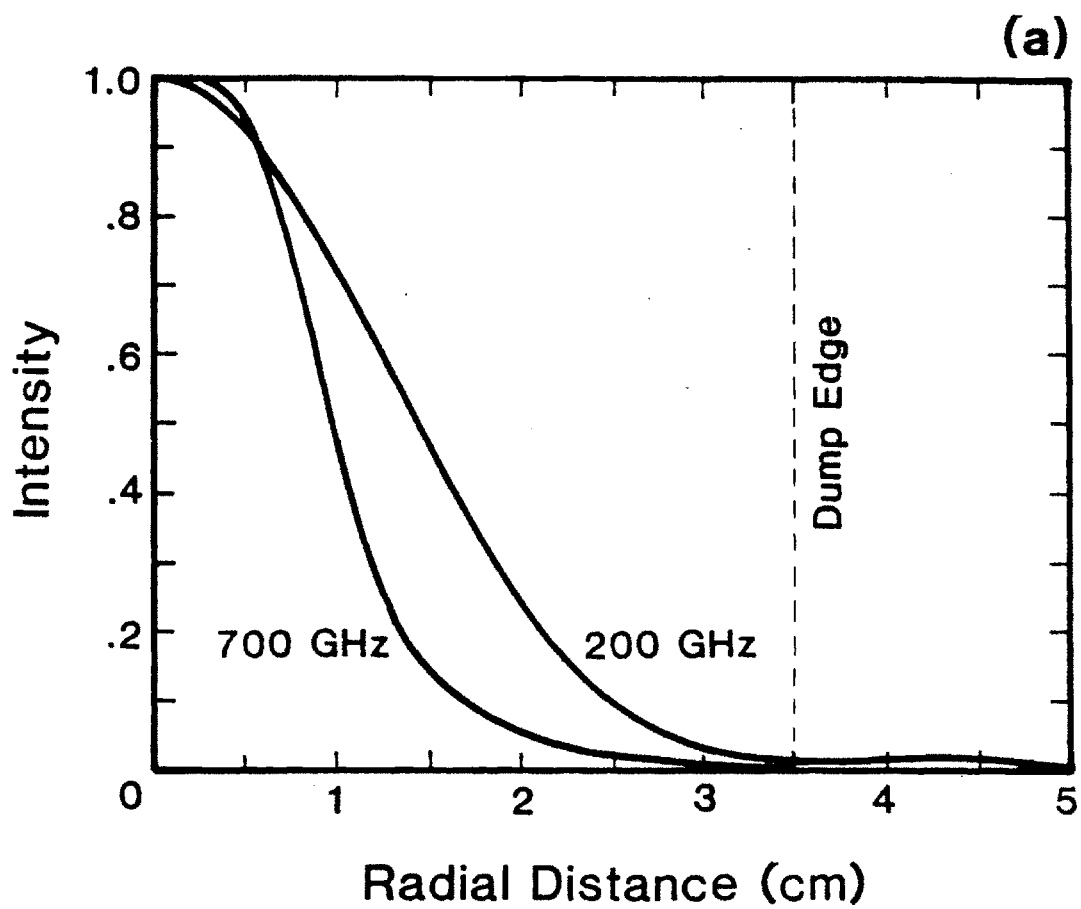
Figure 3.11:
Diffraction spectra at the dump plane. This page: (a) Radial direction. Next page:
(b) Toroidal direction O-mode. (c) Toroidal direction X-mode.

(b)

O Mode

200 GHz   700 GHz

Dump Edge

(c)

X Mode

700 GHz   200 GHz

Dump Edge
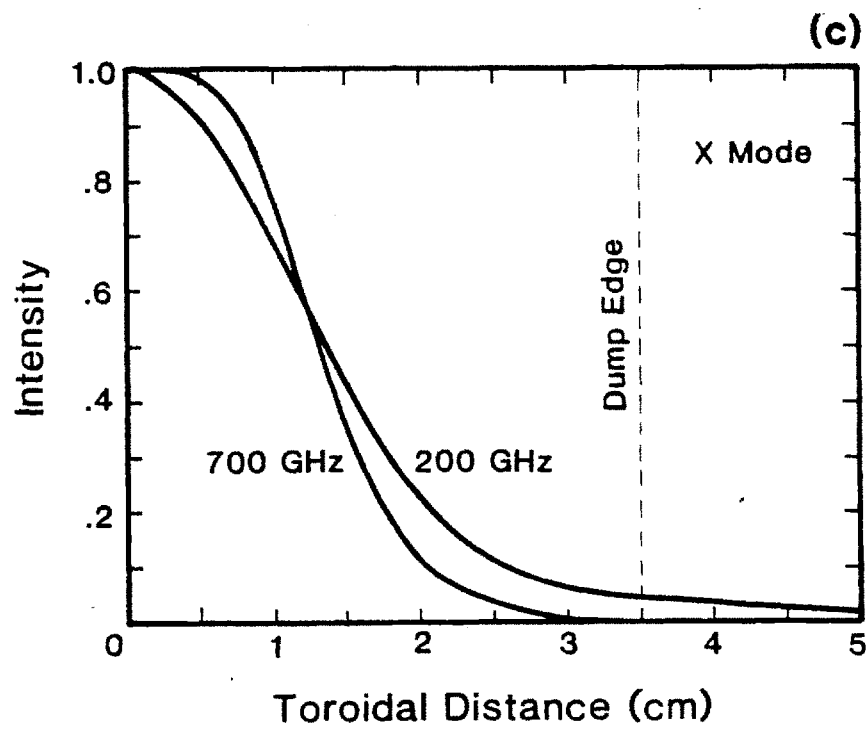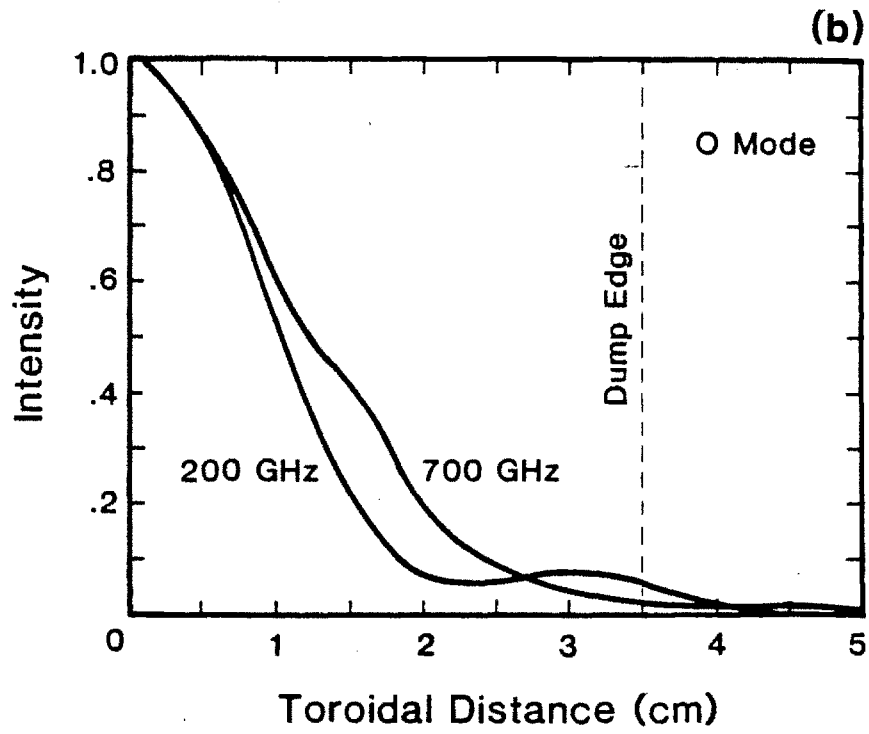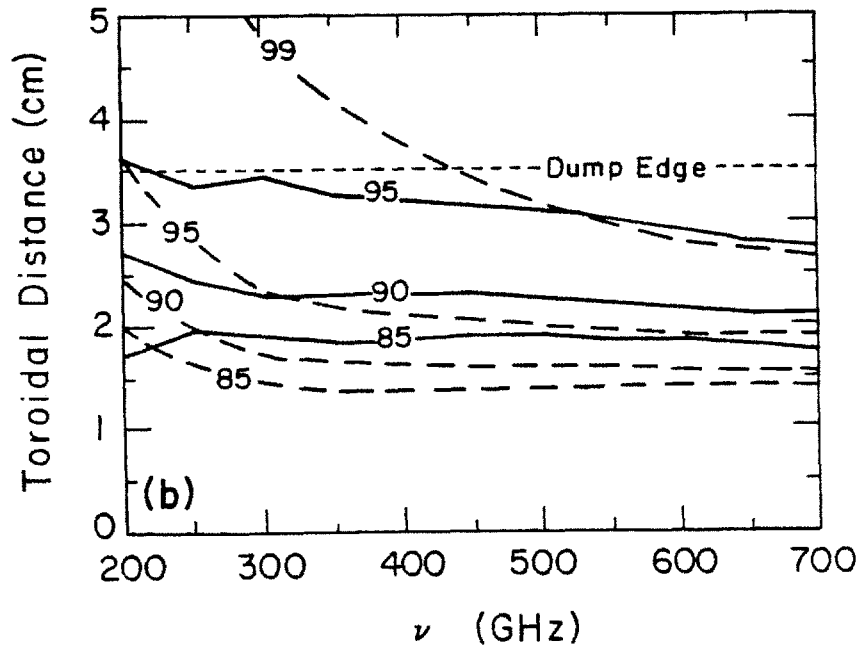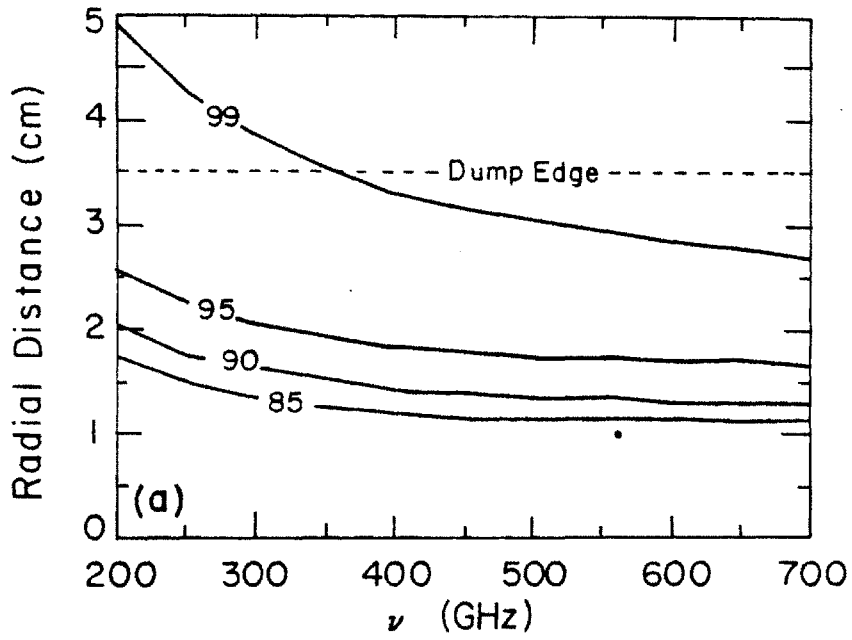
Figure 3.12:
Constant capture fraction contours as a function of frequency and distance. (a) Radial direction. (b) Toroidal direction (solid line — O-mode, dashed line — X-mode).
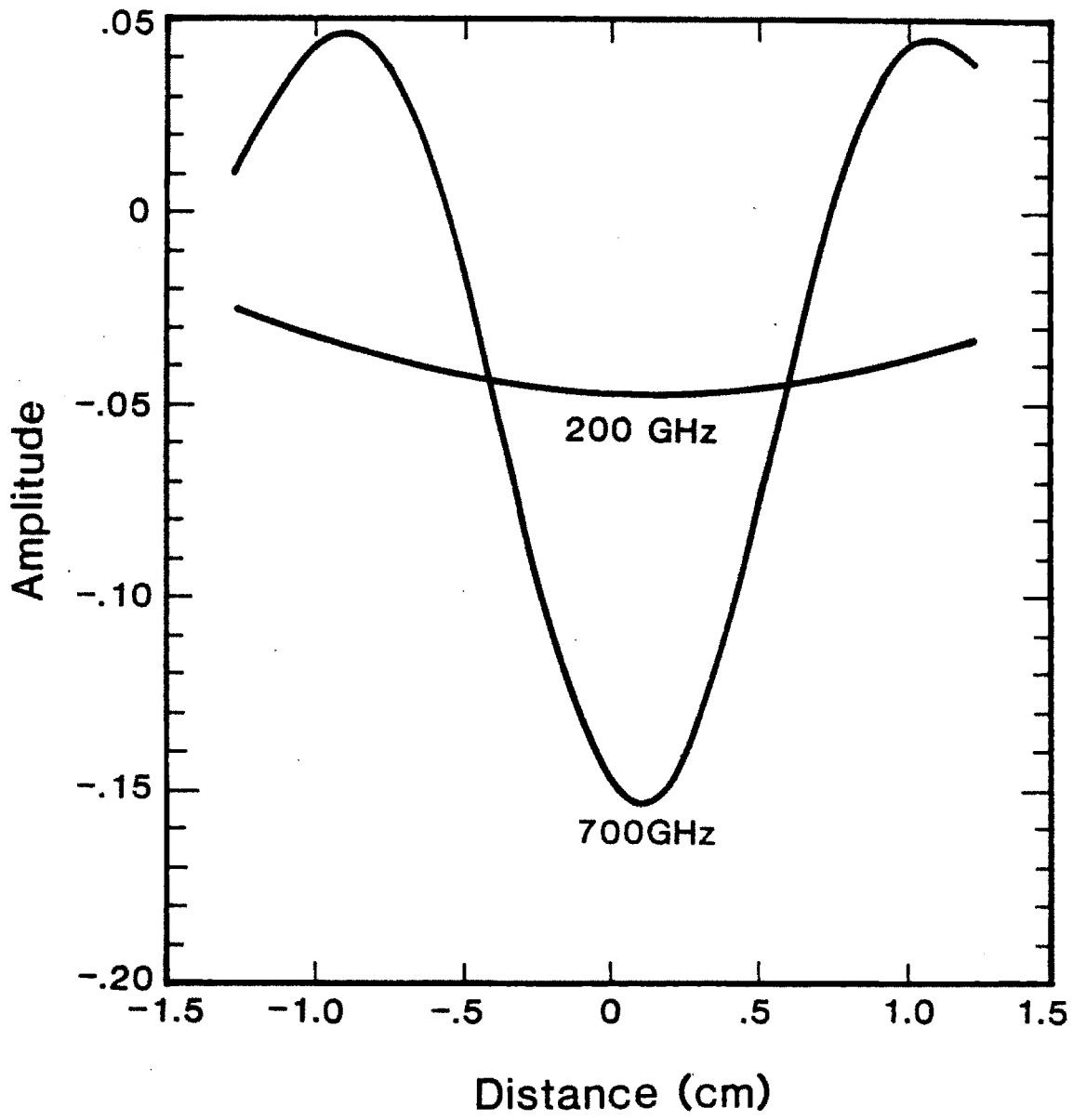
Figure 3.13:
Wave amplitude profiles at the keyhole for 200 and $700GHz$ waves.
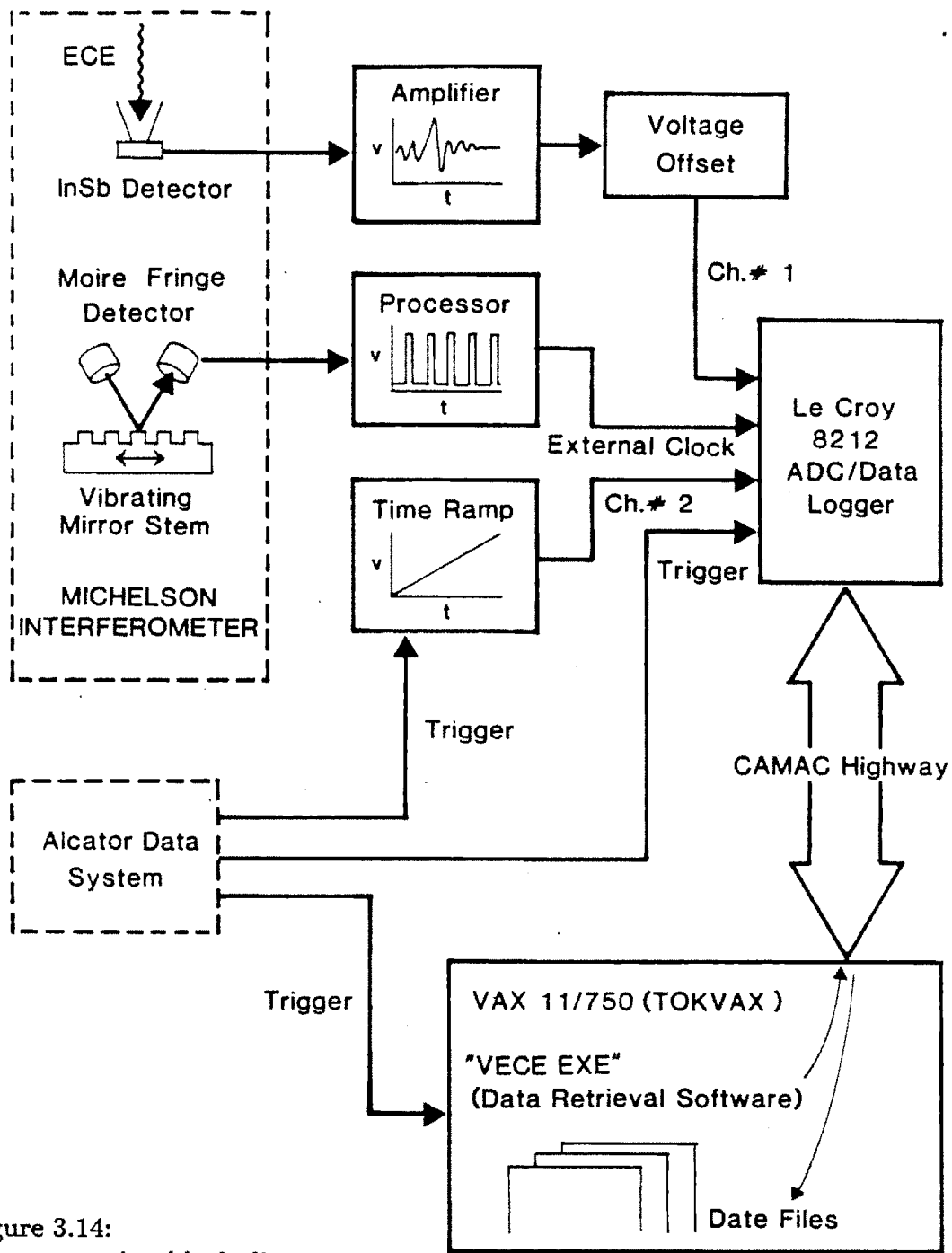
Figure 3.14:
Data processing block diagram.
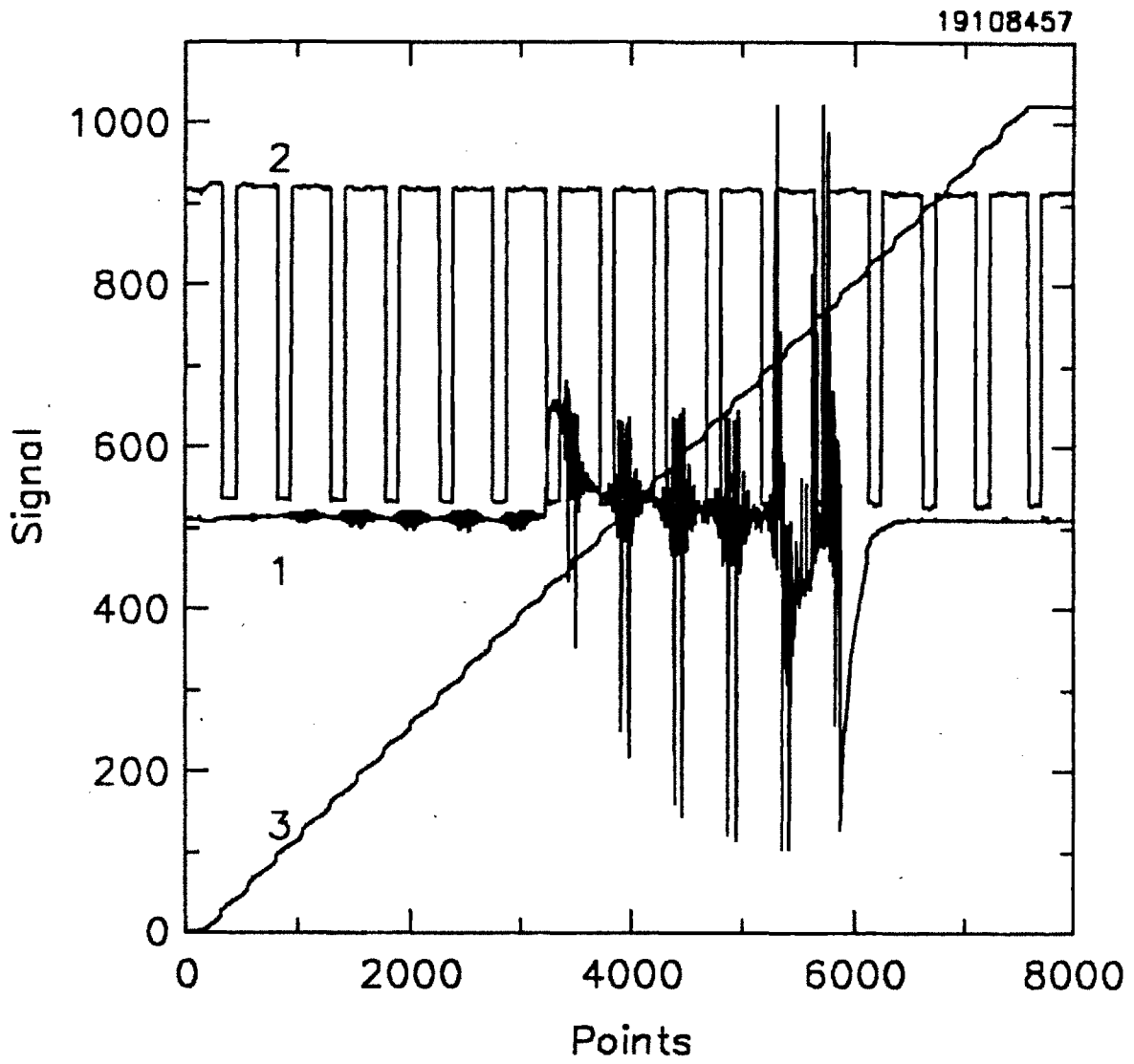
Figure 3.15:
Plot of raw VECE data obtained in one plasma discharge.
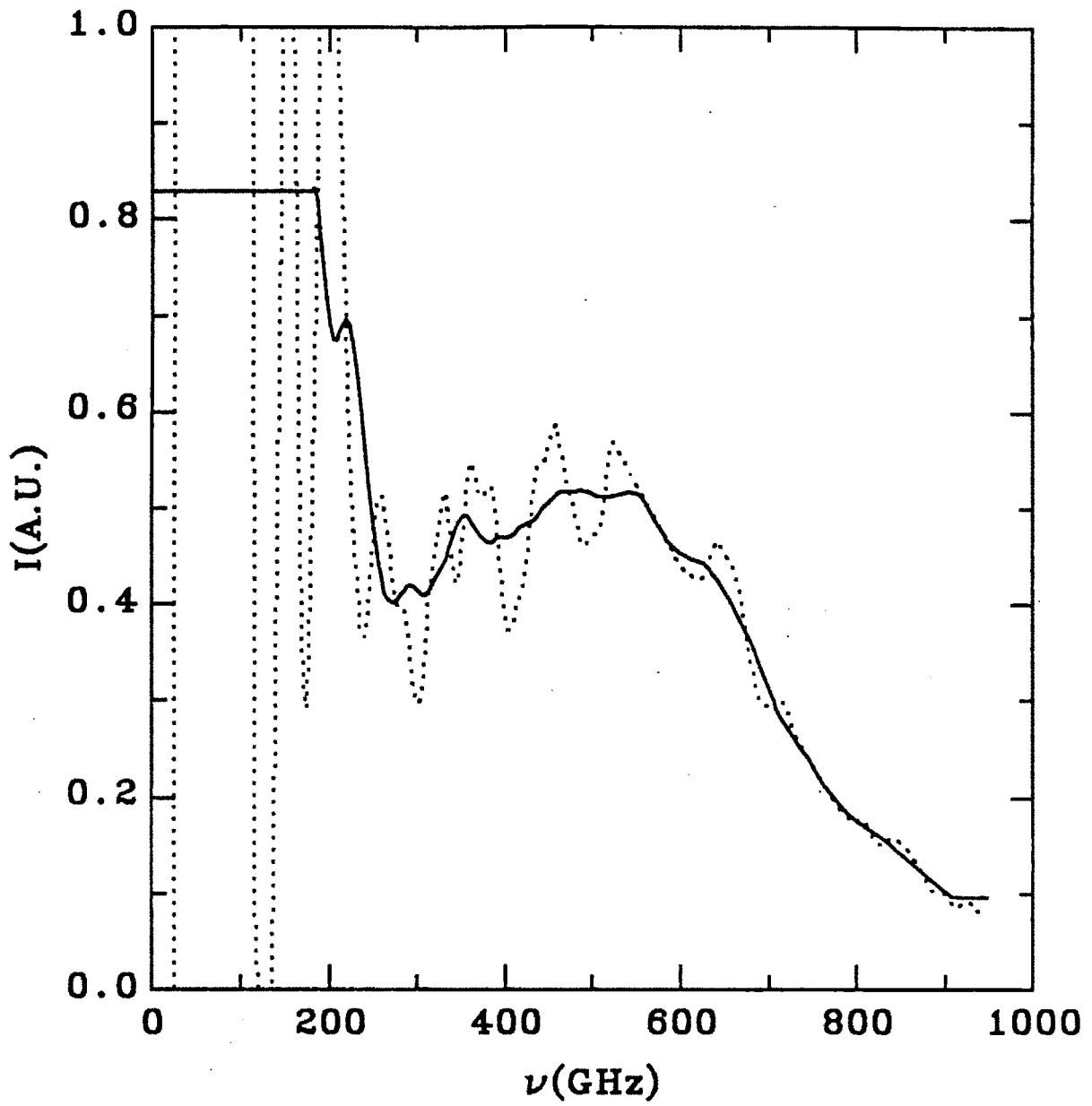
Figure 3.16:
System response curve for both O- and X-modes.
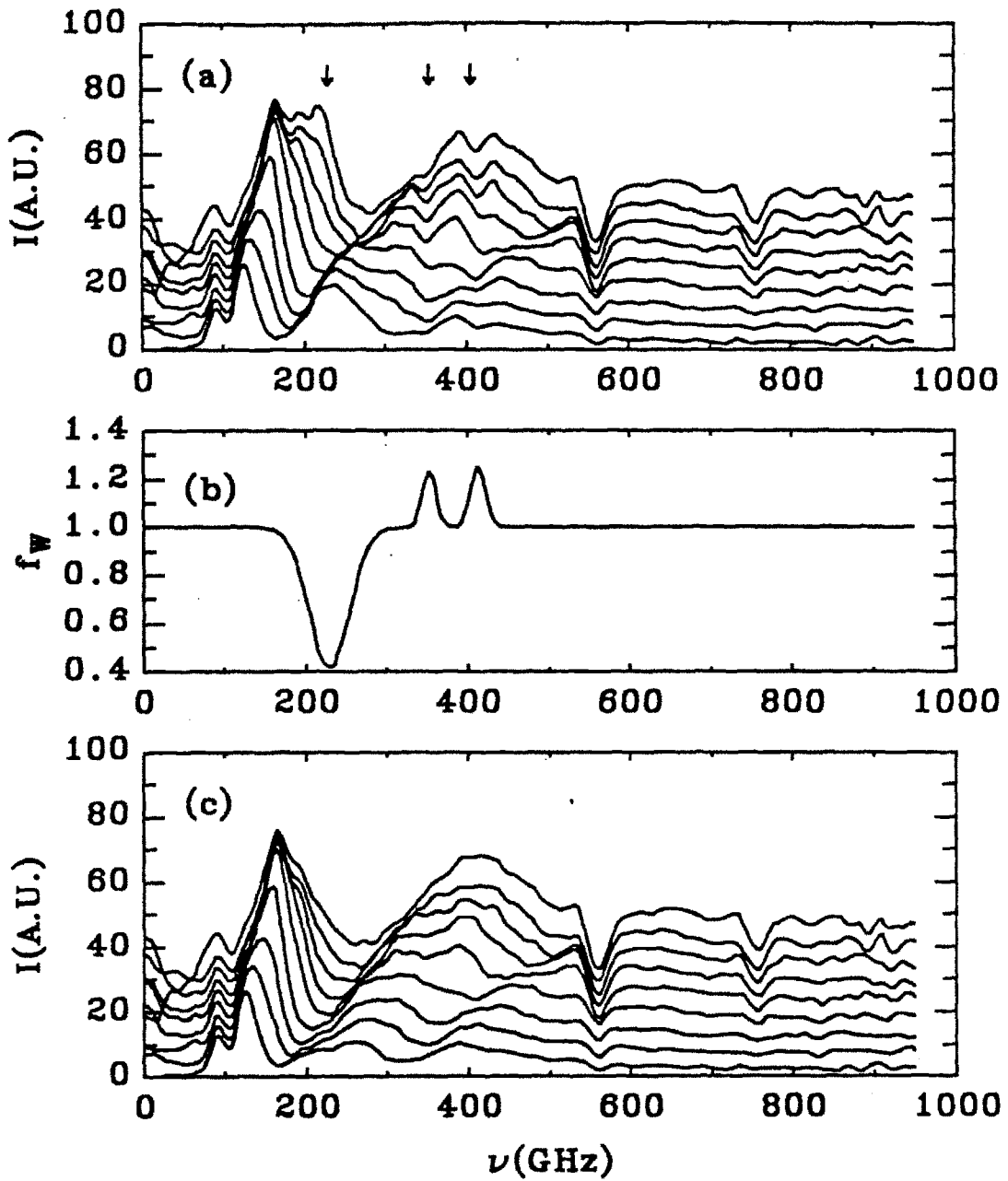
Figure 3.17:
Smoothing of obvious hardware effects by approximation. (a) Uncalibrated spectra(arrows show features introduced by the system). (b) Weighting function. (c) Smoothed spectra.

Table 3.1:
Distances between optical components.

Quantity	Value
Keyhole exit to focussing mirror	246cm
Focussing mirror to aperture	361cm
Keyhole length	27cm
Focussing mirror to aperture image point(toroidal)	237cm
Focussing mirror to aperture image point(radial)	262cm

Table 3.2:
Refractive indices and computed reflectivities (given in %) for different materials. Reflectivities are computed for the parallel and perpendicular electric field orientation.

$-$	Polarization	Pyrex	Macor	Alumina
N	$-$	2.1[65]	2.4[66]	3.1[66]
$\theta_g = \pi/3$	$\parallel$	3×10^{-4}	4×10^{-3}	8×10^{-2}
$\pi/3$	$\perp$	2.0	3.0	7.0
$\pi/4$	$\parallel$	1×10^{-5}	8×10^{-11}	8×10^{-4}
$\pi/4$	$\perp$	0.4	1.0	3.0
$\pi/6$	$\parallel$	1×10^{-5}	2×10^{-5}	7×10^{-6}
$\pi/6$	$\perp$	3×10^{-2}	0.1	0.6

Table 3.3:
Viewing dump specifications.

	PhaseI	*PhaseII*
Surface Dimension	$7 \times 7cm$	$14 \times 14cm$
Groove Width	$0.50cm$	$0.74cm$
Groove Height	$0.60cm$	$0.90cm$
Substrate Thickness	$0.40cm$	$0.49cm$
Number of Grooves	14	19
Groove Angle	45°	45°

Table 3.4:
Measured specular reflectivities(%) of the dumps at 10° incidence angle.

Dump	Unpolarized	$\perp$	$\parallel$	LPF
S.S.	100	100	100	100
Pyrex(H)	0.32	0.46	0.17	0.70
Pyrex(V)	0.074	0.079	0.060	0.25
Macor I(H)	0.58	0.91	0.23	0.75
Macor I(V)	0.13	0.12	0.12	0.27
Alumina(H)	4.2	4.3	3.8	13.
Alumina(V)	1.3	1.2	1.4	5.4

Table 3.5:
Angle integrated total measured reflection (given in %).

Polarization	Pyrex	Macor I	Alumina
Unpolarized	0.57	0.76	8.3
$\perp$	0.79	1.2	8.3
$\parallel$	0.36	0.35	7.7

Table 3.6:
Overall VECE system specifications.

Optical System

Focussing Optic	$f = 152cm$, $d = 15cm$ spherical front surface mirror
Vacuum Interface	4.5" dia. fused quartz window(Phase I) 4.5" dia. crystal quartz window(Phase II)
Instrument Aperture	1" dia. connected to 2" dia. Cu light pipe(Phase I) 1" dia. free standing(Phase II)
Image Magnification	1.52 in toroidal direction 1.38 in radial direction

Viewing Dump

Size	See Table 3.3
Dump Frame	S.S. or Graphite
Dump Groove Orientation	Groove $\parallel B_T$(Phase I) Groove $\perp B_T$(Phase II)
Material	Macor or Pyrex (Phase I) Macor (Phase II)

Michelson Interferometer

Calibrated Frequency Range	$200 - 700GHz(\pm15\%)$
Frequency Resolution	$20GHz$
Temporal Resolution	$15 - 20ms$

Plasma

Minor Radius	16.5cm(Phase I)
	11.5cm(Phase II)

Chapter 4

VERTICAL ECE MEASUREMENT

4.1 Introduction

In this chapter, selected frequency spectra measured with the VECE diagnostic are presented. These data are then examined for the following purposes.

1. Verify the performance of the diagnostic's optical system.

2. Determine any corrections to the nonthermal spectrum needed in order to analyze the distribution function.

The performance of the system refers to its ability to isolate the viewing chord from the rest of the plasma, which is accomplished by the combination of the viewing dump and the well collimated viewing chord. Thus, we choose to compare measurements taken with and without the dump in order to evaluate this performance. The effect of depolarization is evaluated and the cause determined by measuring the polarization ratio from well defined plasma emissions, e.g. the third harmonic emission from thermal plasmas. These discussions carried out using thermal ECE spectra are given in Section 4.2.

In Section 4.3, nonthermal ECE measured with and without the dump are compared and differences in the spectra which stem from the presence of the dump

are examined. Although quantitative assessment is difficult, some inference of the system's effectiveness is given.

In Section 4.4, evidences produced in the two previous sections will be used to come up with an appropriate prescription for post-processing of the measured non-thermal spectra, in preparation for the distribution function diagnosis. Section 4.5 is the chapter summary.

4.2 Thermal Plasma Emission

Optical Depth Characterization

In the conventional radially viewing ECE measurement, it is found, both from theory and experiment, that for present day tokamaks optically thick emissions are measured at the ordinary mode first harmonic and the extraordinary mode second harmonic. The extraordinary mode first harmonic is cut-off when viewed from the tokamak outboard side due to the presence of an evanescent layer, and the rest of the harmonics are optically thin. The optically thick regions for j_1^+ and j_2^- usually fill the antenna pattern of the detection system so that the optical depth characterization is unambiguous.

In the vertical viewing configuration, the question of optical depth along the chord for any particular frequency becomes rather complex. As schematically illustrated in Fig. 4.1, the viewing chord width in the radial direction, which is approximately $3cm$ for the Alcator VECE system, is much broader than the width of a typical thermal resonance in the radial direction, which is given by

$$\Delta R = \frac{(\gamma - 1)}{\gamma} R \leq 1mm. \tag{4.1}$$

Hence, when an optically thick thermal resonance is within the viewing chord, the detector sees two components of the emission which are distinguished by their different degree of interaction with the resonance region.

1. The emission emanating vertically from the resonance layer. Since $\tau \gg 1$, the intensity of this emission is characterized by the radiation temperature at distance x from the edge, where x is determined from

$$\tau \sim 1 \sim \int_0^x \alpha(s)ds, \tag{4.2}$$

where s is the unit vector downward along the resonance column, with its origin at the top plasma boundary. Thus for example, for a plasma of the same temperature profile, the distance at which $\tau \sim 1$ decreases as density increases. The effect of this is that despite constant temperature, the radiation temperature that the emission is characterized by decreases as the density increases.

2. The emission that propagates through the non-resonant region. Even when the resonance occupies a large portion of the viewing chord, this type of emission can enter the detector through wall reflections or by refraction; the latter takes place especially near the resonance where $N \to \infty$.

When the resonance layer is outside the viewing chord, only the emission of the second kind need be considered.

In the case when the resonance is optically thin, i.e.,

$$\tau = \int_0^{2a} \alpha(s)ds \ll 1, \tag{4.3}$$

the emission intensity is characterized by

$$I \simeq \frac{\int j\,ds}{1 - R_{view}}, \tag{4.4}$$

accounting for the reflection coefficient from the viewing chord termination point, R_{view}, similar to Eqn. 3.3.

The situation becomes more complex for the first harmonic X-mode, where two additional effects of the upper-hybrid resonance, ω_{UH}, and the right-hand cut-off, ω_R, which are given by[46]

$$\omega_{UH} = \sqrt{\Omega^2 + \omega_{pe}^2} \tag{4.5}$$

$$\omega_R = \frac{1}{2}(\Omega + \sqrt{\Omega^2 + \omega_{pe}^2}) \tag{4.6}$$

are introduced in addition to the fundamental cyclotron resonance. The X-mode wave is evanescent in the frequency range bound by ω_{UH} and ω_R. For the first harmonic O-mode, the plasma frequency cut-off, $\omega = \omega_{pe}$ will increase ray refraction, but will not in general create an inaccessible region inside the plasma for Alcator since $\omega_{pe} < \Omega$.

In Fig. 4.2, we show the three layers, corresponding to Ω, ω_{UH}, and ω_R (A, B, and C, respectively in the figure) in the Alcator plasma for three different frequencies corresponding to $R_\Omega > R_o$, $R_\Omega < R_o$, and $R_\Omega = R_o$, where R_Ω is the major radius at the resonance and R_o is the major radius at the plasma center. Toroidal field strength of 8 Tesla and an electron density profile of the form

$$n(r) = 1 \times 10^{20} \left[1 - \left(\frac{r}{a} \right)^2 \right]^{1/2} \quad [m^{-3}] \tag{4.7}$$

is assumed. In 4.2(a), the cyclotron resonance is on the low field side, external to the viewing chord. Since ω_{UH} layer absorbs the X-mode cyclotron radiation, the effect of this configuration is to reduce the effective wall surface area. In 4.2(b), the cyclotron resonance is on the high field side, also external to the viewing chord, and the upper hybrid and the right hand cut-off layer bow out into the viewing chord. Owing to refractions that occur on the low field side of this ω_R layer which bends the viewing chord away from the dump, the dump is rather ineffective in this case. The effect of ω_R will continue to bend the viewing chord as long as this layer is reasonably close to the plasma axis. The cyclotron radiation will probably reach the detector in this case even though the evanescent layer exists between the

116

point of origin and the keyhole entrance, by propagating around the limiter shadow region by multiple reflections. Finally 4.2(c) shows the cyclotron resonance at the plasma axis, so that one half of the viewing chord (high field side) is in a similar situation to (a), and the other half is in a similar situation to (b). In reality however, tunnelling of radiation can occur through the evanescent region between ω_{UR} and ω_R layers[74], especially when the distance is small near the edge of the plasma, making clear-cut interpretation difficult.

Thus, for frequencies near Ω, different effects change the effective volume of the plasma, the effective surface area of the reflecting wall, and the viewing chord shape. An additional effect of these thermal layers is that nonthermal emissions that originate in the evanescent region will not propagate, as was discussed in Chapter 2 in reference to Fig. 2.11.

Comparison With and Without the Viewing Dump

In Fig. 4.3, we plot two representative extraordinary mode ECE traces covering the first three harmonics from a $B_T = 8T$ thermal plasma of the same discharge condition during Phase I operation. Trace A(dotted line) was taken with a stainless steel flat plate in place of the viewing dump, and Trace B(solid line) was taken with the Macor viewing dump during Phase I operation. The cyclotron frequency at the center of the plasma is $220GHz(\Omega)$.

Focussing our attention to the second harmonic(2Ω), Trace A shows substantial emission from essentially the entire major radii occupied by the plasma($48 \leq R(cm) \leq 80$, $350 \leq \nu(GHz) \leq 580$). In this respect, the emission is similar to that obtained by the horizontal configuration, and we believe that multiple reflections and the high reflectivity of the stainless-steel are responsible for extending the view. The depression in this spectrum in the range $430 \sim 460GHz$ is caused by the optically thick resonance effect discussed above, i.e., the resonance layer inside the viewing chord decreasing the optical penetration.

117

The second harmonic emission of Trace B is dramatically different from A, and now most of the intensity is concentrated in a narrow peak at $440GHz$ with a full-width-at-half-maximum(FWHM) of $24GHz$. The suppression of emission outside this peak attests to the effectiveness of the dump in absorbing multiply reflected emissions that land on it, preventing reflections into the viewing chord. The FWHM corresponds to $\approx 3.5cm$ in the major radius direction if we attribute the broadening entirely to the magnetic field gradient. This width(presumably near the center of the plasma in the vertical direction) is consistent with our calculations of Chapter 3 of the viewing spot size from diffraction considerations.

The finite intensity outside the narrow peak in Trace B is attributed to reflections from the dump, or more likely its frame, since we found in Chapter 3 that the antenna pattern is slightly larger than the Phase I dump size of $7 \times 7cm$. The effectiveness of the system in removing radiation from outside the viewing chord is defined as

$$\eta_{removal} = \frac{I_A(\omega) - I_B(\omega)}{I_A(\omega)}, \qquad (4.8)$$

where subscripts A and B refer to the traces, and the range of ω excludes the resonance inside the viewing chord. Measurements of $\eta_{removal}$ from the spectra of Fig. 4.3 and other traces in the second harmonic frequency range show $\eta_{removal} = 90 \pm 5\%$. We believe this effectiveness to vary with frequency in a similar manner as some convolution of the dump's frequency response curve (Fig. 3.10) and the constant-capture-fraction contour plots (Fig. 3.12). Thus, magnitude of the variation of the effectiveness over the frequency range of interest is probably within the uncertainty.

The third harmonic profile taken without the viewing dump does not show the depression at the frequency corresponding to the plasma center. This result can be explained by $\tau_3 << 1$, just as in the radial view. Widths of the third harmonic profiles with and without the dump are not very different, probably because the emission in this harmonic is already heavily weighted towards the region inside the viewing chord for two reasons; (1) the stainless steel plate tends to act as an

efficient retro-reflector at these wavelengths, and (2) since $j_3 \propto nT^3$ for optically thin emission. Thus, it is difficult to calculate accurately the system effectiveness in the manner employed for the second harmonic emission.

The interpretation of the first harmonic spectra is difficult due to the presence of various layers discussed above. we shall therefore note only that emission from the first harmonic exists at frequencies corresponding to the resonance in the entire plasma($175 \sim 290GHz$) for both measurements, although with an intensity not too different from the noise level. The emission measured without the dump is larger by a factor of two probably because the dump contributes to reduction of the effective wall reflectivity regardless of whether the viewing chord sees it directly or not.

To summarize:

1. The measured second harmonic emission shows dramatic change by the insertion of the dump. The optically thick nature is confirmed by the central dip in the measurement taken without the dump. The effectiveness of the system calculated at this harmonic is $90 \pm 5\%$.

2. The third harmonic emission without the dump does not exhibit depression at the central frequency so that it is probably optically thin. The profile is narrow for the stainless steel as well as for the dump measurement because the stainless steel plate acts as an efficient retro-reflector and because the optically thin scaling of emission, $j_3 \propto nT^3$, heavily favors the line-of-sight emission.

3. The first harmonic emission is somewhat insensitive to the existence of the dump and difficult to interpret because of additional effects of upper-hybrid resonance and the right-hand cut-off.

Polarization Ratio from Thermal Emissions

Although a reflection of $10 \pm 5\%$ is probably acceptable for performing the harmonic ratio measurement of the stronger polarization(X-mode), it can substantially affect the polarization ratio measurement. This is because 10% of the X-mode contaminating the less intense O-mode can introduce significant enhancement and distortion. Thus, for the distribution function analysis using the polarization ratio, larger dump structure of Phase II is used. Thermal spectra obtained with this dump at $B_T = 5, 6, 7$, and $8T$ are shown in Fig. 4.4. The axes have been shifted for each spectrum for greater clarity. In each group, the spectrum in the foreground is the O-mode polarization while the X-mode is in the background. The two polarizations at each magnetic field are measured from identical discharges.

In this 'waterfall' plot, FWHM at the second harmonic is consistent with Phase I, but the intensity at the wide skirt of the emission is lower by almost a factor of two relative to the central peak, compared to those of Phase I represented by Fig. 4.3. Although measurements without the dump were not performed in Phase II and therefore, comparison of the type shown in Fig. 4.3 is not possible, we believe that all else being the same, the Phase II dump system is more effective by a factor of close to two, i.e., 95% removal efficiency most likely because of the larger surface.

In order to understand the measurements, polarization ratios, I^+/I^-, for the second and the third harmonics are plotted in Fig. 4.5 from the spectrum pairs of Fig. 4.4 and two additional measurements taken at $B_T = 5$ and $9T$. The first harmonic is excluded from the ratio analysis because of its low intensity, large uncertainty, and the effect of upper-hybrid and right-hand cut-off layers on the X-mode discussed previously. The error bars represent the spread in data from observing different time slices in the same discharge pairs.

The second harmonic ratios show a trend of increasing ratio with increasing frequency, and are in the range 0.1 to 0.25. The increase in the density which accompanies the field(frequency) increase can partly account for this trend if we invoke

the argument of the decreasing optical penetration. While the O-mode intensity linearly increases with the density, the X-mode intensity, partially characterized by the blackbody intensity at the penetration point will increase less because of less penetration at higher densities. The amount of depolarized X-mode present in the O-mode intensity is difficult to quantify however, since the exact constitution of the X-mode emission itself is difficult to determine due to the dual nature of its optical depth.

In contrast, the polarization ratios at the third harmonic are approximately constant at 5% regardless of the frequency and other plasma conditions, and neither a trend with the frequency variation nor correlations with the second harmonic ratio can be observed. If the third harmonic emissions from both polarizations are optically thin, then

$$\frac{I_3^+}{I_3^-} \sim \frac{T}{m_e c^2} \tag{4.9}$$

as a simple rule(a more rigorous formula is given below)[12]. Thus, from these plasmas with estimated central electron temperatures of $1 \sim 2keV$, the observed ratio is clearly excessive based on this assumption. Possible mechanisms responsible for the excessive O-mode emission observed include the following.

1. Depolarization inherent in the optical system.

2. X-mode is optically thick, increasing the polarization ratio.

3. X-mode emission from a region in which the magnetic field lines are oblique to B_T due to finite q(tokamak safety factor). This can produce components of the electric field which can be perceived by the detector system as the O-mode emission.

4. Depolarization occurring at the dump.

The depolarization inherent in the optical system was measured at the mock-up site, using the mercury-arc lamp as the broad-band source and with two 1000 lpi wire polarizers, one at the lamp and another in front of the detector. The degree of 'leak' from one polarization to another was determined to be approximately $3 \pm 1\%$ for both polarizations. Thus this effect accounts for more than one half of the observed O-mode emission. As stated in Chapter 3 however, the mock-up did not have the precise geometry. In particular, the plexiglas enclosures whose surface can produce appreciable glazing incidence reflection and depolarization were notably absent. Thus, although we have covered key parts of the plexiglas interior surface with eccosorb screens for the on-site measurements, the possibility exists for the depolarization value of the on-site system to be larger than measured at the mock-up because of the enclosure.

The theoretically expected third harmonic polarization ratios have been calculated using expressions for the emission and absorption of the form[11]

$$j_l^\pm(\omega, \theta = \pi/2) = \left(\frac{\omega_p^2}{\Omega c}\right)\left(\frac{\omega^2 \kappa T}{8\pi^3 c^2}\right) \Phi(l, x, \mu),$$

$$\alpha_l^\pm(\omega, \theta = \pi/2) = \left(\frac{\omega_p^2}{\Omega c}\right) \Phi(l, x, \mu), \tag{4.10}$$

where

$$\Phi(l, x, \mu) = \sqrt{2\pi}\frac{\mu^{5/2}}{x^4} l \sqrt{l^2 - x^2} \exp\left\{-\mu\left(\frac{l}{x} - 1\right)\right\} A_l^\pm\left(\frac{l}{x}\right)$$

$$x = \frac{\omega}{\Omega} \tag{4.11}$$

$$\mu = \frac{m_e c^2}{\kappa T}$$

and

$$A_l^\pm = \frac{(l\beta)^{2l}}{(2l+1)!}\left\{\begin{array}{c}\frac{\beta^2}{2l+3} \\ 1\end{array}\right\} \qquad \text{for } l\beta << 1$$

122

or $\qquad\qquad\qquad\qquad\qquad\qquad\qquad\qquad\qquad\qquad\qquad\qquad\qquad\qquad\qquad$ (4.12)

$$A_l^{\pm} = \frac{\exp\{2l/\gamma\}}{\sqrt{16\pi l^3 \gamma}} \left(\frac{\gamma-1}{\gamma+1}\right)^l \left\{ \begin{array}{c} \frac{\gamma(\gamma^2-1)}{2l} \\ 1 \end{array} \right\} \qquad \text{for } \gamma^3 << l,$$

which applies to Maxwellian plasmas. We can obtain the same result by making use of the equations developed in Chapter 2, but the above expressions are more convenient and less time consuming for Maxwellian distributions. For finite optical depth, the polarization ratio is given by

$$\left(\frac{I^+}{I^-}\right)_\omega = \frac{j^+(\omega)(1-\exp\{-\tau^+(\omega)\})/\tau^+(\omega)}{j^-(\omega)(1-\exp\{-\tau^-(\omega)\})/\tau^-(\omega)} \qquad (4.13)$$

where $\tau = \alpha s$, assuming the use of chord averaged quantities. We have calculated the observed ratio by integrating over the frequency range over which the electron population(in energy) is finite, which is on the order of a few percent of the central frequency. A tabulation of computer calculations for a range of $\overline{T}_e$ and $\overline{n}_e$ is shown in Table 4.1. Ratios for the realistic Alcator parameter range of $\overline{T}_e \leq 1 keV$ and $\overline{n}_e \leq 1.5 \times 10^{20} m^{-3}$ are highlighted in boldface type. These results show that unless the plasma density and temperature reach unrealistically high values(for Alcator), the polarization ratio observed cannot be explained by the finite optical depth hypothesis. In any case, that the ratios vary little with the plasma condition strongly hint to the optical depth not being the cause.

Due to the finite poloidal field, B_p, the magnetic field lines along the viewing chord are not exactly parallel to the toroidal axis. Hence, it follows that extraordinary waves emitted will have a component of its electric field parallel to B_T, which can be perceived by the detector system as an O-mode emission. This is because the O- and X-mode polarizations, as defined by the detection system's polarizer configuration, refers to polarizations parallel and perpendicular to B_T, respectively. Consider the $a = 11.5 cm$ plasma, with a conservative value of the tokamak safety factor, $q(a) = 3$. Then,

$$\frac{B_p}{B_T} \sim \frac{a}{Rq(a)} \sim 0.06. \qquad (4.14)$$

Hence, extraordinary mode emission intensity in this case is

$$\frac{I^-_{\|B_T}}{I^-_{\perp B_T}} \approx 0.06^2 \approx 0.4\%. \tag{4.15}$$

Thus, this contribution is negligible, especially when we consider that in the hottest part of the plasma, $r \ll a$, we have $r/q(r) < a/q(a)$.

The depolarization and reflection at the dump is difficult to quantify based on available data from the dump measurements. This is because in addition to the value of the O-mode polarization reflection into the same mode, the value of the X-mode polarization reflected into the O-mode must be accounted for. If we assume 0.5% total reflection into the O-mode from the dump surface(this is approximately the value determined in Table 3.5 for unpolarized radiation), an intensity equal to $4I^-$ incident on the dump from all directions will account for 40% of the observed O-mode emission. The assumption of an intensity of $4I^-$ incident on the dump is not unrealistic since this corresponds to $R_{eff} \sim 75\%$, and similar magnitude for the wall reflection coefficient has been measured from Alcator A albeit in a different configuration[34].

Thus, consideration of these four effects listed in page 121 show that plasma and magnetic field effects can be ruled out as the source of the observed O-mode emission in the third harmonic. Depolarizations and reflections at the viewing dump and other parts of the optical system appear to be responsible for the observed result.

4.3 Nonthermal Plasma Emission

Having characterized the optical system performance using reproducible thermal plasmas, a question remains: "What effect does the imperfect performance have on the nonthermal spectrum from which we intend to diagnose the electron distribution?" Since nonthermal emissions of the type examined in this thesis tend to come predominantly from localized regions of the plasma cross-section, the spatial intensity distribution is different from the thermal case, and a straightforward

application of reflection and depolarization values obtained in the previous section may not provide the correct result.

With the well-characterized thermal plasma, the imperfection of the system could be spotted by the existence of emission at frequencies not expected by theory, such as the observation of emission at resonance frequencies external to the viewing chord or that of excessive polarization ratios. With nonthermal plasmas, characterization is hard to make since this requires an a priori knowledge of the spatial and velocity distributions of the electrons. (These are the quantities we seek to measure.) The thermal bulk plasma however affects these nonthermal spectrum in predictable ways and such effects are used to observe qualitatively the system effectiveness against nonthermal emissions.

In Fig. 4.6, we show a schematic of a tokamak plasma similar to the one in Fig. 4.1, but this time the emission originates from an energetic tail filling the viewing chord, and the emission frequency corresponds to a thermal resonance on the low field side, consistent with a down-shift due to the relativistic mass increase. As indicated, an emission from the tail can enter the view in two particular ways, (1) directly, and (2) after multiple reflections, with the path crossing the thermal resonance, consequence of which is an attenuation of the ray intensity to the resonance blackbody level provided the resonance is optically thick.

Thus, from this, nonthermal emission observed with no reflection control can be expected to carry a signature of thermal absorption at frequencies where optically thick thermal resonances exist in the plasma. Using the same logic, it can be argued that if such a signature of thermal absorption(BGPAP = back ground plasma absorption profile) does not occur, then the observed spectrum is produced by the radiation that originate entirely from within the viewing chord.

Nonthermal Spectrum Measured Without the Dump

BGPAP is recognized in Fig. 4.7(a), which is a nonthermal spectrum measured without the viewing dump. In this spectrum, the down-shifted first harmonic emis-

125

sion is seen below $220GHz(\Omega)$, and the broad depression at Ω is due to the thermal absorption. Above $250GHz$, the emission shows a sharp rise with frequency as the thermal resonance shifts out of the plasma. The emission at these frequencies and up to $440GHz(2\Omega)$ are the down-shifted second harmonic emission, but at $360GHz$, the intensity starts to decrease sharply, reaching a minimum at 2Ω. This feature between 360 and $440GHz$ is the BGPAP. We note that at the outboard edge of the plasma, the second harmonic cyclotron frequency is $350GHz$, so that the onset of BGPAP agrees well with the plasma edge frequency. That the intensity above 2Ω does not recover to the level seen below 2Ω in a symmetric manner probably indicates that the Doppler broadening, normally symmetric in frequency up-shift and down-shift, is not a strong contributor, i.e., $\Delta\theta/\theta << 1$. Thus, we believe the emission above 2Ω to be mostly from the down-shifted third harmonic. The dip at $560GHz$ is due to an atmospheric water vapor absorption line, whose effect is to block out the frequency spectrum, limiting the distribution function energy range over which the spectrum can be interpreted quantitatively with full confidence.

Nonthermal Spectrum Measured With the Dump

In Fig. 4.7(b), we show a nonthermal spectrum measured with the Phase I dump in place. The down-shifted first harmonic is seen as before, although the depression at Ω is not as wide as in (a), probably due to the lower density. The narrow peak at $270GHz$ is due to the right-hand cut-off(ω_R) close to the line-of-sight (as in Fig. 4.2(b)) reflecting the antenna pattern away from the dump and hence enhancing the observed intensity. Thus it can be argued here that the system is effective just above this frequency. The dip at $380GHz$ is due to a weak water vapor absorption line, while the stronger absorption at $560GHz$ is prominent in this spectrum as well. Not accounting for the $380GHz$ dip, the emission increases with frequency from just above the ω_R peak all the way up to $420GHz$, indicating clearly that BGPAP is absent. A dramatic discontinuity is seen at 2Ω, and the substantially lower emission

126

on the high frequency side is quite consistent with expectations of a purely down-shifted emission. The finite intensity of the down-shifted third harmonic emission continuing from above 2Ω to below is an indication that accounting of harmonic superpositions is required in the $f(\vec{p})$ analysis.

In summary, the presence of the ω_R peak, the absence of the BGPAP, and the large discontinuity at 2Ω all attest to the effectiveness of the system in excluding the multiply reflected radiation in the frequencies above ω_R, as reflected power contamination of known form cannot be observed in this spectrum in this range.

4.4 Post-Processing of Nonthermal Spectra

From the two previous sections, we have the following results characterizing the system performance.

1. Comparison of X-mode intensities with and without the viewing dump at frequencies corresponding to second harmonic thermal resonances external to the viewing chord shows that the system effectiveness in removing the radiation from outside the viewing chord is approximately 90%.

2. Examinations of the third harmonic polarization ratios measured from thermal plasmas indicate that approximately 5% of the X-mode emission contaminates the O-mode spectrum.

3. Absence of any sign of BGPAP near the second harmonic frequency and the sharp discontinuity at this frequency in the nonthermal spectrum measured with the dump indicate high effectiveness of the system.

4. The observation of ω_R peak in the same spectrum indicates that the system is effective at this frequency($\sim 270GHz$), where no quantitative data are available from thermal measurements.

127

5. Asymmetric BGPAP observed at 2Ω in the nonthermal spectrum measured without the dump suggests that Doppler broadening is probably not a significant contributor to the observed intensity.

We shall choose not to apply any post-processing to X-mode nonthermal emission spectra. As a justification for this, we note that even though 10% reflection from the exterior of the viewing chord is observed, the shape of such 'reflected spectrum' is not known, so that the correction is hard to prescribe. We however believe that the shape of the reflected spectrum is probably very close to the directly radiated spectrum, based on observations 3 and 5 above and the symmetry of the keyhole—dump geometry, in which case the correction becomes unnecessary (at least for the relative measurement).

For O-mode nonthermal spectra however, we shall subtract from it an intensity equal to 5% of the X-mode, i.e.,

$$I^{+\prime}(\omega) = I^+(\omega) - 0.05 I^-(\omega). \tag{4.16}$$

We justify this process by pointing to observation 2 above, which can only be explained by X-mode contamination of the O-mode. The use of 'observed' X-mode emission as the 'reflected spectrum' is justified again by up-down symmetry and observations 3 and 5.

4.5 Summary

Various types of ECE spectra measured with the VECE system has been examined in this chapter. Results of these examinations produced figures of merit and qualitative assessments of the system performance.

In observing emissions from thermal plasmas, it was indicated that the conventional notion of the 'optical depth' is no longer useful when the viewing spot size is larger than the resonance region. Because of this, the case of an optically thick

resonance occupying a part of the viewing spot is treated only in a qualitative fashion. Optically thick emissions from outside the viewing chord is used to determine the system effectiveness, which is 90% removal of emission exterior to the viewing region in Phase I. The interpretation of the first harmonic features is difficult due to signal noise and plasma effects. The third harmonic showed no sign of such optical depth complexity so that it is assumed to be entirely optically thin.

Polarization ratios at the second and the third harmonic were measured as a function of the frequency in Phase II. At the second harmonic, the ratios show a definite trend with the density, although quantitative agreement of the observed trend with theory cannot be determined because of the complexity of interpreting the 'optically thick' emission in this configuration. At the third harmonic, the polarization ratio remained constant at approximately 5% over the same range and higher than expected from theory. Inspection of possible causes led to the conclusion that this large ratio is caused mostly by the X-mode contaminating the O-mode as a result of depolarization mechanisms present in the system hardware.

Nonthermal emissions measured with and without the dump showed some striking differences. These include the presence of right-hand cut-off peak in the spectrum with the dump, the presence of BGPAP only in the spectrum taken without the dump, and the sharp discontinuity at 2Ω from the spectrum with the dump; all of which suggest that the system is highly effective in removing radiation external to the viewing chord. No reflected power contamination could be observed in the nonthermal spectrum measured with the dump in Phase I at frequencies above ω_R. Quantitative assessment was not possible since the exact spatial and energy distribution of the electrons are not available.

Based on these findings, we chose not to apply any post-processing to X-mode spectra prior to data analysis. It was decided however to modify O-mode spectra by the prescription of Eqn. 4.16 which corrects for the contamination by the X-mode.
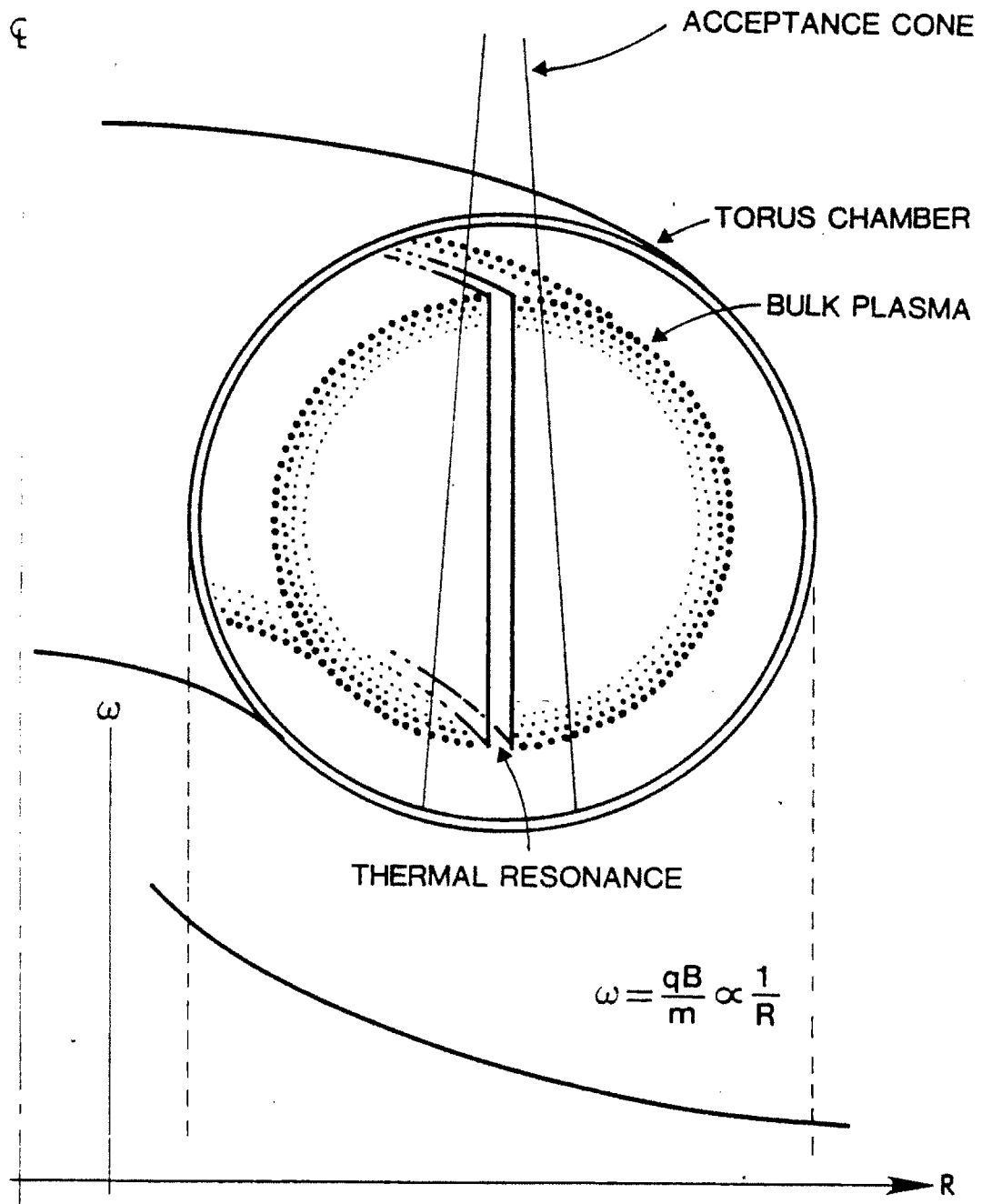
Figure 4.1:
Schematic diagram depicting the thermal resonance within the viewing chord.
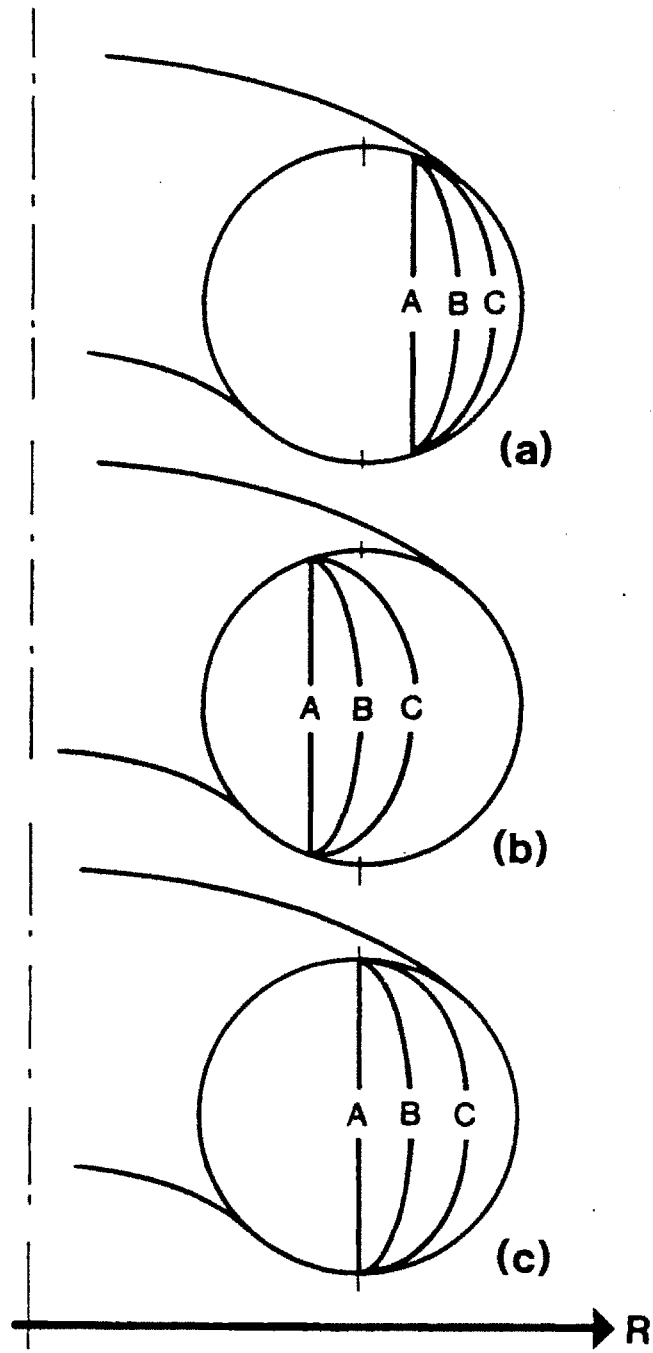
Figure 4.2:

Schematic diagram showing Ω(A), ω_{UH}(B), and ω_R(C) layers for (a) $\omega < \Omega_o$, (b) $\omega > \Omega_o$, and (c) $\omega = \Omega_o$, where Ω_o is the cyclotron resonance on axis.
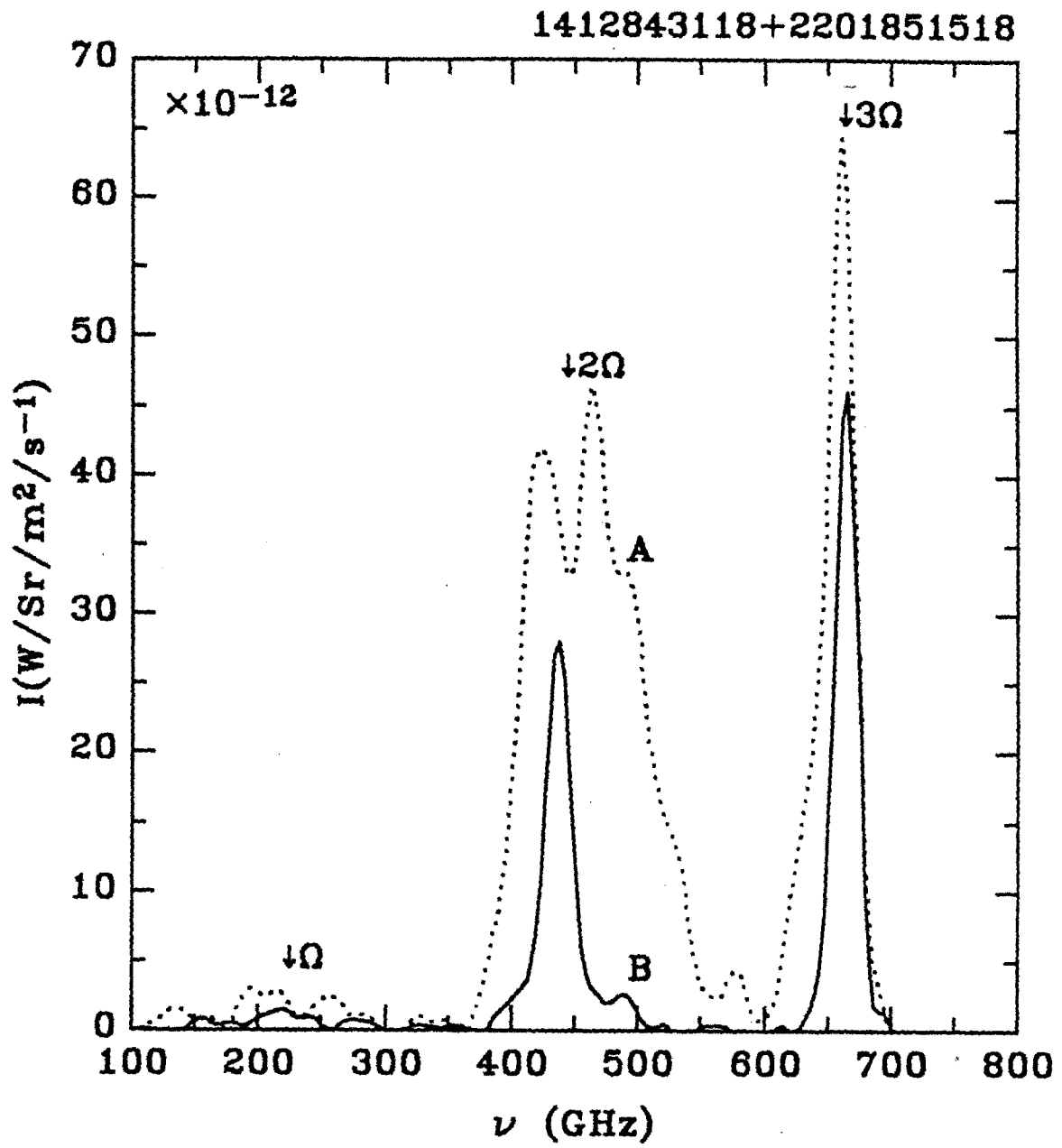
Figure 4.3:
Extraordinary mode thermal emission with and without the viewing dump. ($\bar{n}_e \simeq$ $1.7 \times 10^{20} m^{-3}$, $I_p \simeq 400kA$, and $B_T = 8T$)
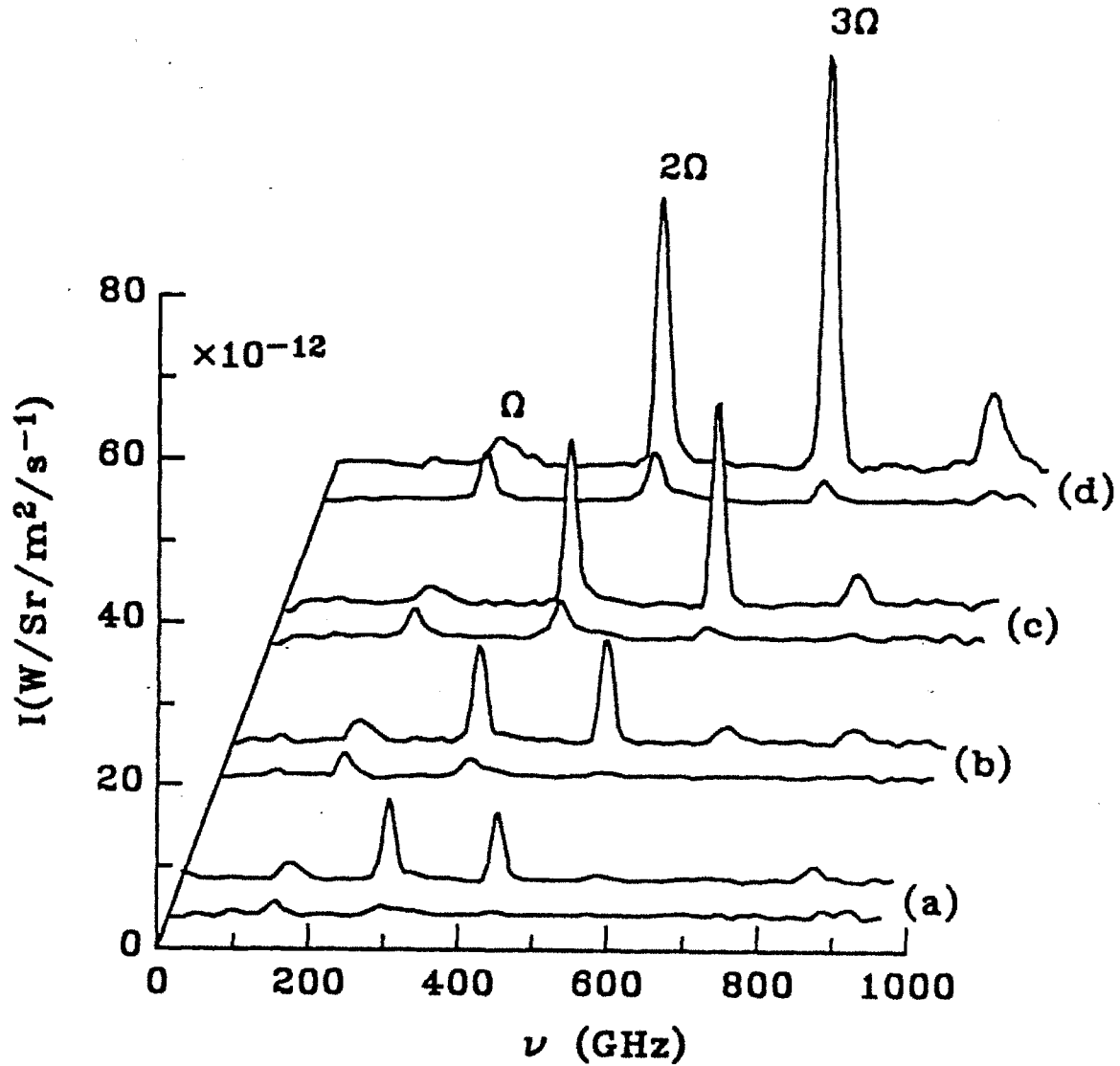
Figure 4.4:
Thermal emissions measured with the viewing dump for ordinary and extraordinary polarizations. (a) $B_T = 5T, \bar{n}_e = 0.5 \times 10^{20}m^{-3}, I_p = 140kA$. (b) $B_T = 6T, \bar{n}_e = 0.5 \times 10^{20}m^{-3}, I_p = 140kA$. (c) $B_T = 7T, \bar{n}_e = 1.4 \times 10^{20}m^{-3}, I_p = 200kA$. (d) $B_T = 8T, \bar{n}_e = 1.8 \times 10^{20}m^{-3}, I_p = 220kA$.
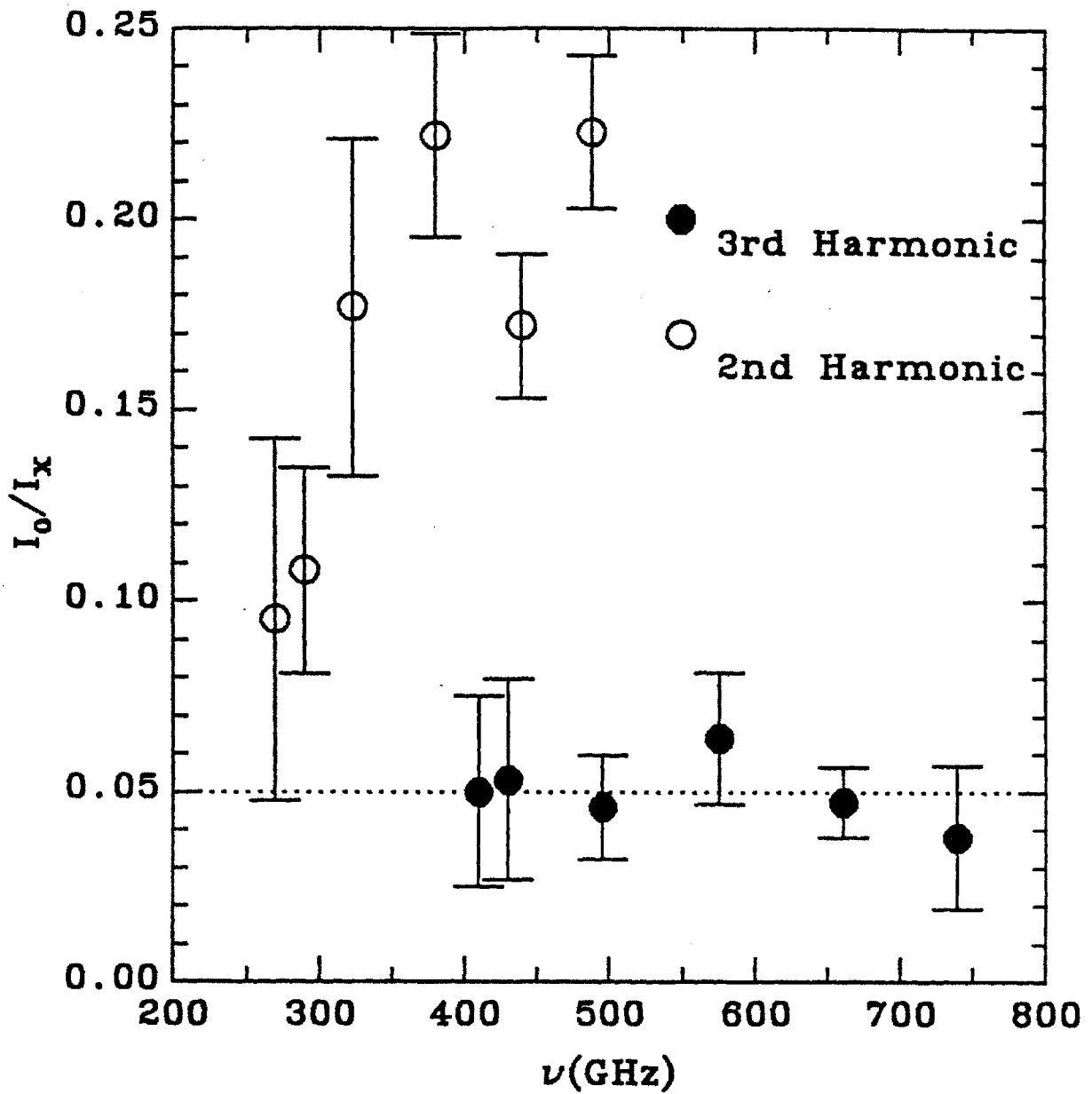
Figure 4.5:
Polarization ratios from the second and the third harmonic emissions from discharges of Fig. 4.4.
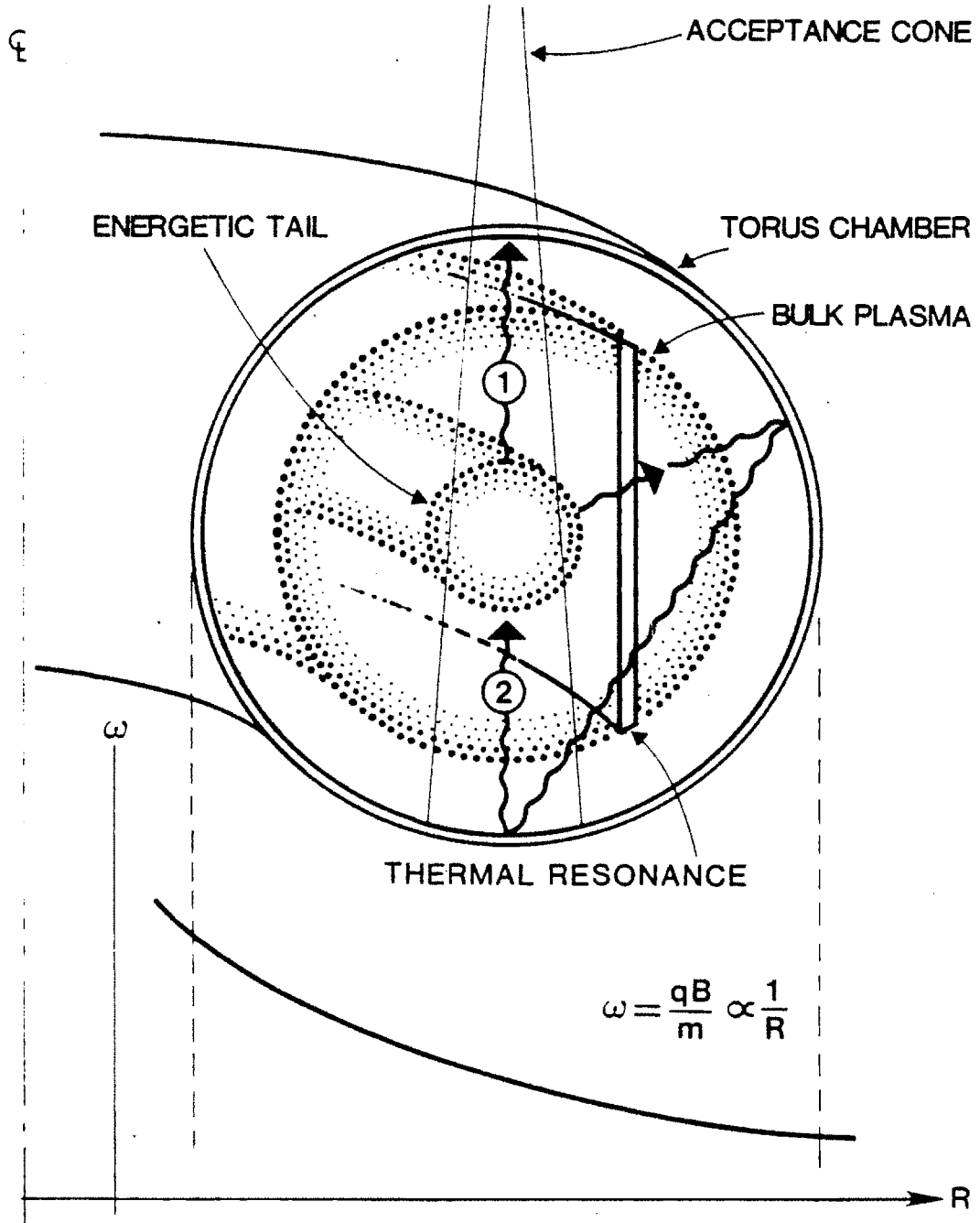
Figure 4.6:
Schematic diagram depicting the thermal resonance outside the viewing chord and an energetic tail filling the viewing chord.
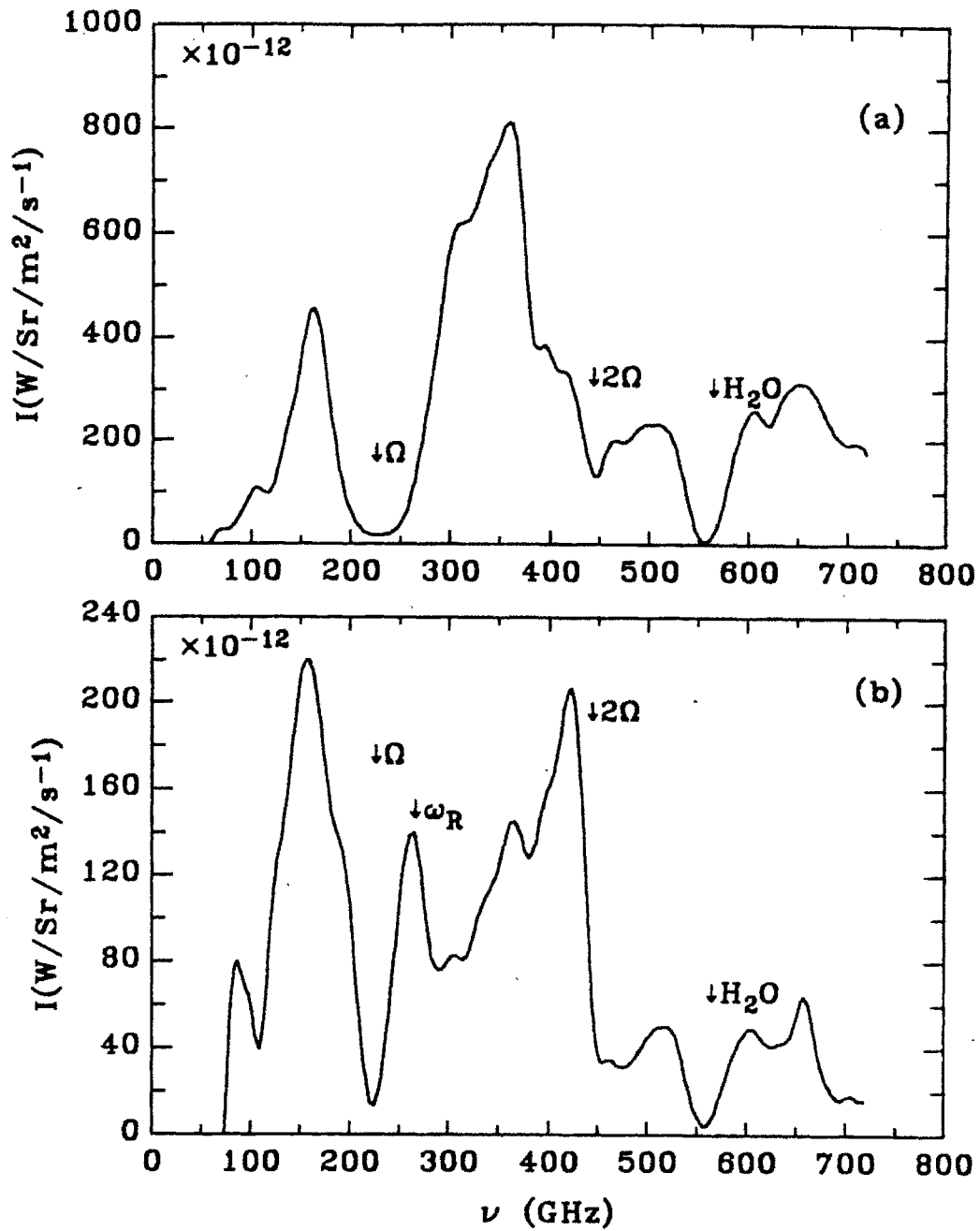
Figure 4.7:
Extraordinary mode non-thermal emission with and without the viewing dump.
(a) $B_T = 8T$, $\bar{n}_e \sim 1.0 \times 10^{20} m^{-3}$, $I_p \sim 200kA$, $P_{RF} \sim 500kW$. (b) $B_T = 8T$,
$\bar{n}_e \sim 0.7 \times 10^{20} m^{-3}$, $I_p \sim 180kA$, $P_{RF} \sim 400kW$.

Table 4.1:
Polarization ratio, I_3^+/I_3^-, calculated from numerical simulations of vertical propagation.

		$s = 23cm,$	$B_T = 8T$			

$\overline{n}_e$	$\overline{T}_e$	0.5	1.0	1.5	2.0	2.5	3.0
0.5		**0.11**	**0.23**	0.37	0.54	0.71	0.91
1.0		**0.12**	**0.27**	0.47	0.71	0.99	1.31
1.5		**0.13**	**0.32**	0.57	0.89	1.27	1.71
2.0		0.14	0.36	0.68	1.08	1.55	2.10
2.5		0.15	0.41	0.78	1.27	1.83	2.48
3.0		0.16	0.46	0.88	1.44	2.10	2.86

$\overline{n}_e$ in units of $10^{20}m^{-3}$.
$\overline{T}_e$ in units of keV.
I_3^+/I_3^- in %.

Chapter 5

ANALYSIS OF NONTHERMAL EMISSION SPECTRA

5.1 Introduction

Nonthermal spectra from three different types of tokamak discharges will be used to illustrate the three methods for diagnosing the electron momentum distributions from VECE diagnostic data. These three methods differ in their treatment of the harmonic superpositions, deducible parameters, and the fitted ratio. Fairly complex methods of diagnosis are necessary because nonthermal spectra measurable in practice defy the straightforward application of ratio analyses, owing to the presence of harmonic superpositions. Those spectra that do not exhibit any harmonic superposition usually have the higher harmonic or the weaker polarization at or below the noise level, making the quantitative analysis impractical.

In Section 5.2, a spectrum measured during a relatively high density lower hybrid heating(LHH) discharge[43] in Phase I is diagnosed. The small amount of superposition enables the recovery of a distribution function that exactly matches the measured spectrum using an iterative process.

Low density lower hybrid current drive(LHCD) discharges[42] produce highly energetic parallel tails to the distribution. A spectrum measured during such a current drive discharge of Phase I is diagnosed in Section 5.3. Because of the substantial

harmonic superposition present in this case, a distribution function characterized by several parameters is used to produce an approximate fit to the spectrum.

The two cases discussed above use the second and the third harmonics of the X-mode as the determinant of the distribution anisotropy(Λ). The third case presented in Section 5.4 on the other hand deals with nonthermal spectra measured in low density ohmic discharges during Phase II. For this, the polarization ratio at the second harmonic, as well as the X-mode third-to-second harmonic ratio are used to again deduce the several parameters for the approximate distribution. In all cases, the first harmonic emission is excluded from the analysis since this emission may not be optically thin, preventing direct application of our tools developed in Chapter 2, and also since the frequency response calibration is uncertain in this frequency range. Comparisons of emissions measured at the first harmonic and the distributions derived from higher harmonics, as well as intercomparisons of the different discharges, will be discussed in Chapter 6.

In the discussions to follow, I_l is used to denote the measured intensity at $l-1 \leq \omega/\Omega \leq l$, regardless of the actual source of the radiation. Thus, for example, I_2 may contain contributions from both j_2 and j_3. Section 5.5 is the chapter summary.

5.2 Lower Hybrid Heating Discharge Results

5.2.1 Discharge Characteristics

Lower hybrid heating is characterized by the $\Delta\phi = 180°$ phasing in the toroidal direction of the 4×4 RF waveguide arrays[75]. This phasing excites symmetric travelling waves in both directions, whose $N_{\parallel}$ (the parallel wave index) spectrum is shown by the dotted line in Fig. 5.1, so that no net current is driven by the wave. The $N_{\parallel}$ spectrum as launched couples and transfers parallel momentum to relatively low energy electrons, enabling rapid energy transfer to the bulk, resulting in heating.

Fig. 5.2 shows the discharge from which the X-mode VECE spectrum is analyzed for the lower hybrid heating case. Five traces show the VECE raw interferogram data, plasma current(I_p), line-averaged density($\bar{n}_e$), hard X-ray, and the loop voltage (V_{loop}). The radio frequency(RF) pulse is indicated on the I_p trace, while the specific scan to be analyzed is indicated by an arrow in the VECE trace.

Focussing our attention primarily to the VECE signal, we observe positive spikes at the beginning of the discharge, especially during $50 \sim 100ms$ period, indicating ω_{pe} emission due to the small amount of high energy electrons present in the discharge. The interferogram signal is low in amplitude until the RF initiation, after which successive interferograms increase in amplitude for an overall increase by a factor of approximately three during the $110ms$ RF pulse. During the RF injection, both I_p and n_e are decreasing, with the value of $\bar{n}_e$ being somewhat lower than the nominal Alcator lower hybrid heating discharge[43]. After the RF is turned off, violent activities are seen on the VECE and the hard X-ray traces. This is presumably due to the redistribution of electrons in momentum space by the Parail-Pogutse instability[76]. Both the loop voltage and the plasma current show no significant change during RF, indicating the RF did not drive substantial amount of current.

Vertical ECE Spectrum

The nonthermal spectrum to be analyzed (indicated by the arrow in Fig. 5.2) is shown in Fig. 5.3, along with a spectrum shown by a broken line taken just before the RF. This thermal spectrum shows the system effectiveness clearly according to discussions in Chapter 4, with the second harmonic peak observed at $440GHz$, consistent with the 8 Tesla toroidal field. The emission below Ω is the residual 'steady' ω_{pe} Cherenkov emission from the small runaway population as noted above[77]. As for the nonthermal spectrum, features of a spectrum similar to this one have already been discussed at length in Section 4.3. We shall point out, in addition, that atmospheric water vapor lines at 380 and $560GHz$ have been linearly interpolated for the analysis to follow, as shown by the dotted lines($364 \sim 398GHz$, $519 \sim 601GHz$).

140

At these interpolated range of frequencies, the actual intensity is at most 15% higher than the interpolated value near $560GHz$, and well within the calibration uncertainty at $380GHz$. These estimates are based on the observation of the general shape of the spectra obtained under different conditions, such as different toroidal fields. (An example of such a field scan is shown in Fig. 3.17.) The spectrum above 3Ω is dominated by noise because of decreasing response of the detector and the decreasing transmission of the fused quartz window in this frequency range.

5.2.2 Distribution Function Diagnosis

The harmonic ratio, $I^-(3\omega)/I^-(2\omega)$, is used to deduce the electron velocity distribution due to the availability only of the X-mode measurement. Lower hybrid heating spectra such as this are particularly suited for the harmonic ratio analysis owing to the small amount of the third harmonic emission overlapping the second. The range of analysis in the frequency spectrum is limited to $\omega_R < \omega \leq 3\Omega$ for previously mentioned reasons of right-hand cut-off layer effect and the high frequency sensitivity degradation.

Computer Code FPFT

The nonthermal spectrum is analyzed using a computer code, FPFT. The function of this code is to find the electron distribution whose ECE exactly matches the measurement over the specified range of frequencies. It references a large data base consisting of tables of Θ vs. Λ for the first six harmonics, generated by a separate code. FPFT is applied to those spectra with only mild harmonic superpositions, with the assumption that the initial evaluation of the harmonic ratio (not correcting for superpositions) is already a good estimate of the true ratio. With this initial harmonic ratio (and hence the distribution), a realistic assumption is used to 'extend' the distribution to higher energies where direct ratio measurement is inaccessible, e.g., above $250keV$ for the I_3/I_2 ratio because at $E > 250keV$, I_3 down shifts below 2Ω.

141

The distribution, described by the parameters f_p and Λ defined in Chapter 2, is extended as follows. For f_p above the cut-off energy, E_c, we shall take

$$f_p(E > E_c) = A \exp\left(-\frac{E}{T}\right),\tag{5.1}$$

where A, the scaling constant, and T are found by fitting the same exponential to f_p in the range $E_c - \Delta E \leq E \leq E_c$.

For Λ above the cut-off energy, we shall take

$$\Lambda(E > E_c) = \frac{\int_{E_c - \Delta E}^{E_c} \Lambda dE}{\Delta E},\tag{5.2}$$

so that the average value of Λ near the cut-off is used for the extension. With $E_c \simeq 250 keV$, ΔE is typically taken to be $50 keV$ although the extended distribution's sensitivity to the exact value of this parameter is small.

The ECE generated using the 'extended' distribution will clearly be an overestimate since we have added more electrons to the system compared to the initial guess. Several iterations are then performed on the parameters of the entire distribution until a set of f_p and Λ with no high energy cut-off assumption predicts a spectrum that closely matches the measured one in the specified range of frequencies. Then, these parameters are optimized systematically to arrive at an exact match. We shall choose to claim as our result only the distribution function parameter values up to E_c. Even though the extended part of the distribution is an integral part of the fit, we believe the constraints imposed for the generation of this extension disqualifies it from being a 'measured' quantity.

As an example, we show in Figs. 5.4 and 5.5 selected outputs of FPFT for the case in which it was executed to recover the electron distribution from an ECE spectrum of a $T = 50 keV$ relativistic Maxwellian distribution generated by Tamor[19].

In Fig. 5.4(a), we show the initial X-mode spectrum in the frequency range $0 \leq \omega \leq 4\Omega$, with the frequency scale adjusted for $B_T = 8T$ emission so that $\Omega = 220 GHz$. The fit is over $\Omega < \omega \leq 3\Omega$, consistent with the use of I_3^- / I_2^- ratio as

the determinant of anisotropy. Figs. 5.4(b), 5.5(a), and 5.5(b) plot I_3/I_2, f_p, and Λ, respectively at various stages of the iteration. Energy is plotted on the abscissa in these plots so that Maxwellian temperature can be obtained by straightforward slope fitting in the f_p plot: No ambiguity arises because of the one-to-one correspondence between energy and momentum,

$$E = m_e c^2 \left[(p^2 + 1)^{1/2} - 1 \right].$$

(5.3)

These traces, as marked, correspond to the initial guess, intermediate result, and the final result. Evident in all three of these plots is the fair accuracy of the initial guess at high energy($E \geq 150keV$). The agreement for the intermediate and the final results extend further downward in energy. At the low energy end($E \leq 50keV$), all these parameters change significantly between iterations. This is because the low energy end is most sensitive to the superposition, owing to its small true emissivity compared to the observed emissivity. For example, emission just below 2Ω, I_2, is dominated by the down-shifted third harmonic, j_3, with the second harmonic emission, j_2, constituting only a small fraction.

In Fig. 5.5, plotted points of the final result should be compared with the dotted lines, which indicate the theoretically calculated parameter values for the source distribution. The $50keV$ Maxwellian is successfully recovered, although we find that the FPFT results break down below about $40keV$ due to the increased uncertainty from the substantial effect that superposition has on these values. We also note however that given our spatial resolution of the experiment in the radial direction, and the presence of optically thick second harmonic thermal emission in practice, these low energy ranges will tend not to be suitable for the straightforward analysis by the tenuous assumption anyway. The resulting ECE from these parameters is indistinguishable from Fig. 5.4(a) in the range $\Omega \leq \omega$. Deviations of f_p and Λ from the true values despite the exact match of the computed and the initial spectrum is believed to come from errors introduced when reconstructing the initial spectrum

143

from Tamor's values, which are given not as intensities at specific frequencies, but as average intensities between preset frequency intervals.

Iterations of this kind using the ECE spectrum generated elsewhere from known distributions is the method whereby the absolute consistency of the code has been checked. The self-consistency check, i.e., the code's ability to recover an arbitrary distribution whose ECE was generated using its own data-base has been performed with similar success(provided the superposition is benign).

Results

The result of the FPFT analysis of the VECE spectrum is given in Fig. 5.6 as plots of f_p and Λ versus the energy, with error bars whose determination is discussed below. The energy range of display is terminated at $230keV$ since this is the point at which downshifted third harmonic emission overlaps with the second harmonic. For this VECE spectrum, tables of Θ vs. Λ computed for $\omega_{pe}^2/\Omega^2 = 0.12$ were used, consistent with the line-average density during this scan. Both f_p and Λ are to be interpreted as line average quantities over the $33cm$ chord in the plasma. f_p is decreasing but persistent all the way up to the $230keV$ limit. The straight line drawn through the f_p points represent an $80keV$ Maxwellian slope fitted to the data(to be discussed further in Chapter 6). Values of Λ are negative and in the range $-6 \leq \Lambda \leq -2$ above 50 keV. At 50 keV, a positive Λ is obtained, probably because of uncertainties in the harmonic superposition estimate. Since the harmonic ratio is insensitive to Λ for $\Lambda > 0$, we artificially force $\Lambda = 0$ for this energy. The water line interpolation affects the confidence of the results in the range $60 \leq E(keV) \leq 130$, as indicated in Fig. 5.6(b).

In Fig. 5.7, the individual harmonic ECE computed from these f_p and Λ (and their respective 'extensions') are overlayed with the measured spectrum. The sum of the individual harmonics of the computed ECE exactly matches the measured in the range $\Omega \leq \omega \leq 3\Omega$ as expected, except at thermal resonances where the

144

assumption of tenuous emission breaks down. Note the relatively small amount of third harmonic downshift below 2Ω indicated by this result.

To illustrate the distribution function, contours of constant $f(\vec{p})$ are plotted in $(p_\parallel, p_\perp)$ space in Fig. 5.8. (The 50 keV data are excluded.) This clearly shows the enhancement of the electron population in the parallel direction, as measured by other experiments[7,44] and predicted by theory[78]. The bump at $p_\parallel \simeq 0.9$ is due to the bump in f_p, although, as the error bars indicate, it is not statistically significant[1].

Error Analysis

The calibration of the Michelson interferometer discussed in Chapter 3 is accurate to approximately $\pm 15\%$ above $200 GHz$. In the following, a standard error propagation analysis is carried out to derive expressions for the errors in f_p and Λ. These errors are evaluated at each energy as shown by the bars in Fig. 5.6.

The uncertainty in the measured spectral intensity is given by,

$$\sigma_I^2 = \sigma_C^2 + \sigma_N^2, \tag{5.4}$$

where σ denotes the normalized error and subscripts I, C, and N refer to measured intensity, calibration, and noise, respectively. This is a consequence of the standard error propagation rule[79],

$$\sigma_z^2 = \sum_{i=1}^{N} \left[\sigma_i^2 \left(\frac{\partial z}{\partial y_i} \right)^2 \left(\frac{y_i}{z} \right)^2 \right], \tag{5.5}$$

where $z = f(y_1, ..., y_N)$. With this, the error in Λ determined from the harmonic ratio can be written as,

$$\sigma_\Lambda^2 = \sigma_{I_3/I_2}^2 \left(\frac{\partial \Lambda}{\partial (I_3/I_2)} \right)^2 \frac{(I_3/I_2)^2}{\Lambda^2}, \tag{5.6}$$

---

[1]This claim is verified by obtaining f_p and Λ for this frequency spectrum with the computer code BESTFIT, described in Section 5.3.

where $\sigma_{I_3/I_2}^2 = \sigma_{I_3}^2 + \sigma_{I_2}^2$. Hence, we note that the slope of curves in Fig. 2.7(a) and (b) determine the coupling of the error into Λ from the harmonic ratio. In particular, for $|\Lambda| \ll 1$, the error in Λ becomes very large compared to the harmonic ratio error owing to the flat slope and the small magnitude of Λ.

The error for f_p, denoted σ_{f_p}, is then given by

$$\sigma_{f_p}^2 = \sigma_I^2 + \sigma_\Theta^2, \tag{5.7}$$

where

$$\sigma_\Theta^2 = \sigma_\Lambda^2 \left(\frac{\partial \Theta}{\partial \Lambda} \right)^2 \frac{\Lambda^2}{\Theta^2} \tag{5.8}$$

since $I \propto f_p \Theta$.

The true dependence of the errors is far more complex since superpositions have to be taken into account. However, we believe this first order propagation of errors to be sufficient for the present purpose. A more detailed account would employ j_3, j_2, etc., the true harmonic emissivities as opposed to I_3 and I_2, the observed intensities. The errors presently calculated in this way indicate as much as a factor of five uncertainty in f_p measurement and a factor of two uncertainty in Λ. These results are the consequence of the fact that the range of Λ lies in the region where the normalized derivatives of Eqns. 5.6 and 5.8 are large, making the errors in these distribution parameters very sensitive to the measurement. It should be noted that the lower end of the error bars in f_p correspond to the upper end of the error bars in Λ and vice versa, so that both a positive error in f_p and a positive error in Λ for example is an unlikely result.

5.3 Lower Hybrid Current Drive Discharge Results

5.3.1 Discharge Characteristics

Compared to the lower hybrid heating case, the current drive experiment is conducted with lower density plasmas for efficient current-carrying tail generation. The

waveguides are phased at $\Delta\phi = \pi/2$ to set up a travelling wave preferentially in one toroidal direction. The $N_\parallel$ spectrum created by such launching phase is shown by the solid line in Fig. 5.1, which shows coupling to relatively high energy electrons

The discharge profile, whose format is identical to the previous discharge profile of Fig. 5.2, is shown in Fig. 5.9. This time, the consequences of the RF pulse are apparent in all but the $\bar{n}_e$ trace. The VECE signal undergoes an order of magnitude increase, while a similar phenomenon is observed in the hard X-ray signal. The current sustainment by the RF wave is evidenced by the flattening of I_p profile and decrease in V_{loop}(to zero) during the RF pulse. Due to the lower density and the higher power, nonthermal VECE signal reaches steady-state within one scan time($< 15ms$) in this discharge, and. the nonthermal spectrum to be analyzed is again indicated by the arrow. Even though current sustainment by the RF generated tail implies a high energy electron distribution with strong asymmetry in the $p_\parallel$ direction, this asymmetry cannot be measured by our configuration as discussed in Chapter 2, so that the measured result should be interpreted as the average of the forward and the backward distributions.

VECE Spectrum

In Fig. 5.10, we show two VECE spectra, just before and during the RF. A noteworthy feature of this figure is the vast difference in intensity of the two traces. Clearly, nonthermal emission from the tail electrons dominate in the upper trace. The shape of the nonthermal ECE is also quite different from that of Fig. 5.3, where even though there is depression at the second harmonic rest mass frequency, the intensities above and below this frequency do not exhibit the sharp 'step' feature, seen with the heating discharge spectrum. This is a consequence of the much broader relativistic spread, resulting in strong harmonic superpositions. The depression at 2Ω is created by both the addition of down-shifted second harmonic emission to the third just below 2Ω, and the thermal reabsorption at 2Ω. The peak above Ω shows the ω_R effect discussed previously, and below Ω is the down-shifted first

147

harmonic emission similar to the higher harmonics. The water vapor absorption line at $560GHz$ is not as prominent as before, but will still be interpolated with the same caveat about its interpretation. The water line at $380GHz$ cannot be identified, probably due to the lower vapor content at the time of the measurement. The spectrum above 3Ω is again noise dominated.

5.3.2 Distribution Function Diagnosis

Because of the considerable harmonic superposition by the highly energetic tail, application of the FPFT code to this spectrum fails, with the initial guess describing a distribution with extreme perpendicular enhancement whose parameters cannot be altered with a reasonable number of iterations. Thus in this case, we shall choose to characterize $f(\vec{p})$ by several parameters and attempt to obtain a reasonable fit between the measured and the computed spectra.

Computer Code BESTFIT

Our approach basically is to produce a reasonable description of $f(\vec{p})$ still based on the f_p and Λ form, and use a few parameters which can reasonably approximate the measurement. To this end, examinations of several candidate forms for f_p and Λ led to the selection of

$$f_p = f_o \exp\left\{ -\frac{E}{T} + \frac{C}{E} \right\} \tag{5.9}$$

and

$$\Lambda = Ap^B, \tag{5.10}$$

where the variables f_o, T, C, A, and B are to be 'measured'. In Eqn. 5.9, the C-parameter, whose inclusion is essential to improving the fit, simulates the low energy transition between the thermal bulk and the energetic tail. The form of Λ is a simple power of p, providing smoothness and flexibility.

While FPFT produces a computed spectrum that is completely identical to the measured one, BESTFIT produced spectrum is idealized, and therefore, not

identical to the measured spectrum. The goodness of the fit is expressed by the quantity χ_ν^2, the statistical parameter defined as[79]

$$\chi_\nu^2 = \frac{1}{\nu} \sum_{i=1}^{N} \left\{ \frac{(I_e(\omega_i) - I_c(\omega_i))^2}{\sigma^2(I_e(\omega_i))} \right\} \quad ; \nu = N - m \qquad (5.11)$$

where N is the total number of fitted points, which we take to be the frequency range of the fit divided by the frequency resolution($\sim 20GHz$), and m is the number of independent variables(five in our case). I_e and I_c are the experimental and computed intensities at ω_i, and $\sigma^2(I_e(\omega_i))$ is the square of the unnormalized uncertainty at ω_i(typically $\pm15\%$). The code attempts to find the optimal parameters that minimize χ_ν^2, whose final value of approximately less than unity implies a statistically sound fit. Fourteen cyclotron harmonics are used for the reconstruction. Owing to the prohibitive amount of data base and computer time required to generate them and to carry out these analyses, BESTFIT is presently available only for $\omega_p^2/\Omega^2 = 0$, which is a good assumption for these low density Alcator discharges.

The code BESTFIT was checked for absolute and self consistencies as before. Cross checks with FPFT using several spectra with benign superposition including the spectrum of Fig. 5.3 showed that use of either code produces nearly the same results, establishing the 'downward-compatibility' of BESTFIT with FPFT.

Results

Fig. 5.11 shows the measured lower hybrid current drive spectrum and the computer generated ECE. The frequency range over which the fit was optimized according to the above prescription is shown by the two horizontal lines near the abscissa. They correspond to $1.2 \leq \omega/\Omega \leq 1.9$ and $2.2 \leq \omega/\Omega \leq 2.7$, covering much of the second and the third harmonic down-shifted emission. It is evident from this figure that the magnitude of superposition is much more substantial compared to the lower hybrid heating result, especially for the third harmonic.

The f_p and Λ profiles in the range $10 \leq E(keV) \leq 250$ that generate this spectrum are shown in Fig. 5.12. The profiles are the result of a fit with $T = 110keV$, $C = 40keV$, $A = -2.0$, and $B = 2.4$. At the low energy end, the plot of f_p shows a gradual transition in slope from the thermal to the tail, introduced by the finite C-parameter. The Λ profile shows a somewhat artificially constrained form, with $-3 < \Lambda < 0$ being smaller in magnitude than in the lower hybrid heating case indicating a more isotropic distribution, although still with significant parallel enhancement consistent with expectations of the existence of a current carrying tail. The dashed lines flanking the solid traces in Fig. 5.12 show the possible regions of f_p and Λ values, obtained from an aggregate error analysis discussed below. The contour plot shown in Fig. 5.13 shows the smooth contours which are the consequence of our assumptions about the shape of $f(\vec{p})$. They indicate less anisotropy than the case of lower hybrid heating of Fig. 5.8, consistent with the result that $|\Lambda|_{LHCD} < |\Lambda|_{LHH}$.

To investigate the effect of the C-parameter in Eqn. 5.9, the same spectrum was fitted by BESTFIT, but with the C-parameter artificially constrained to zero. The result is $T = 80$, $A = -3.2$, and $B = 0.7$, with the χ_ν^2 parameter more than a factor of two larger than the previous result, the overlay of the computed and the measured spectra shows large discrepancies in the low energy regions near 2Ω and 3Ω.

Error Analysis

In the BESTFIT analysis, the shape of $f(\vec{p})$ is constrained by Eqns. 5.9 and 5.10 so that the result is insensitive to narrow frequency fluctuations on the measured spectrum. Instead, the dominant source of uncertainty is the relative sensitivity calibration of the down-shifted second harmonic range of frequencies, $\Omega \leq \omega \leq 2\Omega$, to the down-shifted third harmonic range of frequencies, $2\Omega \leq \omega \leq 3\Omega$, which we believe to be accurate to within $\pm 15\%$. Thus, in order to investigate this effect, BESTFIT was applied to a 'distorted' spectrum, in which the intensity at the second

150

harmonic range of frequencies was increased or decreased by 15%. The results of these distorted analyses are the dotted lines flanking the solid lines in Fig. 5.12. The choice of the second harmonic as the range of distortion will provide the worst case result since its magnitude is more directly reflective of the single harmonic emissivity due to the smaller superposition compared to the higher harmonics.

The errors for Λ at high energies are comparable in magnitude to the error bars derived for the FPFT case. The smaller spread in Λ at lower energies is the consequence of the constraint imposed on its form. The error in f_p also shows a similar trend, with magnitudes similar to the lower hybrid heating case. The constrained forms of f_p and Λ force the error magnitudes to be small for the low energy region, which is misleading since it is the low energy end that is most sensitive to superpositions, and therefore, large uncertainties are expected. On the other hand however, it is probably safe to assume $\Lambda \simeq 0$ for these low energies since the higher collisionality of the low energy electrons will help rapid isotropization.

5.4 Low Density Ohmic Discharge Results

VECE data from low density ohmic discharges were obtained in Phase II using the smaller minor radius plasma and the larger viewing dump. Pairs of identical discharges have been used to obtain data from the O- and the X-modes. Thus, in this section, analysis of the two nonthermal spectra obtained during a set of identical discharges is carried out using both the three-to-two harmonic ratio of the X-mode and the polarization ratio at the second harmonic. The O-mode spectrum presented in this section has been processed using the prescription of Eqn. 4.16, and the O-mode harmonic ratio is not used in the analysis because we believe that substantial distortion of this quantity may have resulted from the post-processing.

5.4.1 Discharge Characteristics

The discharge profile from which the spectrum is taken is shown in Fig. 5.14, in the format similar to the two previous figures. The difference here is that the two VECE traces, corresponding to the O- and the X-mode measurements from identical discharges, have been included and the loop voltage trace has been removed. The density is extremely low for an Alcator ohmic discharge at $\overline{n}_e < 0.3 \times 10^{20} m^{-3}$. It is this low density relative to the ohmic induction that promotes part of the electron population to accelerate, causing 'slideaway'[80] or 'runaway'[5] discharges. VECE signals exhibit strong enhancements due to the nonthermal emission throughout most of the discharge. The onset of the nonthermal activity coincides with the hard X-ray signal increase, and other parameters, I_p, and $\overline{n}_e$ both remain roughly constant during the nonthermal activity, indicating 'steady' energetic tail sustainment. Although the hard X-ray trace shows steadily increasing periodic structure, the effect responsible for this appears not to affect the VECE signal, probably because the source of this hard X-ray activity lies outside the line-of-sight, or the electrons causing this effect are of such low density or of high energy that this activity cannot be detected by the ECE system. Essentially identical spectra are obtained during the period $150 \sim 300ms$. This then enables us to use the approach whereby the frequency spectra which measure the same 'tail' emission are averaged to produce one representative spectrum for the discharge.

Vertical ECE Spectra

The two VECE spectra are shown in Fig. 5.15. Fig. 5.15(b) shows the X-mode which exhibits similar kind of structures as the current drive case of Fig. 5.10, indicating the presence of emissions from highly relativistic electrons and severe harmonic superpositions. A notable difference is the apparent absence of the ω_R peak, presumably due to the extremely low density of the discharge. The O-mode

spectrum shown in Fig. 5.15(a) has a substantially lower intensity than the X-mode throughout the frequency range, although the harmonic features are similarly identifiable. The $560GHz$ water vapor absorption line dips will be filled in as before, but the $760GHz$ water vapor dips will be left untouched since they are outside of the fitting range. (This line became visible in the Phase II data because of the use of crystal quartz window with less attenuation at this frequency.)

5.4.2 Distribution Function Diagnosis

With both polarizations present, the X-mode harmonic ratio, I_3^-/I_2^-, and the second harmonic polarization ratio, I_2^+/I_2^-, can be fitted. The O-mode harmonic ratio, I_3^+/I_2^+, is excluded from the analysis due to the possibility of substantial uncertainty.

Computer Codes BESTFIT & BESTPAIR

In order to utilize the existing software capability, the analysis using the harmonic ratio is carried out with BESTFIT, just as in the case of the current drive spectrum. A different code, BESTPAIR, takes the two spectra and executes the fit to the polarization ratio, independent of the harmonic ratio results. This two-step process provides 'bracketing' of the distribution parameters, even if an accurate determination of the harmonic superposition is not possible. Thus, the final product of these two spectra analysis is the two descriptions of f_p and Λ, one from BESTFIT, and the other from BESTPAIR.

Results

Fig. 5.16 again shows the two spectra, this time plotted on the same scale. The smooth dotted curve overlayed on the measured X-mode spectrum shows the harmonic ratio fit to the X-mode, while the dashed curves in the downshifted second harmonic range of frequencies show the fit according to the second harmonic polarization ratio. The frequency ranges over which the fittings were performed are

indicated by solid lines near the abscissa. These ranges are the same as for the current drive case.

The four distribution parameters (excluding f_o) that produce these fits are: For the harmonic ratio,

$$T = 100, \quad C = 40, \quad A = -1.25, \quad B = 1.50. \tag{5.12}$$

For the polarization ratio,

$$T = 85, \quad C = 60, \quad A = -5.0, \quad B = -0.15. \tag{5.13}$$

As can be seen by the similarity of the fitted curves at the down-shifted second harmonic range of frequencies, parameters that characterize f_p (which is sensitive to the fit of a single harmonic profile) are not grossly different. The large differences in A and B arise since Λ is sensitive to the ratios rather than the individual harmonic shape.

A single $f(\vec{p})$ that produces an acceptable fit with both I_3^-/I_2^- and I_2^+/I_2^- could not be found with the present prescription. For these spectra, and for other low density ohmic discharges in which polarization ratios were measured in general, the result of BESTFIT underestimates the polarization ratio, i.e., the computed O-mode using the BESTFIT derived $f(\vec{p})$ is weaker than the measured value. The result of BESTPAIR on the other hand underestimates the harmonic ratios of both polarizations, i.e., the computed third harmonics using the BESTPAIR derived $f(\vec{p})$ are weaker than the measured values.

The discrepancy between the two distributions is evident in Fig. 5.17, where both distribution function parameters, along with the aggregate error analysis results, are plotted. In this figure, solid lines show the fits from BESTFIT and BESTPAIR, with labels 'H' and 'P' referring to the harmonic and the polarization result, respectively. The dotted-line error curves belong to the harmonic ratio result, and the dashed-line error curves belong to the polarization ratio result. The upper error curve for the harmonic ratio in the Λ plot is indistinguishable from the $\Lambda = 0$ axis. The harmonic

ratio error curves are produced using the $\pm15\%$ distortion on the second harmonic fitting range as before, while for the polarization ratio, distortions of $\pm25\%$ were introduced to the O-mode intensity. This 25% value takes into account, according to the error propagation principle of Eqn. 5.5, the uncertainty of the post-processing prescription which consists of the uncertainties in the 5% contamination value and the X-mode intensity in addition to the uncertainty in the unprocessed O-mode measurement.

In the figure, the larger distortion value of the polarization ratio result manifests in the wider space between the polarization error curves. The shapes of f_p from the two fits are quite similar, but with a major discrepancy in the magnitude despite the fact that computed spectra from the two fits agree well in the X-mode second harmonic range of Fig. 5.16. This is due to the large difference in the magnitude of the Θ values for each fit brought about by the different Λ values. As for the Λ values themselves, the discrepancy is substantial. The Λ spectrum from the polarization ratio should probably be interpreted as a constant Λ of approximately -5. The large negative values of Λ at the low energy end is probably an artifact of the fitting process, since the computed O-mode spectrum does not agree with the measurement near 2Ω anyway. In any case, both fits indicate parallel enhanced distributions as expected, which indicates the presence of high energy electrons accelerated by the toroidal electric field.

Analysis

The nature of the discrepancy is consistent with the effects of insufficient accounting of superpositions, as discussed in Section 2.6, so that the true parameters for $f(\vec{p})$ probably lie somewhere in between those in Eqns. 5.12 and 5.13. Thus, although the examination of the two ratios 'bracket' the probable range of f_p and Λ, more precise information is clearly desired. In particular, the source of the discrepancy should be determined with fair confidence in order to make the results credible.

That calibration uncertainties can cause the discrepancy is evident by noting how the error boundaries from the two results overlap, essentially throughout the energy range for f_p and at high energies for Λ. Thus, uncertainties in the measurement are probably responsible for a part of the discrepancy, and because of this, we shall choose to take, as our best estimate, the distribution of the harmonic ratio error curve that lies between the 'H' and the 'P' solid line curves. The parameters for this distribution are

$$T = 125, \quad C = 40, \quad A = -3.2, \quad B = 1.30. \tag{5.14}$$

In Fig. 5.18, we present the contour plot for this distribution. For comparison, the contour plots of the two individual ratio estimates, whose parameters are given in Eqn. 5.12 and 5.13 are plotted in Fig. 5.19. It is seen that the difference between the two individual ratio results in the latter figure is substantial, while the two contours Fig. 5.18 and Fig. 5.19(a), which are not too dissimilar, show a typical difference as a result of the 15% aggregate distortion analysis also carried out for the lower hybrid current case.

The hypothesis that insufficient accounting of harmonic superposition can cause this discrepancy for these spectra is a little more difficult to show rigorously. This is because we have no information on the shape of the distribution above $E \simeq 250 keV$ that is responsible for the superpositions, so that adding more parameters to the approximation, especially to modify the high energy, is unjustified.

To show however that increasing the superposition will make the two ratios more consistent, we show in Fig. 5.20 the same two spectra with the dotted lines showing computed emissions from a single $f(\vec{p})$. The fit was over both harmonics for both modes. This $f(\vec{p})$ has the parameters $T = 70$, $C = 40$, $A = -4.0$, and $B = -0.15$, but the form of f_p is modified such that

$$f_p \;=\; f_{p1} = f_o \exp\left\{-\frac{E}{T} + \frac{C}{E}\right\} \quad \text{for } E \leq 300 keV$$

$$f_p \;=\; f_{p2} = f_o' \exp\left\{-\frac{E}{4T}\right\} \quad \text{for } E > 300 keV \tag{5.15}$$

where f_o' is defined such that $f_{p1}(300keV) = f_{p2}(300keV)$, with Λ shape given by Eqn. 5.10 as before. Thus, this f_p represents an 'ad hoc' addition of higher energy tail in the energy range above the valid range of the VECE analysis. The addition of the high energy tail increasing the computed emission is clearly seen at the low end of the second harmonic fitting range, where the computed emission deviates from its monotonic decrease with frequency and extends further downward.

It is probably a fortuitous coincidence that the above 'ad hoc' prescription produced a well fitted $f(\vec{p})$ for the particular spectra, but this illustrates clearly that for these spectra with severe harmonic overlap, the distribution at high energies can be a critical determinant to the fitting process. We believe this result may explain the source of the discrepancy between the two fits, by proving that increase in the harmonic superpositions by the prescription can produce a good match. The f_p profile from this ad hoc fit fall close to the upper error curve of the harmonic ratio result in Fig. 5.17, while the Λ profile lies close to, but below the region where the lower error curve of the harmonic ratio and the upper error curve of the polarization ratio exist.

5.5 Summary

In this chapter, different methods, represented by the computer codes FPFT, BEST-FIT, and BESTPAIR, were used to diagnose the electron momentum distribution from the VECE spectrum. These methods differed in their range of applicability with regard to the amount of harmonic superposition, and the use of different ratios. Summary of the three computer codes are given in Table 5.1.

In Section 5.2, the FPFT code was used on the VECE spectrum measured during a lower hybrid heating discharge to produce $f(\vec{p})$ whose computed ECE exactly matched the measured data. The applicability of FPFT is limited to those spectra with benign superpositions such that the initial measurement of the X-mode harmonic ratio, I_3^-/I_2^-, is already a good approximation to the final result.

The measured $f(\vec{p})$, described by the parameters $f_p(p)$ and $\Lambda(p)$, showed parallel enhancement consistent with expectations from lower hybrid physics. The error propagation analysis revealed that the values of Λ and f_p are very sensitive to uncertainties in the measurement for the Λ values observed.

In Section 5.3, examination of the VECE spectrum measured during a lower hybrid current drive discharge showed strong enhancement of the nonthermal emission due to the energetic electron population coupled with indications of severe harmonic superpositions. To analyze this type of spectrum, the BESTFIT code, which determines the several parameters of $f(\vec{p})$ (given by Eqn.s 5.9 and 5.10) whose computed ECE spectrum approximates the measured, was developed. This code is compatible with FPFT for the mild harmonic superposition cases, but with an additional capability to fit to spectra with severe harmonic superpositions. Since the 'shape' of $f(\vec{p})$ is constrained by the several parameters characterization, error analysis for the results of this code involves finding the sets of parameters corresponding to the extreme cases of error, by aggregate distortions of the measured spectrum. Result of BESTFIT application to the lower hybrid current drive VECE spectrum produces $f(\vec{p})$ which is more isotropic than the heating result, although still with appreciable parallel enhancement.

In Section 5.4, an attempt was made to recover a distribution function that is consistent with both the X-mode harmonic ratio and the second harmonic polarization ratio. The VECE spectra measured for this purpose during low density ohmic discharges exhibit features similar to the lower hybrid current drive spectrum, suggesting the presence of severe harmonic superpositions. Thus, BESTFIT is employed for the harmonic analysis, and the BESTPAIR code is employed for the polarization analysis. Using the same constraints on the shapes of f_p and Λ as before, we find a substantial discrepancy between the distribution function parameters derived from the two ratios, although the error curves generated using the aggregate distortion method do overlap. The nature of the discrepancy in Λ

between these two $f(\vec{p})$'s shows a trend that can be explained by invoking the insufficient accounting of the harmonic superposition. The finding that the two ratios can be made to agree on a single $f(\vec{p})$ using an 'ad hoc' addition of a high energy component to the distribution substantiates this claim. However, since the spectral features are insensitive to these distributions at high energies, no justifiable way of determining the high energy component exists in the present measurements.

In summary, electron momentum distributions can be diagnosed from the X-mode harmonic ratio; in detail for the case of mild harmonic superpositions, and in smoothed form for the case of severe harmonic superpositions. The question of whether the superpositions are accurately accounted for or not is in part answered by our analysis of the polarized spectra from the low density ohmic discharge, which suggest that with the presently available tools and measurements, harmonic superpositions cannot be fully accounted for, resulting in a slight overestimate of Λ and an underestimate of f_p from the X-mode harmonic ratio from those spectra with severe harmonic superpositions.
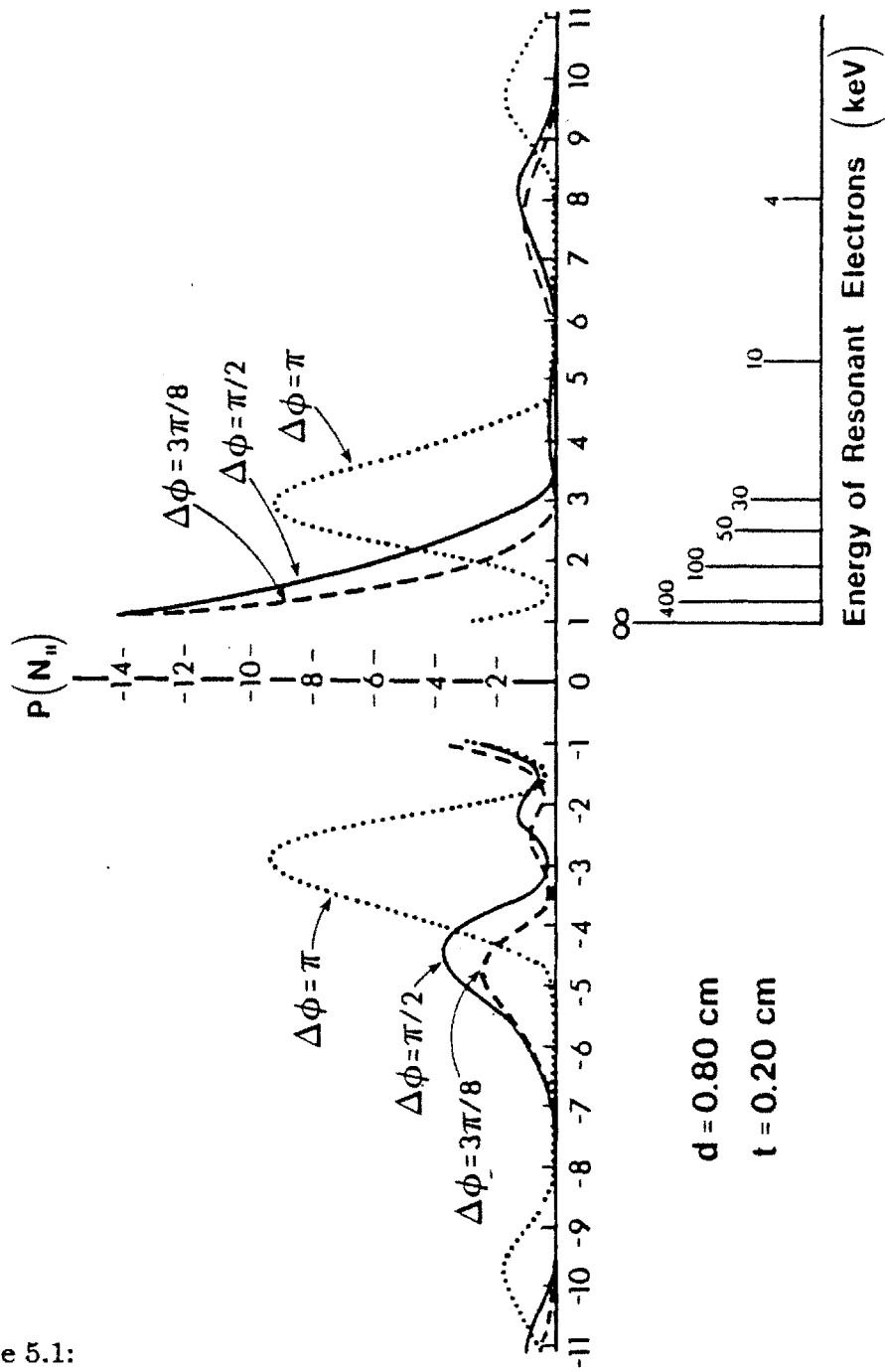
Figure 5.1:
Alcator C Brambilla spectra.
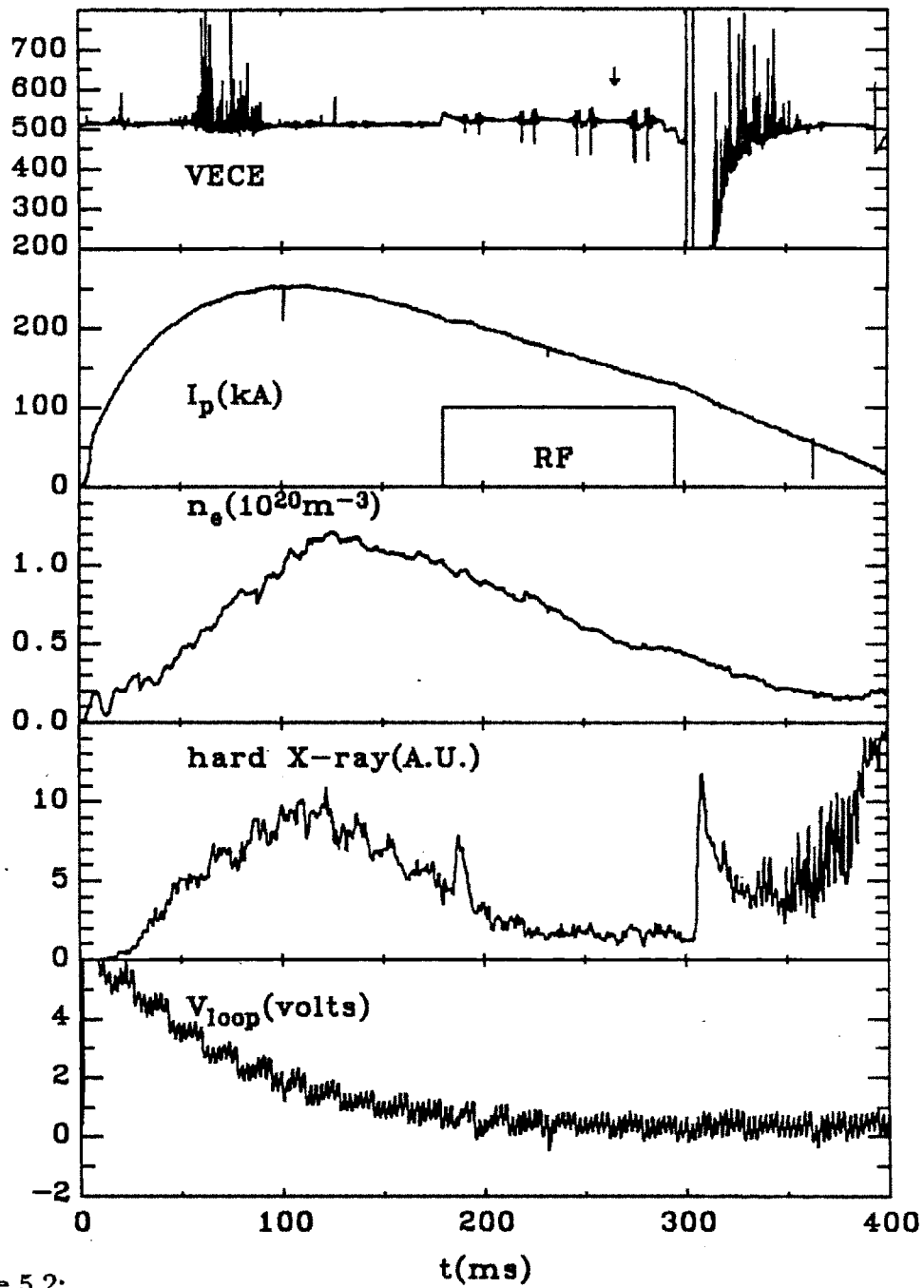
Figure 5.2:

Lower hybrid heating discharge trace. $B_T = 8T$, $P_{RF} = 400kW$.
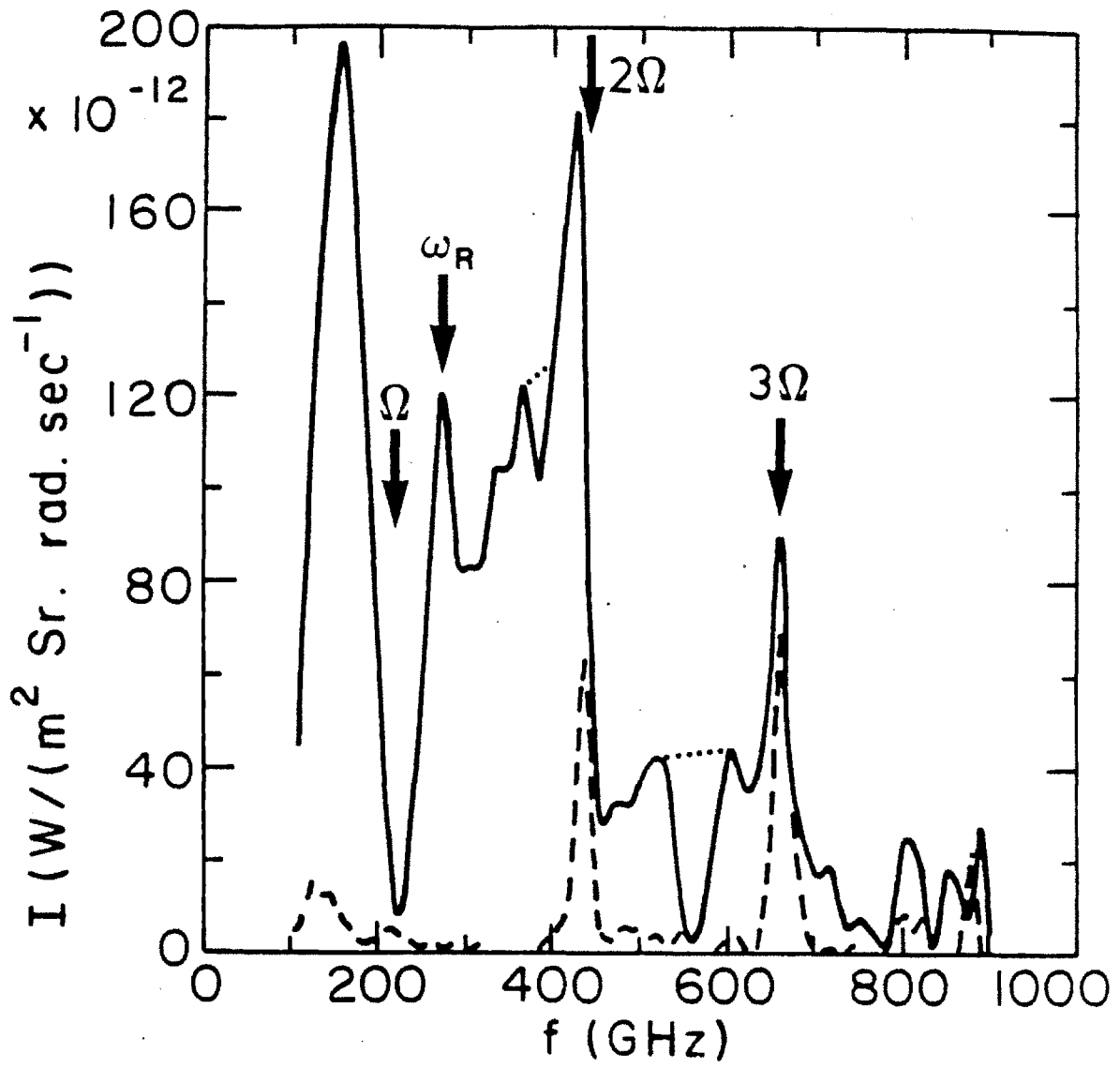
Figure 5.3:
VECE spectra before and during lower hybrid heating.
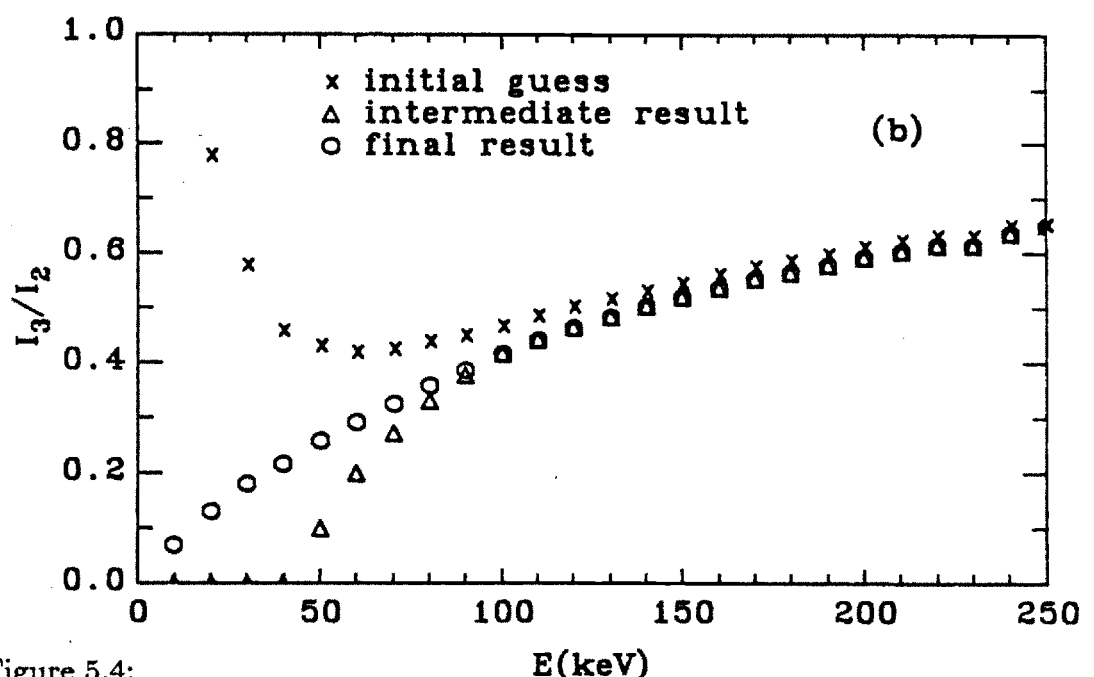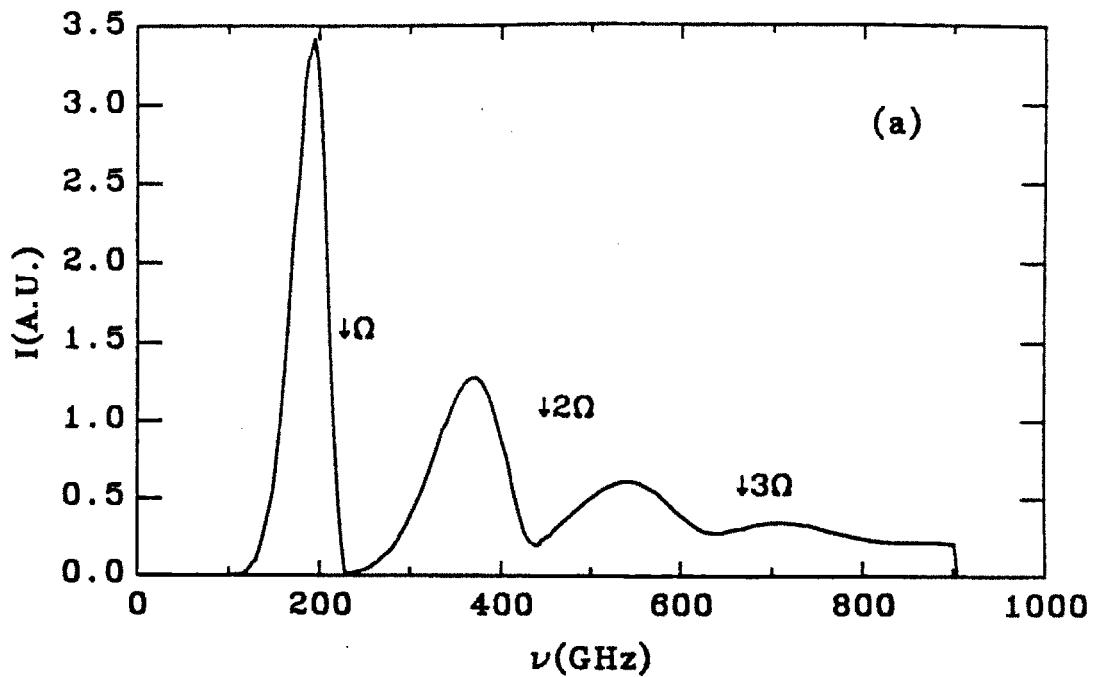
Figure 5.4:

Example of FPFT analysis using an ECE spectrum generated by a $50 keV$ Maxwellian distribution. (a) ECE spectrum. (b) Harmonic ratio.
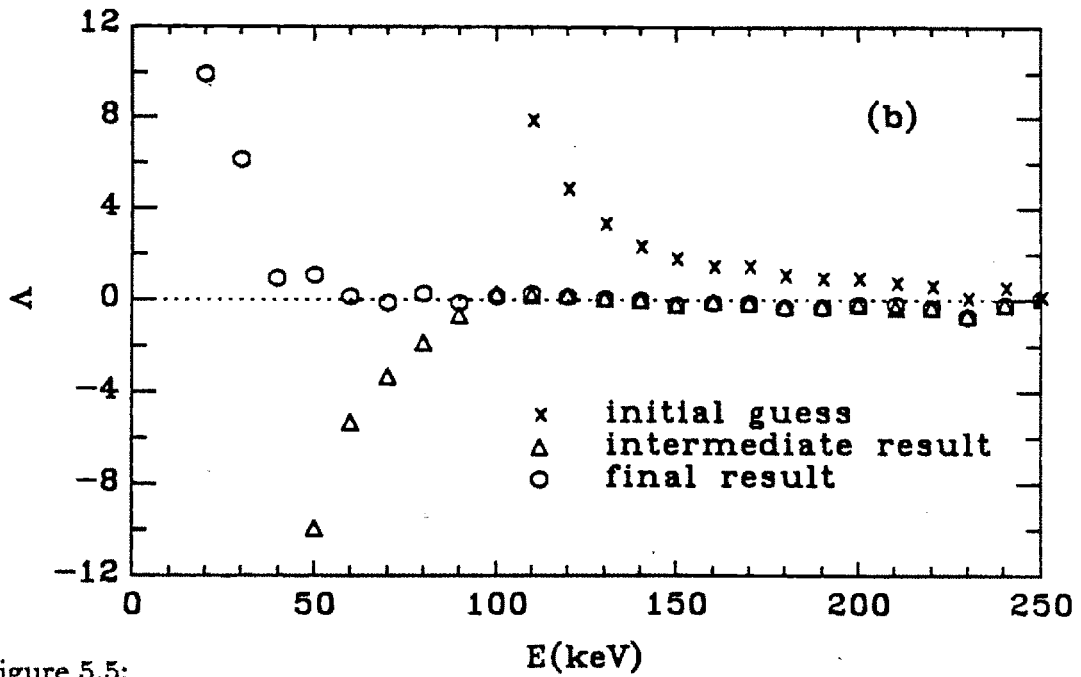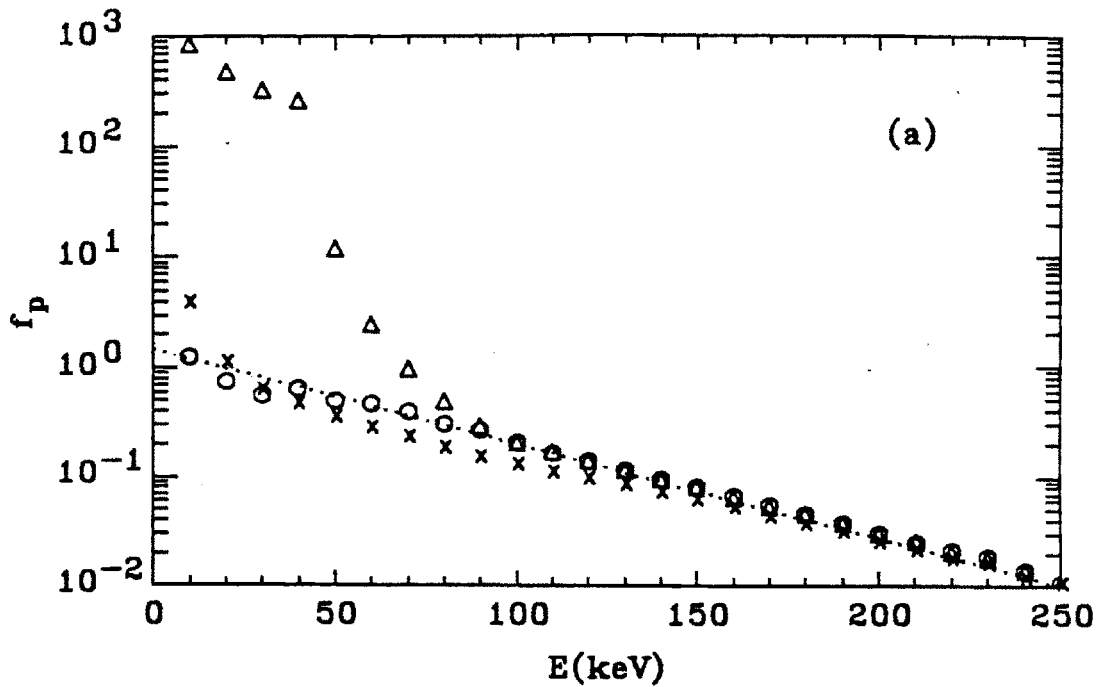
Figure 5.5:

Example of FPFT analysis using an ECE spectrum generated by a $50 keV$
Maxwellian distribution. (a) Predicted f_p. (b) Predicted Λ
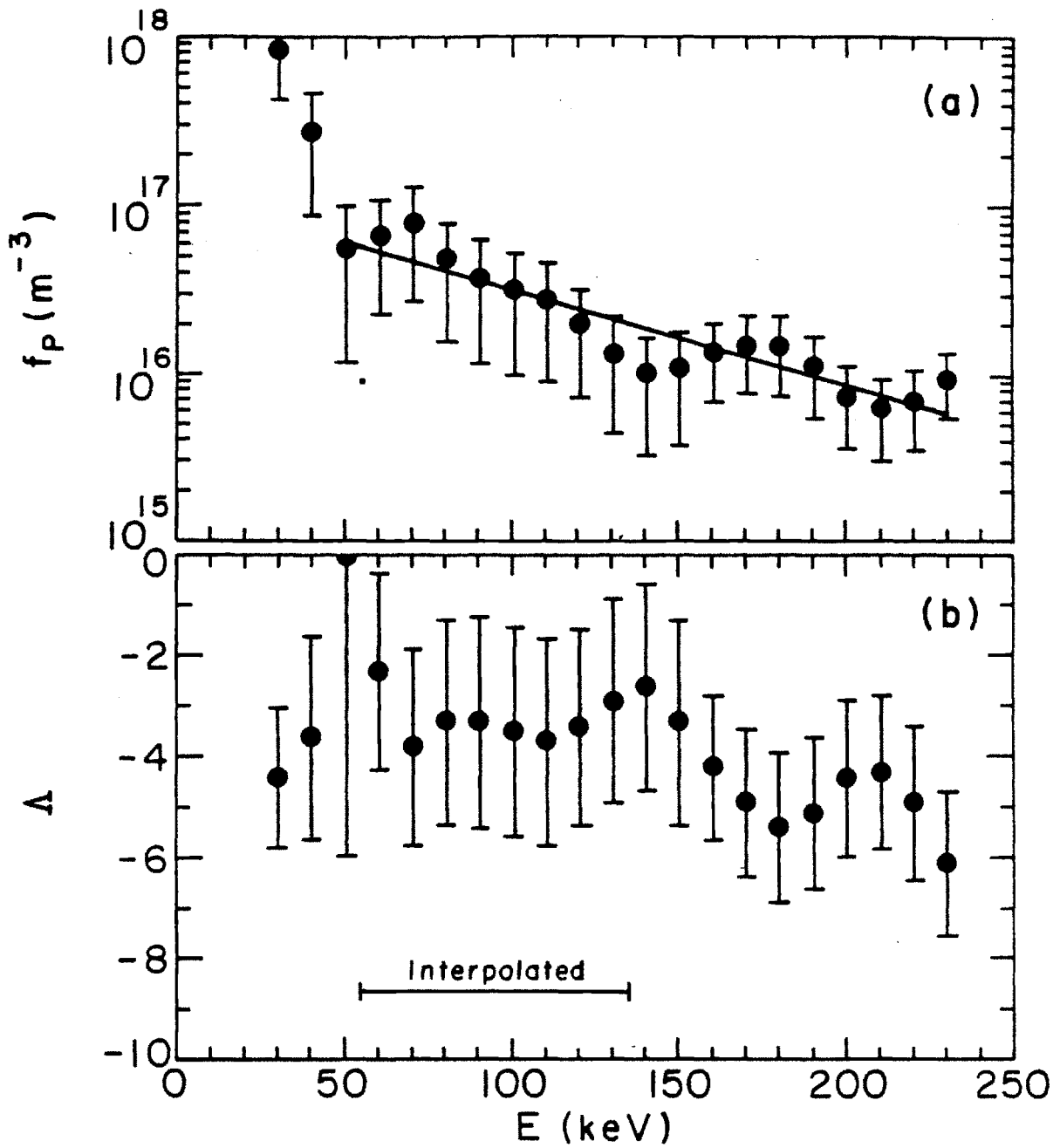
Figure 5.6:
Distribution function parameters for the lower hybrid heating discharge. (a) f_p. (b) Λ.
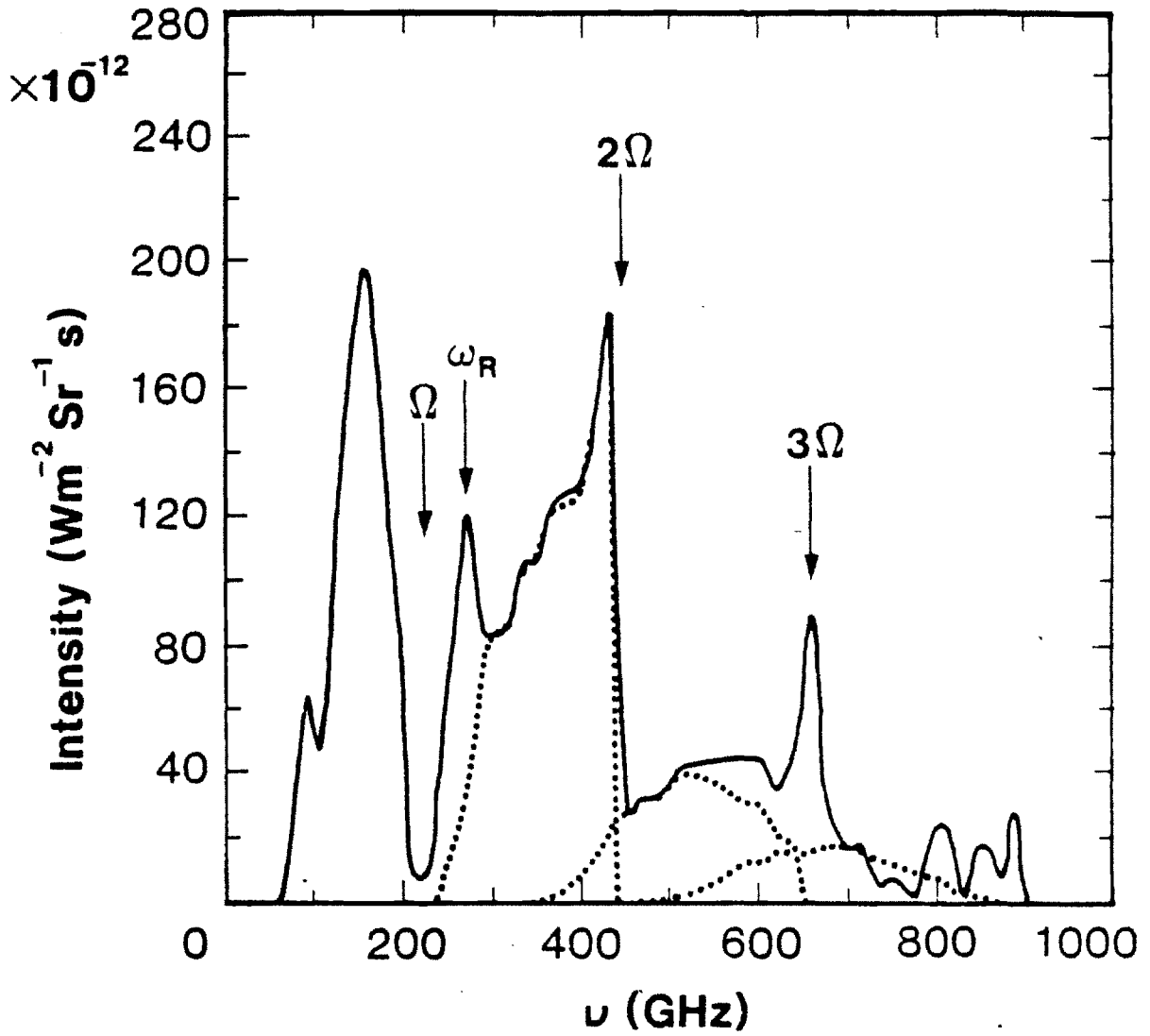
Figure 5.7:
Measured and computed spectra for the lower hybrid heating discharge.
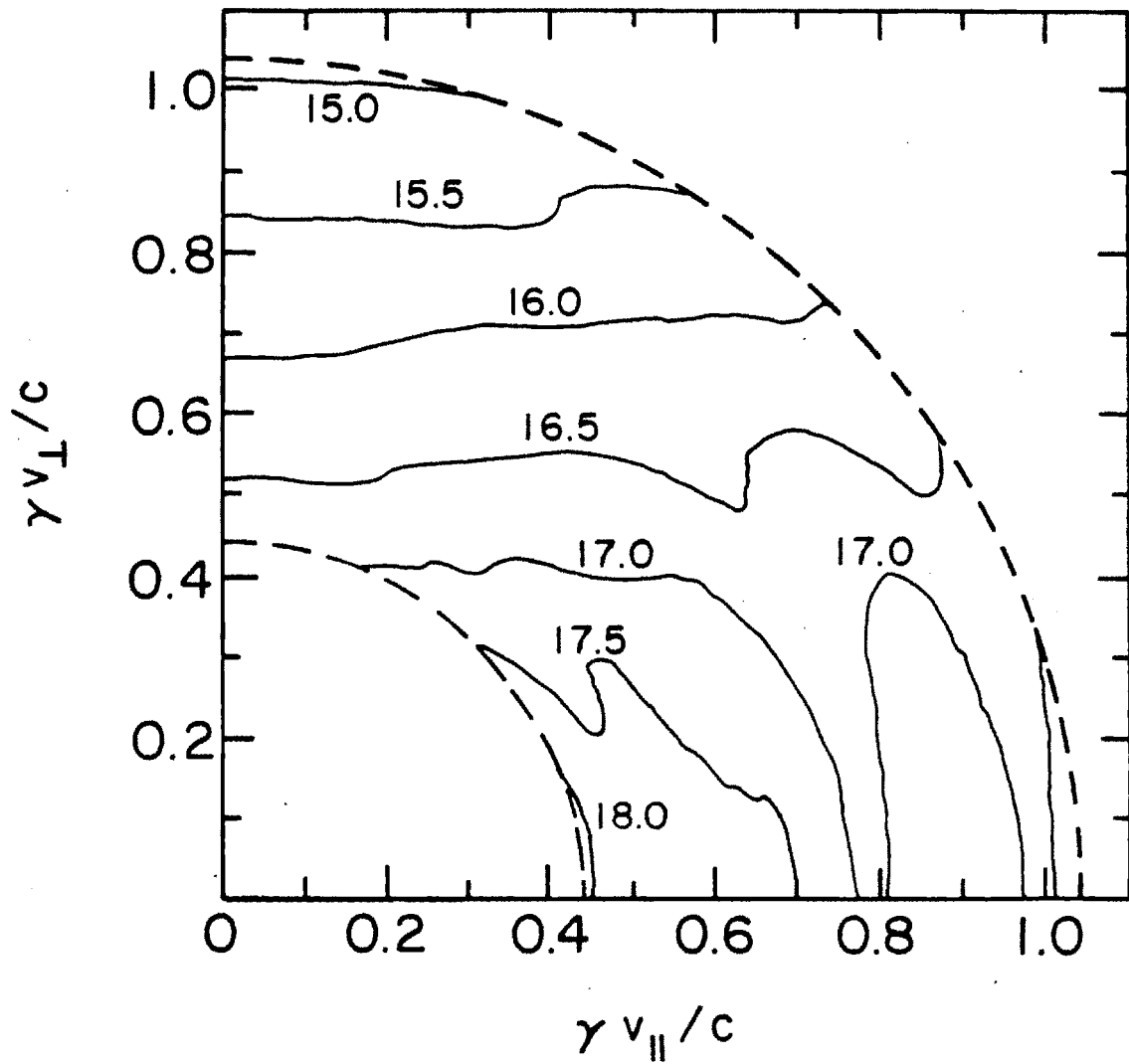
Figure 5.8:
Distribution function contours for the lower hybrid heating discharge. Contour magnitudes are given in $\log(f_p(m^{-3}))$.
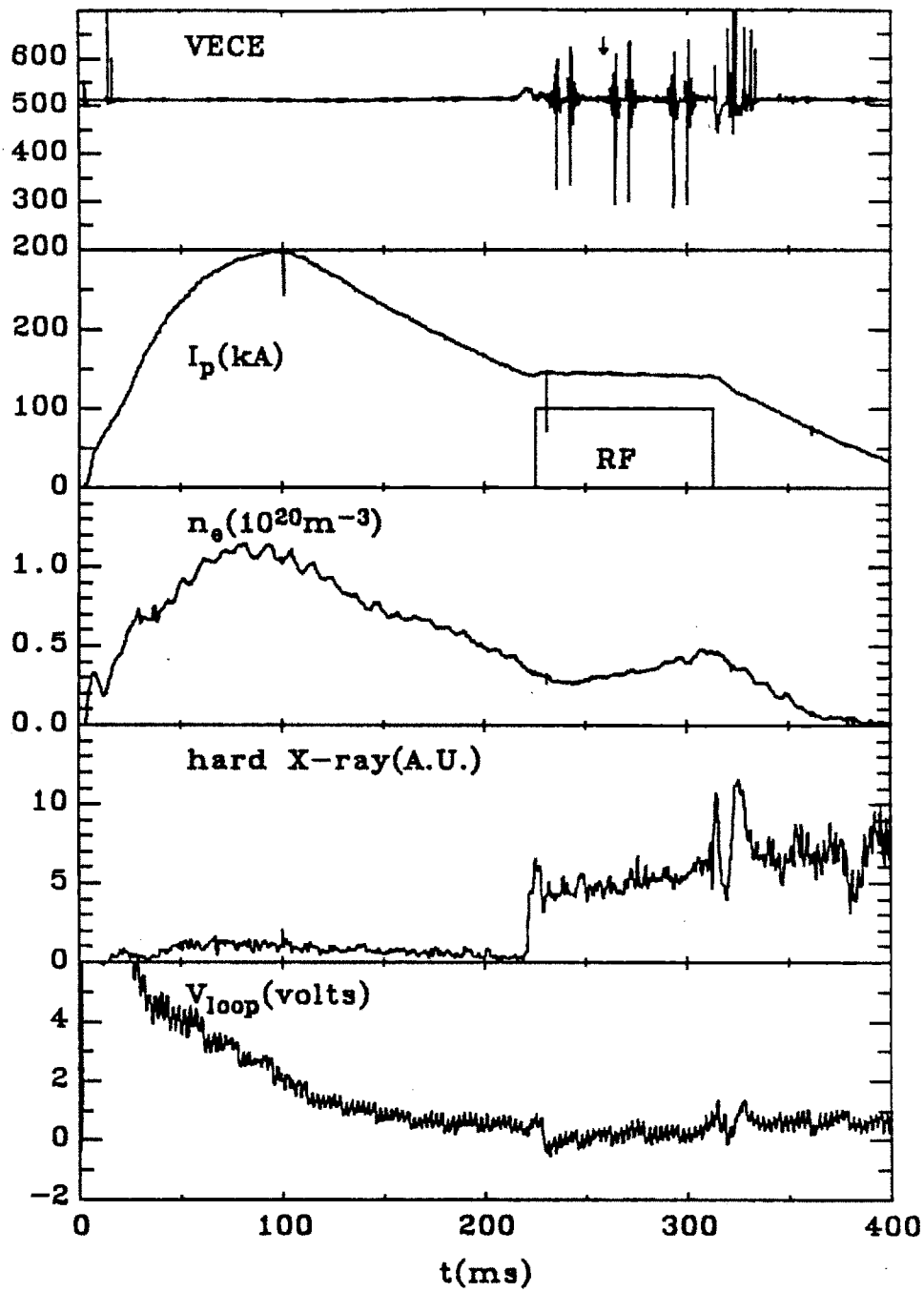
Figure 5.9:
Lower hybrid current drive discharge trace. $B_T = 8T$, $P_{RF} = 800kW$.
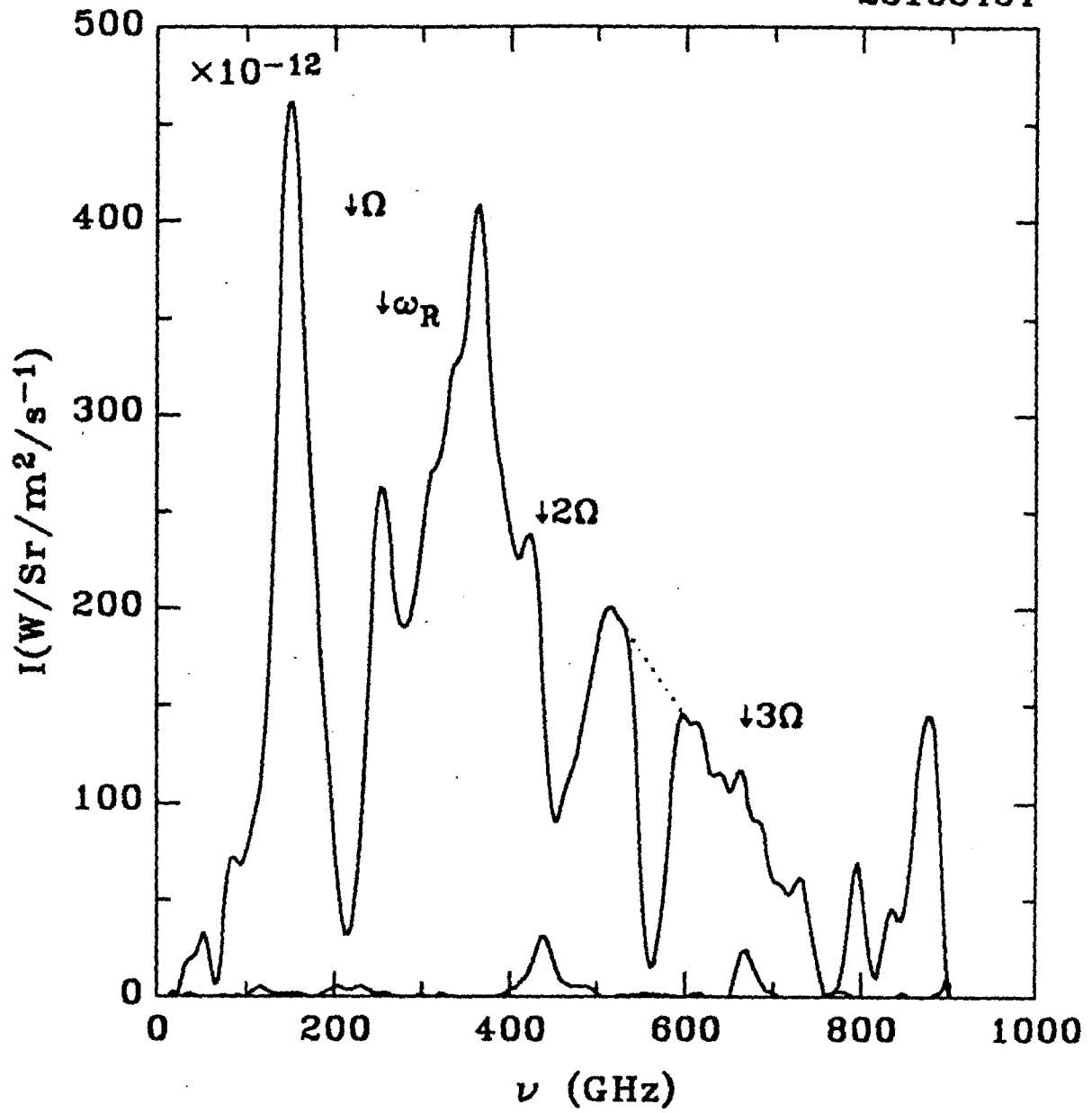
Figure 5.10:
VECE spectra before and during current drive.
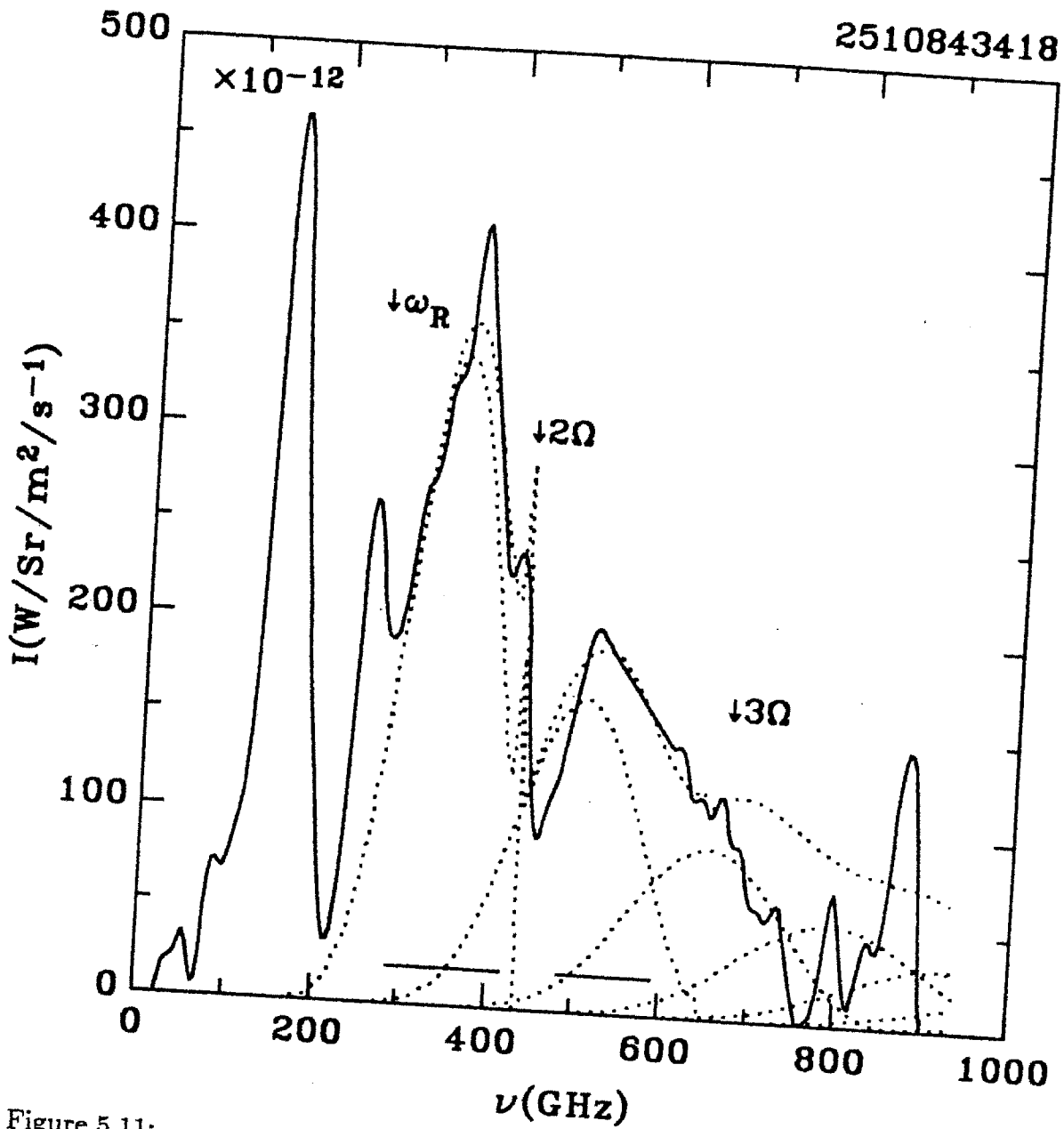
Figure 5.11:
Measured and computed spectra for the current drive discharge. $\chi_\nu^2 = 0.3$.
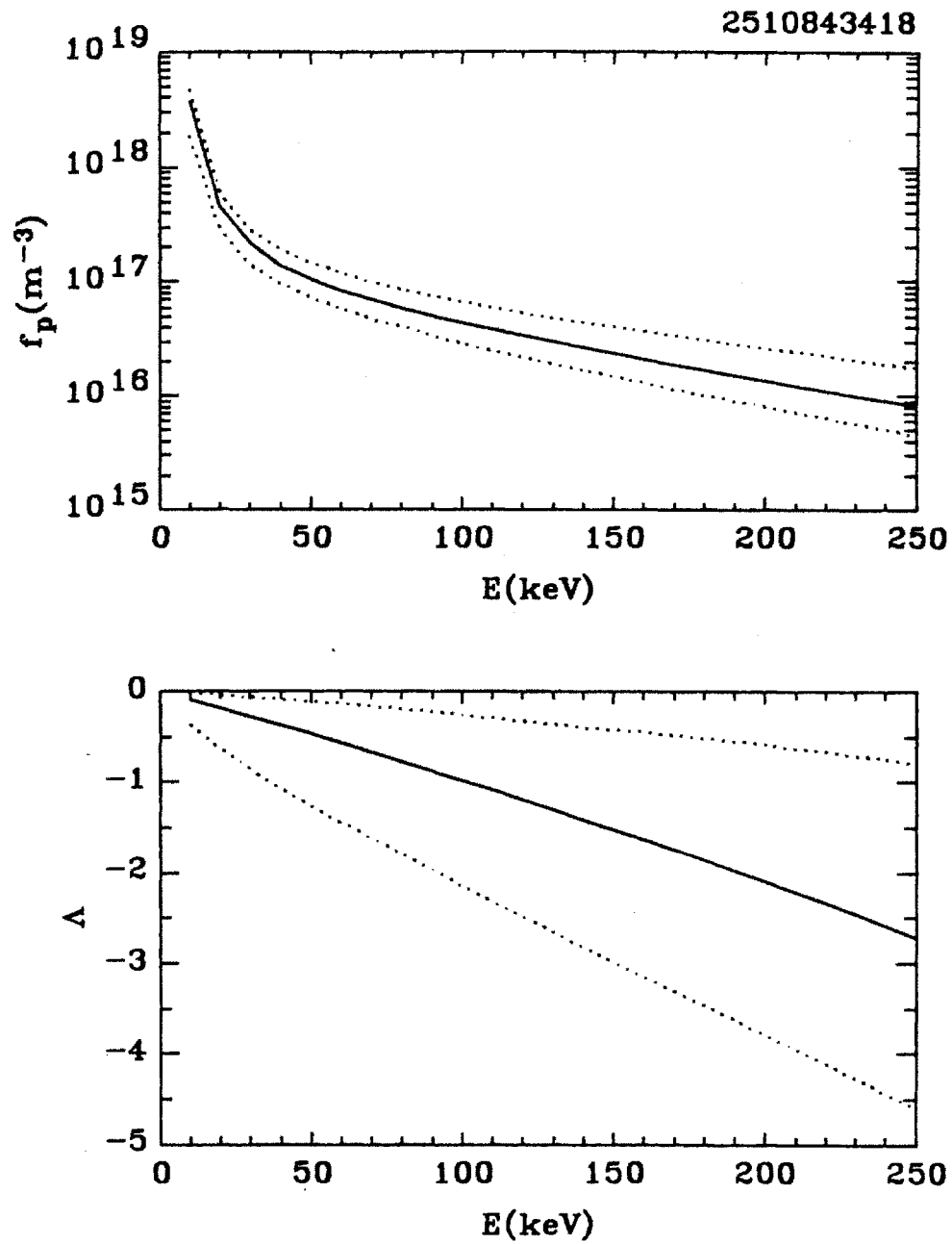
Figure 5.12:
Distribution function parameters for the current drive discharge. (a) f_p. (b) Λ.
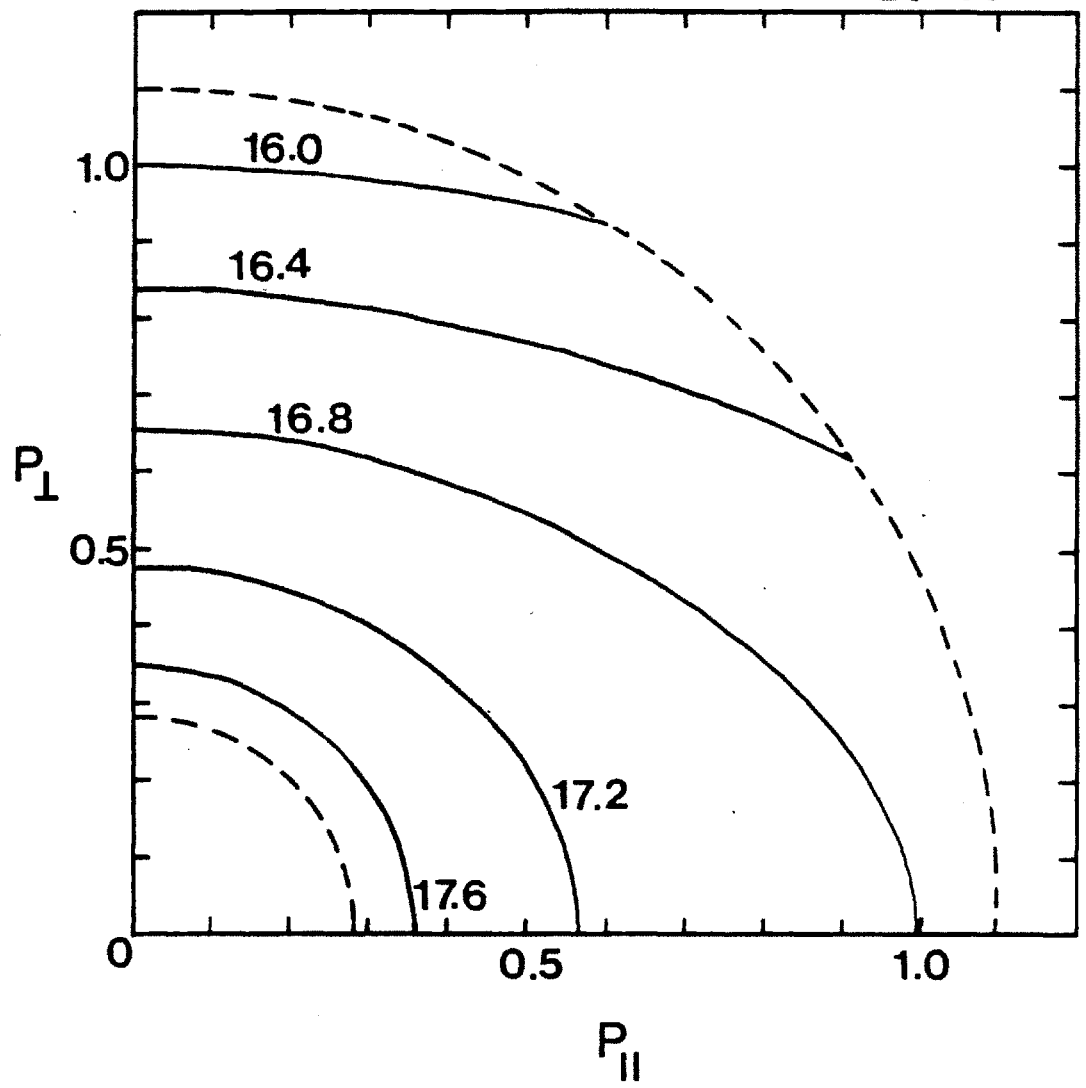
Figure 5.13:
Distribution function contours for the current drive discharge. Contour magnitudes
are given in $\log(f_p(m^{-3}))$.
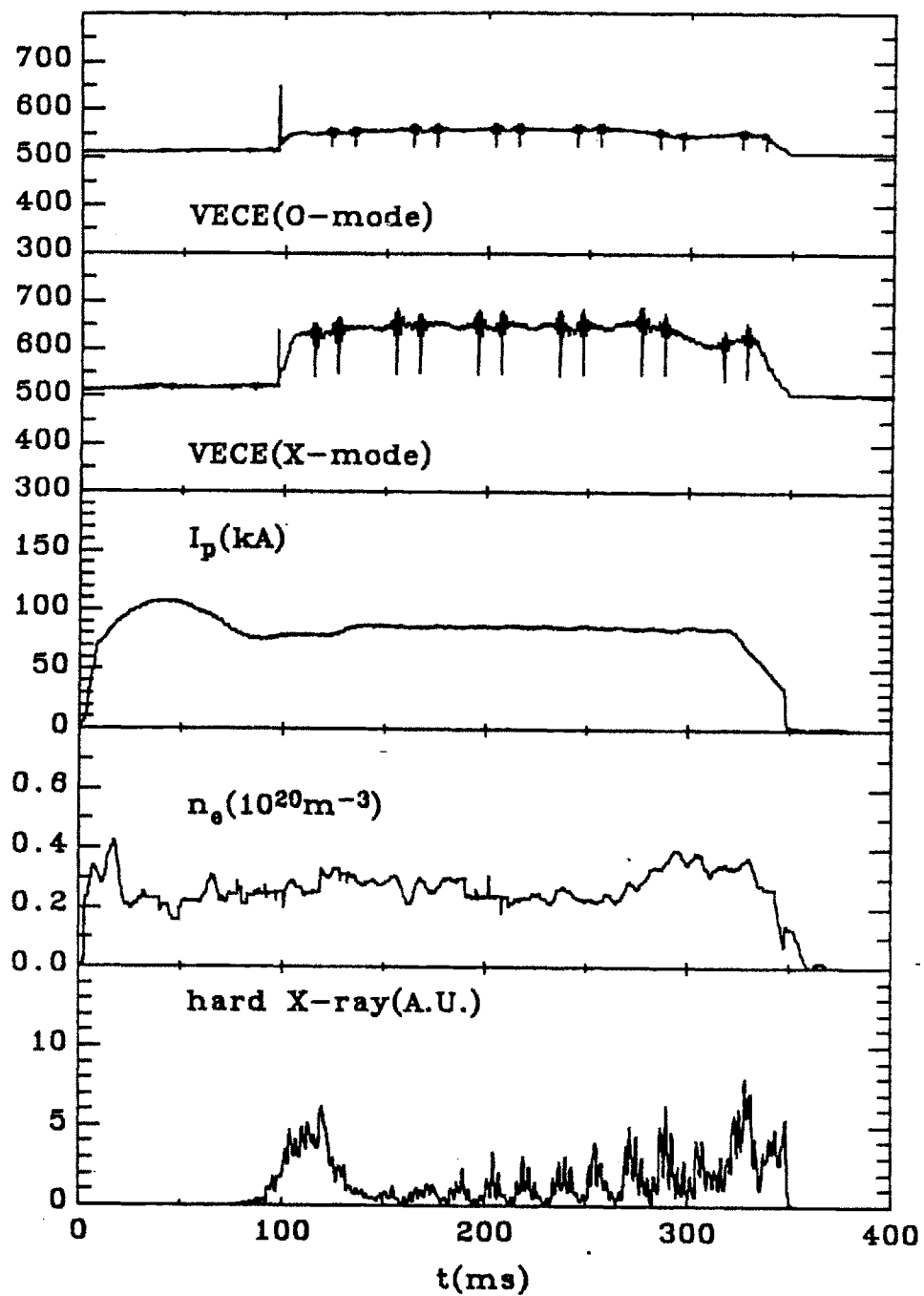
Figure 5.14:
Low density ohmic discharge trace. $B_T = 8T$.
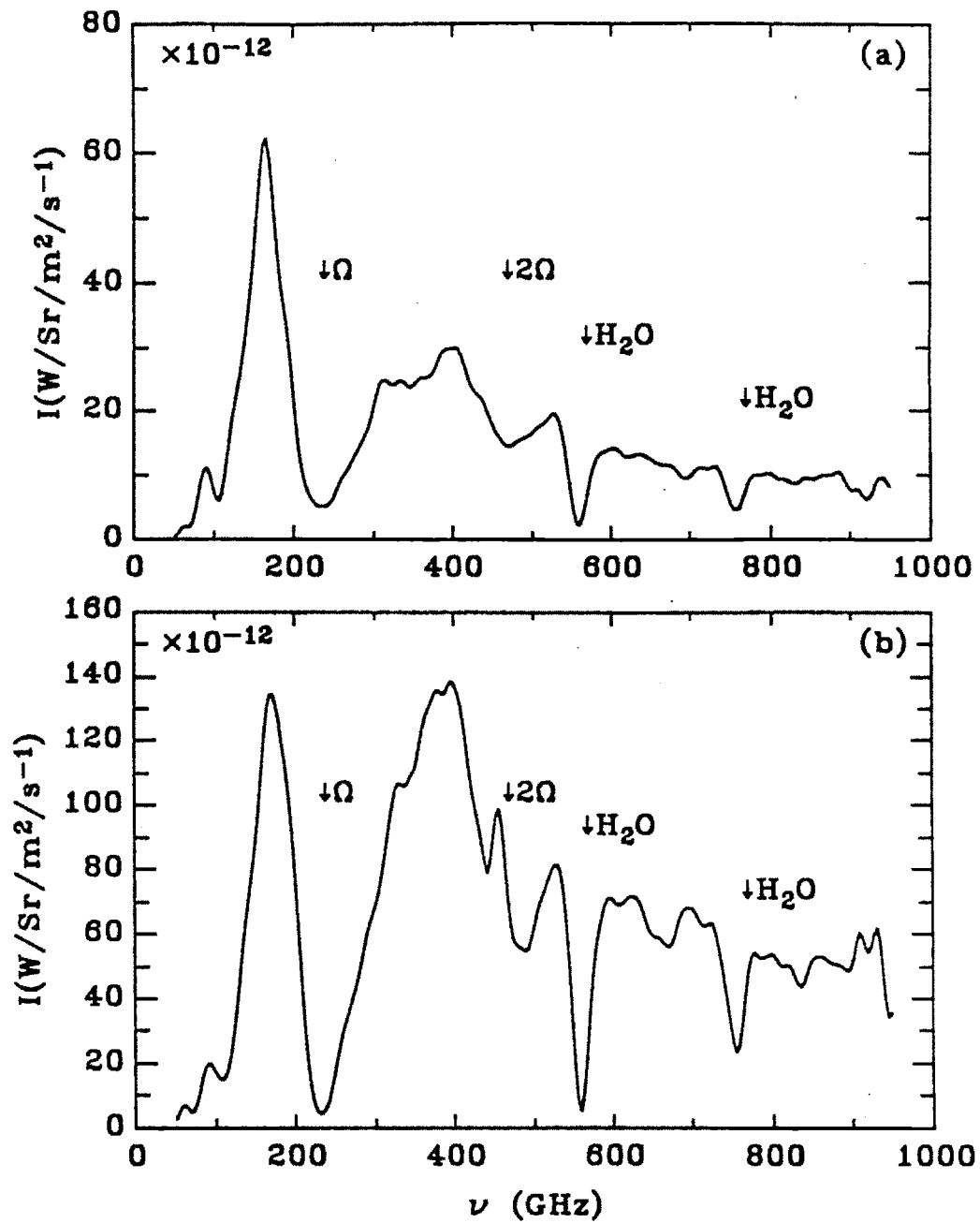
Figure 5.15:
VECE spectra from low density ohmic discharges. (a) O-mode. (b) X-mode.
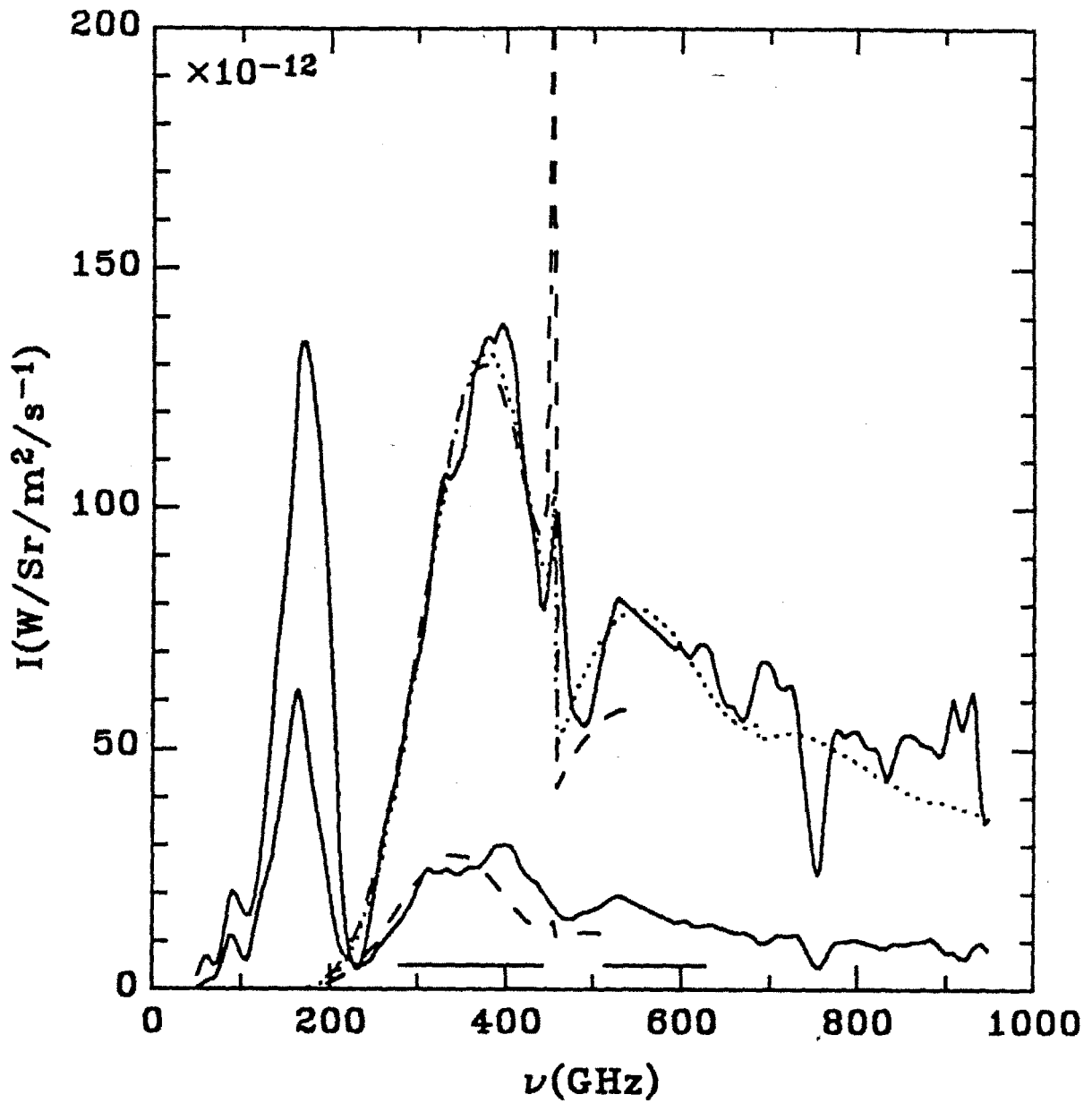
Figure 5.16:
Measured and computed spectra the for low density ohmic discharge. $\chi_\nu^2 = 0.2$ from the harmonic ratio. $\chi_\nu^2 = 0.6$ from the polarization ratio.
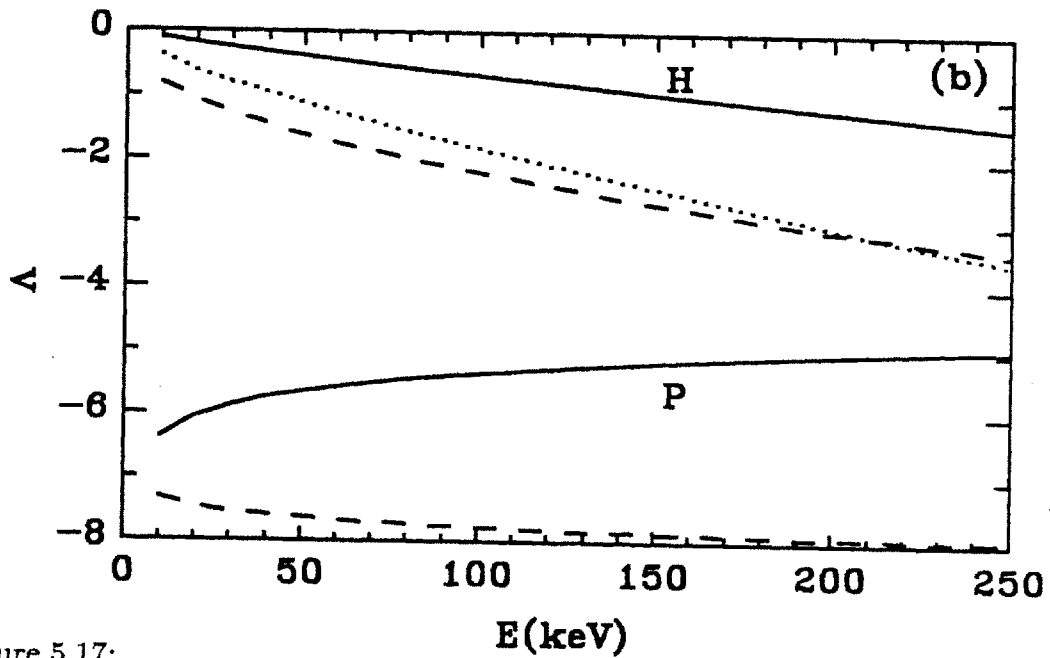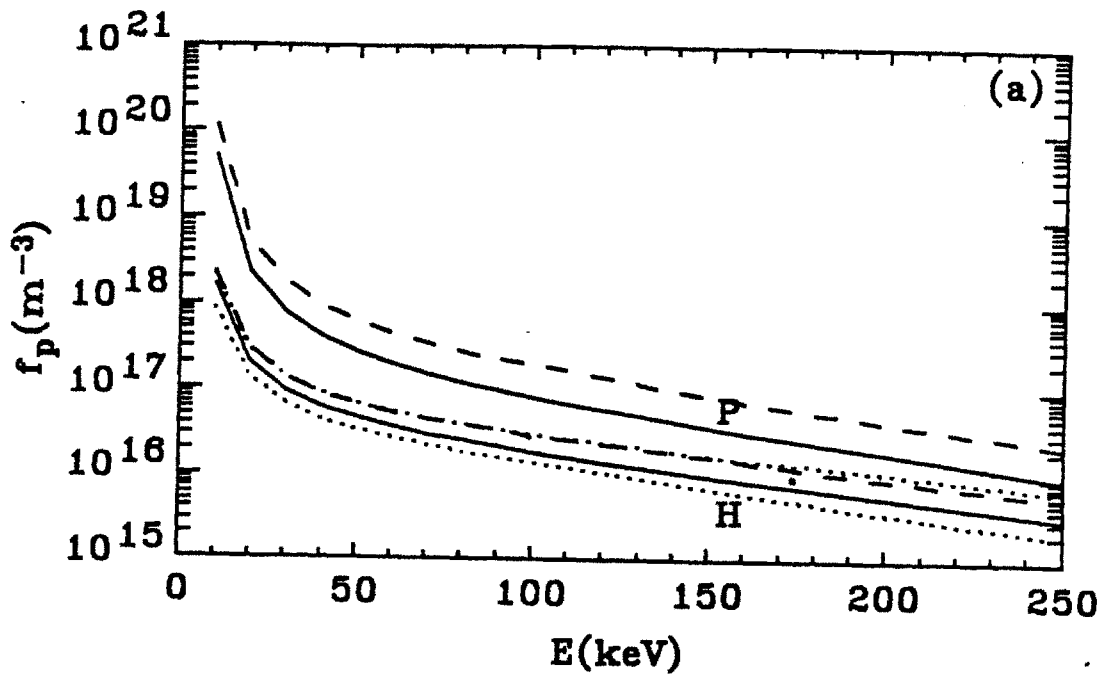
Figure 5.17:

Distribution function parameters for the low density ohmic discharge. (a) f_p. (b) Λ. 'P' and 'H' refer to the results of the polarization and the harmonic ratio analyses, respectively.
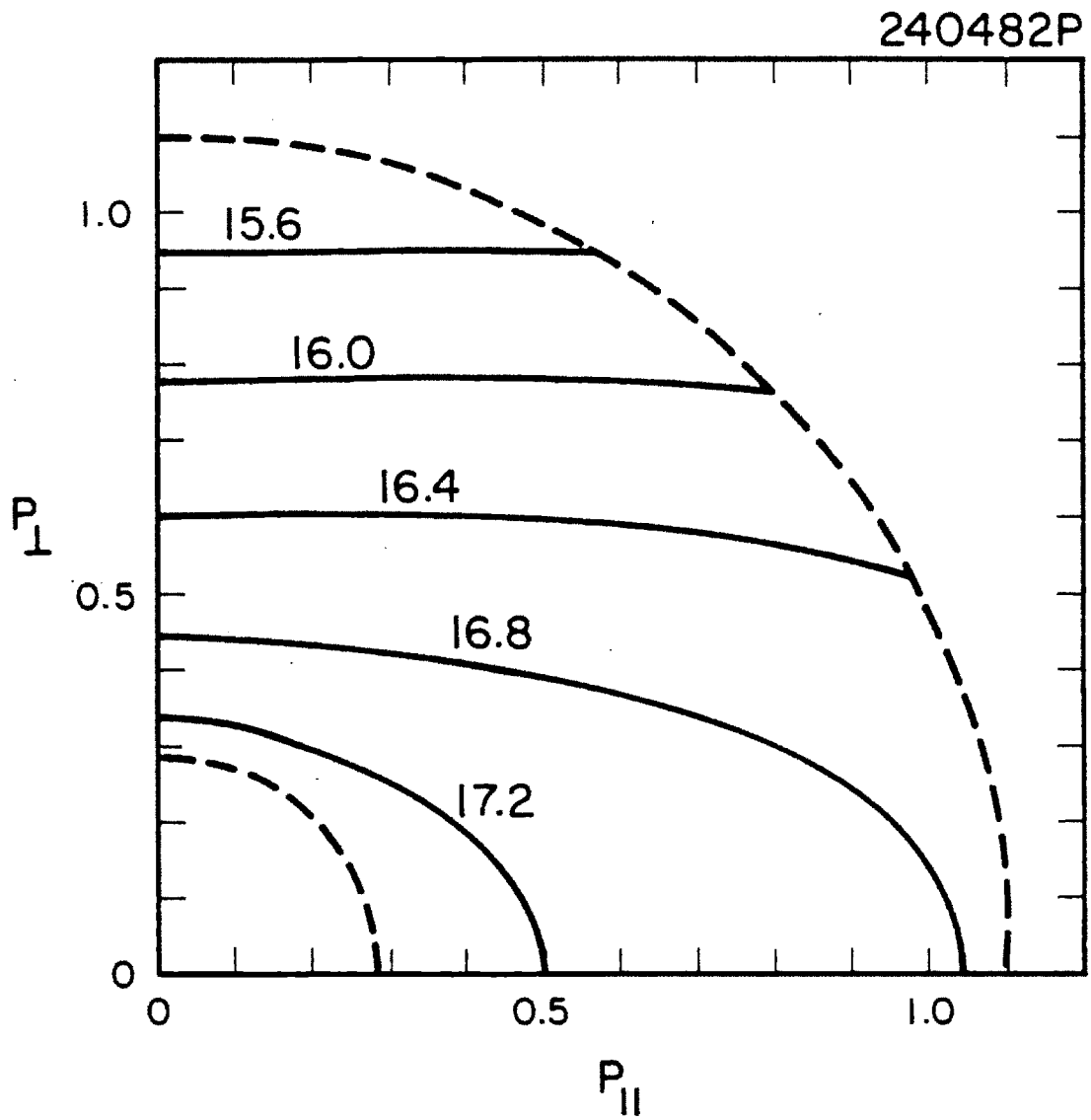
Figure 5.18:
Distribution function contours for the low density ohmic heating discharge. Contour magnitudes are given in $\log(f_p(m^{-3}))$.
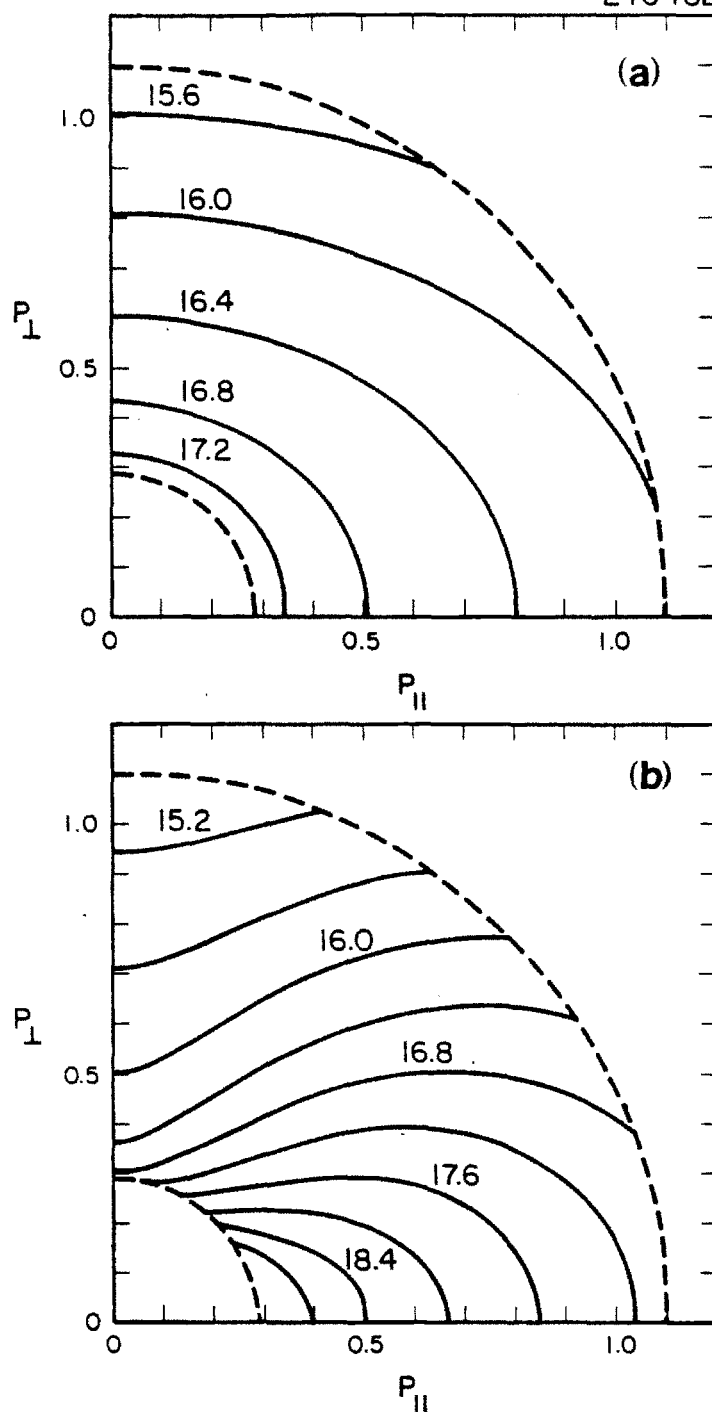
Figure 5.19:
Distribution function contours for the low density ohmic heating discharge from the individual ratio analyses. (a) From harmonic ratio. (b) From polarization ratio. Contour magnitudes are given in $\log(f_p(m^{-3}))$.
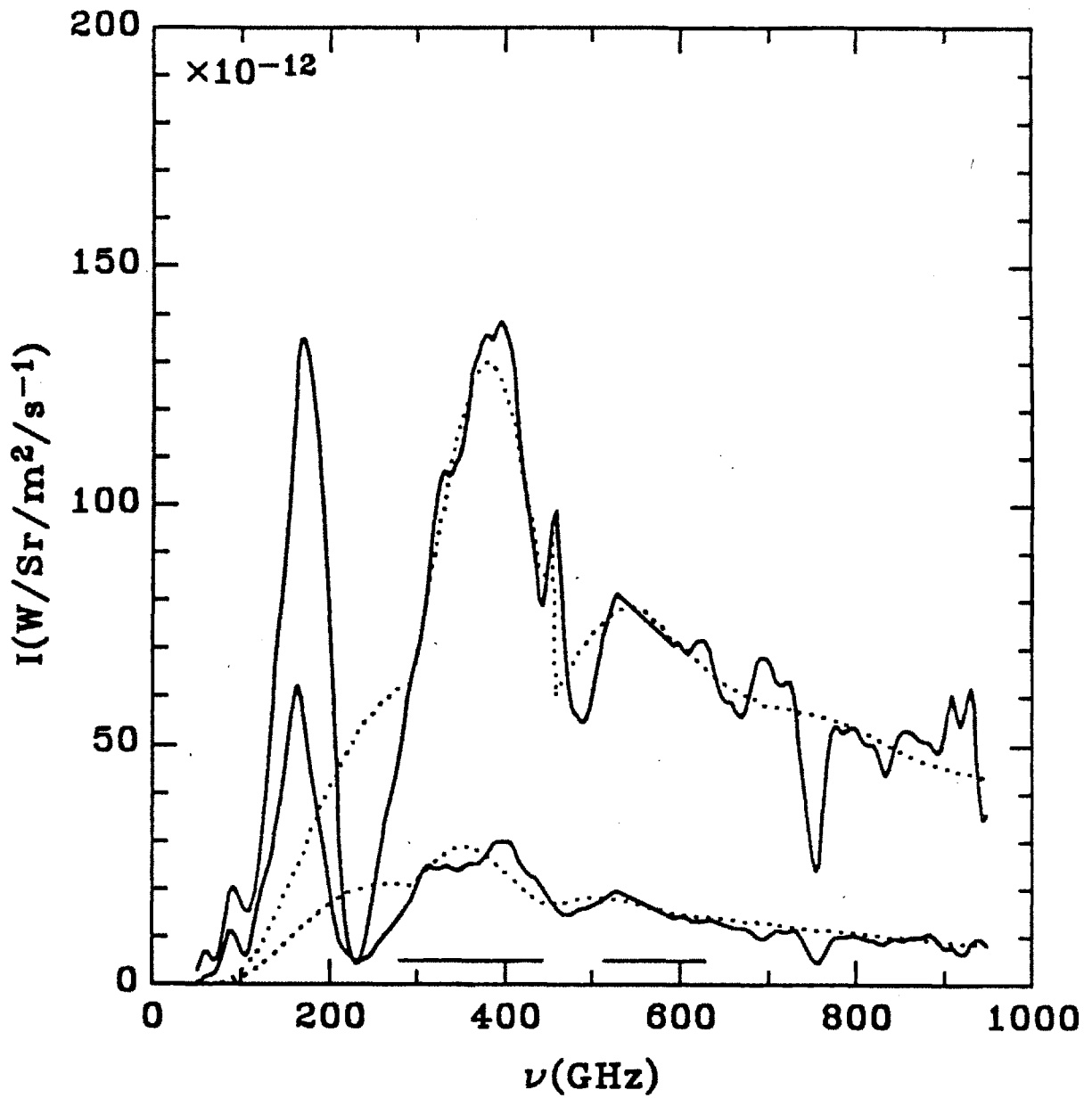
Figure 5.20:
Measured and computed spectra for the low density ohmic discharge, the fit was performed using the 'ad hoc' form of f_p, defined in Eqn. 5.15. $\chi^2_\nu = 0.2$.

Table 5.1:
Summary of the three computer codes.

Code Name	FPFT	BESTFIT	BESTPAIR
Application	Lower Hybrid Heating Discharge	Lower Hybrid Current Drive Discharge	Low Density Ohmic Discharge
Capability	Resolve mild harmonic super-position	Resolve severe harmonic super-position	Resolve severe harmonic super-position
Fitted Ratio	j_3^-/j_2^-	j_3^-/j_2^-	j_2^+/j_2^-
Number of Harmonics	6	14	14
Output	Spectra of f_p and Λ	Five Parameters f_o, T, C, A, B	Five Parameters f_o, T, C, A, B
Error Analysis	Error bars at each energy	Aggregate second harmonic distortion	Aggregate O-mode distortion

Chapter 6

DISCUSSION

6.1 Introduction

Having measured electron distributions from nonthermal VECE data, we now proceed to discuss in detail their characteristics.

In Section 6.2, our results, which are the spectra of f_p and Λ as functions of the total energy, are described using more 'conventional' parameters such as the density and temperatures usually associated with distribution characterizations in the literature. Both exact and approximate forms for the definitions of temperatures will be presented. Using these 'conventional parameters' description, the three distributions diagnosed in Chapter 5 are compared amongst themselves and against theoretical expectations.

In Section 6.3, the down-shifted first harmonic emission spectra which have been excluded from the analysis of Chapter 5 are examined. First, the formalism is established for calculating the absorption coefficient, which is then used to determine the optical thickness of the harmonics and thus the perpendicular temperature inferred by the first harmonic intensity.

In Section 6.4, the angular hard X-ray diagnostic, which is in many ways complementary to the VECE diagnostic, is discussed in detail, after which results from the two diagnostics from nominally similar lower hybrid current drive discharges are presented and compared.

181

The question of how the nonthermal distribution evolves with time in some discharges is addressed in Section 6.5. Although the temporal resolution of the diagnostic is insufficient for the fast time scale phenomena present in most discharges, examples of the diagnostic's capability to address temporal issues are presented. Section 6.6 is the chapter summary.

6.2 Electron Distribution Properties

6.2.1 Definitions

Common parameters that define electron distributions(thermal as well as nonthermal) include the total density, one or two temperatures, a pitch-angle, and perhaps parameters characterizing the 'drift' or the 'off set' of the distribution. For magnetized plasmas with gyro-symmetry, it is also common to define directional (parallel and perpendicular to the magnetic field) temperatures. In this section, definitions of these parameters as functions of f_p and Λ are presented in exact and analytical forms.

Recalling our definition of the distribution function,

$$
\begin{aligned}
f(\vec{p}) &= f_p(p) f_\theta(p, \theta_p) \\
&= f_p(p) L \exp\{-\Lambda(p) \cos^2 \theta_p\},
\end{aligned}
\tag{6.1}
$$

we note that since f_θ integrated over the pitch-angle is normalized for any $\Lambda(p)$, the electron density information can be recovered from the f_p data alone, such that

$$
n_e|_{p_1}^{p_2} = 4\pi \int_{p_1}^{p_2} f_p p^2 dp,
\tag{6.2}
$$

where p_1 and p_2 refer to the lower and upper limits of the range for which n_e is computed. In this way, often quoted quantities such as the 'tail density' can be evaluated.

In the case of temperature characterization, the natural requirements on the definition of such parameters are:

1. They should describe (qualitatively) the spread of the distribution (in the appropriate direction).

2. They should be equal to the temperature of the distribution in the limit of an isotropic thermal distribution

Characterization of a distribution by a single Maxwellian 'temperature' is misleading for largely nonthermal or significantly anisotropic distributions, although a reasonable fit by a Maxwellian temperature to the pitch-angle averaged distribution can be obtained from the VECE data over limited range of energies. We define T_{eff}, the effective temperature of the distribution as that value which best fits the expression

$$f(p) = f_o \exp\left\{-\frac{m_e c^2}{T_{eff}}\sqrt{1+p^2}\right\},\qquad(6.3)$$

over some specified range in p. The straight line drawn in Fig. 5.6(a) shows the result of fitting a $T = 80 keV$ Maxwellian to the range $50 \le E(keV) \le 230$. This effective temperature is equivalent to the T-parameter obtained from BESTFIT and BESTPAIR in the range where the effect of the C-parameter is negligible.

For lower hybrid heating and current drive experiments, special interest exists in the determination of the perpendicular temperature as a function of the parallel momentum, $T_\perp(p_\|)$. To evaluate this quantity, we take the approach whereby a two dimensional Maxwellian is fitted to the distribution in $p_\perp$ space at a single value of $p_\|$, such that the evaluated $T_\perp$ best fits the expression

$$f(p_\perp, p_\| = \text{const.}) = f_o \exp\left\{-\frac{m_e c^2}{T_\perp(p_\|)}\sqrt{1+p_\|^2+p_\perp^2}\right\}.\qquad(6.4)$$

Consistent with this definition of $T_\perp$, we can define an effective parallel temperature, $T_\|$ by first computing the parallel distribution

$$f(p_\|) = 2\pi \int_0^\infty f(p_\perp, p_\|)p_\perp dp_\perp.\qquad(6.5)$$

183

and finding $T_{\parallel}$ such that the value optimizes the fit to the expression

$$f(p_{\parallel}) = f_o \exp\left\{-\frac{m_e c^2}{T_{\parallel}}\sqrt{1+p_{\parallel}^2}\right\}. \tag{6.6}$$

The shape of the distribution described by the f_p and Λ characterization is not always easy to fit by these Maxwellian forms, and the fit becomes particularly difficult for the results of FPFT, which permit the existence of 'bumpiness' in the distribution. As an example, we show in Fig. 6.1 $p_{\parallel} = const.(0.82)$ slices from the contour plots of Fig. 5.8 and Fig. 5.13(cross marks), along with fits generated by the optimization of Eqn. 6.4. These show that while for the FPFT result(a), the goodness of the fit obviously varies from slice to slice due to the freedom allowed in its choice of f_p and Λ at each energy, the BESTFIT result slice(b) is well approximated by the relativistic Maxwellian.

Analytical Approximations

In order to obtain T_{eff}, $T_{\perp}$, and $T_{\parallel}$ as defined by the above forms, the distribution function must first be generated, appropriate 'slices' or averages evaluated, and then fitted to relativistic Maxwellians to arrive at the temperatures. It will be useful therefore to derive an approximate analytical result which eases the computation and provides more insight.

Assuming that the distribution can be well approximated by a relativistic Maxwellian of Eqn. 6.3, the 'local' temperature can be recovered by differentiation with respect to p^2,

$$\frac{\partial f}{\partial p^2} = -\frac{m_e c^2}{T}f(p)\frac{1}{2\gamma} \tag{6.7}$$

so that

$$\frac{1}{\hat{T}_{local}} = -\frac{2\gamma}{f(p)}\frac{\partial f}{\partial p^2} \tag{6.8}$$

where $\gamma = \sqrt{1+p^2}$ and $\hat{T}$ is the normalized temperature in units of $m_e c^2$. For an identically Maxwellian distribution, T is constant regardless of the value of p used

for its evaluation. In the case of the VECE distribution, the pitch-angle integrated $\hat{T}$ can be obtained from just the f_p spectrum.

By analogy, we shall define

$$\frac{1}{\hat{T}_{\perp local}} = -\frac{2\gamma}{f} \frac{\partial f}{\partial p_{\perp}^2} \tag{6.9}$$

and

$$\frac{1}{\hat{T}_{\parallel local}} = -\frac{2\gamma}{f} \frac{\partial f}{\partial p_{\parallel}^2}, \tag{6.10}$$

as our local perpendicular and parallel temperature. To obtain averages of these quantities over some restricted volume of momentum space, we shall perform integrals weighted by f so that the definitions of the temperatures become

$$\frac{1}{\hat{T}} = \frac{\int -2\gamma \frac{\partial f}{\partial p^2} d^3 p}{\int f d^3 p}, \tag{6.11}$$

$$\frac{1}{\hat{T}_{\perp}} = \frac{\int -2\gamma \left. \frac{\partial f}{\partial p_{\perp}^2} \right|_{p_{\parallel}} d^3 p}{\int f d^3 p}, \tag{6.12}$$

and

$$\frac{1}{\hat{T}_{\parallel}} = \frac{\int -2\gamma \left. \frac{\partial f}{\partial p_{\parallel}^2} \right|_{p_{\perp}} d^3 p}{\int f d^3 p}. \tag{6.13}$$

These temperatures thus evaluated are the average values over the specified arbitrary volume. We shall find it convenient to take as our volume the resonant contour, $\gamma = const.$, because this will allow the characterization of the directional temperature by reference to f_p and Λ at a single point in energy. Using the VECE distribution function definition of $f(\vec{p})$, and assuming for simplicity $\Lambda = const.$, i.e.,

$$\left. \frac{\partial f_\theta}{\partial p} \right|_\theta = 0, \quad \text{and hence} \quad \left. \frac{1}{f} \frac{\partial f}{\partial p} \right|_\theta = \left. \frac{1}{f_p} \frac{\partial f_p}{\partial p} \right|_\theta, \tag{6.14}$$

we substitute Eqn. 2.44 into Eqn. 6.12 and make use of the definition for the pitch-angle integrated temperature, $\hat{T}$(Eqn. 6.11), to obtain

$$\frac{1}{\hat{T}_\perp} = \frac{1}{\hat{T}} - \frac{2\gamma\Lambda}{p^2} \int_0^{\pi/2} \cos^2\theta_p f_\theta \sin\theta_p d\theta_p$$

$$= \frac{1}{\hat{T}} - \frac{\gamma}{p^2}\left\{1 - L\exp(-\Lambda)\right\}, \tag{6.15}$$

where

$$L = \frac{1}{\int_0^1 \exp(-\Lambda x^2)dx} \tag{6.16}$$

is the normalization factor of f_θ, in a slightly different form than Eqn. 2.13. The integral over θ_p was evaluated using the substitution $x = \cos\theta_p$, and a subsequent integration by parts.

When Λ is large and negative, it can be shown that

$$L\exp(-\Lambda) \simeq 2|\Lambda|, \tag{6.17}$$

so that Eqn. 6.15 becomes

$$\frac{1}{\hat{T}_\perp} \simeq \frac{1}{\hat{T}} - \frac{\gamma}{p^2}\left\{1 - 2|\Lambda|\right\}$$

$$\simeq \frac{1}{\hat{T}} + \frac{2\gamma|\Lambda|}{p^2}. \tag{6.18}$$

Thus, the approximate value of $T_\perp$ at a specific p can be obtained from the effective temperature in the vicinity and Λ.

We can arrive at an approximate form for the parallel temperature by a similar method, although it will not be useful for our results since $\partial f/\partial p_\parallel > 0$ for these distributions with parallel enhancements. Nevertheless, it should be useful in analyzing perpendicularly enhanced distributions such as those occurring in mirror devices. Noting that the parallel derivative of the VECE distribution is

$$2\frac{\partial f}{\partial p_\parallel^2} = \frac{1}{p}\left(\frac{\partial f}{\partial p} - \frac{\tan\theta_p}{p}\frac{\partial f}{\partial \theta_p}\right)$$

$$= \frac{1}{p}\left(\frac{\partial}{\partial p}(f_p f_\theta) - \frac{2\Lambda\sin^2\theta_p}{p}f_p f_\theta\right), \tag{6.19}$$

186

we make the same assumptions stated in Eqn. 6.14 to obtain

$$\frac{1}{\hat{T}_\parallel} = \frac{1}{\hat{T}} + \frac{2\Lambda\gamma}{p^2} - \frac{\gamma}{p^2}\left\{1 - L\exp(-\Lambda)\right\}. \tag{6.20}$$

Assuming this time the limit of perpendicularly enhanced anisotropy, $\Lambda \gg 1$, this expression reduces to

$$\frac{1}{\hat{T}_\parallel} = \frac{1}{\hat{T}} + \frac{2\gamma\Lambda}{p^2}, \tag{6.21}$$

an identical form as for $\hat{T}_\perp$ except for the absence of the modulus operator. These expressions satisfy the requirements for the directional temperature definitions set forth at the beginning of this section: They qualitatively describe the spread of the distribution in the appropriate direction, as indicated by their Λ dependence, and for thermal plasmas, the Λ terms vanish so that $\hat{T} = \hat{T}_\perp = \hat{T}_\parallel$. As implied by these expressions for $T_\perp$ and $T_\parallel$, approximately constant directional temperatures are obtained by setting $|\Lambda| \propto p^2$. We see that this is in fact roughly the case for the BESTFIT and BESTPAIR results with $B = 1.3 \sim 2.4$ for the distributions diagnosed, so that approximately constant $T_\perp$ and $T_\parallel$ are expected for the range where $1/\hat{T}$ is constant, i.e., outside the transition region.

Error Analysis

The uncertainties in these temperatures and the density can be found by evaluating them for error curve distributions instead of the true distributions in the case of BESTFIT and BESTPAIR produced results. For the FPFT result, the error in the tail density can be estimated by using the maximum and minimum values of f_p, represented by the upper and the lower bounds traced out by the error bars.

For the temperatures however, the uncertainties are not straightforward to evaluate for FPFT results because the error bars in this case represent possible uncertainties at each energy, and no assumption is made about inter-energy correlations. Thus, for evaluation of the error of quantities defined over a finite energy range,

these error bars are not adequate representations. For the perpendicular temperature however, we can estimate the error by assuming that locally, Λ variations are small and the uncertainties are strongly correlated, so that the error in the temperature can be defined as

$$\sigma_{T_\perp}^2 = \sigma_\Lambda^2 \left(\frac{\partial T_\perp}{\partial \Lambda}\right)^2 \frac{\Lambda^2}{T_\perp^2}.$$

(6.22)

These prescriptions are applied to the estimate of errors of the Chapter 5 results and presented below.

6.2.2 Comparison Among Different VECE Results

As a concise summary with an aim to highlight the differences and similarities, the density and temperatures evaluated by Eqns. 6.2 through 6.6 are presented in Table 6.1 for the three distributions of Chapter 5. For the low density ohmic discharge case, we shall use the intermediate result as represented by the distribution of the error curve which falls between the results from the two different ratio analyses. For the lower hybrid current drive and low density ohmic results, the effective temperature is taken to be the T-parameter value of the optimized fit. For $T_\perp$, average values from each spectra over the frequency range are quoted, as they do not vary by more than 20%.

The results show approximately the same effective temperatures for all three cases, despite the different origins of the nonthermal tail. However, it is probably not a representative parameter for these largely anisotropic distributions as discussed earlier. The ohmic discharge measures the largest parallel temperature, with the lower hybrid current drive having the next largest, followed by the heating case. The perpendicular temperatures differ by a factor of two among these cases, with the current drive case having the highest and the heating case having the lowest. The difference in $T_\perp$ between the heating and the current drive cases will be discussed

in connection with theory below. The tail density is approximately the same for the two lower hybrid cases, while the ohmic case is somewhat lower.

The uncertainties in each evaluated quantity are shown in the table by +(plus) superscripts and −(minus) subscripts. These errors were obtained according to the discussion above, where for the LHH result, $T_\perp$ error was calculated using Eqn. 6.22, and the error in $\bar{n}_{tail}$ was calculated by taking the maximum and minimum values of the error bars for f_p. For the LHCD case, the uncertainties quote the difference between the quantities derived from the true $f(\vec{p})$ curve and the two extreme error curve distributions of Fig. 5.12. Since the intermediate error curve distribution is taken to be the most appropriate solution to the ohmic case, the uncertainties in this case are characterized by the values obtained from the two ratio analyses without spectral distortion, i.e., the solid curve distributions in Fig. 5.17. Thus, in this case, the uncertainties for T_{eff} and $T_\parallel$ both are below the quoted value, resulting in '+0' uncertainty.

If we apply the analytical form of the perpendicular temperature, we obtain $T_\perp = 26keV$ at $E = 200keV$ for the lower hybrid heating case, in good agreement with the numerically fitted result. For the lower hybrid current drive case, $T_\perp = 49keV$ at $E = 200keV$, somewhat underestimating the value since Λ is only slightly more negative than -1.

6.2.3   Comparison of Results with Theoretical Expectations

The behavior of the nonthermal electron distribution during current drive has been under extensive investigation due to its importance in the energy balance and the optimization of the non-inductive current drive scheme[78,81,82]. These studies treat the problem using the relativistic one- or two-dimensional Fokker-Planck equation with a quasilinear parallel diffusion term representing the parallel momentum transfer from the RF wave to the electron population.

Numerical computations based on such a model predict an enhanced parallel distribution in the form of a plateau in the range of $p_\parallel$ where the wave-particle

189

coupling exists. The computation of the perpendicular temperatures indicates increase in this quantity with decrease in the mean $N_\parallel$ of the coupled wave, i.e., with increase in the value of $p_\parallel$ to which the wave couples[83,84]. The perpendicular temperature predicted by these codes are $T_\perp \sim 30keV$ for the $N_\parallel$ spectrum ranging from 1.5 to 5.0, coupling to electrons up to $\sim 400keV$ in energy(see Fig. 5.1) in an Alcator discharge with $T_e = 1keV$[84]. An additional result common to these cases is the abrupt enhancement of $T_\perp$ and the decrease in population at parallel momenta above the plateau value.

The lower hybrid heating and current drive discharge results both show the enhancement of the high-energy electron population in the parallel direction as forecasted by theory. However, the parallel 'tail' forms not a plateau, but a high temperature slope. The $30keV$ perpendicular temperature measured for the heating case agrees with the code prediction above, although this parameter depends crucially on the $N_\parallel$ spectrum at the coupling region and not the launched spectrum so that quantitative comparison is difficult to establish. The higher $T_\perp$ for the current drive results in our case is consistent with the increase in $T_\perp$ with the energy of the coupled electrons predicted by the numerical analyses. The increase in $T_\perp$ above the highest $p_\parallel$ coupled cannot be investigated in our measurement because the value of energy that this $p_\parallel$ corresponds to is usually beyond the energy limit imposed by the harmonic superposition.

Finally, distributions obtained from Fokker-Planck code simulations do not have the transition region found in our measurement (represented by the finite C-parameter), i.e., the bulk temperature slope suddenly changes to a plateau in the theory. This is probably due to the choice of an oversimplified diffusion coefficient on the part of the code analysis. The role of these transition regions may become significant for evaluations of secondary quantities such as the current carried by the tail, the tail energy content, and the tail-to-bulk energy transfer rate.

6.3 First Harmonic Emission

6.3.1 Absorption Coefficient Calculation

In order to understand the mechanisms contributing to the first harmonic intensity, and to confirm our assumptions of the tenuous plasma approximation at frequencies other than the thermal resonances in the second and the third harmonics, the method to compute the absorption coefficient from the VECE distribution is presented.

Substituting Eqn. 2.42 into Eqn. 2.10 and restricting our discussion to the X-mode, we obtain

$$
\alpha_l(\omega) = \frac{e^2\omega}{8\pi^2\epsilon_o c}\frac{N_r^2}{N_\pm}2\pi p^3 2 \int_0^{\pi/2}\left[N_- K\frac{\gamma}{p}J_l(x) + \sin\theta_p J_l'(x)\right]^2
$$
$$
\times \left\{-\frac{8\pi^3\gamma}{N_r^2\omega^2 m_e}\frac{1}{p_\perp}\frac{\partial f}{\partial p_\perp}\right\}\sin\theta_p d\theta_p,
\tag{6.23}
$$

using notations familiar in Chapter 2. The perpendicular derivative of the distribution can be evaluated explicitly in terms of f_p and Λ,

$$
\frac{1}{p_\perp}\frac{\partial f}{\partial p_\perp} = \frac{f_\theta}{p}\left\{\frac{\partial f_p}{\partial p} + f_p\left[\frac{\partial\Lambda}{\partial p}\left(\frac{1}{L}\frac{\partial L}{\partial\Lambda} - \cos^2\theta_p\right)\right.\right.
$$
$$
\left.\left. +\frac{2\Lambda\cos^2\theta_p}{p}\right]\right\},
\tag{6.24}
$$

where

$$
\frac{1}{L}\frac{\partial L}{\partial\Lambda} = \frac{1}{2\Lambda}\left\{1 - L\exp(-\Lambda)\right\}.
\tag{6.25}
$$

This, of course, is identical to Eqn. 2.44, but with $\partial f_\theta/\partial p$ evaluated explicitly.

From our assumption that f_p and Λ are line-averaged quantities, we immediately obtain the perpendicular optical depth by

$$
\tau_l(\omega) = \alpha_l(\omega)s,
\tag{6.26}
$$

191

where s is the length of the plasma column within the viewing chord ($33cm$ in Phase I and $23cm$ in Phase II).

A problem arises in trying to use FPFT generated data for the optical depth calculation since negative α is sometimes obtained at those energies where bumps in the distribution exist. To avoid occurrence of such a situation, f_p in the relevant range is fitted by a Maxwellian and Θ is recomputed using the smoothed f_p and the unsmoothed j_2, since $j_2 \propto \Theta_2 f_p$. The Λ values corresponding to the smoothed f_p are then found from the Θ vs. Λ tables. We believe this to be a sound procedure since the relative size of the error bars to the fluctuations make the latter statistically insignificant.

In Fig. 6.2 we plot, as a function of the resonant electron energy, the optical depths for the X-mode first and the second harmonics calculated from the three distributions of Chapter 5. Dotted lines show the optical depth calculated from the error distributions of the current drive result. These show, as expected, optical depths in the 'grey' to 'thick' regimes for the first harmonic, justifying our initial conjecture about the optical depth at this harmonic.

At the second harmonic, the values are below $\tau_2 \leq 0.18$. The effect of this small but finite τ_2 on the observed spectrum is given by

$$F = \frac{1 - e^{-\tau_2}}{\tau_2}, \tag{6.27}$$

where F is the coefficient modifying the tenuous emissivity. Examples of some values are; for $\tau_2 = 0.25$, $F = 0.88$; for $\tau_2 = 0.15$, $F = 0.93$; and for $\tau_2 = 0.05$, $F = 0.98$. Thus, even taking the worst case of $\tau_2 = 0.25$ which is the case of the extreme error curve for the current drive distribution at $170keV$, the modification is within the calibration uncertainty, and for more plausible cases, practically negligible. Thus, we find that for these Alcator tokamak nonthermal emissions, of which the lower hybrid current drive case represents the most intense spectrum, the use of tenuous assumption for the second harmonic emission is quite justified.

6.3.2 Comparison of Results

The perpendicular temperature inferred from the first harmonic radiation temperature can be calculated by using the prescription of Eqn. 2.54.

In Fig. 6.3, we present plots of the perpendicular temperature as a function of the total energy, assuming pure down-shift of frequency due to the relativistic mass increase. We note here that at these ($\leq 200GHz$) frequencies, as much as a factor of two uncertainty is present in the relative and absolute calibration. The solid lines indicate the inferred perpendicular temperature, $T_\perp$, while the dotted lines show the radiation temperature, T_r, defined as the temperature of the emission intensity assuming it is a blackbody radiation. The inferred perpendicular temperature dependences with energy are strongly correlated with the emission itself, since the optical depth varies little over the energy range. The perpendicular temperatures are increasing with energy steeply, which disagree with our observations from $f(\vec{P})$ that approximately constant $T_\perp$'s are obtained, although a simple minded extrapolation of the results beyond $250keV$ by assuming constant τ_1 will provide eventually downward sloping perpendicular temperatures. Absolute values of the perpendicular temperatures from these plots do pass through the values of $T_\perp$ determined from the higher harmonics, although all these discharges having approximately the same temperatures is inconsistent with our previous observations. The relatively low perpendicular temperature values inferred below $100keV$ may be a consequence of plasma effects discussed in Chapter 4 affecting the measurement. The somewhat lower $T_\perp$ of the ohmic result compared to the others above $200keV$ may indicate that radiation enhancement is taking place for the two lower hybrid cases, where the smaller dump was more succeptable to multiple reflections at these long wavelengths.

We believe that despite the apparent agreement in the magnitude of perpendicular temperatures obtained from the two separate measurements, the disagreement in the trend with energy, and the difference from discharge to discharge strongly suggest that mechanisms such as the plasma effects, the calibration uncertainty or

the low dump effectiveness make the result from the first harmonic highly unreliable at present.

6.4 Comparison of Results with X-Ray Measurements

The measurements from lower hybrid current drive discharges are compared to the results obtained from the angular hard X-ray diagnostic by Texter[44]. Although the two diagnostics were not collecting data simultaneously, results of similar discharges are available.

Angular Hard X-Ray Diagnostic

As briefly mentioned in Section 1.2, another, somewhat more 'established' method of diagnosing nonthermal electron distribution involves the detection of high energy bremsstrahlung photons or 'hard X-rays'[7,9,44]. These hard X-rays are emitted from energetic electrons with known energy spectra and radiation pattern so that measurement of energy spectra at different angles to the magnetic field yields information both on the energy distribution and the anisotropy.

Owing to the fact that an electron of kinetic energy E can emit a photon of energy in the range $0 < E_{h\nu} \leq E$, the discrimination of electrons by their energy is difficult with this measurement. Discrimination of the pitch-angle is accomplished to some degree for high electron and photon energies due to extremely forward peaked emission patterns. These two points are illustrated in Fig. 6.4, where 6.4(a) shows the bremsstrahlung emission spectrum in energy for a $50keV$ electron[85], extending well into low energies below $h\nu = 10keV$. In 6.4(b), The angular emissivity for a $20keV$ photon emitted from the $50keV$ electron is plotted, which shows the asymmetry, with a peak near the direction of the electron motion, $\theta = 0$.

The approach presently used to measure $f(\vec{p})$ from the angular hard X-ray (AHX) data is to fit the measurements obtained at several angles to the magnetic

field at several photon energies, with computed bremsstrahlung emission from a distribution of the form

$$f(\vec{p}) = f_o \exp \left\{ -\frac{p_\perp^2}{2T_{perp}} - \frac{p_\parallel^2}{2T_\parallel} \right\}. \qquad (6.28)$$

This is a gaussian distribution in normalized momenta, whose shape deviates from the fully relativistic Maxwellian for large $p_\perp^2$ and $p_\parallel^2$, i.e., when the assumption $\sqrt{1+p^2} \simeq 1 + p^2/2$ is no longer valid. The parallel temperature, $T_\parallel$ can have two different values, T_f and T_b, in the forward($p_\parallel > 0$) and backward($p_\parallel < 0$) directions. The normalization constant, f_o, is usually not determined from the AHX measurement itself due to uncertainties in the bremsstrahlung cross-sections that arise from their strong dependence on Z_i, the charge of the colliding ions. Instead, in current drive experiments, f_o is determined by requiring that the anisotropy described by $f(\vec{p})$ account for all the RF driven current. A high energy cut-off, E_c, may be used in addition to Eqn. 6.28 for $f(\vec{p})$ specification, so that this formulation represents a three(T_{perp}, T_f, and T_b) or a four(plus E_c) parameter fit to the measurement.

Comparison and Discussion

In a spirit similar to that of Fig. 6.4, the energy(frequency) and angular spectra for perpendicular ECE are plotted in Fig. 6.5 to illustrate the difference in the two diagnostics. In 6.5(a), the discreteness of emission in frequency is indicated, with the finite line widths representative of the broadening mechanisms or the instrumental resolution. In 6.5(b), the relatively broad angular dependences are plotted for j_2^-, j_3^-, and j_2^+; the dependence for $90° \leq \theta \leq 180°$ is a mirror image of the $0° \leq \theta \leq 90°$ plot.

Taking into account the presently available instrumentation and practical limitations of the measurements, the relative strengths of VECE and AHX diagnostics are summarized.

VECE advantages over AHX:

1. Sensitivity to low energy($\leq 100keV$) structure. This is evidenced by the effect that the C-parameter has on the fit to the VECE nonthermal spectrum. Because of the photon energy continuum, low energy photons measured from AHX do not necessarily represent low energy electron information.

2. Faster time resolution ($\sim 15ms$ vs. $> 1s$). Due to the relatively low photon count rate at present, AHX spectra with sufficient S/N can be obtained only by accumulating the data over several plasma discharges. On the other hand, ECE time resolution, with its copious radiation, is limited only by the instrument's frequency scanning time.

3. More detailed $f(\vec{p})$ characterization (provided the harmonic superposition is small). This reflects the ability of the VECE resonance to discriminate in electron energy.

4. Measurement of the absolute density. This is not currently carried out in AHX due to uncertainties in the bremsstrahlung cross-section determination owing to the various ion species present in the plasma.

AHX advantages over VECE:

1. Sensitivity to the forward-backward asymmetry. Because of the radiation pattern for high energy photons by high energy electrons that are sharply peaked, and the angular view made easy by the absence of appreciable wall reflections, the AHX diagnostic has an excellent forward-backward discrimination power.

2. Sensitivity to the high energy($\geq 500keV$) population. The harmonic superposition prevents gaining information on high energy electrons from VECE, whereas for AHX, the energy range is limited only by the count-rate which decreases with energy as the electron population and the bremsstrahlung cross-section decreases.

These comparisons show that the two methods of distribution diagnosis are complementary, with AHX sensitive to greater energy range and anisotropy, while VECE has the merits of being able to diagnose bulk-tail transition regions and the faster time resolution.

The distribution functions obtained from VECE and AHX diagnostics are compared in Table 6.2. The discharges from which the measurements were taken are nominally similar for the two methods, and they coincide with the discharge of Fig. 5.9, so that VECE result is given by f_p and Λ plotted in Fig. 5.12. A major difference does exist in the injected RF power, but the bulk plasma parameters (I_p and $\bar{n}_e$) indicate that the power coupled to the tail is probably not too different. The distribution function parameters obtained from the AHX measurement that specifies the right-hand side of Eqn. 6.28 are $T_{perp} = 100keV$, $T_f = 500keV$, and $T_b = 100keV$ with no cut off assumption. Uncertainties on these temperatures are $\pm20\%$. In order to compare the two results under the same conditions, the distribution properties defined in Section 6.2 are evaluated from the AHX distribution by first converting it into the f_p and Λ description, since a computer software which calculates T_{eff}, $T_{\parallel}$, etc., from the VECE distribution was already available. Little error is introduced in the conversion process since observations indicate that the distribution of Eqn. 6.28 is well represented by the f_p and Λ description.

In order to check that the BESTFIT result is consistent with the X-ray description, this code was applied to the ECE spectrum computed from the AHX distribution of Eqn. 6.28 with the above-mentioned temperatures. The result is $T = 150$, $C = 0$, $A = 2.5$, and $B = -2.0$. These parameters give results for the electron properties that are very close to the AHX values calculated directly and presented in Table 6.2. Thus, any difference in the parameters obtained for VECE and AHX is real, and not an artifact of the different data-processing involved.

The distribution diagnosed from the AHX data has higher values of the three temperatures compared to the VECE result, and the difference is a factor of approximately 1.4 in all cases. Although this constant factor is probably a coincidence,

these differences indicate that the distribution measured by the AHX diagnostic is more energetic. The discrepancy in the tail density fraction is significant but is believed to come primarily from the difference in the definition. In the case of AHX, the photon intensity does not provide an absolute population measurement. Instead, the procedure is to obtain the difference in forward-backward populations, assume they carry all the current, and determine the magnitude from I_p and the assumed tail profile. On the other hand, the tail population from VECE is determined directly according to Eqn. 6.2. In addition, the integral is in the range $50 - 250keV$, and the entire chord averaged quantity is assumed with no profiling effects. Thus, the often peaked tail profiles(gaussian with $0.5 \leq r/a \leq 0.75$ depending on plasma conditions and photon energies[44]) assumed in the X-ray result can probably account for most of the difference observed.

6.5 Transient Phenomena

For the lower hybrid heating case, a total of thirty-seven scans from five discharges, whose density ranged from $\omega_{pe}^2/\Omega^2 = 0.06$ to 0.23 at $B_T = 8T$ and $P_{RF} \simeq 400kW$, were examined for parametric dependences. The results were essentially negative. The range of parameters for these discharge results are $-6 \leq \Lambda \leq -2$, $0.5 \times 10^{17} \leq n_{tail}(m^{-3}) \leq 1.5 \times 10^{17}$, and $20 \leq T_\perp(keV) \leq 40$. The factor of three increase seen on the VECE trace of Fig. 5.2 is believed to be reflective of the increase in the first harmonic intensity brought about by the decrease in the density, as theoretically investigated in Section 2.3 and shown for representative values of density in Fig. 2.11(b). This hypothesis is supported by the fact that the system response curve is most sensitive at low frequencies corresponding to the down-shifted first harmonic emission. That the density-effect-corrected emission is approximately constant throughout such discharges is verified by the observation of negligible trend in n_{tail} with the bulk density.

198

As noted earlier in Chapter 5, most current drive discharges have nonthermal tail maturing times of less than one VECE scan time($15ms$) so that temporal evolution studies cannot be performed. The 'matured' tail may increase or decrease slightly in density, but this is often all that is observed. In a few of the discharges however, some distinct tail evolution is observed. An example of a discharge with such a phenomenon is shown in Fig. 6.6. This discharge represents a current ramp-up experiment with the RF power, as seen by the upward sloping I_p during the pulse. The VECE amplitude evolves very slowly compared to other LHCD discharges. The scans marked A, B, and C are Fourier analyzed and the frequency spectra are shown in Fig. 6.7. These three spectra show, in addition to successive increases in the overall intensity, increasing I_3/I_2 ratios. The electron distribution parameters analyzed by BESTFIT from these and one more spectrum are plotted in Fig. 6.8, as a function of time.

In Fig. 6.8(a), we note that $T_\parallel$ shows a sharp decrease between A and B, then slowly increases the rest of the pulse, while $T_\perp$ is steadily increasing with time. The C-parameter remains approximately constant, indicating the maintenance of a steady 'transition region'. T_{eff} undergoes a small change, but for anisotropic distributions such as these, this quantity has little physical significance. In Fig. 6.8(b), we observe an increase in the density by approximately a factor of two, as expected from the intensity increase observed in the spectra plot.

What appears to be happening in this discharge in a relatively long time scale of a few VECE scans is that initially, a very anisotropic tail is created. Low $T_\perp$ at this stage indicates the dominance of parallel momentum transfer by the waves over the pitch-angle scattering. As the density of the tail increases however(point B and beyond), the parallel diffusion is checked, and relative increase in the pitch-angle scattering increases the perpendicular temperature.

6.6 Summary

In this chapter, discussions concerning the electron distributions analyzed from the nonthermal VECE measurements were presented.

To put the VECE measured distributions in perspective, the density and temperatures were defined in exact and analytical forms for these distributions. Comparison of the three distributions diagnosed in Chapter 5 showed that the lower hybrid current drive distribution has the highest perpendicular temperature while the low density ohmic discharge distribution has the highest parallel temperature. The approximate formula for the perpendicular temperature predicts values in good agreement with computed results.

A brief summary of theoretical expectations of lower hybrid RF distributions showed that the parallel enhancement of these measured distributions is predicted, as is the dependence of $T_\perp$ on the launched wave spectrum. Low energy transition region represented by the C-parameter in our results is absent from theory, while the harmonic superposition prevents us from making comparisons in the higher energies where theory predicts enhancement of the perpendicular temperature.

Calculations of the cyclotron absorption coefficient, carried out in Section 6.3 based on the diagnosed distributions, justified the assumptions of the optically thin second harmonic emission and the optically thick or 'grey' first harmonic emission in the X-mode. Based on this result, the perpendicular temperature inferred from the first harmonic radiation temperature and the optical depth was calculated. The trend in energy of this perpendicular temperature was dissimilar to the result obtained directly from the distribution itself, although the magnitudes were in general agreement. Indications, including low $T_\perp$ at low energies, and a lower $T_\perp$ for the ohmic result, suggest that the thermal plasma effects and multiple reflections may be the cause of this result.

The VECE result during current drive was compared with the result obtained by the angular hard X-ray diagnostic, which in many ways complement the VECE

diagnostic. A consistent comparison showed that despite nominally similar plasma discharge conditions, the distribution present during the AHX measurement was somewhat more energetic. The difference in the quoted values of the tail density is believed to be reconcilable with proper account for the profile effects.

Because of the short frequency scanning time compared to the length of the RF pulse, the evolution of the nonthermal distribution, where present, can be measured by the VECE diagnostic. While most nonthermal VECE spectra reached steady-state within one scan time, some discharges during lower hybrid current ramp-up experiments displayed a transient phenomenon characterized by initially large then decreasing $T_\parallel$, and increasing $T_\perp$ and n_{tail}. This observation appears to be consistent with the model where the competing effects of parallel momentum transfer by the wave and the pitch-angle scattering affect the directional temperatures.
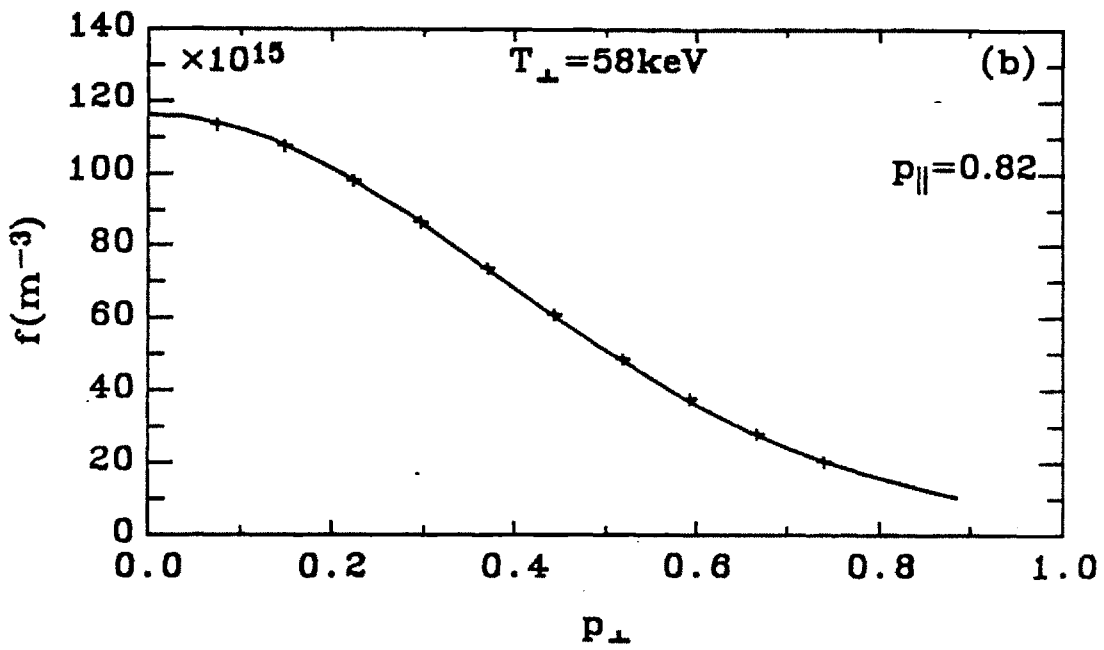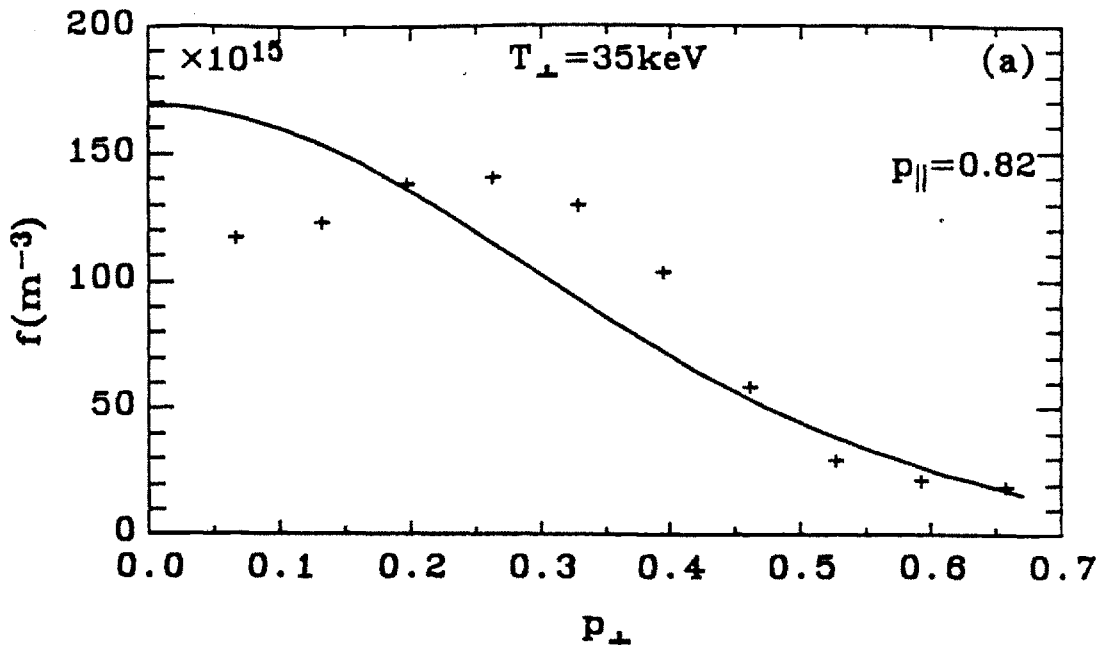
Figure 6.1:
Perpendicular temperatures fitted at constant $p_\parallel$ to the VECE distribution of (a)Fig. 5.8 and (b)Fig. 5.13.
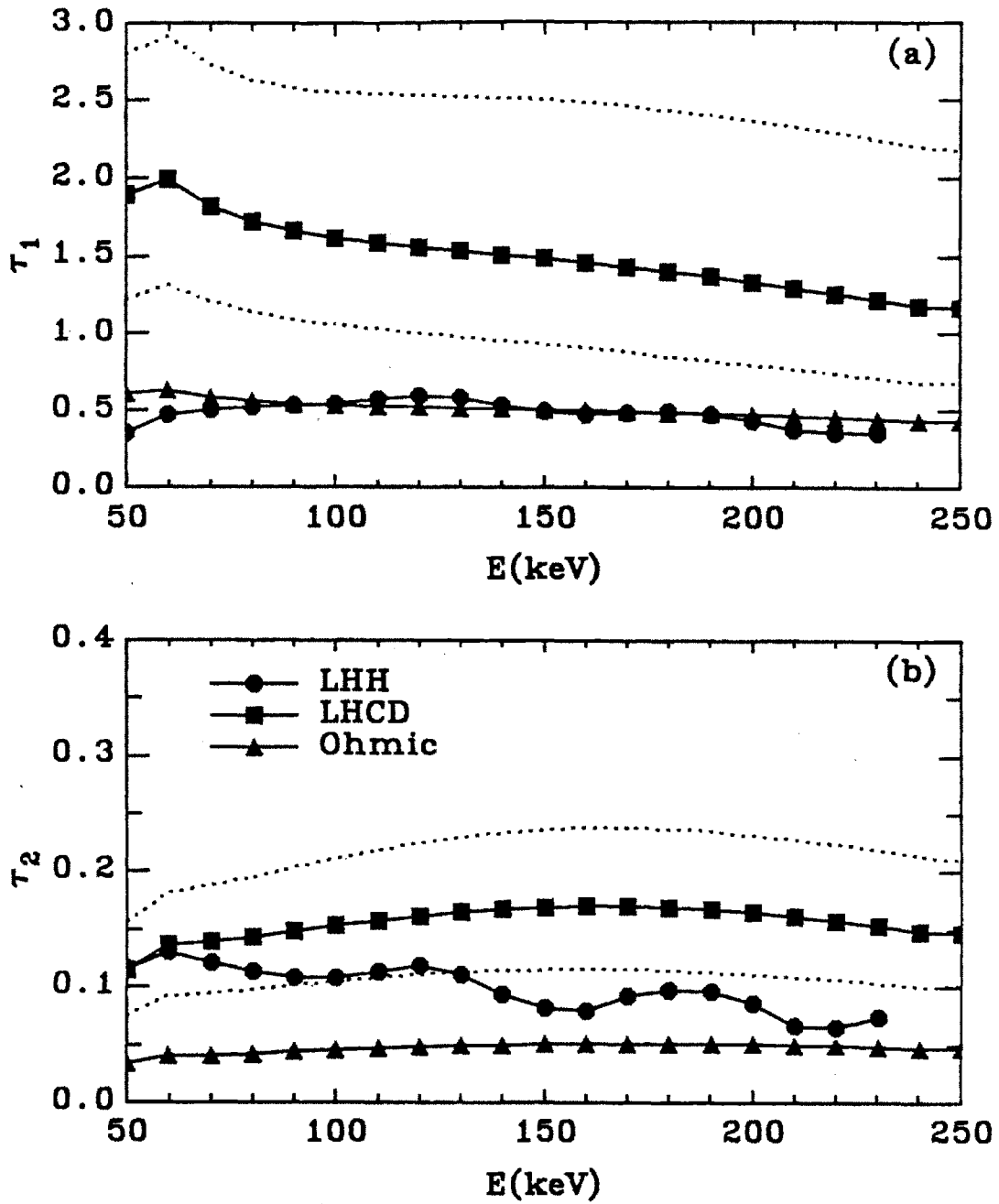
Figure 6.2:
Optical depths calculated from diagnosed $f(\vec{p})$ plotted versus energy for (a) the first harmonic and (b) the second harmonic.
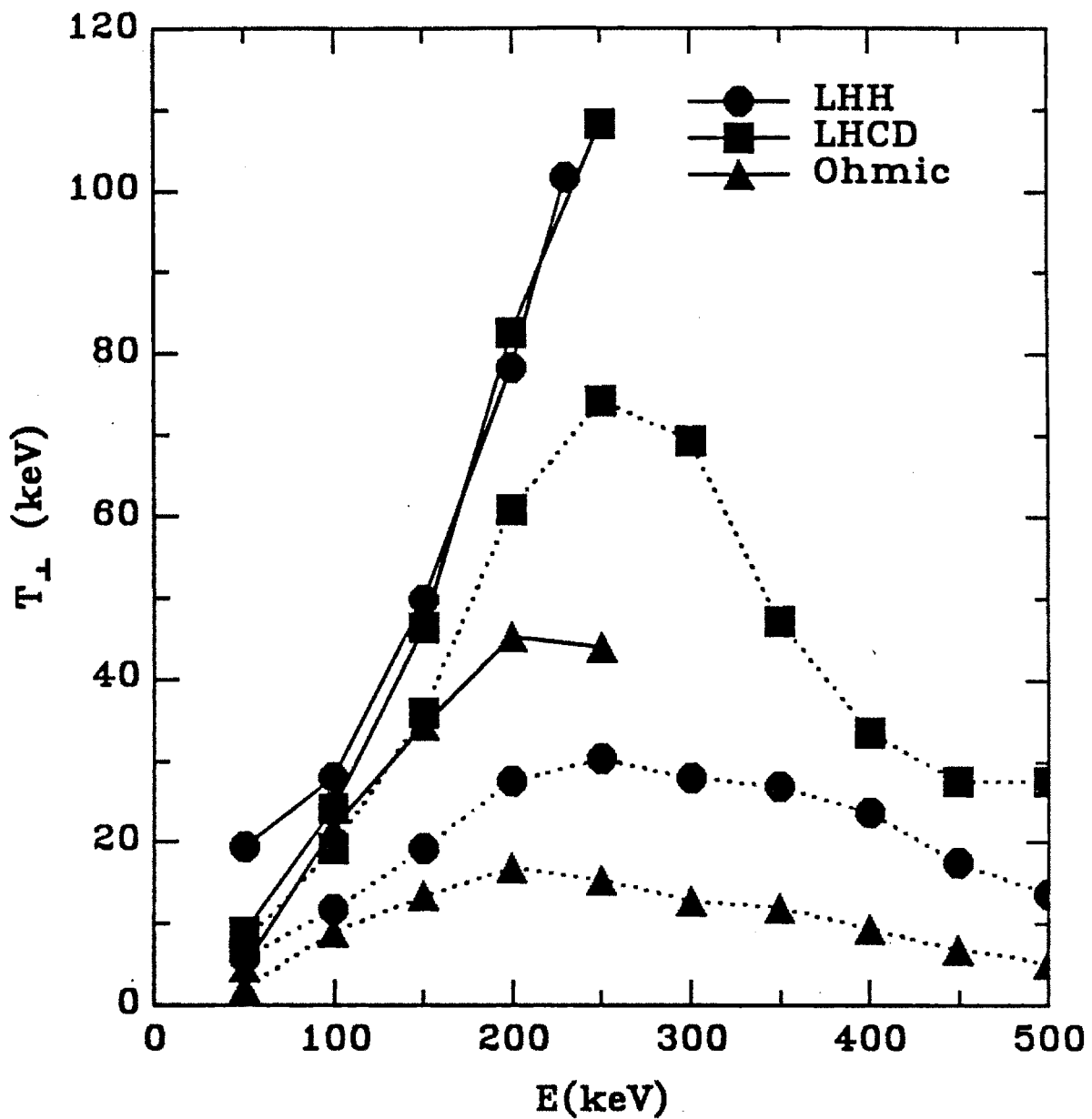
Figure 6.3:
Perpendicular temperature obtained from the first harmonic emission and τ_1 computed from $f(\vec{p})$ for the three discharges. Dotted lines indicate the radiation temperature of the first harmonic spectra.
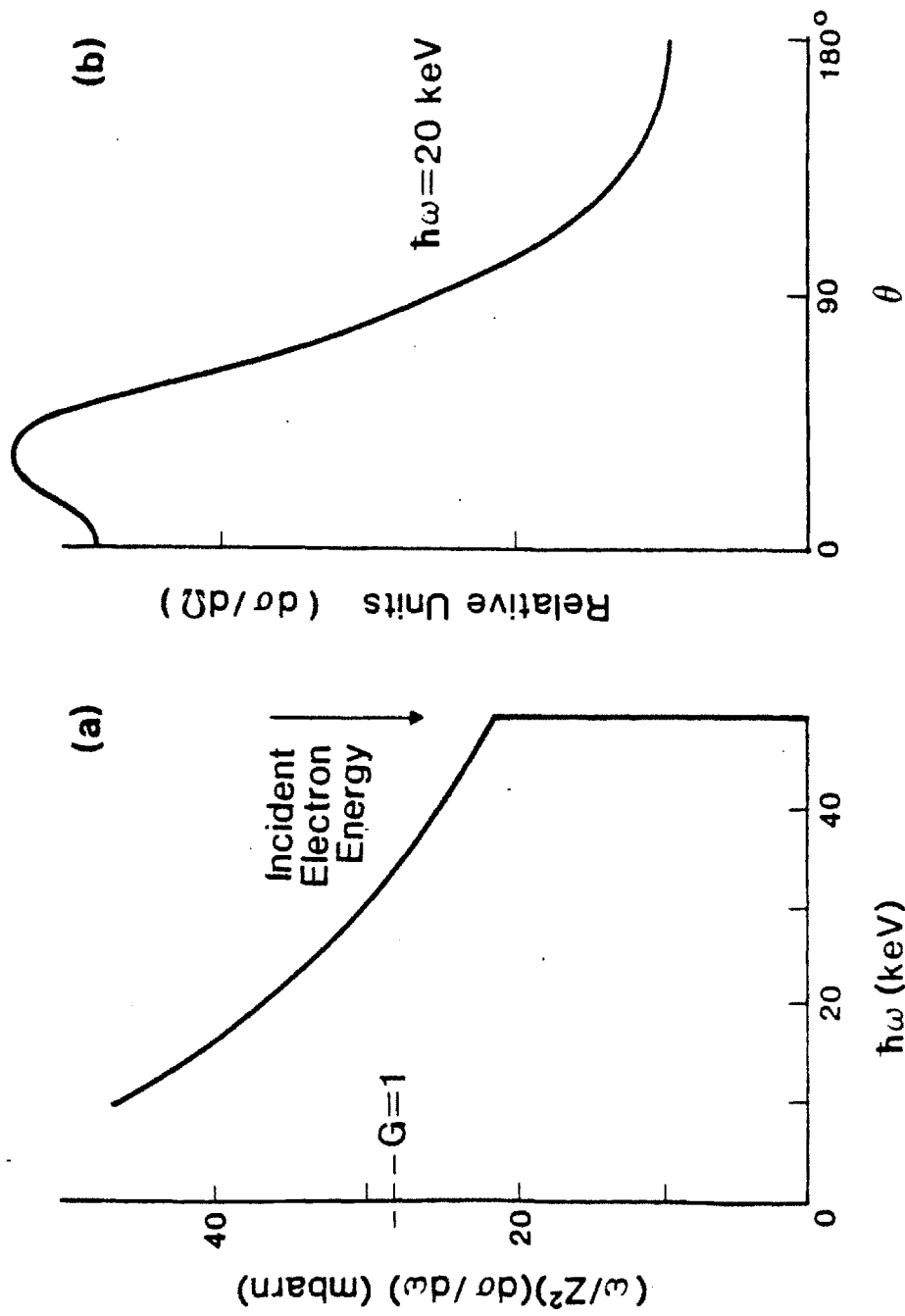
Figure 6.4:
The single-particle bremsstrahlung emission spectral characteristics for a $50keV$ electron. (a) Angle averaged energy spectrum. (b) Angular distribution at $h\nu = 20keV$.
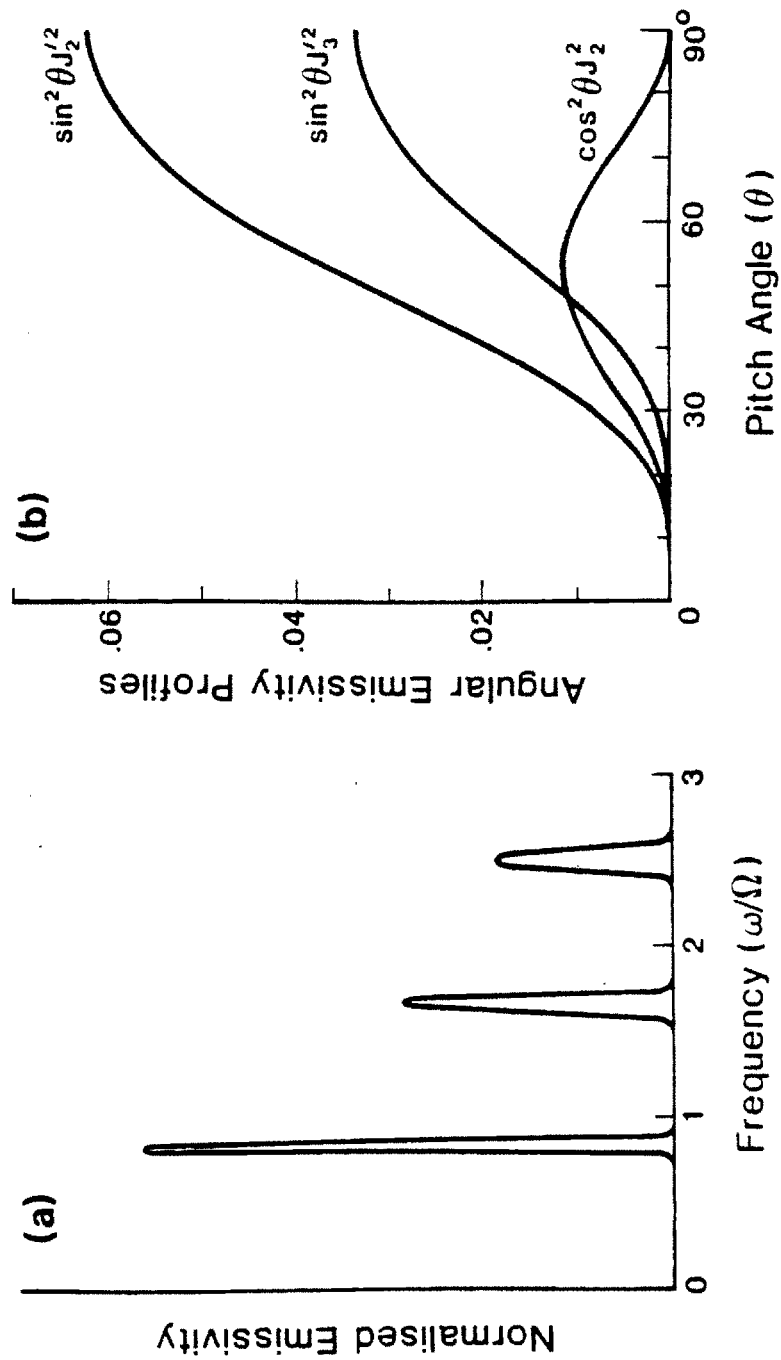
Figure 6.5:

The single-particle cyclotron emission spectral characteristics. (a) Frequency spectrum for a $\gamma = 1.2$ electron. (b) Angular distribution for a $\gamma = 1.7$ electron; $\sin^2 \theta J_2'^2 \propto j_2^-$, $\sin^2 \theta J_3'^2 \propto j_3^-$, and $\cos^2 \theta J_2^2 \propto j_2^+$.
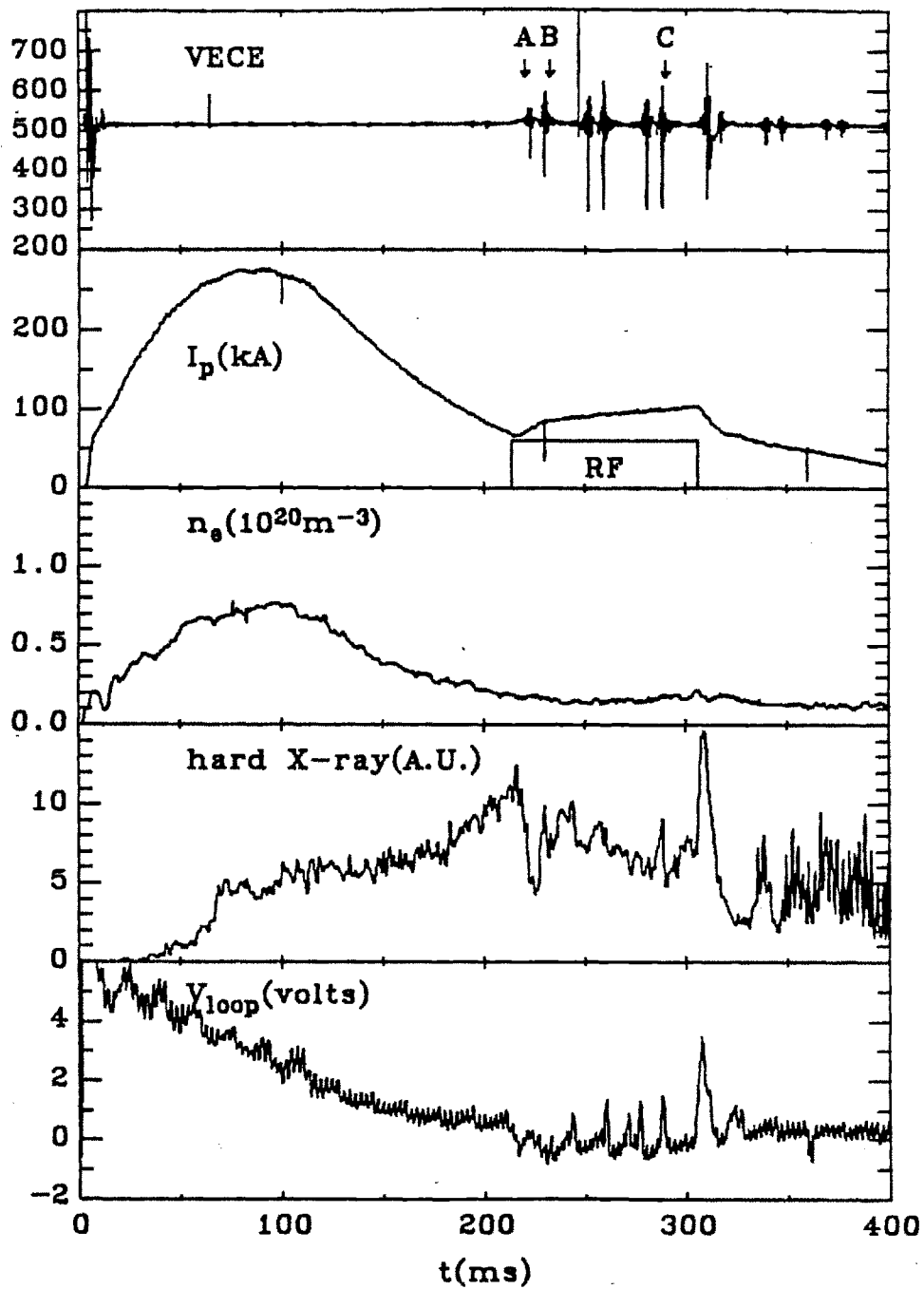
Figure 6.6:
Plasma discharge trace for the transient phenomena analysis. $B_T = 8T$, $P_{RF} = 400kW$.
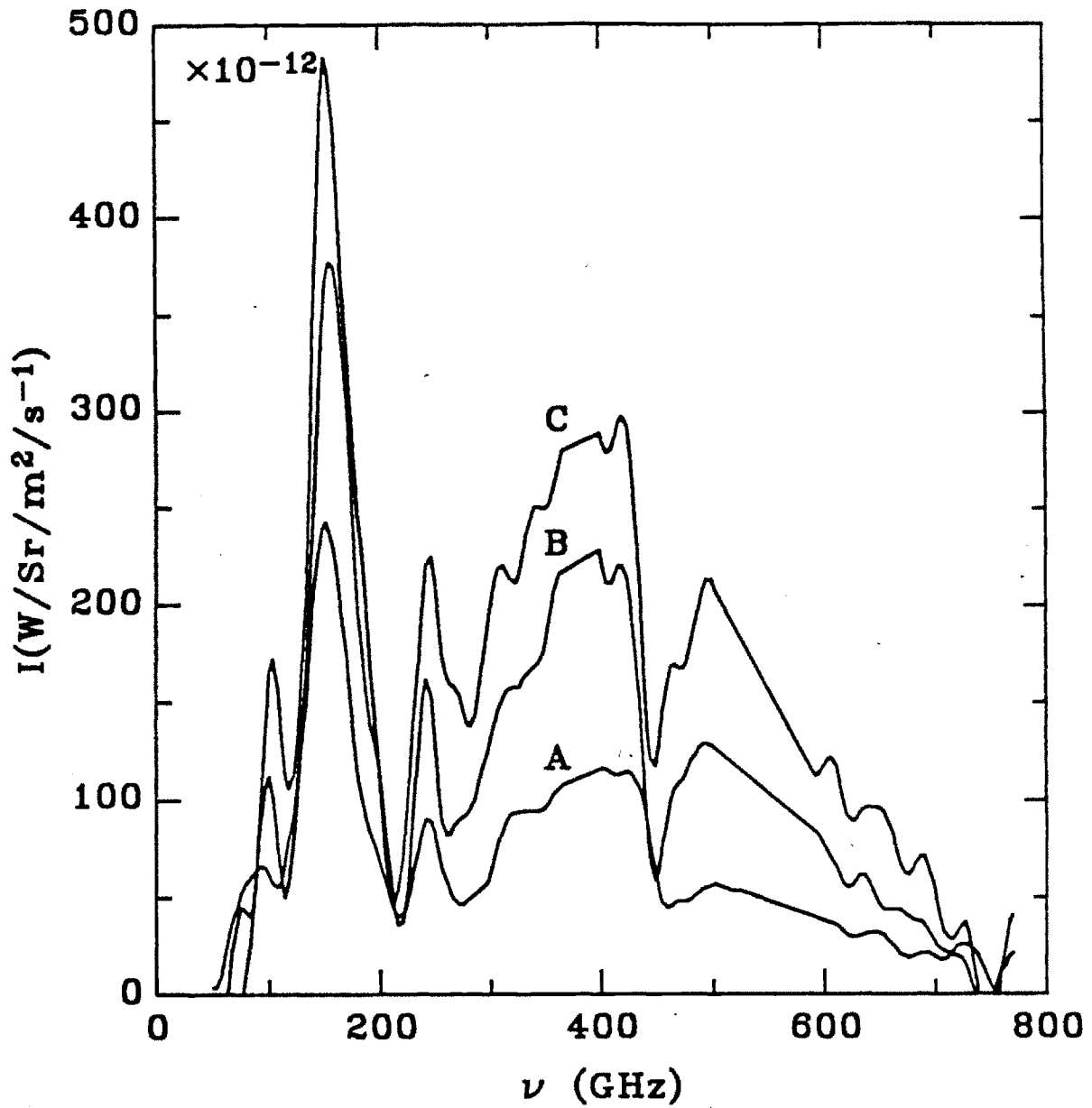
Figure 6.7:
Evolution of VECE spectra in the discharge of Fig. 6.6. $\Omega = 220 GHz$.
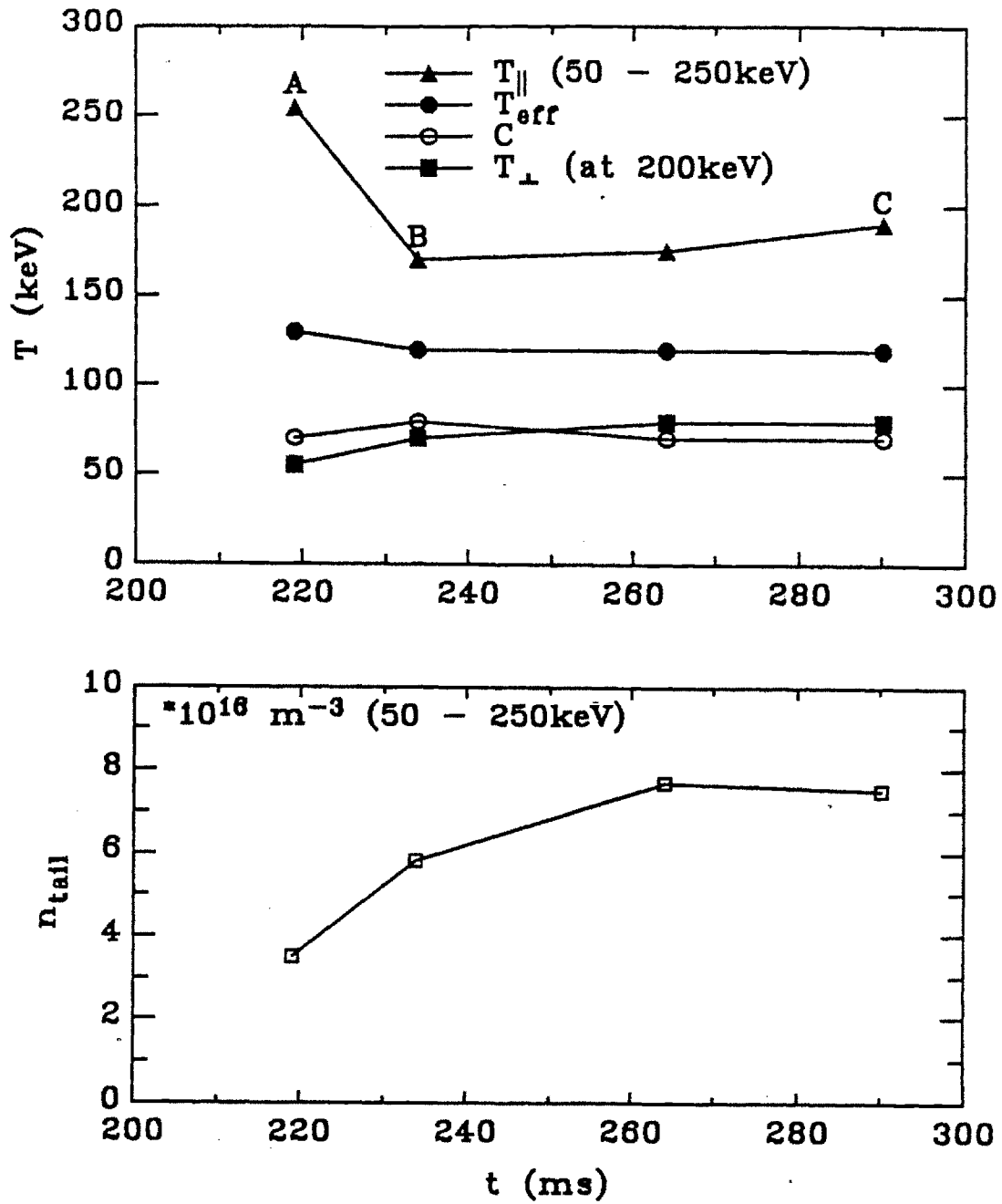
Figure 6.8:

Evolution of distribution function parameters in the discharge of Fig. 6.6. (a) Temperatures. (b) Tail density.

Table 6.1:
Comparison of the three distributions analyzed in Chapter 5.

$$B_T = 8T$$

$$(50 \leq E(keV) \leq 250)$$

	LHH $(\Delta\phi = 180°)$	LHCD $(\Delta\phi = 90°)$	Ohmic
$P_{RF}(kW)$	400	800	—
$I_p(kA)$	180	160	80
$\bar{n}_e(\times 10^{20} m^{-3})$	0.7	0.4	0.3
$T_{eff}(keV)$	80 †	$110 \, ^{+25}_{-20}$	$125 \, ^{+0}_{-40}$
$T_{\parallel}(keV)$	180 †	$200 \, ^{+150}_{-100}$	$290 \, ^{+0}_{-170}$
$T_{\perp}(keV)$	$30 \, ^{+8}_{-8}$	$60 \, ^{+15}_{-15}$	$50 \, ^{+20}_{-20}$
$\bar{n}_{tail}(\times 10^{20} m^{-3})$	$9.5 \, ^{+4.8}_{-4.8} \times 10^{-4}$	$1.2 \, ^{+0.8}_{-0.4} \times 10^{-3}$	$6.1 \, ^{+9.5}_{-2.5} \times 10^{-4}$
$\bar{n}_{tail}/\bar{n}_e$	1.4×10^{-3}	3×10^{-3}	2×10^{-3}

† Uncertainty data not available from FPFT.

Table 6.2:
Comparison of vertical ECE and angular hard X-ray results.

LHCD($\Delta \phi = 90°$)

$\overline{n}_e = 0.3 - 0.4 \times 10^{20} m^{-3}, 130 \leq I_p(kA) \leq 160, B_T = 8T$

	VECE	AHX[44]
$P_{RF}(kW)$	800	300
$T_{eff}(keV)$	110	160
$T_{\parallel}$	200	280
$T_{\perp}(keV)$	60	85
n_{tail}/n_e	3×10^{-3}(average) $(50 - 250keV)$	7×10^{-3}†(peak)

† determined from forward-backward asymmetry and I_p.

Chapter 7

SUMMARY AND CONCLUSIONS

7.1 Summary and Conclusions

Nonthermal electron velocity distributions occur in magnetically confined toroidal plasmas due to a variety of conditions such as the lower hybrid heating, current drive, and the low density ohmic discharge. A group of diagnostics using the electron cyclotron emission(ECE) are suited for the measurement of these distributions, one and the most interesting variation to date of which is investigated in this thesis.

Although previous attempts at measuring the electron distribution, $f(\vec{p})$, using ECE have been successful, the presence of various spectral broadening mechanisms and the difficulty in isolating the desired mechanism, namely the frequency downshift due to the relativistic mass increase, have prevented fullest utilization of the potential of ECE as the $f(\vec{p})$ diagnostic.

The approach followed in this thesis is to negate the spectral broadening due to the spatial magnetic field gradient and the Doppler effects by constructing a narrow view through the center of a tokamak plasma, terminated at a highly absorbing submillimeter wave dump. In this way, only the perpendicular emission from a region of approximately constant magnetic field is detected, and the relativistic mass

broadening will discriminate the electrons according to their total energy. The first few cyclotron harmonics are measured, since this choice minimizes the phenomenon of harmonic superposition which can scramble the one-to-one correspondence between the frequency and the energy. The electron population at a specific energy is inferred from the emission at that frequency which corresponds to the energy, while the 'anisotropy' of the distribution in momentum or velocity space is estimated from cyclotron harmonic or polarization ratios. The measurement was performed on the Alcator C tokamak at the Plasma Fusion Center of the Massachusetts Institute of Technology in the 1984 − 1986 period.

The theoretical development regarding this work consisted of taking, as the starting point, a generalized cyclotron emissivity formula which takes into account the finite density effects, and developing that into forms directly relevant to the measured quantities. To this end, an electron distribution description unique to this work was developed in the form characterized by $f_p(p)$, the line-averaged phase space density of electrons at a momentum, p, and $f_\theta(p, \Lambda)$, which is the pitch-angle distribution at p. The quantity Λ is the 'anisotropy factor' whose value is negative for a parallel enhanced distribution and positive for a perpendicularly enhanced distribution.

Further, that part of the emissivity which includes the pitch-angle dependence is grouped into a newly defined quantity, $\Theta(p, \Lambda)$ convenient for normalized numerical analysis. Computer generated plots of Θ versus Λ and harmonic and polarization ratios of the emission versus Λ illustrate how the measured intensity ratios can be directly converted to Λ, hence defining the pitch-angle distribution. Analytical approximations in the limit of $|\Lambda| \gg 1$ provide useful physical insight to the procedure. Investigations of the cyclotron absorption process, the finite density effects and implementation issues completed the theoretical development.

Major components of the Vertical Viewing Electron Cyclotron Emission(VECE) diagnostic consists of the Michelson interferometer and the InSb detector; the viewing dump; relaying and focussing optics; and data acquisition hardware and software. While the Michelson system including the data acquisition environment is fairly standard, the design and performance of the vacuum-compatible viewing dumps, the diffraction analysis carried out on the optical system, and the frequency response calibration measurement deserve elaboration.

Four viewing dumps of different materials and sizes were fabricated, based on a simple design principle and with tight spatial constraints and the need for vacuum compatibility. These dumps made of Pyrex, Macor, and alumina all exhibited high performance upon their measurement. The absorption of Pyrex and Macor of $\geq 99\%$ was deemed satisfactory for use in the VECE diagnostic system.

Due to the viewing spot size which is on the order of the dump dimension for the earlier measurements, the full Fresnel diffraction analysis was conducted on the major optical components to quantify the dump-captured fraction of the view. The numerical analysis carried out for different frequencies and diffraction mechanisms showed over 95% coverage by the smaller dump and more with the larger dump, under the assumption of vacuum propagation.

Spectral response of the system was calibrated using a mercury-arc lamp, whose intensity is below the typical plasma intensity by three orders of magnitude. Thus, even the patiently measured system response curve, obtained by averaging a large number of frequency scans, has an accuracy only of about $\pm 15\%$, which has consequences on the uncertainties introduced into the measured results.

Thermal and nonthermal spectra measured by the VECE diagnostic were examined prior to the distribution function diagnosis. This showed that the earlier dump with its small size was in actuality effective in removing 90% of the multiply reflected radiation, while the larger dump used in the later measurements appears to work somewhat more efficiently. The polarization ratios obtained in the later

measurements with the larger dump showed depolarization of about 5%, which can only be accounted for by system imperfections. In spite of these observations, the nonthermal spectra compared with and without the dump showed marked difference illuminating the dump effectiveness, and no signature of multiple reflections could be observed. Hence in considering the distribution function diagnosis, it was decided to ignore the 10% multiple reflection observed by the system using thermal spectra, but it was decided to correct the weaker(O-mode) polarization by the 5% depolarization inherent in the system.

The actual diagnosis of the distribution function took on different forms, depending on the degree of harmonic superposition observed and the availability of more than one emissivity ratio. The second and the third harmonics were utilized, while the first harmonic was deemed unsuitable for the analysis because of uncertainties in the optical depth and the response calibration in this frequency range.

For lower hybrid heating discharge measurements, where the nonthermal spectra showed only small signs of harmonic superposition, a computer code called FPFT was used to come up with the nonthermal electron distribution that exactly matches the frequency spectrum. The resulting distribution indicated Λ in the range $-6 \sim -2$, showing marked parallel enhancement.

For lower hybrid current drive discharge measurements, the nonthermal spectra showed signs of severe harmonic superposition, which invalidated the application of FPFT. Thus, a distribution function defined by five parameters, T, C, A, and B, whose ECE approximately fits the measured spectrum was recovered by the computer code BESTFIT. As anticipated, the harmonic superposition was severe and the resulting small and negative Λ values implied a parallel but a much more isotropic distribution compared to the heating result.

Low density ohmic discharge measurements produced nonthermal spectra similar to the current drive case, i.e., with signs of severe harmonic superposition. For this measurement however, both the harmonic and the polarization ratios were

available, and individual fits to these ratios 'bracketed' the distribution, with the approximately overlapping error regions suggesting the best estimate of the distribution to be in this regime. It was shown that the discrepancy in the results from the two individual fits, although not prohibitive because estimated errors overlap, may be explained by the omission of a higher energy component to the distribution which the VECE diagnostic has no capability to predict.

Since the distributions diagnosed are presented in a form unique to this diagnostic result, exact and approximate prescriptions were set forth to characterize these distributions by more conventional parameters; the density and effective and directional temperatures. The comparison of the distributions from the three classes of discharges show the current drive distribution to have the largest $T_\perp$, the perpendicular temperature, and the low density ohmic discharge distribution to have the largest $T_\parallel$, the parallel temperature. These values for the density and temperatures are in the range $6.1 \leq \bar{n}_{tail}(10^{16}m^{-3}) \leq 12$, $80 \leq T_{eff}(keV) \leq 125$, $180 \leq T_\parallel(keV) \leq 290$, and $30 \leq T_\perp(keV) \leq 60$. Qualitative comparison of the lower hybrid discharge results with existing theoretical and computational works shows good agreement in the areas of parallel enhancement and the perpendicular temperature dependence with the wave parameters.

The first harmonic emission was found to be optically thick or 'grey' as conjectured, based on the calculation of the optical depth from the diagnosed distribution. The perpendicular temperature inferred from the first harmonic radiation temperature however showed little agreement in trend with that calculated directly from $f(\vec{p})$, although the general range of the values was correct. This discrepancy in trend is believed to be due to the effects of thermal plasma layers and the system inefficiency in removing multiple reflections at this frequency.

The result of VECE diagnosis for the current drive discharge was compared with the result of the angular hard X-ray(AHX) diagnostic. The two diagnostics have many complementary characteristics. Consistent analysis of results showed

somewhat higher temperature predictions by the AHX diagnostic despite the data from nominally similar discharges. Finally, inspection of time varying phenomena showed the capability of the VECE diagnostic in analyzing tail evolutions.

In conclusion, the original contributions of this thesis are the following:

1. Development of an electron cyclotron emission theory with direct relevance to the diagnosis of arbitrary nonthermal electron distributions. A description of the distribution in which the parameters are obtained directly from the measured quantity are formulated.

2. Design, fabrication, and performance tests of compact, vacuum-compatible submillimeter viewing dumps, with measured absorptivities in excess of 99%.

3. Measurement of thermal and nonthermal emission from an isolated vertical chord in a tokamak plasma, in which significant reduction of the effects of wall reflections are observed.

4. Development of methods and computer codes that analyze electron distribution functions from nonthermal VECE data with account for harmonic superpositions.

5. Diagnosis of electron distributions from the nonthermal VECE spectra from lower hybrid heating, current drive, and low density ohmic discharges in the Alcator C tokamak.

7.2   Recommendations for Future Work

Recommendations for future efforts include both improvements to the present result and further topics of investigation.

The first improvement is the reduction of uncertainty through the generation of a more confident calibration curve. This can be realized by the use of a more intense

217

blackbody source, roof-top mirrors in the Michelson interferometer, and extended time commitment. In conjunction with this matter, an experimental set-up in which calibration can be performed on site is highly desirable. Highly reliable wider frequency calibration will realize the analysis of fine structures of the spectra, as well as increase confidence on the first harmonic interpretation. The second improvement requires the removal of atmospheric water vapor absorption lines which is a very hard problem to solve in practice. For future measurements, use of an evacuated beam-line is highly recommended.

The characterization of optical depth in the vertical view is an as yet unresolved problem. The effect of wave-particle interactions on wave propagation is extremely complicated and is a formidable topic by itself.

Finally, the vertical viewing electron cyclotron diagnostic with an improved calibration will be a powerful instrument for diagnosing nonthermal plasmas. A plasma discharge of particular interest is the electron cyclotron resonance heated discharge, in both tokamaks and mirrors.

Appendix A

FRESNEL DIFFRACTION AND PARALLEL-PLATE WAVEGUIDE PROPAGATION

A.1 Circular Aperture Fresnel Diffraction

Here, a concise summary of the problem of three dimensional light distribution near a focus is given. For a more complete treatment, consult Born and Wolf [86].

Consider a spherical, monochromatic wave emerging from a circular aperture and converging towards the axial focal point, O, as shown in Fig. A.1(a). Provided the radius of curvature of the wave front, f_c, the aperture diameter, a, and the wavelength, λ, are such that

$$f_c >> a >> \lambda, \tag{A.1}$$

the amplitude, U at any point P is given by

$$U(P) = -\frac{iAe^{-ikf_c}}{\lambda f_c} \int \int_W \frac{e^{iks}}{s} dS, \tag{A.2}$$

where standard notations are used and integral is over the entire aperture. Here, the inclination over the wavefront has been neglected. Defining normalized variables,

$$u = \frac{2\pi}{\lambda} \left(\frac{a}{f_c} \right)^2 z \tag{A.3}$$

$$v = \frac{2\pi}{\lambda}\left(\frac{a}{f_c}\right)\sqrt{x^2 + y^2}, \tag{A.4}$$

and transforming the integration from dS to $d\Omega$, we obtain, noting the azimuthal symmetry,

$$U(P) = -\frac{2\pi i a^2 A}{\lambda f^2}e^{i(\frac{f}{a})^2 u}\int_0^1 J_0(v\rho)e^{-\frac{1}{2}iu\rho^2}\rho d\rho, \tag{A.5}$$

where ρ is the normalized radius of the aperture, and J_o is the Bessel function.

In order to evaluate the integral, it is separated into the real and imaginary parts,

$$2\int_0^1 J_0(v\rho)e^{-\frac{1}{2}iu\rho^2}\rho d\rho = C(u,v) - iS(u,v). \tag{A.6}$$

The quantities, $C(u,v)$ and $S(u,v)$ can be expressed in terms of Lommel functions, defined as

$$U_n(u,v) = \Sigma_{s=0}^\infty(-1)^s\left(\frac{u}{v}\right)^{n+2s}J_{n+2s}(v), \tag{A.7}$$

$$V_n(u,v) = \Sigma_{s=0}^\infty(-1)^s\left(\frac{v}{u}\right)^{n+2s}J_{n+2s}(v). \tag{A.8}$$

$U(V)$ is used when $|u/v| < 1 (|u/v| > 1)$. Special cases of $u = 0, v = 0,$ and $|u/v| = 1$ will not be discussed here, although straightforward evaluation of limits will provide the results[86]. It is revealing to note that when $|u/v| < 1$, the point of observation lies in the geometrical shadow, while when $|u/v| > 1$, the point of observation lies in the illuminated region. Evaluating Eqn. A.6, we get, for $|u/v| < 1$,

$$C(u,v) = \frac{\cos\frac{1}{2}u}{\frac{1}{2}u}U_1(u,v) + \frac{\sin\frac{1}{2}u}{\frac{1}{2}u}U_2(u,v), \tag{A.9}$$

$$S(u,v) = \frac{\sin\frac{1}{2}u}{\frac{1}{2}u}U_1(u,v) - \frac{\cos\frac{1}{2}u}{\frac{1}{2}u}U_2(u,v). \tag{A.10}$$

For $|u/v| > 1$,

$$C(u,v) = \frac{2}{u}\sin\frac{v^2}{2u} + \frac{\sin\frac{1}{2}u}{\frac{1}{2}u}V_0(u,v) - \frac{\cos\frac{1}{2}u}{\frac{1}{2}u}V_1(u,v), \tag{A.11}$$

220

$$S(u,v) = \frac{2}{u}\cos\frac{v^2}{2u} - \frac{\cos\frac{1}{2}u}{\frac{1}{2}u}V_0(u,v) - \frac{\sin\frac{1}{2}u}{\frac{1}{2}u}V_1(u,v). \qquad (A.12)$$

Intensity distribution, $I(P) = |U(P)|^2$, is readily given by

$$I(u,v) = \left(\frac{2}{u}\right)^2 \left[U_1^2(u,v) + U_2^2(u,v)\right] I_0, \qquad (A.13)$$

for $|u/v| < 1$ and the form

$$I(u,v) = \left(\frac{2}{u}\right)^2 \left[1 + V_0^2(u,v) + V_1^2(u,v) - 2V_0(u,v)\cos\left\{\frac{1}{2}\left(u + \frac{v^2}{u}\right)\right\}\right.$$
$$\left. - 2V_1(u,v)\sin\left\{\frac{1}{2}\left(u + \frac{v^2}{u}\right)\right\}\right] I_0 \qquad (A.14)$$

is convenient for $|u/v| > 1$. I_0 is the intensity at the geometrical focus, $u = v = 0$.

A.2 Long Slit Fresnel Diffraction

The Fresnel diffraction from a long slit is treated to second order. Fig. A.1(b) shows the geometry and the notation. The distance between the observation point, P, and a source point at the slit, x', is given by

$$\begin{aligned}
r &= \sqrt{(x - x')^2 + z^2} \\
&= \sqrt{x^2 + x'^2 - 2xx' + z^2} \\
&= \sqrt{R^2 + x'^2 - 2xx'} \\
&= R\sqrt{1 + \frac{x'^2}{R^2} - \frac{2xx'}{R^2}}.
\end{aligned} \qquad (A.15)$$

To a good approximation, the last expression can be expanded to give

$$r \simeq R + \frac{x'^2}{2R} - \frac{xx'}{R}. \qquad (A.16)$$

Substituting this expression for r in the Huygens-Fresnel principle equation [67], we obtain

$$E(x) = \frac{ik}{2\pi}e^{-ikR}\int_{-D/2}^{D/2} A(x')\frac{e^{-ikx'^2/R+ikxx'/R}}{r}L\,dx' \qquad (A.17)$$

221

where the time dependence was neglected and $A(x')$ is the wave amplitude distribution across the slit.

The intensity distribution is then given by

$$I(x) = I_0(C(x)^2 + S(x)^2), \tag{A.18}$$

where $I_0 = k^2 L^2 / 4\pi^2$ and

$$C(x) = \int_{-D/2}^{D/2} A(x') \cos\left\{-kR - \frac{kx'}{2R} + \frac{kxx'}{R}\right\} dx', \tag{A.19}$$

$$S(x) = \int_{-D/2}^{D/2} A(x') \sin\left\{-kR - \frac{kx'}{2R} + \frac{kxx'}{R}\right\} dx'. \tag{A.20}$$

In the limit that $x' << x$, this reduces to the familiar Fraunhofer diffraction result[67].

A.3 Parallel-Plate Waveguide Propagation

Consider a pair of conducting plates constituting a parallel waveguide. The boundary conditions for the wave amplitude distribution across the waveguide entrance are

$$\left(\frac{\partial E_n}{\partial n}\right)_{wall} = 0 \quad \text{and} \quad (E_t)_{wall} = 0. \tag{A.21}$$

Thus, any waveform propagating into the waveguide that does not immediately satisfy these conditions couple to a number of modes that do.

Assuming that the arbitrary input wave is symmetric about the midplane, it can be expressed by a Fourier cosine series,

$$Y(x) = \sum_{n=0}^{\infty} A_n \cos\left(\frac{n\pi x}{D}\right), \tag{A.22}$$

where $Y(x)$ is the input wave amplitude distribution across the waveguide mouth, $-D/2 < x < D/2$. Thus, finding A_n identifies the propagating modes and their

amplitudes. We obtain the coefficients, A_n, by integrating both sides of Eqn. A.22 by the expression, $2 \int_0^{D/2} \cos\{m\pi x/D\} dx$ to get

$$2 \int_0^{D/2} Y(x) \cos\left(\frac{m\pi x}{D}\right) dx = \sum_{n=1}^{\infty} 2 \int_0^{D/2} A_n \cos\left(\frac{n\pi x}{D}\right) \cos\left(\frac{m\pi x}{D}\right) dx$$

$$= 2 \int_0^{D/2} A_m \cos^2\left(\frac{m\pi x}{D}\right) dx \qquad (A.23)$$

where orthogonality[87] was used in the second equality. The left hand side can be evaluated to provide the final expression for A_m,

$$A_m = \frac{4}{D} \int_0^{D/2} Y(x) \cos\left(\frac{m\pi x}{D}\right) dx. \qquad (A.24)$$

(a)

(b)

Figure A.1:
Circular aperture diffraction geometry(a) and long slit diffraction geometry(b).

Appendix B

LIST OF PUBLICATIONS FROM THIS WORK

As of August 1986

1. K. Kato and I.H. Hutchinson. *Design and Performance of Compact Submillimeter Beam Dumps.* PFC/RR-84-11, MIT Report, 1984.

2. K. Kato and I.H. Hutchinson. Vertical Viewing Electron Cyclotron Emission Diagnosis of Non-Thermal Electron Distributions. Bulletin of the American Physical Society, 29:1223, 1984.

3. I.H. Hutchinson and K. Kato. *Diagnosis of Mildly Relativistic Electron Distributions by Cyclotron Emission.* PFC/JA-85-15, MIT Report, 1985. Nuclear Fusion, 26:179, 1986.

4. K. Kato and I.H. Hutchinson. Performance Analysis of the Vertical Viewing ECE Diagnostic for Non-Thermal Electron Distribution Measurement. In *IEEE International Conference on Plasma Science, Catalogue No. 85 CH 2199-8,* page 21, Pittsburgh, 1985.

5. I.H. Hutchinson and K. Kato. Diagnosis of Mildly Relativistic Electron Distributions by Cyclotron Emission. Bulletin of the American Physical Society, 30:1494, 1985.

6. K. Kato and I.H. Hutchinson. Measurement of Non-Thermal Electron Distributions using the Vertical Viewing ECE Diagnostic. *Bulletin of the American Physical Society*, 30:1494, 1985.

7. K. Kato and I.H. Hutchinson. *Non-Thermal Electron Velocity Distribution Measured by Electron Cyclotron Emission in Alcator C Tokamak.* PFC/JA-85-37, MIT Report, 1985. Physical Review Letters, 56:340, 1986.

8. K. Kato and I.H. Hutchinson. *Design and Performance of Compact Vacuum-Compatible Viewing Dumps.* PFC/JA-86-3, MIT Report, 1986. Review of Scientific Instruments, 57:1242, 1986.

9. I.H. Hutchinson, K. Kato and S.C. Texter. *Measurement of Mildly Relativistic Electron Distribution Function During Lower Hybrid Heating and Current Drive.* Review of Scientific Instruments, 57:1951, 1986.

10. K. Kato and I.H. Hutchinson. *Alcator C Vertical Viewing Electron Cyclotron Emission Diagnostic.* PFC/CP-86-6, MIT Report, 1986. Review of Scientific Instruments, 57:1959, 1986.

11. K. Kato and I.H. Hutchinson. Measurements of Polarized Electron Cyclotron Emission from Alcator C. Abstract submitted to the Americal Physical Society Division of Plasma Physics Meeting, 1986.

Bibliography

[1] A. Einstein. Zur Electrodynamik bewegter Körper. *Annalen der Physik*, 17:891, 1905.

[2] B. Coppi and J. Rem. The Tokamak Approach in Fusion Research. *Scientific American*, 227:65, 1972.

[3] N.J. Fisch. Confining a Tokamak Plasma with RF-Driven Currents. *Phys. Rev. Lett.*, 41:873, 1978.

[4] I. Fidone, G. Giruzzi, G. Granata, and R.L. Meyer. Electron Cyclotron Heating in RF Current-Driven Tokamak Plasmas. *Phys. Fluids*, 27:661, 1984.

[5] H. Knoepfel and D.A. Spong. Runaway Electrons in Toroidal Discharges. *Nucl. Fusion*, 19:785, 1979.

[6] A.S. Wan, T.F. Yang, B. Lipschultz, and B. LaBombard. Janus, a Bidirectional, Multifunctional Plasma Diagnostic. *Rev. Sci. Instrum.*, August 1986.

[7] S. von Goeler, J. Stevens, S. Bernabei, M. Bitter, T.K. Chu, P. Efthimion, N. Fisch, W. Hooke, K. Hill, J. Hosea, F. Jobes, C. Karney, R. Motley, P. Roney, S. Sesnic, K. Silber, and G. Taylor. Angular Distribution of the Bremsstrahlung Emission During Lower Hybrid Current Drive on PLT. *Nucl. Fusion*, 25:1515, 1985.

[8] D.A. Boyd. Experimental Measurements on Non-Maxwellian Distributions. In *Proc. 4th Int. Workshop on ECE and ECRH*, page 145, Rome, March 28–30 1984.

[9] J. Stevens, S. von Goeler, S. Bernabei, M. Bitter, T.K. Chu, P. Efthimion, N. Fisch, W. Hooke, J. Hosea, F. Jobes, C. Karney, E. Meservey, R. Motley, and G. Taylor. Modelling of the Electron Distribution Based on Bremsstrahlung Emission During Lower-Hybrid Current Drive. *Nucl. Fusion*, 25:1529, 1985.

[10] B.A. Trubnikov. Plasma Radiation in a Magnetic Field. *Doklady Acad.*, 3:913, 1958.

[11] G. Bekefi. *Radiation Processes in Plasmas*. Wiley, New York, 1966.

[12] F. Engelmann and M. Curatolo. Cyclotron Radiation from a Rarefied Inhomogeneous Magnetoplasma. *Nucl. Fusion*, 13:497, 1973.

[13] R. Cano and TFR Group. Electron Temperature Radial Profile Deduced from Cyclotron Emission in TFR. In *Controlled Fusion and Plasma Physics(Proc. 7th European Conf.)*, page 14b, Lausanne, 1975.

[14] P. Brossier, A.E. Costley, D.S. Komm, G. Ramponi, and S. Tamor. Electron Cyclotron Emission from Tokamak Plasmas. In *Plasma Phys. and Controlled Nucl. Fusion Research, 1976, Vol.1*, page 401, IAEA, 1977.

[15] I.H. Hutchinson. Submillimeter Emission in Alcator Tokamak. *Infrared Phys.*, 18:763, 1978.

[16] F.J. Stauffer, D.A. Boyd, R.C. Cutler, and M.P. McCarthy. TFTR Michelson Interferometer Electron Cyclotron Emission Diagnostic. *Rev. Sci. Instrum.*, 56:925, 1985.

[17] A.E. Costley, R.J. Hastie, J.W.M. Paul, and J. Chamberlain. Electron Cyclotron Emission from a Tokamak Plasma — Experiment and Theory. *Phys. Rev. Lett.*, 33:758, 1974.

[18] H.P. Freund and C.S. Wu. Effects on the Spontaneous Emission of Synchrotron Radiation from Weakly Relativistic Electrons. *Phys. Fluids*, 20:963, 1977.

[19] S. Tamor. *The Absorption Coefficient of a Magnetized Plasma for Cyclotron Radiation*. Technical Report LAPS-26 SAI77-593-LJ, Science Applications, Inc., April 1977. .

[20] H.P. Freund, C.S. Wu, L.C. Lee, and D. Dillenburg. Spontaneous Synchrotron Emission from a Plasma with an Energetic Runaway Electron Tail. *Phys. Fluids*, 21:1502, 1978.

[21] G. Giruzzi, I. Fidone, G. Granata, and R.L. Meyer. Electron Cyclotron Emission in a RF Current Driven Tokamak Plasma. *Phys. Fluids*, 27:1704, 1984.

[22] C.M. Celata and D.A. Boyd. Cyclotron Radiation as a Diagnostic Tool for Tokamak Plasmas. *Nucl. Fusion*, 17:735, 1977.

[23] I. Fidone, G. Granata, R.L. Meyer, E.H. Jornada, R.S. Schneider, and L.F. Ziebell. Electron Cyclotron Emission from Tokamak Plasmas with Mildly Superthermal Electrons. *Phys. Fluids*, 23:1336, 1980.

[24] D. Winske and D.A. Boyd. Synchrotron Emission from a Relativistic Loss-Cone Distribution with Application to the ELMO Bumpy-Torus Experiment. *Phys. Fluids*, 26:755, 1983.

[25] D. Winske, Th. Peter, and D.A. Boyd. Synchrotron Emission from Runaway Electron Distributions. *Phys. Fluids*, 26:3497, 1983.

[26] R.F. Ellis, D.B. Robinson, and G.D. Tsakiris. Spectrum of Synchrotron Emission Parallel to a Magnetic Field for Relativistic Loss-Cone-Type Energy Distributions. *Phys. Rev. A*, 26:3683, 1982.

[27] T. Uckan and N.A. Uckan. Synchrotron Emission from the Relativistic Ring Electrons in the ELMO Bumpy Torus. *Phys. Fluids*, 25:2372, 1982.

[28] A. Murdoch, D.A. Boyd, and R.F. Ellis. Electron Cyclotron Emission from Mirror Trapped Energetic Electrons: Theoretical Computations and Analysis. In *Bull. Am. Phys. Soc. Vol.30*, page 1420, October 1985.

[29] F.J. Stauffer, D.A. Boyd, and A.W. Trivelpiece. An Algorithm to Determine Electron Energy Distributions from Synchrotron Radiation Measurements. *Physics Letters*, 57A:401, 1976.

[30] G.D. Tsakiris, D.A. Boyd, D.A. Hammer, A.W. Trivelpiece, and R.C. Davidson. Electron Energy Distribution of a Mirror Confined Relativistic Plasma Inferred from Synchrotron Radiation Measurements. *Phys. Fluids*, 21:2050, 1978.

[31] D.J. Campbell, A. Eberhagen, and S.E. Kissel. Analysis of Electron Cyclotron Emission from Non-Thermal Discharges in Asdex Tokamak. *Nucl. Fusion*, 24:297, 1984.

[32] H.W. Piekaar and W.R. Rutgers. *Cyclotron Radiation from Thermal and Non-Thermal Electrons in the Wega-Stellarator*. Technical Report 80-128, Rijnhuizen, Netherlands, November 1980.

[33] E. Mazzucato, P. Efthimion, and I. Fidone. Absorption of Cyclotron Waves at Down-Shifted Frequencies by an Energetic Electron Tail in the PLT Tokamak. *Nucl. Fusion*, 25:1681, 1985.

[34] I.H. Hutchinson and D.S. Komm. Electron Cyclotron Emission in Alcator Tokamak. *Nucl. Fusion*, 17:1077, 1977.

[35] S. Tamor. Interpretation of Cyclotron Radiation Spectra from Runaway Discharges in TFR. *Nucl. Fusion*, 19:455, 1979.

[36] J.S. Machuzak, private communication, 1986.

[37] Massachusetts Institute of Technology, Plasma Fusion Center, Technical Research Programs, January 1984.

[38] C. Weggel, W. Hamburger, B. Montgomery, and N. Pierce. The Alcator C Magnetic Coil Systems. In *Proceedings of the 7th Symposium on Engineering Problems of Fusion Research*, page 54, Knoxville, Tennessee, 1977.

[39] D.B. Montgomery. *The Alcator Project*. Technical Report, Francis Bitter National Magnet Laboratory, 1974.

[40] R.R. Parker, M. Greenwald, S.C. Luckhardt, E.S. Marmar, M. Porkolab, and S.M. Wolfe. Progress in Tokamak Research at MIT. *Nucl. Fusion*, 25:1127, 1985.

[41] M. Greenwald, D. Gwinn, S. Milora, J. Parker, R. Parker, S. Wolfe, M. Besen, F. Camacho, S. Fairfax, C. Fiore, M. Foord, R. Gandy, C. Gomez, R. Granetz, B. LaBombard, B. Lipschultz, B. Lloyd, E. Marmar, S. McCool, and D. Pappas. Energy Confinement of High-Density Pellet-Fueled Plasmas in the Alcator C Tokamak. *Phys. Rev. Lett.*, 53:352, 1984.

[42] M. Porkolab, J.J. Schuss, B. Lloyd, Y. Takase, S. Texter, P. Bonoli, C. Fiore, R. Gandy, D. Gwinn, B. Lipschultz, E. Marmar, D. Pappas, R. Parker, and P. Pribyl. Observation of Lower-Hybrid Current Drive at High Densities in the Alcator C Tokamak. *Phys. Rev. Lett.*, 53:450, 1984.

[43] M. Porkolab, B. Lloyd, Y. Takase, P. Bonoli, C. Fiore, R. Gandy, R. Granetz, D. Griffin, D. Gwinn, B. Lipschultz, E. Marmar, S. McCool, A. Pachtman, D. Pappas, R. Parker, P. Pribyl, J. Rice, J. Terry, S. Texter, and R Watterson. High-Power Electron Landau-Heating Experiments in the Lower Hybrid Frequency Range in a Tokamak Plasma. *Phys. Rev. Lett.*, 53:1229, 1984.

[44] S.C. Texter. *Plasma X-Ray Spectroscopy During Lower Hybrid Current Drive in Alcator*. Technical Report PFC/RR-85-24, M.I.T., December 1985.

[45] M. Bornatici, R. Cano, O. DeBarbieri, and F. Engelmann. Review Paper: Electron Cyclotron Emission and Absorption in Fusion Plasmas. *Nucl. Fusion*, 23:1153, 1983.

[46] T.H. Stix. *The Theory of Plasma Waves*. McGraw-Hill, New York, 1962.

[47] N.I. Furashov. Far Infrared Absorption by Atmospheric Water Vapor. *Optics and Spectroscopy*, 20:234, 1966.

[48] J.B. Marion and W.F. Hornyak. *Physics for Science and Engineering, Part 2*. Saunders College, New York, 1981.

[49] Manufactured by the National Physical Laboratory of Great Britain.

[50] NAD 2155, manufactured by NAD, Inc., Norwood Massachusetts.

[51] Supplied by Specac, Orpington, Kent, Great Britain.

[52] Manufactured by Dr. Johannes Heidenhain, Traunreut, GmbH. Supplied along with the air-bearing by Specac, Orpington, Kent, Great Britain.

[53] R. J. Bell. *Introductory Fourier Transform Spectroscopy*. Academic Press, New York, 1972.

[54] Supplied by QMC Instruments, London, Great Britain.

[55] E.H. Putley. Indium Antimonide Submillimeter Photoconductive Detectors. *Appl. Opt.*, 4:649, 1965.

[56] Manufactured by Infrared Laboratories, Tucson, Arizona.

[57] S.E. Kissel. *Thermal and Non-Thermal Submillimetre Emission from Alcator Tokamak*. Technical Report PFC/RR-82-15, M.I.T., 1982.

[58] W.M. Rohsenow and H. Choi. *Heat, Mass, and Momentum Transfer*. Prentice Hall, New Jersey, 1961.

[59] P. Woskoboinikow, H.C. Praddaude, W.J. Mulligan, D.R. Cohn, B. Lax, and H.R. Fetterman. D_2O Laser Thomson Scattering and Submillimeter Heterodyne Receiver Measurements. In *6th Int. Conf. Infrared and Millimeter Waves, Conf. Digest, IEEE Cat. No. 81 CH1645-1 MTT*, 1981.

[60] Manufactured by Emerson & Cuming, Inc., Canton, Massachusetts.

[61] P. Woskoboinikow, R. Erickson, and W.J. Mulligan. Submillimeter-Wave Dumps for Fusion Plasma Diagnostics. *Int. Journal IR and MM Waves*, Vol. 4:1045, 1983.

[62] M.A. Sengstacke, R.N. Dexter, and S.C. Prager. Polarized Electron Cyclotron Emission in the Tokapole II Tokamak. *Phys. Fluids*, 28:403, 1985.

[63] V.O. Altemose and A.R. Kacyon. *Vacuum Compatibility of Machinable Glass Ceramics*. Corning Tech. Paper, Corning Glass Works, Corning, N.Y.

[64] Material selection based on private communication with Woskoboinikow, P., 1983.

[65] K.H. Breeden and A.P. Sheppard. A Note on the Millimeter and Submillimeter Wave Dielectric Constant and Loss Tangent Value of Some Common Materials. *Radio Science*, 3:205, 1968.

[66] M.N. Afsar and K.J. Button. Precise Millimeter Wave Measurements of Complex Refractive Index, Complex Dielectric Permittivity and Loss Tangent of GaAs, Si, Al2O3, BeO, Macor and Glass. *IEEE Tr. Microwave Theory and Techniques*, MTT-31:217, 1983.

[67] G. Bekefi and A. Barrett. *Electromagnetic Vibrations, Waves, and Radiation*. MIT Press, Cambridge, Mass., 1977.

[68] Grinding of dump pieces were done at Ceramic Grinding Company, Waltham, Massachusetts.

[69] M.F. Kimmitt. *Far-Infrared Techniques*. Pion, London, NW2, 1970.

[70] I.H. Hutchinson and S.E. Kissel. Calibration of a Rapid-Scan Michelson Interferometer and InSb Detector. In *Proc. 4th Int. Conf. Infrared and Millimeter Waves and their Applications*, page 76, Miami Beach, 1979.

[71] LeCroy Research Systems, Palo Alto, Calif.

[72] C.C. Gomez. *Study of Electron Temperature Evolution During Sawtoothing and Pellet Injection Using Thermal Electron Cyclotron Emission in the Alcator C Tokamak*. Technical Report PFC/RR-86-8, M.I.T., 1986.

[73] M.F. Kimmitt. *A Far Infrared Spectrometer*. Technical Report No. 716, Royal Radar Establishment, Ministry of Aviation, 1965.

[74] J.J. Schuss and J.C. Hosea. Mode Conversion and Harmonic Generation at the Upper Hybrid Layer in Toroidal Plasmas. *Phys. Fluids*, 18:727, 1975.

[75] J.J. Schuss, M. Porkolab, D. Griffin, S. Barilovits, M. Besen, C. Bredin, G. Chihoski, H. Israel, N. Pierce, D. Reiser, and K. Rice. Engineering Aspects of Lower Hybrid Microwave Injection into the Alcator C Tokamak. In *Proceedings of the Fifth Topical Meeting on the Technology of Fusion Energy*, Knoxville, Tennessee, 1983.

[76] V.V. Parail and O.P. Pogutse. The Kinetic Theory of Runaway Electron Beam Instability in a Tokamak. *Nucl. Fusion*, 18:303, 1978.

[77] K. Swartz, I.H. Hutchinson, and K. Molvig. Plasma Frequency Radiation in Tokamaks. *Phys. Fluids*, 24:1689, 1981.

[78] C.F.F. Karney and N. Fisch. Numerical Studies of Current Generation by Radio-Frequency Waves. *Phys. Fluids*, 22:1817, 1979.

[79] P.R. Bevington. *Data Reduction and Error Analysis for the Physical Sciences.* McGraw-Hill, New York, 1969.

[80] A.A.M. Oomens, L.Th.M. Ornstein, R.R. Parker, Schüller, F.C., and R.J. Taylor. Observation of High-Frequency Radiation and Anomalous Ion Heating on Low-Density Discharges in Alcator. *Phys. Rev. Lett.*, 36:255, 1976.

[81] K. Hizanidis and A. Bers. Steady-State RF-Current Drive Theory Based Upon the Relativistic Fokker-Planck Equation with Quasilinear Diffusion. *Phys. Fluids*, 27:2669, 1984.

[82] V.B. Krapchev, D.W. Hewett, and A. Bers. Analytic Solution of the 2-D Fokker-Planck Equation for LH Current Drive. In *Proc. 4th Int. Symposium on Heating in Toroidal Plasmas*, page 674, Rome, March 21–28 1984.

[83] D. Hewett, K. Hizanidis, V. Krapchev, and A. Bers. Two-Dimensional and Relativistic Effects in Lower Hybrid Current Drive. In D.F.H. Start, editor, *Proceedings of the IAEA Technical Committee Meeting on Non-Inductive Current Drive in Tokamaks*, pages Vol. II, 124, UKAEA Association CLM-CD, 1983.

[84] K. Hizanidis, D.W. Hewett, and A. Bers. Solution of the Relativistic 2-D Fokker-Planck Equation for LH Current Drive. In *Proc. 4th Int. Symposium on Heating in Toroidal Plasmas*, page 668, Rome, March 21–28 1984.

[85] H.W. Koch and J.W. Motz. Bremsstrahlung Cross-Section Formulas and Related Data. *Rev. Modern Phys.*, 31:920, 1959.

[86] M. Born and E. Wolf. *Principles of Optics.* Pregamon Press, address, 1983.

[87] F.B. Hildebrand. *Advanced Calculus for Applications.* Prentice-Hall, New Jersey, 1976.